Pontifícia Universidade Católica
do Rio de Janeiro

Gustavo Vinicius Lourenço Moisés

Effects of yield stress and thixotropy in non-Newtonian isodense displacement

TESE DE DOUTORADO

Thesis presented to the Programa de Pós-Graduação em Engenharia Mecânica of the Departamento de Engenharia Mecânica, PUC-Rio as partial fulfillment of the requirements for the degree of Doutor em Engenharia Mecânica.

Advisor: Profa. Mônica Naccache
Co-Advisor: Prof. Ian Frigaard

Rio de Janeiro
April 2016

Pontifícia Universidade Católica
do Rio de Janeiro

Gustavo Vinicius Lourenço Moisés

Effects of yield stress and thixotropy in non-Newtonian isodense displacement

Thesis presented to the Programa de Pós-Graduação em Engenharia Mecânica of the Departamento de Engenharia Mecânica do Centro Técnico Científico da PUC-Rio, as partial fulfilment of the requirements for the degree of Doutor.

Profa. Mônica Feijó Naccache
Advisor
Departamento de Engenharia Mecânica – PUC-Rio

Prof. Ian Alistair Frigaard
Co-Advisor
University of British Columbia

Prof. Paulo Roberto de Souza Mendes
Departamento de Engenharia Mecânica – PUC-Rio

Prof. Luis Fernando Alzuguir Azevedo
Departamento de Engenharia Mecânica – PUC-Rio

Prof. Roney Leon Thompson
Universidade Federal Fluminense

Prof. Geraldo Afonso Spinelli Martins Ribeiro
Departamento de Engenharia Mecânica – PUC-Rio

Dr. Rafael Mendes
Petrobras

Prof. Márcio da Silveira Carvalho
Coordinator of the Centro Técnico Científico da PUC-Rio

Rio de Janeiro, April 12nd, 2016

Gustavo Vinicius Lourenço Moisés

The author graduated from the University of Brasília (Brasília, Brazil) in Controls and Automation Engineering in 2003 and obtained his Master degree at UNICAMP in Electrical Engineering in 2005. In 2004 he started to work as a petroleum engineer at Petrobras, where he works as a technical consultant in multiphase flow simulation, flow assurance and artificial lift, primarily in pre-salt fields development projects.

Bibliographic data

Moisés, Gustavo Vinicius Lourenço

Effects of yield stress and thixotropy in non-Newtonian isodense displacement / Gustavo Vinicius Lourenço Moisés ; adviser: Mônica Naccache ; co-adviser: Ian Frigaard. – 2016.

186 f. : il. color. ; 30 cm

Tese (doutorado)–Pontifícia Universidade Católica do Rio de Janeiro, Departamento de Engenharia Mecânica, 2016.

Inclui bibliografia

1. Engenharia mecânica – Teses. 2. Tensão limite. 3. Tixotropia. 4. Experimentos. 5. Deslocamento de fluidos. I. Naccache, Mônica. II. Frigaard, Ian. III. Pontifícia Universidade Católica do Rio de Janeiro. Departamento de Engenharia Mecânica. IV. Título.

CDD: 621

Acknowledgments

To my advisors Professors Naccache and Frigaard for the daily based support and keep going attitude.

To Professors Paulo de Souza Mendes, Luiz Fernando Azevedo and Roney Thompson and my co-workers Rafael Mendes and Geraldo Spinelli for revising this thesis.

To Petrobras, CAPES and PUC-Rio, for the financial support, without which this work would not have been accomplished.

To my wife Cynthia, who I love most, for the courage of following me with 2 children to the frozen prairies of Canada.

To my daughter Beatriz for her tenderness support that conquered my heart since she opened her dazzling blue eyes.

To my son Pedro for his incredible way to make me laugh in any circumstances.

To my family in Brasília, specially mom and dad, for developing a buttressed base that bears out my life.

To my friends Denise Diniz and Sérgio Paulo that were always there.

To the Búzios project team, mainly Ivan Noville and João Gabriel, who worked with the strength of a thousand men.

To Geraldo Spinelli, Guilherme Peixoto, José Ricardo and Cezar Paulo for the confidence in me.

To the Rheology Group (GReo) of PUC-Rio for their constant support, particularly to Alexandra, Aline, Bruna and Priscila.

To Alba Kamran for his mentoring in how to run experiments and write articles.

To Geoff Dunbrack, Sara Hormozi, Sean Buxton and Perry Yabuno for your kindness trouble shooting guidance during the intense experimental campaign.

To Steven Dong and Alessander Gosselin for their help in running the experiments in a hot summer of Vancouver.

To the Brazilian funding agencies (MCTI/CNPq, CAPES, FAPERJ and FINEP) for supporting the science development in Brazil.

To NSERC/Schlumberger for partial funding for the experimental programme via CRD project 444985-12.

To Vancouver the most beautiful city of the world where I should always come back.

Abstract

Moisés, Gustavo Vinicius Lourenço; Naccache, Mônica (Advisor); Frigaard, I. (co-Advisor). **Effects of yield stress and thixotropy in non-Newtonian isodense displacement**. Rio de Janeiro, 2016. 186p. Tese Doutorado - Departamento de Engenharia Mecânica, Pontifícia Universidade Católica do Rio de Janeiro.

The yield stress appearance when gelation occurs in wax crude oils constitutes a significant problem in subsea flowline in deepwater oil production systems. In essence, there exist two stages in a pipeline flow restart after a long shutdown: apply a large enough differential pressure in order to mobilize the gel in the pipe, i.e. a process of *fluid start-up* or inject miscible fluid with low viscosity, preferably Newtonian, at the pipe inlet, to flush the gelled oil out of the pipe, i.e. a process of *fluid displacement*. We investigate yield stress and thixotropy effects over non-Newtonian fluid flows in a horizontal pipe, considering the fluid start- up and the fluid displacement in the isodense limit. The yield stress and thixotropic properties of waxy crude oils are rheologicaly simulated by water base fluids, Carbopol solutions and Laponite suspensions. The results of experimental and numerical studies of isodense displacement of a yield stress fluid are presented. Three distinct flow types belonging to this central displacement are identified in the experiments namely *corrugated*, *wavy* and *smooth* depending on the level of the residual layer variation along the pipe. The transition between these flow regimes is found to be a function of the ratio between the inertial stress and the characteristic viscous stress of the viscoplastic fluid. Besides, the influence of NaCl and Laponite concentrations in the rheological parameters of Laponite suspensions is detailed and the impact of thixotropy in the start-up of Laponite suspensions are analyzed based on experimental results.

Keywords

Yield stress; thixotropy; fluid displacement; flow regimes; experiments.

Resumo

Moisés, Gustavo Vinicius Lourenço; Naccache, Mônica; Frigaard, Ian. **Efeitos da tensão limite e tixotropia em deslocamento de fluidos não-Newtonianos de mesma densidade**. Rio de Janeiro, 2016. 186p. Tese de Doutorado - Departamento de Engenharia Mecânica, Pontifícia Universidade Católica do Rio de Janeiro.

O aparecimento de tensão limite decorrente da gelificação de óleo parafínicos constitui um problema significativo em linhas submarinas nos sistemas de produção de petróleo em água profundas. Essencialmente, existem dois modos para garantir retorno da produção em oleodutos após longas paradas: aplicar um elevado diferencial de pressão suficiente para mover o gel no duto, *reinício de produção*, ou injetar um fluido misccível de baixa viscosidade, preferencialmente Newtoniano, na entrada do duto, processo denominado *deslocamento de fluido*. Nós investigamos os efeitos da tensão limite e da tixotropia no escoamento de fluidos não Newtonianos em dutos horizontais, considerando tanto o reinício de produção quanto o deslocamento de fluidos sem diferença de densidade. Tanto a tensão limite como as propriedades tixotrópicas dos óleos parafínicos foram simuladas reologicamente por fluidos base água, soluções de Carbopol e suspensões de Laponita. Os resultados experimentais e os estudos numéricos do deslocamento de fluidos com tensão limite sem diferença de densidade são apresentados. Três tipos distintos de escoamento, que pertencem a categoria deslocamento central, foram identificados nos experimentos e chamados de *corrugado*, *ondulado* e *liso* a depender do nível de variação da camada residual ao longo do duto. A transição entre esses regimes foi identificada como da razão entre a tensão inercial e a tensão característica do fluido viscoplástico. Além disso, a influência das concentrações de NaCl e Laponita nos parâmetros reológicos das suspensões de Laponita é detalhada e o impacto da tixotropia no reinício de produção de suspensões de Laponita foi analisada com base em dados experimentais.

Palavras-chave

Tensão limite; tixotropia; deslocamento de fluidos; regime de fluxo; experimentos.

Contents

Lista de Figuras

Lista de Tabelas

Nomenclature

$\hat{\alpha}_L$ Parameter of light intensity conversion []

$\hat{\beta}$ Angle between the vertical line and the loop position [°]

$\hat{\beta}_L$ Parameter of light intensity conversion []

$\hat{\dot{\gamma}}$ Shear rate [1/s]

$\hat{\dot{\gamma}}_c$ Characteristic shear rate [1/s]

$\dot{\gamma}(\mathbf{v})$ Strain tensor

$\hat{\dot{\gamma}}_c^F$ Critical shear rate for Fluent Herschel-Bulkley model regularization [1/s]

$\delta\overline{C}$ Standard deviation of the depth-averaged concentration $\overline{C}_y$[-]

δd_c Standard deviation of $d_c/2$[-]

δd_f Standard deviation of $d_f/2$[-]

δd_i Standard deviation of $d_i/2$[-]

δV_f Standard deviation of the spatially varying front velocity V_f [-]

$\delta\overline{Q}$ Uncertainty of $\overline{Q}$ [-]

ϵ Relative roughness [-]

ϵ_i Equivalent roughness from variable i[-]

ϵ_c Equivalent roughness from C [-]

ϵ_{eq} Average roughness [-]

ϵ_f Equivalent roughness from V_f [-]

$\hat{\eta}$ Effective viscosity [Pa.s]

$\hat{\eta}_0$ Effective viscosity limit at low shear rates in the Newtonian plateau region [Pa.s]

$\hat{\eta}_\infty$ Effective viscosity limit at high shear rates in the Newtonian plateau region [Pa.s]

$\hat{\eta}_c$ Characteristic viscosity [Pa.s]

η^{Dapra} Dimensionless radius from Dapra and Scarpi (2005) [-]

η_{infty}^{Dapra} Dimensionless asymptotic plug radius from Dapra and Scarpi (2005) [-]

θ^{Dapra}	Dimensionless stress from Dapra and Scarpi (2005) [-]
λ	Structured parameter [-]
λ_{eq}	Equilibrium structured parameter [-]
$\hat{\mu}$	Newtonian fluid viscosity [Pa.s]
$\hat{\mu}_1$	Viscosity of Newtonian fluid 1 [Pa.s]
$\hat{\mu}_2$	Viscosity of Newtonian fluid 2 [Pa.s]
$\hat{\rho}$	Fluid density [kg/m3]
$\hat{\rho}_1$	Density of fluid 1 [kg/m3]
$\hat{\rho}_2$	Density of fluid 2 [kg/m3]
$\boldsymbol{\tau}$	Deviatoric stress
$\hat{\tau}$	Stress [Pa]
$\hat{\tau}_c$	Characteristic Stress [Pa]
$\hat{\tau}_i$	Interface stress in region II [Pa]
$\hat{\tau}_y$	Yield Stress [Pa]
$\hat{\tau}_w$	Wall stress in region II [Pa]
v	Dimensionless axial velocity from Dapra and Scarpi (2005) [-]
$\hat{v}_2$	Kinematic viscosity of fluid 2 [m²/s]
a	Build-up rheological parameter from (Souza Mendes, 2011) [-]
b	Break-down rheological parameter (Souza Mendes, 2011) [-]
C	Concentration of fluid 2 [-]
$\overline{C}$	Mean concentration of fluid 2 in the tube section [-]
C_{max}	Maximum ink concentration for exponential model [-]
$\overline{C}_y$	Depth-averaged concentration [-]
$\hat{d}$	Displacing fluid diameter/width [m]
d_C	Equivalent displacing diameter from $\bar{C}$ [-]
d_f	Equivalent displacing diameter from Vf [-]
$\hat{d}_{min}$	Minimum inner diameter of the displacing fluid [mm]
$\widehat{D}$	Tube diameter [mm]

Dif Average diffusion coefficient between two fluids [ ]

f Friction factor []

$g(t)$ Mean velocity transient function [mm/s]

$\hat{g}$ Gravitation acceleration [m^2/s]

G' Elastic Modulus [Pa]

G'' Viscous Modulus [Pa]

$\hat{h}$ Residual layer thickness [mm]

H Heaviside unit-step function [-]

I Ionic Strength or NaCL concentration [mol/L]

$\widehat{K}$ Fluid consistency index of Herschel-Bulkley model [$Pa.s^n$]

$\widehat{K}_{Cross}$ Consistency index parameter from Cross relation [1/s]

$\widehat{K}_N$ Fluid consistency index from modified Herschel-Bulkley model with a Newtonian plateau [$Pa.s^n$]

L_N Characteristic length that shows the influence of the front in the Newtonian fluid area in region *iii* [-]

L_{NN} Characteristic length that shows the influence of the front in the non-Newtonian fluid area in region *iii* [-]

$\hat{L}$ Tube Length [m]

$\hat{L}_0$ Equivalent length if mean velocity is considered [m]

$\hat{L}_C$ Computational tube length [m]

$\hat{L}_{Ta}(\hat{t})$ Meniscus position in the axial direction $\hat{x}$ at time $\hat{t}$ [m]

$\hat{L}_{Ta}$ Meniscus position in the axial direction $\hat{x}$ for $\hat{t} = \hat{t}_{exp}$ [m]

m Remaining fluid fraction [-]

m_1 Remaining fluid fraction by Taylor's method [-]

m_2 Remaining fluid fraction by velocity method [-]

m_3 Remaining fluid fraction by residual layer method [-]

$m_{\max}$ Maximum remaining fluid fraction [-]

n Power law index of Herschel-Bulkley model [-]

n_N Power law index from modified Herschel-Bulkley model with a Newtonian plateau [-]

n_x	Number of pixels in axial direction of a tube section [-]
n_y	Number of pixels in the radial direction of a tube section [-]
n_{Cross}	Power law index from Cross relation [1/s]
N	Total number of images of an experiment [-]
$\hat{P}$	Pressure [Pa]
$\hat{P}_0$	Pressure at $\hat{x} = 0$ mm [Pa]
$\hat{P}_{outlet}$	Pressure at tube outlet [Pa]
Q	Bulk experimental data quality [-]
$\overline{Q}$	Mean value of Q [-]
Q_0	Flow rate at steady state from Dapra and Scarpi (2005) [m^3/s]
$\hat{r}$	Radial position [mm]
$\hat{R}$	Tube radius [mm]
$\hat{s}_r$	Mesh element size in the radial direction $\hat{r}$ [m]
$\hat{s}_x$	Mesh element size in the axial direction $\hat{x}$ [m]
S	Tube section [-]
$\hat{t}$	Time [s]
$\hat{t}_c$	Characteristic time [s]
t_{eq}	Equilibrium time [s]
$\hat{t}_{exp}$	Total experimental time [s]
$\hat{t}_f$	Time prior the ball valve closure [s]
$\hat{t}_{min}$	Minimum time to cross one mesh element in $\hat{x}$ direction [s]
$\hat{t}_{SS}$	Time to reach steady state conditions [s]
$\hat{T}$	Surface tension [Pa.m]
U	Magnitude of axial velocity [mm/s]
$\mathbf{v}$	Velocity vector
$\hat{V}_0$	Mean flow velocity [mm/s]
$\hat{V}_0(\hat{t})$	Mean velocity at time $\hat{t}$ [mm/s]
V_f	Dimensionless front velocity [-]

$\overline{V}_f$ Average of V_f [-]

$\hat{V}_f$ Front velocity at fully developed flow [mm/s]

$\hat{V}_f(\hat{t})$ Front velocity at time $\hat{t}$ [mm/s]

$\hat{V}_{max}$ Maximum velocity along the tube [mm/s]

$\hat{V}_{max}^{N}$ Maximum velocity in the Newtonian area [mm/s]

$\hat{V}_{max}^{NN}$ Maximum velocity in the non-Newtonian area [mm/s]

$\hat{x}$ Axial position [mm]

$\hat{x}_i$ Position along the interface [m]

$\hat{x}_f$ The axial position of the front (bubble) tip [m]

$\hat{w}$ Final discharged fluid weight [kg]

$\hat{w}(\hat{t})$ Discharged fluid weight at time $\hat{t}$ [kg]

$\hat{w}_0$ Weight of the fluid in the tube when full [kg]

$\hat{w}_{HS}$ Channel width of a Helen-Shaw cell [m]

At Atwood number [-]

B Bingham number [-]

B_N Newtonian Bingham number [-]

Ca Capillary number [ ]

F Parameter from Petitjeans and Maxworthy (1996) that compares gravitational forces to viscous effects [-]

Fr Froude number [-]

M Viscosity stress ratio [-]

Pe Ratio between advection flow and diffusion [-]

Re Reynolds number [-]

Re_h Hydraulic Reynolds number [-]

Re_L Threshold Reynolds from laminar to transitional flow [-]

Re_N Newtonian Reynolds number [-]

Re_T Threshold Reynolds from transitional to turbulent flow [-]

Life is far too important a thing ever to talk seriously about.

Oscar Wilde*, Lady Windermere's Fan*

1
Introduction

This thesis investigates yield stress and thixotropy effects over non-Newtonian fluid flows in a horizontal pipe. Two flow types are considered: non-Newtonian fluid start-up and isodense displacement of yield stress fluid by a less viscous Newtonian fluid. Start-up and displacement flows are presented in our ordinary life activities such as opening the tap for brushing our teeth. However, we are interested in non-Newtonian fluid flows that includes squeezing the tube to move the tooth paste out of it.

In industry, there are processes in which is necessary to remove gelled or soft-solid from a duct. Examples include bio-medical applications (mucus, biofilms), cleaning of equipment, food processing. Although such displacement problems have applications in many areas (oceanography, hydrology, food and chemical engineering), our main motivation comes from complex displacement flows that exist in many processes related to the oil and gas industry.

We performed start-up and displacement experiments of non-Newtonian fluids in a 4 m long loop. Instead of waxy crude oils or drilling mud, environmentally friend laboratory fluids (water based) are considered. The yield stress and thixotropic properties of a waxy crude oil are rheologically simulated by Carbopol solutions and Laponite suspensions.

We studied in details the influence of yield stress in fluid displacement by experimental and numerical simulation analyses. The results show the displacement efficiency, the amount of residual mass after flushing, and how the rheological parameters and differential pressure influence the yield stress fluid displacement. The fluid dynamics is also presented by contours, variable distribution and velocity profiles. We also mapped different regimes based on the residual layer roughness.

We also performed experiments to understand how thixotropy affects the start-up flows. First, the Laponite rheological characterization is developed to understand how rheological parameters of Laponite suspensions are influenced by the Laponite and NaCl concentrations. Second, the transient analysis of start-up is presented and velocity profile evolution and thixotropy effects are described.

1.1
Motivation

One of the main issues in deepwater production in the oil industry is the blockage of production lines, caused by the growth of paraffin crystals that occur when temperature drops below the Wax Appearance Temperature (WAT). In general, the produced oil presents some amount of wax that turns into paraffin crystals when temperature is lower than WAT, resulting in a gel-like structure with rheological properties completely different from that of the crude oil (Venkatesan et al. (2005) [1]) at reservoir temperature. The appearance of a yield stress when gelation occurs constitutes a significant problem in static conditions that occur in the restart flow, needed after a shutdown.

In essence, there exist two stages in a flow pipeline restart, as described by Frigaard et al. (2007) [2]. The first stage is to apply a large enough differential pressure in order to mobilize the gel in the pipe i.e. a process of *fluid start-up*. This is related to the pipeline length and to the fluid yield stress and bulk compressibility (Vinay et al., 2005 [3], 2006 [4], 2007 [5]; Wachs et al., 2009 [6]; Dapra and Scarpi, 2005 [7]).

The second stage consists of the injection of either miscible fresh oil or any other low viscosity fluid (preferably Newtonian, e.g. sea water, diesel) at the pipe inlet, to flush the gelled oil out of the pipe, i.e. a process of *fluid displacement*. During this second stage mostly laminar flows occur, due to the relatively high yield stress of the gelled fluid and/or other process constraints.

Fluid displacement is an ordinary operation of flow assurance in ultra deep water field development. Hydrate blockage mitigation and wax deposition remediation, such as pigging, are examples of fluid displacement applications (Fung et al., 2006 [8]; Thomason, 2000 [9]).

The recent discoveries of petroleum reserves in the pre-salt layers of Santos basin (Brazil) reinforce the need for new engineering solutions and better understanding of the phenomena to minimize investment and operational costs associated, specially to waxy crude oil pipeline restarts (Pinho et al., 2011 [10]) and well constructions.

Well services usually apply non-Newtonian fluids where fluid displacement is also a major concern. The fluids involved during drilling and cementing (drilling

mud and cement slurry) are designed to minimize mixing at the fluids interface to avoid fluid contamination. Since the fluid displacement efficiency affects the cementing quality, it is necessary to understand the fluid displacement mechanism in details.

In Canada, horizontal well construction is another motivation for our study. Horizontal wells can increase well productivity and allow production of reservoirs under cities and preserved areas such as lakes and Indian reserves. In addition, they are part of the SAGD technology, an enhanced oil recovery (EOR) method that consists of injecting steam on a horizontal well and producing from one twin parallel well to improve reservoir recovery factor of highly viscous oil, thus increasing Canadian oil reserves.

The displacement flow of yield-stress fluids in general is a complex topic, due to the large number of flow parameters involved. Various flow regimes can be observed depending on the respective balances of inertial, viscous and buoyant stresses, see Taghavi et al. (2012) [11]; Alba et al. (2013) [12]. Allouche et al. (2000) [13] have shown that in a plane channel geometry and depending on the range of flow and rheological parameters, a fully static layer of the displaced yield stress fluid may be left behind after pumping the displacing fluid. Similar static layers were analytically detected in a pipe geometry by Frigaard et al. (2007) [2]. Gabard and Hulin (2003) [14] experimentally studied the isodense displacement flow of viscoplastic fluids by a Newtonian water-glycerol solution in a vertical pipe, confirming the existence of static residual layers. The residual film thickness in their experiments was found to be approximately 25% of the radius.

The effect of fluids density difference on viscoplastic (Carbopol solution) displacement flows has been explored in detail in previous studies. Two main flow regimes have been identified, for both nearly-horizontal (Taghavi et al., (2012) [11]) and inclined (Alba et al., 2013 [12]; Alba and Frigaard, (2016) [15]) geometries: namely *central* and *slump* displacements. A residual film thickness of ≈ 0.26 radius of the pipe is found in the central regime which is close to that reported in Gabard and Hulin (2003) [14] for isodense displacements. The central flows observed in Taghavi et al. (2012) [11]; Alba et al., 2013 [12] and Alba and Frigaard (2016) [15] are very similar to those found in *core removal* phase of water-toothpaste displacement from Cole et al. (2010) [16] and Palabiyik et. al (2014) [17].

In the context of central flows, Wielage-Burchard and Frigaard (2011) [18] studied the effect of inertia and flow *pulsation* on static residual wall layer thickness through 2D computations. Thinner layers were found at higher Reynolds numbers due to the locally increased energy production around the finger. Both small and large amplitudes were considered to study the effect of the flow rate pulsation.

The slump regimes found in Taghavi et al. (2012) [11]; Alba et al. (2013) [19] and Alba and Frigaard (2016) [15] emerge at larger fluid density differences and can be entirely different than the central regimes. Depending on the magnitude of the destabilizing buoyant stress, these flows can develop into exotic *ripped* and *corkscrew* modes (Alba et al., 2013 [12]). The slump flows have also been analytically investigated through *thin-film* type models for both channel (Alba et al., 2013 [19]) and pipe (Moyers-Gonzalez et. al., 2013 [20]) geometries.

Therefore, there is a strong industrial motivation to better understand those flows. The application of this knowledge in process design would lead to the reduction of environmental impact and an increase in displacement/restart efficiency and productivity.

1.2
Problem of Study

This thesis investigates yield stress and thixotropy effects of non-Newtonian fluids in a horizontal pipe. Two major flows are considered: (i) isodense displacement of a yield stress fluid by a less viscous Newtonian fluid; (ii) non-Newtonian fluid start-up. The approaches taken to understand the displacement flows in this thesis are both experimental and numerical. Only experiments are considered for non-Newtonian fluid start-up.

The major part of the results are obtained by experiments carried out in a lab scale apparatus explained in chapters 3, 4 e 6. Computational Fluid Dynamics (CFD) is also used to numerically solve the governing equations and further understand the fluid displacement flow. A commercial software (*FLUENT*) is employed for this. The final aim of these integrated studies is to better understand the physics behind displacement flows and start-up, to give quantitative measure of the design parameters, when feasible, and to improve the fluid displacement process as a whole.

1.3
Thesis Outline

This PhD thesis is organized in eight chapters. Chapter 2 presents a fluid displacement literature review. Although we are interested in the laminar displacement of non-Newtonian miscible fluids in a tube, we also review fluid displacements experiments including Newtonian fluids, as references for numerical model validation. Additional theoretical and experimental details are given as they pertain to each chapter.

In chapter 3, after describing the experimental set-up and procedure, preparation of the fluids samples and measurement of their rheological properties are presented. In the next chapter, after the descripton of a typical displacement experiment, taking into account all the data acquired, the fluid displacement experiments results are detailed. Three flow regimes, namely *corrugated*, *wavy* and *smooth*, are characterized and later classified in dimensionless maps.

The influence of different concentrations of NaCl and Laponite on the rheological properties of Laponite suspensions, specially yield stress and thixotropic parameters, is presented in chapter 5. In chapter 6 thixotropy effects on yield stress fluid start-up are described experimentally and its results are analyzed.

Chapter 7 is dedicated to the numerical simulations of isodense displacement of yield stress fluid by a less viscous Newtonian fluid in *FLUENT*, a finite volume commercial software from ANSYS. The numerical code is validated with experimental displacement fluid results from the literature, considering the displaced fluid as Newtonian and shear thinning. The yield stress displacement flow is then analyzed in detail. The impact of flow rate and rheological parameters on the displacement flow is presented.

In the last chapter, the conclusions of this work are drawn from the experimental and numerical results presented in the preceding chapters. Appendix A shows the experimental procedures, i.e. flowmeter calibration, ink concentration definition and post processing for data analysis. Appendix B presents some thixotropic models from literature.

2
Literature review - Fluid Displacement

Displacing a fluid by another one is an important phenomenon that has been under study for centuries. The studies were preluded by buoyancy experiments of Archimedes, that enticed by a suspicious king, found an ingenious way to prove that a crown may not only be forged by gold. Two important factors affect the displacement flow: geometry and fluids involved. Different types of geometries can be considered such as parallel plates and pipes associated to different inclinations. Besides buoyancy and rheology differences, the fluids miscibility is an important characteristic that needs to be considered.

Although we are interested in the laminar displacement of non-Newtonian miscible fluids in a tube, we did a review over fluid displacements experiments including the Newtonian fluids for they will serve as reference for numerical model validation. For didactic purpose this bibliography review is divided in categories based on the fluids miscibility and rheological characteristics of the fluids.

2.1
Immiscible Newtonian-Newtonian fluid displacement

Saffman and Taylor (1958) [21] performed experiments in which a viscous Newtonian fluid confined between closely spaced parallel sheets of glass, a Helen-Shaw cell, is driven out by a less viscous one. Assuming that the fluids remain completely separated along a defined interface (no diffusion), the motion in a Hele-Shaw is mathematically analogous to a two-dimensional flow in a porous medium. Another analogy also mentioned is the expressions representing the instability of accelerated interfaces between fluids of different densities where round-ended fingers of the less dense fluid penetrates into the more dense one.

When a fluid is displaced by a less viscous and immiscible fluid, a finger/fingers may be formed and a residual layer of the viscous fluid is left behind after the interface (front or tip of the meniscus) has passed. The instabilities observed during this displacement are called Saffman-Taylor. Figure 2-1

reproduces from [21] one experiment in the Hele-Shaw channel dimensions 0.08 x 2.54 x 91 cm and shows an uniform finger of water at 2.26 mm/s penetrating Shell Diala oil ($\hat{\mu}$=0.30Pa.s and $\hat{\rho}$=875 kg/m^3). In this thesis, we adopt the convention of denoting dimensional quantities with symbol ˆ (e.g. the Newtonian fluid viscosity $\hat{\mu}$ and dimensionless quantities without.)

Figure 2-1 - Finger of water at 2.26 mm/s penetrating Shell Diala oil ($\hat{\mu}$ =0.30 Pa.s and $\hat{\rho}$ = 875 kg/m3) in the Hele-Shaw channel dimensions 0.08 x 2.54 x 91 cm from [21].

The values of the finger width ($\hat{d}$) and the channel width ($\hat{w}_{HS}$) are measured and experimental values for $\hat{d}/\hat{w}_{HS}$ ratio are plotted as ordinates and the Capillary number ($Ca = \hat{\mu}\hat{V}_0/\hat{T}$) as abscissa where $\hat{\mu}$ is the viscous fluid viscosity, $\hat{V}_0$ is the mean flow velocity and $\hat{T}$ the surface tension. The experiments results with water as displacing fluid from [21] are reproduced in figure 2-2. We applied the correction mentioned by [22] that the actual abscissa values are twice those originally shown in [21].

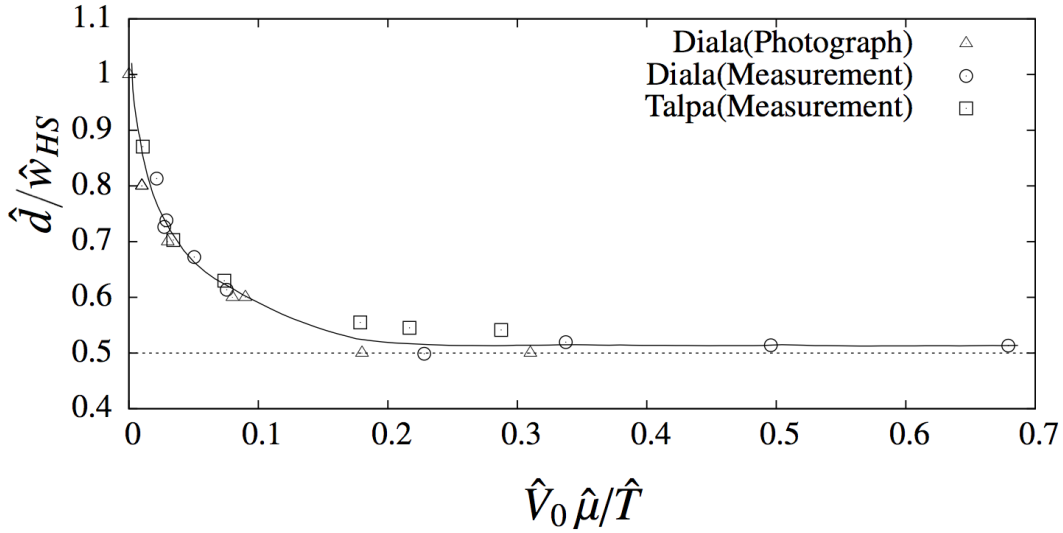

Figure 2-2: Measured values of $\hat{d}/\hat{w}_{HS}$ for water penetrating two oils (Diala and Talpa) from Saffman and Taylor (1958) [21] with abscissa correction mentioned by [22].

Saffman and Taylor (1958) [21] informed that in spite of the viscosity ratio from the displacing and displaced fluids, the points obtained with two oils (Diala

and Talpa) appear to fall nearly on the same curve and the value of $\hat{d}/\hat{w}_{HS}$ rapidly decreases as capillary number increases till it reaches a value greater than ½ even for using air instead of water as the finger, or using oil penetrating into glycerine.

The schematic of the of the long Hele-Shaw cell for photographing finger from [21] is reproduced in figure 2-3. It represents one of the pioneers experiments of fluid displacement with the use of cameras and the equipments applied have their analog in modern experiments, for instance, the flash-bulb was replaced by LED stripes and the tracing paper screen for fish-tanks and light diffusers. The reservoir and valves themselves are quite the same. Moreover, the gravitational driven system is still under use, but pressure based systems such as air compressors and pumps are also considered nowadays.

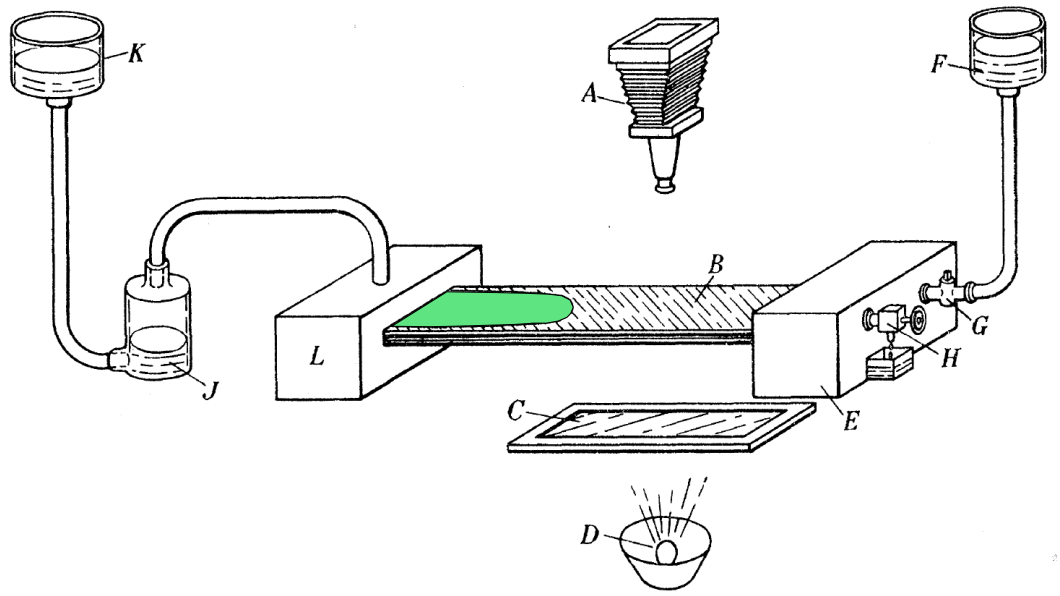

Figure 2-3: Arrangement of long Hele-Shaw cell for photographing finger reproduced from Saffman and Taylor (1958) [21]: camera (A); channel (B); tracing paper screen (C); flash-bulb (D); downstream reservoir (E); vessel of more viscous fluid (F); cock (G); needle valve (H); bottle (J); water vessel (K); upstream reservoir (L).

Taylor (1961) [23] performed immiscible fluid displacement experiments in a horizontal tube. It consists of blowing air into one end of 4 ft long tube containing a viscous Newtonian fluid (glycerin and water solutions of golden syrup). As described by [23], a round-ended air column travels down the tube forcing some of the liquid out at the far end and leaving a fraction m in the form of a layer covering the wall. The experimental apparatus was projected to guarantee large values of

capillary number without increasing the flow speed to such an extent that the stresses due to inertia were comparable with those due to viscosity. Two tube diameters ($\widehat{D}$) were considered 2 and 3 mm.

In the procedure from [23] when the apparatus was ready for the experiment, a specific ball valve of the set-up was suddenly opened and at the same moment a stopwatch was started ($\hat{t} = 0s$). The meniscus then moved along the tube. After the meniscus had gone some way along the tube the ball valve was suddenly closed and simultaneously the stop-watch stopped. The position of the meniscus was read and the length of air column in the tube determined ($\hat{L}_{Ta}$). The crucible located at the far end of the tube was weighted and the weight $\widehat{w}$ of the discharged viscous fluid was measured. The weight of the fluid in the tube when full was $\widehat{w}_0 = \frac{\Pi}{4}\hat{\rho}\widehat{D}^2\hat{L}_{Ta}$, where $\hat{\rho}$ is the density of the fluid. The remaining fluid fraction *m* can be estimated by equation 2-1:

$$m = 1 - \frac{\widehat{w}}{\widehat{w}_0} \qquad 2\text{-}1$$

The residual layer can also be represented by the ratio of the mean and front velocity as described in equation 2-2, and by the ratio of the mean residual layer thickness ($\hat{h}$) and tube diameter ($\widehat{D}$) in equation 2-3.

$$m = 1 - \frac{\hat{V}_0}{\hat{V}_f} \qquad 2\text{-}2$$

$$m = 1 - \left(1 - \frac{2\hat{h}}{\widehat{D}}\right)^2 \qquad 2\text{-}3$$

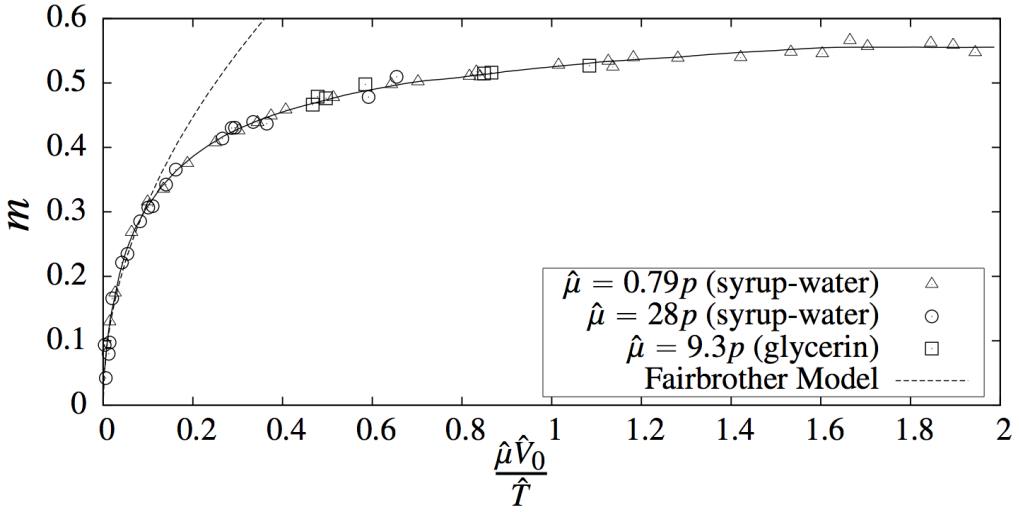

Figure 2-4: Experimental results from Taylor (1961) [23].

The results from [23] presented on figure 2-4 show that Fairbrother and Stubbs (1935) model [24] for $m = \left(\frac{\hat{\mu}\hat{V}_0}{\hat{T}}\right)^{\frac{1}{2}}$ have a good agreement with his experiment for $\hat{\mu}\hat{V}_0/\hat{T}$ less than 0.09 and suggests that *m* reaches a limiting value when stresses due to viscosity are much greater than those to surface tension.

Later, Cox (1962) [25] with Golden Syrup displaced by carbon tetrachloride experiments with controlled temperature, showed that the asymptotic value of *m* was 0.6. The amount of fluid left behind in the tube was found from measurements taken on the photographic negative. In all photographs it was apparent that the finger width tended to an asymptotic value within about 1 ½ tube diameter of the nose. An example of a typical finger photography obtained by [25] is reproduced in figure 2-5.

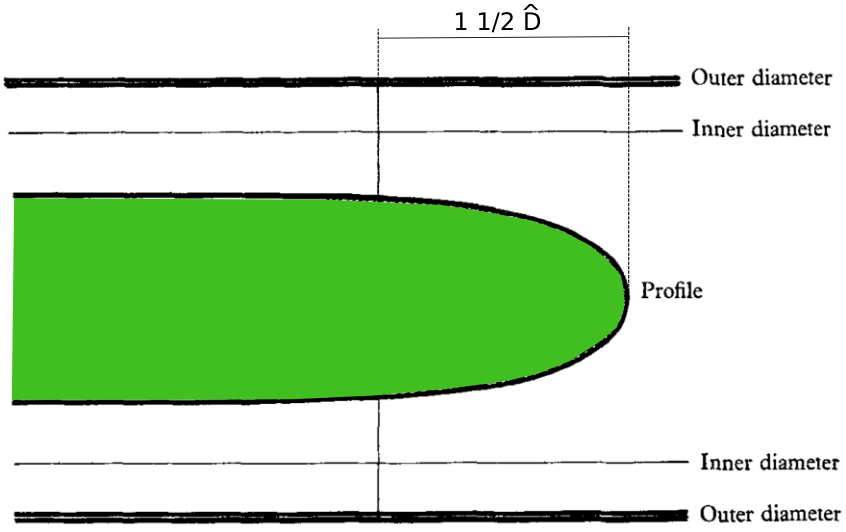

Figure 2-5: Typical finger profile from Cox (1962) [25].

2.2
Miscible Newtonian-Newtonian fluid displacement

Petitjeans and Maxworthy (1996) [26] performed miscible fluid displacement experiments of Newtonian viscous fluid (glycerine), fluid 2 with viscosity $\hat{\mu}_2$ and density $\hat{\rho}_2$, by a less viscous one (a glycerine-water solution), fluid 1 with viscosity $\hat{\mu}_1$ and density $\hat{\rho}_1$, in capillary tubes ($\widehat{D}$=1 to 4 mm). Different tube orientation (vertical and horizontal), viscosity ratio between displaced and displacing fluids, gravity influence and mean flow velocities were considered. The residual layer of the viscous fluid left behind in the tube wall was measured for different

experimental setups. A schematic of miscible Newtonian displacement in a capillary tube presented in Petitjeans and Maxworthy (1996) [26] is reproduced in figure 2-6.

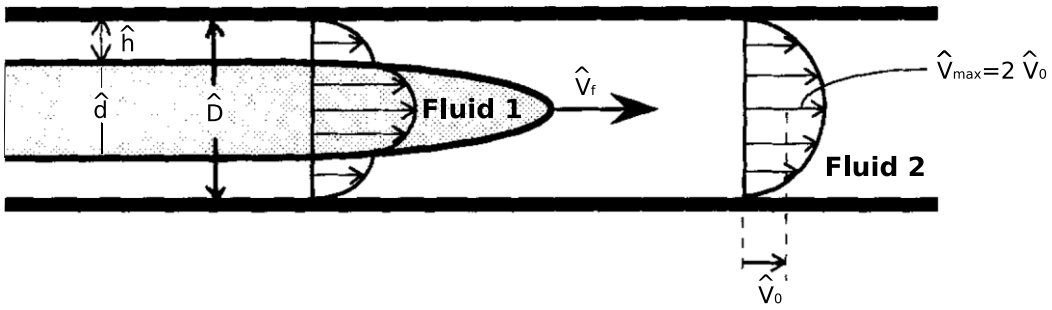

Figure 2-6: Schematic of miscible displacement in a capillary tube from Petitjeans and Maxworthy (1996) [26].

In Petitjeans and Maxworthy (1996) [26] the viscosity ratio of the two fluids $M = \frac{\hat{\mu}_1}{\hat{\mu}_2}$ as allowed to range from ≈ 0 to 1 and for different mean velocities the residual layer *m* was measured. The Peclet number in the form $Pe = \frac{2\hat{V}_0\,\hat{D}}{\widehat{Dif}}$ was used as non-dimensional parameter, where $\widehat{Dif}$ represents the average diffusion coefficient between two fluids. The methodology applied to calculate the diffusion coefficient of glycerin and the water-glycerine solutions is presented in [26].
In order to take into account the effect of gravity, the parameter $F = \hat{g}[(\hat{\rho}_1 - \hat{\rho}_2)/\hat{\rho}_2]/\hat{D}^2/\hat{\upsilon}_2\hat{V}_{max}$ which compares gravitational to viscous forces was considered. As a result, *F* is positive in the destabilized case (heaviest fluid is on the top), and negative in the stabilized case, while *F*=0 when the tube is horizontal or the two fluids have the same density.

The figure 2-7 reproduces the Petitjeans and Maxworthy (1996) [26] curves of *m* as a function of *Pe* for tubes of different diameters, oriented vertically and horizontally, and for *M*=0.01, *M*=0.12 and *M*=0.40. From the curves on figure 2-7, for large *Pe* all the curves tend to the same value of *m*, which depends only of *M*. For small *Pe*, the behavior of *m* depends strongly on tube diameter, orientation and gravity that strongly influenced the intruding finger.

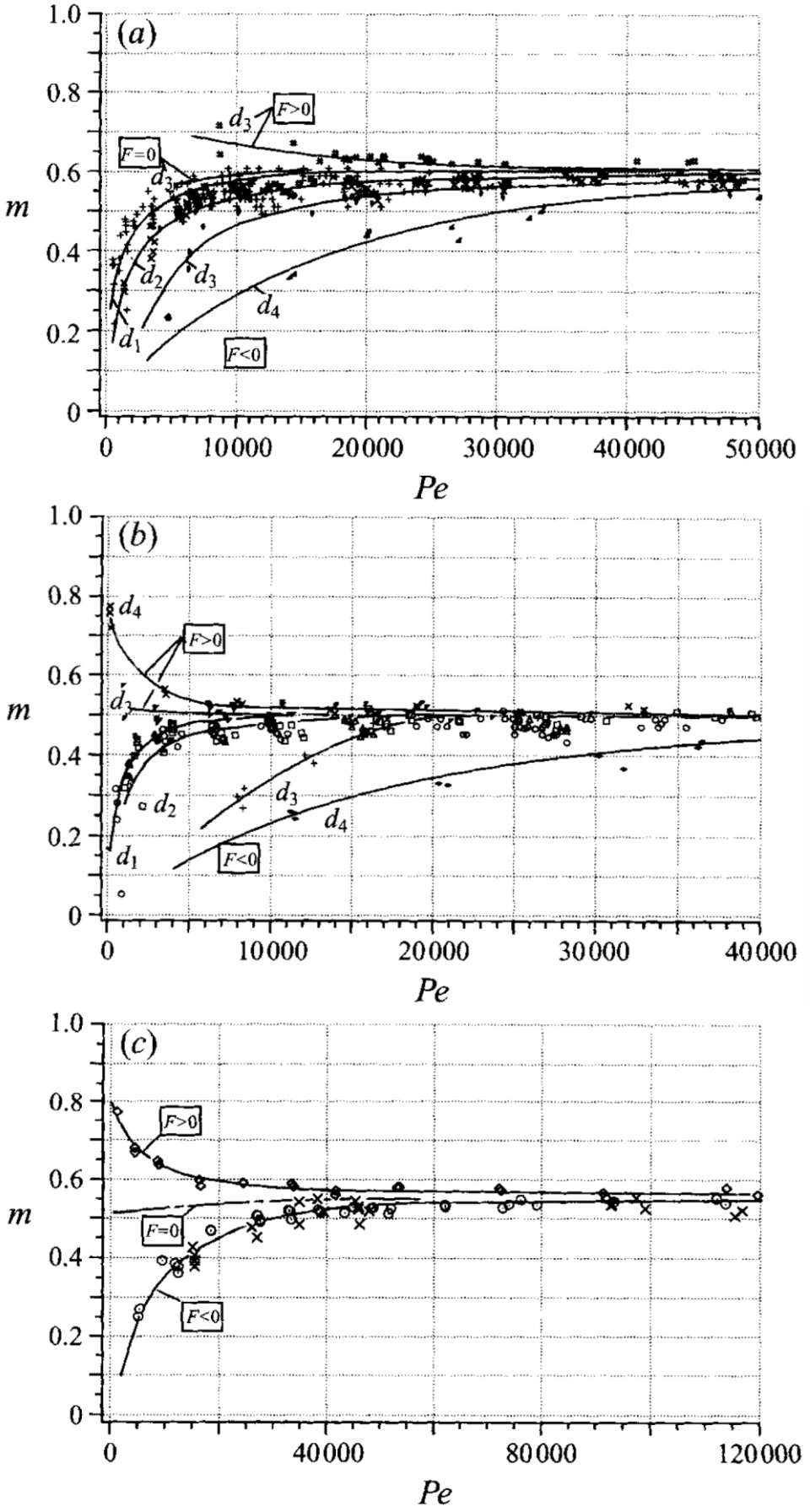

Figure 2-7: Residual layer *m* versus Peclet (*Pe*) for (a) M=0.01; (b) M=0.12 and (c) M=0.4 from Petitjeans and Maxworthy (1996) [26].

The figure 2-8 reproduces asymptotic value of *m* for large Peclet that depends only on the viscosity ratio *M* for the experiments of [26] and numerical simulations for Chen and Meiburg (1996) [27]. For lower *M*, asymptotic *m* increases to a value of 0.61.

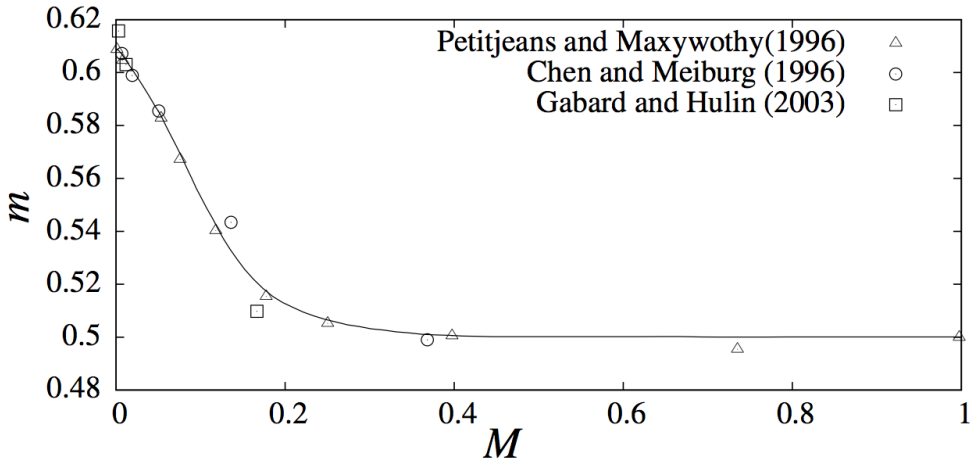

Figure 2-8: The asymptotic value of *m* at large *Pe*, as a function of *M* for numerical simulations of Chen and Meiburg (1996) [27] and the experiments of Petitjeans and Maxworthy (1996) [26] and Gabard and Hulin (2003) [14].

Besides, Petitjeans and Maxworthy (1996) [26] drew a parallel between miscible and immiscible displacements. In the immiscible displacement, the capillary number is an important parameter for its dynamics. On the other hand, for miscible displacement, the dynamics are determined by convective and diffusive effects. Infinite capillary number can be interpreted as immiscible flow with zero surface tension. In the same way, infinite Peclet number can be interpreted as a miscible flow with zero diffusion. In other words, it is possible to formally identify the interface between two immiscible fluids without surface tension with that between two miscible fluids without molecular diffusion. In that sense, the asymptotic value of *m* should be the same in both the immiscible and miscible cases. Cox (1962) [25] experiments showed an asymptotic value of 0.60 for immiscible displacement and Petitjeans and Maxworthy (1996) [26], 0.61 for miscible case.

Petitjeans and Maxworthy (1996) [26] also detected a finger splitting with the displacing fluid lighter than that displaced. The sketches of the cross-section along the tube length are reproduced in figure 2-9.

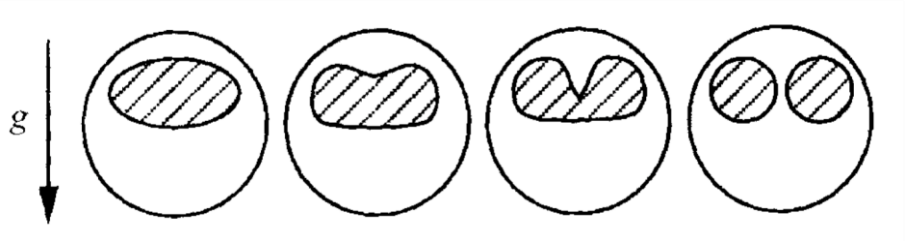

Figure 2-9: Sketches of the cross-section along the tube length of finger splitting from Petitjeans and Maxworthy (1996) [26].

Gabard and Hulin (2003) [14] performed isodense experiments of Newtonian-Newtonian fluid displacements in a vertical tube namely with water-glycerol solutions of different viscosities displaced by $CaCl_2$-water solutions of matched density whose characteristics are listed in table 2-1. For all three viscosity ratios (M=0.167, M=0.012 and M=0.003) investigated by [14], the residual film thickness is independent of the displacement velocity.

Table 2-1: Rheological parameters of fluids considered in the Newtonian-Newtonian fluid displacement experiments from Gabard and Hulin (2003) [14].

Water-C_{Cacl_2} sol.		Water-glycerol sol.		Viscosity ratio	Density
C_{Cacl_2}(%)	$\hat{\mu}_1$ (Pa.s)	$C_{glycerol}$ (%)	$\hat{\mu}_2$ (Pa.s)	M	$\hat{\rho}$ (kg/m^3)
20	0.0016	68	0.0096	0.167	1175
26	0.0029	92	0.25	0.012	1241
28	0.0032	96	1.12	0.003	1260

For the two lowest M values, the residual film thickness is 38% of the tube radius while, for the largest one, it is of the order of 29%. The respective residual layers m are plotted as a function of the viscosity ratio M in figure 2-8. They agree with the numerical simulations of Chen and Meiburg (1996) [27] and the experimental results of Petitjeans and Maxworthy (1996) [26].

2.3
Immiscible non-Newtonian fluid displacement

The immiscible displacement of viscoplastic liquids (Carbopol solutions from 0.1% to 0.17%) in capillary tubes was examined by De Souza Mendes at al. (1997) [28]. The loop experimental set up had 600 mm long glass tube of 3 mm diameter placed horizontally. The air was used as the displacing fluid and its flow rate was

controlled by pressurized tank and flow-control valves. The yield stress range of Carbopol solutions varied from 8 to 79 Pa.

De Souza Mendes at al. (1997) [28] observed perfect displacements and low-curvature air-liquid interfaces at low flow rates, whereas imperfect displacement and higher-curvature of the meniscus were observed for higher flow rates. Moreover, the interface curvature increased as mean velocity increased, as well as the residual film layer of the viscoplastic fluid. As the velocity increases, the residual layer increases, and smooth layer uniform thickness was observed.

2.4
Miscible non-Newtonian fluid displacement

2.4.1
Shear Thinning Fluid

Gabard and Hulin (2003) [14] used Xanthan-water solutions (concentrations of 0.5 to 3 g/L) as shear-thinning displaced fluids. They were displaced by water-glycerol mixtures of same density. Glycerol had to be added to the 0.5g/l Xanthan-water solution to give it a large enough maximum viscosity compared to the injected fluid. The rheological properties of the Xanthan-water solutions were described by the Cross relation:

$$\hat{\eta} = \hat{\eta}_{\infty} + \frac{\hat{\eta}_0 - \hat{\eta}_{\infty}}{1 + (\widehat{K}_{Cross}\hat{\dot{\gamma}})^{n_{Cross}}} \qquad 2\text{-}4$$

where $\hat{\eta}$ represents the effective viscosity of the fluid, $\hat{\dot{\gamma}}$ the shear rate, $\hat{\eta}_{\infty}$ the viscosity limit at high shear rates and $\hat{\eta}_0$ the viscosity limit at low shear rates in the Newtonian plateau region. The limiting viscosity at high shear rates was considered to be equal equal to the viscosity of water 0.001Pa s. The rheological parameters values in equation 2-4 for the Gabard and Hulin (2003) [14] experimental solutions are listed in Table 2-2 together with the characteristics of the injected Newtonian solutions.

Figure 2-10 displays the variation of the residual film thickness as a function of the mean velocity ($\widehat{V}_0$) for the different water-Xanthan solutions used in Gabard experiments. Specific features have been observed at low displacement velocities for shear-thinning fluids (water-Xanthan solutions), the residual film increases as

Table 2-2: Rheological parameters of water-Xanthan solutions from Gabard and Hulin (2003) [14] shear thinning experiments.

Water-glycerol solutions		Water-Xanthan solutions				Density
$C_{glycerol}$ (%)	$\hat{\mu}_1$ (Pa.s)	$C_{Xanthan}$ (%)	$\hat{\eta}_0$ (Pa.s)	$\widehat{K}_{Cross}$ (s)	n_{Cross} ( )	$\hat{\rho}$ (kg/m^3)
4.8	0.0011	0.1	0.34	7.4	0.55	1011
4.8	0.0011	0.15	1.88	85	0.59	1011
4.8	0.0011	0.2	7.39	350	0.62	1011
4.8	0.0011	0.3	32.9	350	0.68	1011

the displacement velocity decreases and reaches values of the same order of magnitude of Newtonian-Newtonian fluid displacement for low viscosity ratio ($M \approx 0$). On the other hand, the residual film decreases as mean velocity increases from zero up to 100 mm/s and reaches a limit at higher velocities of the same magnitude order of Newtonian fluids displacement for high viscosity ratio (M=1). This is only true if macroscopic diffusion is neglected. Gabard and Hulin (2003) [14] studied the Xanthan instabilities in their work and showed that these instabilities are influenced by the fluids rheology and mean velocity.

If no macroscopic diffusion is considered (no instabilities), low velocity implies low shear rates and consequentially high viscosity for shear thinning fluids. So, the effective viscosity ratio of shear thinning fluids is a function of mean velocity.

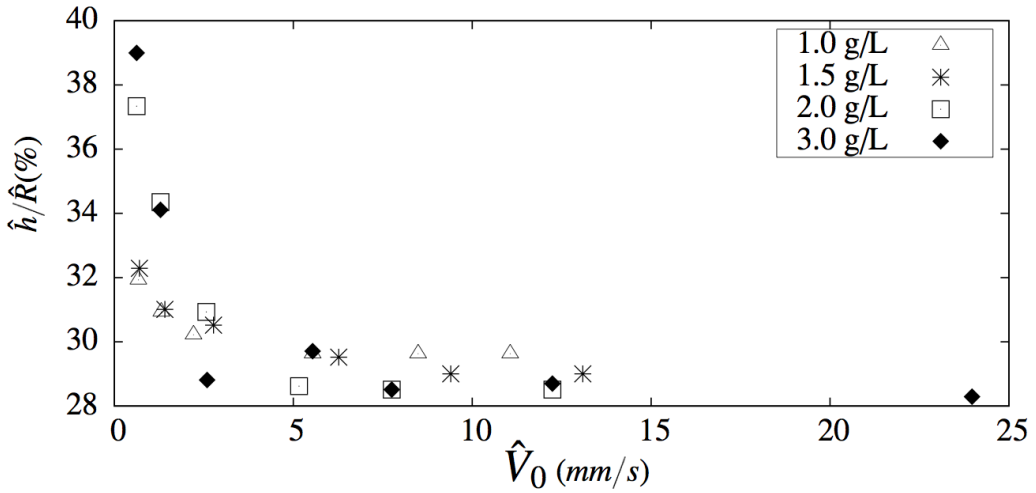

Figure 2-10: Residual film thickness as a function of mean velocity for water-Xanthan solutions of different concentration from Gabard and Hulin (2003) [14].

Gabard and Hulin (2003) [14] performed a set of simulations using the commercial finite volume code FIDAPTM with rheological parameters corresponding to the experimental fluids but couldn't reproduce the residual film behavior observed in the experiments.

2.4.2
Yield Stress Fluid

Gabard and Hulin (2003) [14] also performed experiments with yield stress fluids (water-Carbopol solutions from 1.0 to 1.5 g/l) displaced by less viscous Newtonian fluid (water-glycerol solutions). The rheological properties of the Carbopol solutions approximately verified the Herschel-Bulkley relation between the shear stress $\hat{\tau}$ and the shear rate $\hat{\dot{\gamma}}$:

$$\hat{\tau} = \hat{\tau}_y + \hat{K}\hat{\dot{\gamma}}^n, \hat{\tau} \geq \hat{\tau}_y$$
$$\hat{\dot{\gamma}} = 0, \hat{\tau} < \hat{\tau}_y. \qquad 2\text{-}5$$

Here, $\hat{\tau}_y$ represents the fluid yield stress; $\hat{K}$ fluid consistency index and n a power law index. The rheological parameters of Carbopol and water-glycerol solutions are listed in table 2-3.

Table 2-3: Rheological parameters of Carbopol and water-glycerol solutions from Gabard and Hulin (2003) [14] yield stress fluid displacement experiments.

Water-glycerol solutions		Water-Carbopol-glycerol solutions				Density
C_{sugar} (%)	$\hat{\mu}$ (Pa.s)	C_{carb} (%)	$\hat{\tau}_y$ (Pa)	$\hat{K}$ (Pa s)^n	n	$\hat{\rho}$ (kg/m^3)
19	0.0018	0.07	0	0.56	0.65	1070
19	0.0018	0.14	2.5	25.8	0.47	1070
19	0.0018	0.15	5.0	32.1	0.46	1070

Figure 2-11 displays the variations of residual layer with mean velocity for Carbopol-water solutions of different concentrations (two of them with a finite yield stress and the third one with a zero yield stress).

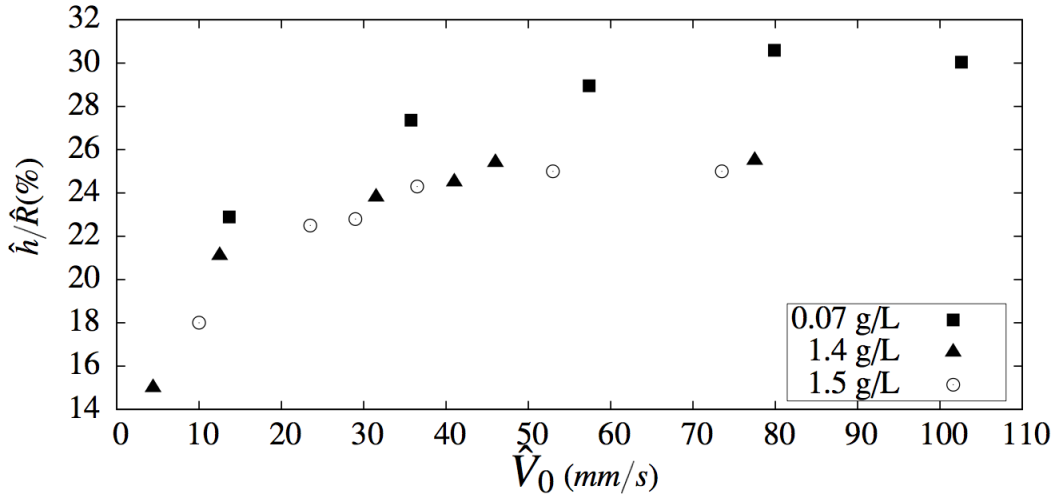

Figure 2-11: Residual film thickness as a function of mean velocity for Carbopol solutions of different concentration from Gabard and Hulin (2003) [14].

A constant residual film thickness is reached for velocities $\hat{V}_0$ above 40 mm/s. At smaller displacement velocities, in contrast with the case of shear-thinning fluids, the residual film increases with mean velocity instead of decreasing. On the opposite high-velocity limit, the constant asymptotic value of the residual film thickness is lower for the two more concentrated solutions (24 to 25%) than for shear thinning fluids without a yield stress (28 to 30%). In addition, for the less concentrated Carbopol solution (with a zero yield stress), the residual film thickness has a value 28 to 29% comparable to that for Xanthan solutions.

All results obtained with yield stress fluids indicate therefore that a non-zero yield stress further decreases the residual film thickness. Gabard and Hulin (2003) [14] reported that the boundary of the residual displaced fluid film was rough for low velocities for yield stress fluid displacement in a plexiglass tube. Figure 2-12 shows the video frames of fluid displacement for different displaced fluids reproduced from Gabard and Hulin (2003) [14].

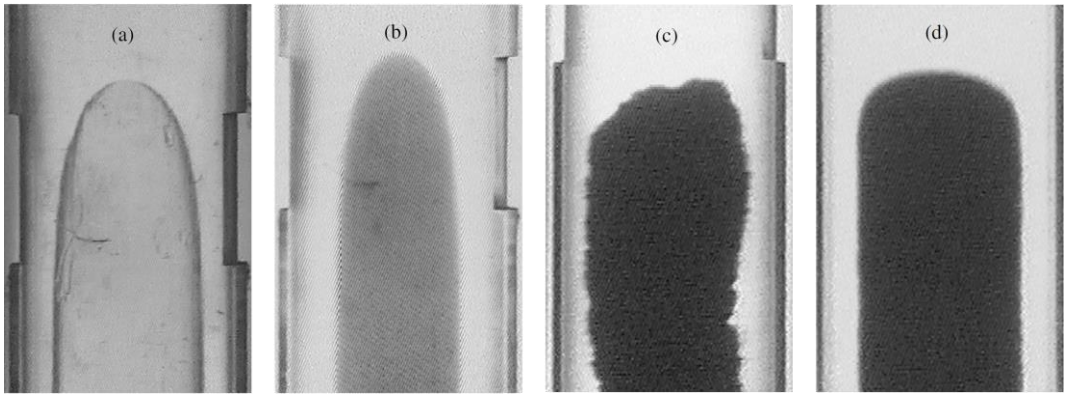

Figure 2-12:Video frames of fluid displacement for different displaced fluids reproduced from Gabard and Hulin (2003) [14]:(a) Newtonian fluid; (b) Shear-thinning fluid; (c) Yield stress fluid for low velocity; (d) yield stress fluid for high velocity.

2.5
Summary from the fluid displacement literature review

We presented the literature review of a Newtonian fluid (fluid 1) displacing fluids (fluid 2) with different rheological characteristics, such as Newtonian, shear thinning and yield stress fluids. In the Newtonian-Newtonian fluid displacement, the Hele-shaw cell classic experiments from Saffman and Taylor (1958) [21] and the blowing air experiments in a horizontal tubes from Taylor (1961) [23] were

detailed. A parallel between the early experiments and the modern ones was drawn. Other important review that was taken under consideration was the experiments from Petitjeans and Maxworthy (1996) [26] associated to the numerical results from Chen and Meiburg (1996) [27].

In the non-Newtonian fluid displacement the displaced fluid rheological properties and the experimental results from Gabard and Hulin (2003) [14] are presented and will be applied for numerical code validation on chapter 7 . One interesting observation reported by [14] related to the boundary of the residual displaced fluid film for low velocities, in particularly for yield stress fluid displacement, will be addressed in the experimental yield stress fluid displacement in chapter 4 .

3
Experimental Methodology

This chapter presents the set-up and procedures for fluid displacement and start-up experiments. The acquisition system and data processing are detailed. Besides, the preparation of the fluids samples and their rheological characterization are described.

3.1
Experimental description

Displacement and start-up flow experiments are performed in a 4-m long horizontal transparent acrylic pipe, with internal diameter ($\widehat{D}$) equal to 19.05 mm, as shown in figure 3-1. The apparatus used in the current study is the same as the one adopted in Taghavi et al. (2012) [11], Alba et al. (2013) [12], Alba and Friggard (2016) [15] for studying the displacement flows in inclined pipe, except that the aluminum frame set-up has been tilted to horizontal position, using a ball-screw jack ($\hat{\beta}$= 90°).

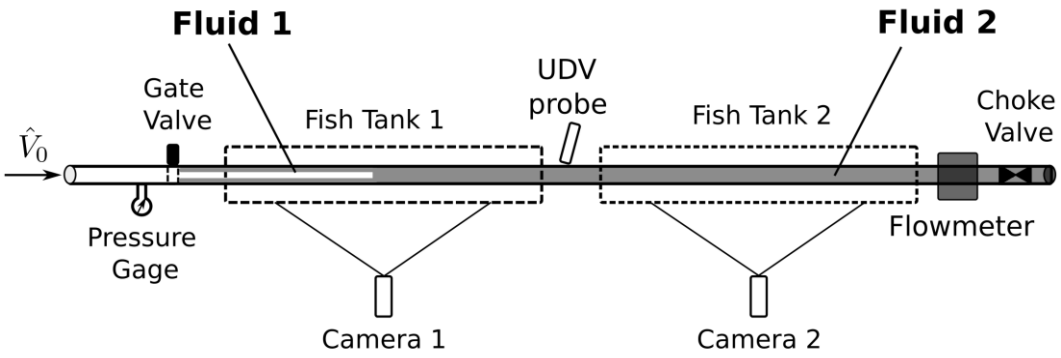

Figure 3-1: Schematic view of the experimental set-up. The shape of the interface is illustrative only.

Moreover, a pressure gage has been added to the system to complement the measurements. It is important to point out that solenoid valves have been replaced by hand-operated PVC globe valves. The valves replacement is necessary, mainly for thixotropic experiments, to mitigate the solenoid valve disturbances such as transient effects (short time response) and localized shear. The internal design in

this type of valve provides an extra pre-shearing and alters the shear history of the fluid as will be shown in chapter 6.7.1 . Besides, since the loop was set to horizontal position, the solenoid valves are not necessary any more.

For start-up experiments, the whole loop is filled with a clear fluid and no images are acquired. Due to its complexity, in this chapter the loop description will consider only the fluids displacement experiments. The start-up experiments will be described in details in chapter 6 .

The pair of fluids used in each displacement test have the same densities, but different viscosities. The displacing fluid 1 is Newtonian (glycerol or NaCl solution), whereas the displaced fluid 2 is a Carbopol solution, colored with a small amount of ink.

A pneumatically operated gate valve placed 80 cm from one end of the pipe ($\hat{x}$= 0 mm) initially segregates the two fluids. Prior to the experiment, the section of the pipe downstream of the gate valve is filled with fluid 2 and the upstream part with fluid 1. The fluids are driven into the flow loop using pressurized acrylic tanks ($\approx$ 70 kPa) to achieve a steady flow rate and avoid disturbances that could be induced by a pump. The imposed flow rate is controlled by a choke valve located downstream.

Before discharging the fluids, the flow rate is recorded using a magnetic flow meter (model FMG200 Omega). In addition, the fluid discharge mass ($\hat{w}$) during each experiment is measured with a scale (Sartorium 1 g readability), located after the flow meter. Fluids densities, $\hat{\rho}$, are measured with a density meter (DMA 15N, Anton Paar), with resolution of 0.0001 g/cm^3. Both mass and fluids densities are used in the flow meter calibration procedure, provided in the appendix 10.1 .

Video recordings of the displacement are realized simultaneously to provide quantitative image analysis and extract information regarding the large-scale features of the flow such as the velocity of the displacing front. The same image acquisition and processing system has been successfully implemented previously in Taghavi et al. (2012) [29], Alba et al. (2013) [12], Alba and Friggard (2016) [15]. The imaging system consists of 2 high-speed digital cameras with 4096 gray-scale levels (Basler Scout scA1600 and scA1400), with images recorded at a frequency of 3 Hz. Stripes of Light Emitting Diodes (LEDs) have been used along with light diffusers in order to provide homogeneous lighting. To reduce light refraction errors

and further enhance the quality of the images, two *fish* tanks have been placed around the main pipe.

The ink concentration of fluid 2 was defined using standard light calibration techniques from Alba (2013) [30]. As a result, the pixel light intensity is converted to a normalized concentration value varying from 0 (pure displaced fluid 1) to 1 (pure displacing fluid 2). Images obtained at regular time intervals during the experiment are post processed to give calibrated snapshots of the concentration and spatiotemporal diagrams of the averaged concentration profiles along the the pipe. The image processing methodology and the detailed description for transforming light intensity in to concentration is provided in appendix 10.2.2 .

Supplementary velocity field measurement is accomplished using an Ultrasonic Doppler Velocimeter (UDV) probe that is placed between the two *fish* tanks ($\hat{x}$= 1560 mm). The UDV used is the DOP2000 (model 2125, Signal Processing SA) with 8 MHz, 5 mm (TR0805LS) transducers at a duration of 0.5 μs with an axial resolution around 0.375mm. Polyamid seeding particles with a mean particle diameter of 50 μm and a volumetric concentration equal to 0.2 g/L are added to both fluids to obtain robust UDV echo. The UDV data processing and its different form of representation are described in appendix 10.3 .

The pressure before the gate valve is monitored by a pressure gauge transducer with 0-5 V DC output (PX329-015G5V, from Omega, maximum gage pressure of 1034 kPa). The pressure gage is installed upstream, in the Newtonian fluid region. The pressure output signal is connected to a National Instrument board PCI/PXI-6221 (68-Pin), with the calibration curve provided by the manufacturer.

3.2
Fluid preparation and rheology

This section details the fluid preparation protocol and how the rheological parameters are obtained. Since the rheological tests are performed for every fluid sample, the parameters will be presented in the chapter where the experiment is analyzed.

3.2.1
Newtonian fluid

The displacing fluid 1 is a Newtonian salt or glycerol-water solution. Salt or glycerol is added to water until the density of fluid 1 matches that of fluid 2 ($\hat{\rho}_1 = \hat{\rho}_2 = \hat{\rho}$). Due to the low concentration of glycerol and NaCl added (less than 0.1% wt), the viscosity of fluid 1 remains close to that of water ($\hat{\mu} \approx 0.001$ Pa.s) in our experimental analysis. All rheological properties and density of fluid 1 were evaluated at the experiment room temperature ($\approx 23°$ C).

3.2.2
Carbopol

Fluid 2 is a Carbopol (EZ-2, Noveon Inc.) solution in the range of 0.07 to 0.12 in weight (% wt). Apart from its similar rheological properties to waxy crude oil, Carbopol solutions are water-based, and have the advantage of being transparent, non-toxic, and environmentally-friendly. Carbopol is a polymer with high molecular weight cross-linked acrylic acid chains, widely used industrially as thickener, e.g. in pharmaceutical products and cleaners.

We designed a Carbopol solution protocol that consists of gradually adding Carbopol powder to water in a 40 l PVC tank, using a mixer with a helicoidal dual blade (Eurostar Power model, from IKA Werke), rotating at 400 rpm. After addition of the Carbopol powder to the water, the solution remains in the mixer at 400 rpm for 30 minutes. When a homogeneous Carbopol solution is obtained, sodium hydroxide (NaOH) solution diluted in deionized water is slowly added to the mixture by the side of the container to minimize the air bubble entrainment. The Carbopol-NaOH solution is stirred for 5 minutes to ensure that we have achieved an even gel solution throughout the whole container volume.

The weight-to-weight Carbopol to NaOH ratio is 3.5, chosen to neutralize the mixture and form a yield stress fluid, keeping the pH in the range of 6-8. The Carbopol solution temperature and pH are measured using a mini thermocouple from Omega (resolution of 0.1° C), and a waterproof pH meter (pHTester 30 model with accuracy of 0.01, from Eutech Inst.) respectively. The pH meter is calibrated using pH standard solutions. Rheological tests of the Carbopol solution are

performed in the same day of the experiments, using a rotational rheometer (Kinexus, from Malvern) with parallel serrated plates, with 20 mm diameter and 2 mm gap. Temperature is controlled during the test to match that in the experimental room.

For each Carbopol solution, the rheological flow curve data is fitted to a Herschel-Bulkley equation:

$$\hat{\tau} = \hat{\tau}_y + \widehat{K}\hat{\dot{\gamma}}^n, \hat{\tau} \geq \hat{\tau}_y$$
$$\hat{\dot{\gamma}} = 0, \hat{\tau} < \hat{\tau}_y. \qquad 3\text{-}1$$

Here, $\hat{\tau}_y$ represents the fluid yield stress, $\widehat{K}$is the fluid consistency index and *n* is the power law index. Bifurcation tests similar to Coussot et al. (2012) [31]\ are performed to define the yield stress for the rheological model fit. Subtracting the yield stress from the flow curve, we then fit $\widehat{K}$ and *n* as a linear fit in log-log coordinates. The power law data fitting considered only data points for shear rate lower than 500 1/s. For $\hat{\dot{\gamma}}$> 500 1/s, the rheological behavior of Carbopol solutions diverge from the tuned Herschel Bulkley model. Figure 3-2 presents example rheological data for the Carbopol solutions used in our displacement experiments and the corresponding fitted Herschel-Bulkley model curves.

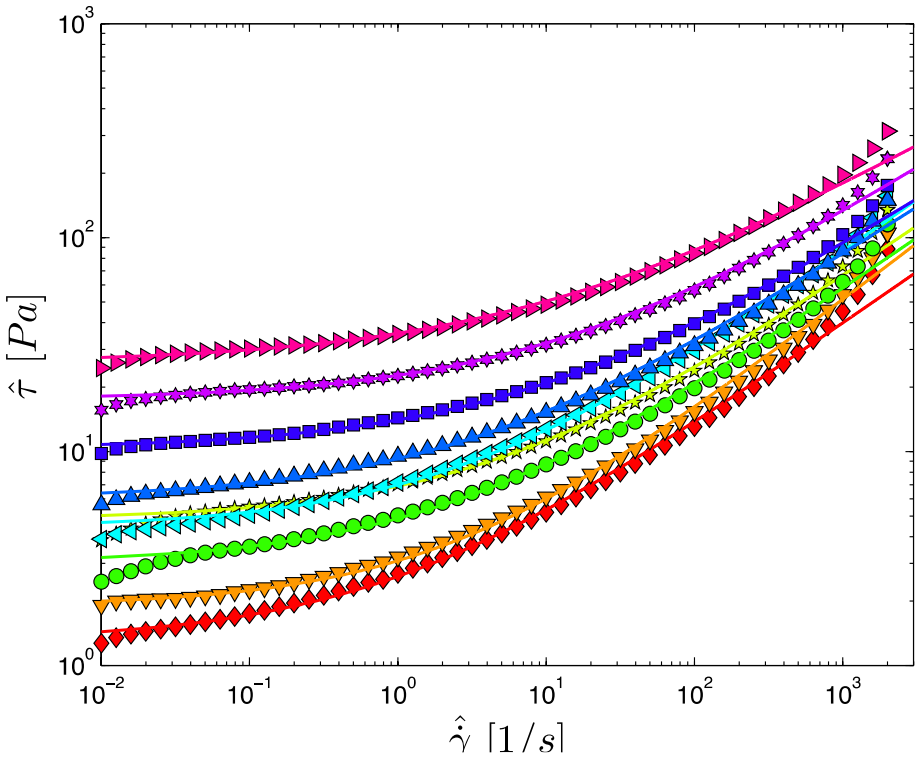

Figure 3-2: Flow curves and their respective Herschel-Bulkley models for Carbopol solutions of displacement experiments (solid line). Different markers represent experimental batch A(◊), B(▼), C(◄), D(○), E(★), F(▲), G(□), H(●) and I(►), as given in table 4-1.

3.2.3
Laponite

In the start-up experiments, besides the carbopol solutions, Laponite suspensions are considered. Laponite is a synthetic crystalline layered silicate colloid with crystal structure and composition closely resembling the natural smectite clay hectorite as described by Cummins (2007) [32]. Because of the chemical structure of the clay, the faces of the disks are charged negatively when the particles are suspended in an aqueous solution. Depending on the pH of the solution, it appears that the sides of the disks can be charged positively (Bonn et al., 1999 [33]).

When Laponite is dispersed in water, the exchangeable sodium ions hydrate, causing the clay to swell initially and to separate completely (Cummins, 2007 [32]).This gives a clear colloidal dispersion (a sol) of anionic Laponite platelets and hydrated sodium ions in solution (Escudier and Presti, 1996 [34]).

The synthetic colloid Laponite exhibits an array of different phases and behaviors due to both attractive and repulsive interactions, anisotropy and net charge, as well as an anisotropic charge distribution (Cummins, 2007 [32]). Many authors (Mourchid et.al, 1995 [35]; 1998 [36]; Tanaka et al., 2004 [37]; Ruzicka et al., 2006 [38]; Mongondry et al., 2006 [39]) studied states diagrams of Laponite dispersions as a function of Laponite concentration and the concentration of added salt. Details of Laponite diagram and how NaCl and Laponite concentration affect the rheology of Laponite solutions will be presented in chapter 5.

To guarantee reproducibility of Laponite suspensions, we designed a Laponite solution protocol that consists of gradually adding baked Laponite Rd powder to ultra-pure water at pH =10 obtained by addition of NaOH in a 40 L Polyvinyl Chloride (PVC) tank, while the blade is rotating at 1600 rpm then mixing it for 30 minutes. The ionic strength of the suspension is subsequently adjusted by adding the NaCl solution in the Laponite suspension. The Laponite aqueous solution is stirred vigorously (1600 rpm) for more 30 minutes.

During the preparation protocol validation, for high ionic strength, the viscosity of the suspension increased very rapidly when the NaCl solution was added to the mixture and the suspension appeared to be in-homogenous. To minimize this side effect, the NaCl solution is added to the Laponite solution in a

ramp mode near to the blade influence area. Due to the non-Newtonian characteristic of the Laponite suspensions, during the stirring time, it is necessary to check with the blade is influence the whole sample, the fluid tends to stop moving near the recipient edge. If necessary, the blade position must be altered to get a homogenous sample.

To avoid atmospheric contamination of the sample and consequently, a Ph reduction, the Laponite solution is preserved in a closed bucket for an initial aging time. The rheological properties of Laponite dispersions are known to change over time. Although the aging period could be as long as a year, the samples are kept at rest for at least for 7 days after their preparation, period of time that the major changes take place as described by Labanda and Lorens (2005) [40]. The Laponite solutions temperature and pH are measured after the fluid preparation and before the experiment.

Due to aging effects of Laponite suspension, before the rheological tests for flow curve definition, the sample is rejuvenated or pre-sheared. Since its viscosity goes from infinity (low shear rates) to ten times the water viscosity (high shear rates), it is necessary to apply different geometries based on the viscosity range, i.e., for high viscosities (greater than 0.025Pas) the plate-plate geometry is applied, for low viscosity, the couette or double couette. It was necessary to set a maximum pre-shearing based on the Laponite suspension for plate-plate geometry to avoid the sample splashing. After a step change of stress or shear rate, the new steady state condition would take more than 1 hour to be achieved. Both Laponite and NaCl concentrations influence the time required to reach steady state solution after a step change in stress or shear rate.

During the rheological tests it was necessary to take special measures to avoid the sample degradation, for instance, the sample was covered to minimize the water evaporation and atmospheric CO_2 contamination. Besides, the sample was discarded after 6 hours of rheological tests. To minimize slippage and/or shear banding, only serrated (cross hatched) plates were used in the plate-plate geometry.

Rheological tests of Laponite suspensions were performed in Brazil and Canada, using AR-G2 and ARES-G2 rheometers from TA instruments and Kinexus rheometer from Malvern, respectively. The rheological experiments to identify the influence of thixotropy and yield stress in Laponite suspensions were developed in GReo laboratory at PUC-Rio and they will be detailed in chapter 1 . The Laponite

suspension flow curves for different Laponite and NaCL concentrations obtained during these tests and its respective Herschel-Bulkley model are presented in figure 3-3. Table 3-1 presents the Herschel-Bulkley parameters for Laponite suspension considering different Laponite and NaCl concentrations.

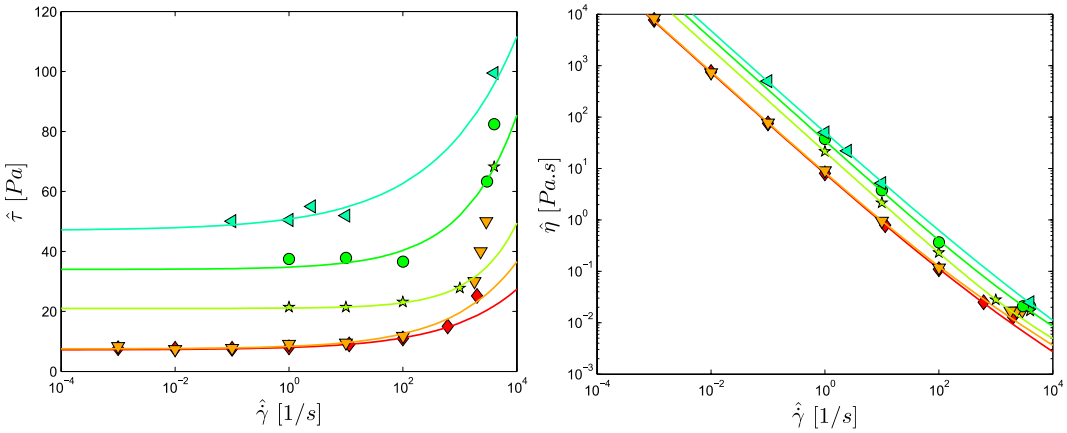

Figure 3-3: Flow curve of Laponite suspensions for different Laponite and NaCL concentrations: 2.0%wt and 10^{-4} mol/L (◊); 2.0%wt and 10^{-3} mol/L (▼); 2.0%wt and 10^{-2} mol/L (★); 2.5 %wt and 10^{-2} mol/L (○); 3.0%wt and10^{-4} mol/L (◄).

In the Laponite suspensions, the yield stress is directly obtained from flow curve data points. The bifurcation tests Coussot et al. (2012) [31] are also performed and will be considered in the analysis of the influence of NaCL and Laponite concentrations over yield stress of Laponite suspensions. From our rheological experiments, the yield stress identified in the bifurcation is greater than the flow curve prediction as detected in the carbopol solution.

Similar to the Carbopol solutions, the power law data fitting considered only data points for low shear rate and the rheological behavior of Laponite suspensions diverge from the tuned Herschel-Bulkley model for high shear rate.

Table 3-1: Parameters of Herschel-Bulkley model for Laponite suspensions.

Laponite Concentration	NaCl Concentration	Herschel-Bulkley model parameters		
		$\hat{\tau}_y$	n	$\widehat{K}$
(%wt)	(mol/L)	(Pa)	(-)	(Pa.s^n)
2.0	10^{-4}	7.2	0.353	0.78
2.0	10^{-3}	7.5	0.381	0.87
2.0	10^{-2}	21	0.591	0.12
2.5	10^{-2}	34	0.455	0.78
3.0	10^{-2}	47	0.308	3.81

The Laponite suspension flow curve can be modeled alternatively by a modified Herschel-Bulkley model with a Newtonian plateau given by:

$$\hat{\tau} = \hat{\tau}_y + \widehat{K}_N \hat{\dot{\gamma}}^n + \hat{\eta}_\infty \hat{\dot{\gamma}}, \hat{\tau} \geq \hat{\tau}_y$$
$$\hat{\dot{\gamma}} = 0, \hat{\tau} < \hat{\tau}_y. \qquad 3\text{-}2$$

Here, $\widehat{K}_N$ represents the modified fluid consistency index; *n* the modified power law index and $\hat{\eta}_\infty$ the viscosity of the Newtonian plateau for high shear rates. The modified Herschel-Bulkley parameters are presented in table 3-2.

Table 3-2: Parameters of modified Herschel-Bulkley model with a Newtonian plateau for Laponite suspensions.

Laponite	NaCl	Herschel-Bulkley model parameters			
Concentration	Concentration	$\hat{\tau}_y$	n_N	$\widehat{K}_N$	$\hat{\eta}_\infty$
(%wt)	(mol/L)	(Pa)	( )	(Pa.s^n)	Pa.s
2.0	10^{-4}	7.2	0.187	0.97	0.0085
2.0	10^{-3}	7.5	0.186	0.59	0.0085
2.0	10^{-2}	21	0.237	0.34	0.0085
2.5	10^{-2}	34	0.162	3.08	0.009
3.0	10^{-2}	47	0.089	4.46	0.015

For the Laponite concentration of 2%wt, as the NaCl concentration increases, the yield stress and the power law index increase. On the other hand, for the same NaCl concentration 10^{-2} mol/L), as the Laponite concentration increases, the yield stress increase and the power law index decreases. The viscosity of the Newtonian plateau $\hat{\eta}_\infty$ seems to be only influenced by the Laponite concentration.

3.3
Summary of experimental methodology

The experimental set-up, including the acquisition system and the data processing, was described and the displacement procedure presented. The fluids preparation protocol and the rheological performed tests were detailed. Besides, the influence of Laponite and salt concentrations on the Herschel-Bulkely model parameters of Laponite suspensions was analyzed.

4
Isodense Fluid Displacement - Experimental Results

In this chapter, we experimentally study the displacement flow of yield stress fluids in the *isodense* limit, which is of critical importance in designing the second stage of pipeline restart flows. In particular, we are interested in investigating the displacement flow of a yield stress fluid by a less viscous Newtonian fluid in a horizontal tube. Moreover, the focus of our study is on *miscible* fluids. The *immiscible* displacement flows are governed by different dynamics.

The novelties of our study include the following. First, most of the studies available in the literature on viscoplastic displacement flows consider the limit of immiscible fluids (Poslinski et al., 1995 [41]; Dimakopoulos and Tasmopoulos, 2003 [42], 2004 [43]; de Souza Mendes et al., 2004 [44]; de Sousa et al., 2007 [45]; Thompson et al., 2010 [46]; Freitas et al., 2013 [47]; Swain et al., 2015 [48]) and/or buoyant flows (Moyers-Gonzalez et al., 2013 [20];Taghavi et al., 2012 [11]; Alba et al., 2013 [19],c [12]; Alba and Frigaard, 2016 [15]). Despite its importance, there are only very few studies available in the literature focusing on miscible non-buoyant (isodense) flows. The existing works only consider a limited range of flow and rheological parameters such as the (Newtonian) Reynolds number, Re_N, and Bingham number, B_N, (see section 4.2 for definition). For instance, $0 \lesssim Re_N \lesssim 2000$ and $0 \lesssim B_N \lesssim$\1000 in the 2D computations of Wielage and Frigaard (2011) [18], and $0 \lesssim Re_N \lesssim 1000$ and $0 \lesssim B_N \lesssim 7000$ in the experiments of Gabard and Hulin (2003) [14].

The current experimental study covers a much broader range of parameters ($Re_N \in [87 - 3764]$ and $B_N \in [360 - 48200]$). Secondly, surface modulations (roughness) and instabilities present in the viscoplastic displacement flows have not been captured in previous simulations such as Wielage and Frigaard (2011) [18]. Although these modulations have been identified in the experimental work of Gabard and Hulin (2013) [14], they have not been characterized based on the governing flow parameters. Only *bulk* flow characteristics of these flows such as average residual film thickness have been quantified in the literature (and only partly). It has recently been found that the surface roughness plays can significantly

affect the flow dynamics and overall displacement/cleaning efficiency Palabiyik et al. (2014) [17]. For the first time, we have investigated the problem of isodense displacement of viscoplastic fluids in depth providing a comprehensive picture of various regimes that are likely to appear, in terms of the important governing dimensionless parameters of the flow.

This chapter is organized as follows. In section 4.1 , the rheological characterization of the fluids applied in the displacement experiments are presented. In the next section, the dimensionless groups applied in the experimental analysis are presented. A typical displacement experiment, taking into account all the flow data acquired, is described in section 4.3 . In section 4.4 , various flow regimes, namely *corrugated*, *wavy* and *smooth*, are characterized and classified in terms of the dimensionless groups governing the system.

4.1
Displacement fluids

Table 4-1 presents the Herschel-Bulkley parameters $\hat{\tau}_y$, n and $\widehat{K}$ for each Carbopol solution considered in the displacement experiments. It can be observed that the power law index varies from 0.40 to 0.54, where lower values are related to higher Carbopol concentrations. Both yield stress $\widehat{K}$, and consistency index $\widehat{K}$ increase as Carbopol concentration overall increases.

Table 4-1: Composition and properties of fluids used in each experiment set.

Experiment set			Fluid 1		Fluid 2			
#	Temperature (°C)	Density (kg/m^3)	Mixed water solution	$\hat{\mu}$ (10^{-3} Pa.s)	Carbopol (%wt)	$\hat{\tau}_y$ (Pa)	n	$\widehat{K}$ (Pa.s^n)
A	22.5	998.4	Glycerol	0.898	0.07	1.3	0.49	1.31
B	23.5	998.4	NaCl	0.913	0.07	1.9	0.54	1.19
C	24.4	998.4	NaCl	0.926	0.08	3.0	0.49	1.87
D	26.8	997.5	NaCl	0.962	0.08	4.8	0.49	2.10
E	26.8	997.5	NaCl	0.962	0.09	4.4	0.50	2.60
F	24.9	998.2	NaCl	0.934	0.09	6.0	0.46	3.27
G	24.4	998.5	Glycerol	0.926	0.10	10.3	0.45	3.77
H	22.7	998.6	Glycerol	0.901	0.11	17.5	0.45	5.21
I	24.5	998.1	Glycerol	0.928	0.12	26.0	0.40	9.72

4.2
Parameters range studied - Displacement Experiments

The following dimensionless parameters are considered in the experimental analyse of yield stress fluid displacement:

- Reynolds number

$$Re = \frac{8\hat{\rho}\hat{V}_0^2}{\hat{\tau}_c}, \quad 4\text{-}1$$

where $\hat{\rho}$ is the common density of the fluids, $\hat{V}_0$ is the mean velocity and $\hat{\tau}_c$ is the characteristic stress given by:

$$\hat{\tau}_c = \hat{\tau}_y + \hat{K}\hat{\dot{\gamma}}_c^n, \quad 4\text{-}2$$

with $\hat{\dot{\gamma}}_c = 8\hat{V}_0(3n+1)/4n\,\hat{D}$, representing the shear rate at the wall of a power law fluid considered as a characteristic shear rate;

- Viscous stress ratio

$$M = \frac{\hat{K}\hat{\dot{\gamma}}_c^n}{8\hat{\mu}\hat{V}_0/\hat{D}}, \quad 4\text{-}3$$

where $\hat{\mu}$ is the viscosity of the Newtonian fluid;

- Bingham number

$$B = \frac{\hat{\tau}_y}{\hat{K}\hat{\dot{\gamma}}_c^n}. \quad 4\text{-}4$$

An additional number that arises in buoyant displacements is the Atwood number: $At = (\hat{\rho}_1 - \hat{\rho}_2)/(\hat{\rho}_1 + \hat{\rho}_2)$. Using *At* helps to put our results in a wider context: since $\hat{\rho}_1 = \hat{\rho}_2 = \hat{\rho}$, we have *At*=0. It is worth mentioning that at times it is convenient to consider a Newtonian Reynolds number, given by

$$Re_N = \frac{\hat{\rho}\hat{V}_0\hat{D}}{\hat{\mu}} = M(1+B)Re, \quad 4\text{-}5$$

and also a Newtonian Bingham number as

$$B_N = \frac{\hat{\tau}_y\hat{D}}{8\hat{\mu}\hat{V}_0} = MB. \quad 4\text{-}6$$

Taghavi et al. (2012) [11] and Alba et. al. (2013) [12] identified two regimes of non-isodense yield stress displacements: central and slump. The central regime is characterized by the central flow of the heavy displacing fluid flowing within the light displaced layer, while in the slump regime the displacing layer moves closer

to the lower region of the tube, underneath the displaced fluid. The transition between these two types of displacement is governed by the ratio of Re_N/Fr

$$\frac{Re_N}{Fr} = \frac{\hat{\rho}_1([\hat{\rho}_1 - \hat{\rho}_2]\hat{g}\hat{D}^3)^{1/2}}{[\hat{\rho}_1 + \hat{\rho}_2]^{1/2}\hat{\mu}}, \qquad 4\text{-}7$$

where $\hat{g}$ is the gravitational acceleration, and *Fr* represents the densimetric Froude number $Fr = \hat{V}_0/(At\hat{g}\hat{D})^{1/2}$. According to Taghavi et al. (2012) [11] and Alba et al. (2013) [12], the transition between the central and slump flows occurs in the range 600< Re_N/Fr<800. In our experiments, since no density difference is applied (*At*=0), Re_N/Fr tends to zero as *Fr* goes to infinity. Therefore, all our isodense experiments can be classified to be in the central regime.

The parameter range covered in our displacement experiments is given in table 4-2. The characteristic shear rate range for all experiments is 2-100 1/s, so the fitted Herschel Bulkley model represents the rheological Carbopol behavior quite well during the fluid displacement experiments. Besides, the complexities of low shear rate rheology are largely avoided. Every experiment can be represented by a set of dimensionless parameters (*Re, B, M*) or dimensionally by a corresponding experimental set number (table 4-1), and the mean velocity ($\hat{V}_0$).

Table 4-2: Parameter ranges used in the displacement experimental study.

Parameter	Range
$\beta(°)$	90
$\hat{V}_0$(mm/s)	5 – 185
$\hat{\dot{\gamma}}_C$	2 – 100
$\hat{\tau}_C$ (Pa)	1.3 – 26.0
Re	0.02−8.20
B	0.16 – 1.51
M	256 – 4350
Re_N	87 – 3764
B_N	360 – 48200
At	0
Fr	∞

4.3 Typical Experimental Results

In this section we present in detail the analysis of a typical displacement experiment (taken from set A, for $\hat{V}_0$=38.4 mm/s, i.e. Re=1.66, B=0.22 and M=400).

After setting the tank pressure and/or the choke position at the end of the flow loop, the gate valve is opened. The signals of the upstream pressure and flow rate over time are presented in figure 4-1 and the snapshots of the flow in figure 4-2.a.

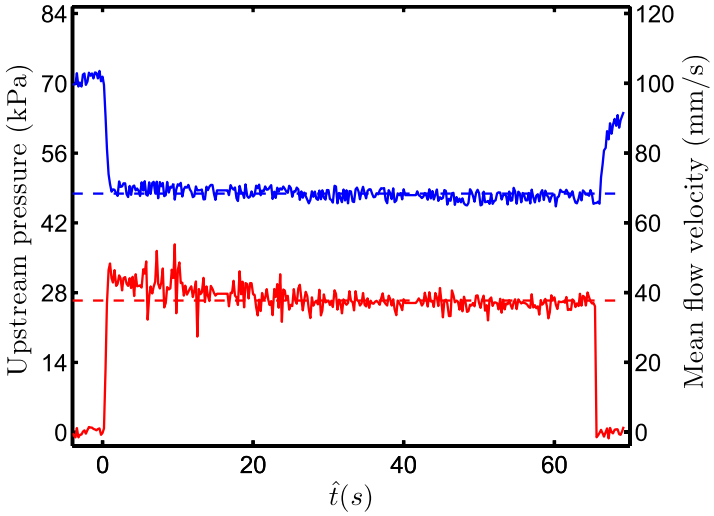

Figure 4-1: Variation of the signals of the upstream pressure (top curve) close to the gate valve ($\hat{x}$ = 0) and the mean flow velocity (bottom curve) over time, for a typical experiment carried using the experimental set A for $\hat{V}_0$=38.4 mm/s. The broken lines show the mean values of the developed flow. The experiment starts at $\hat{t}$=0 s and finishes at $\hat{t} \approx$ 66 s.

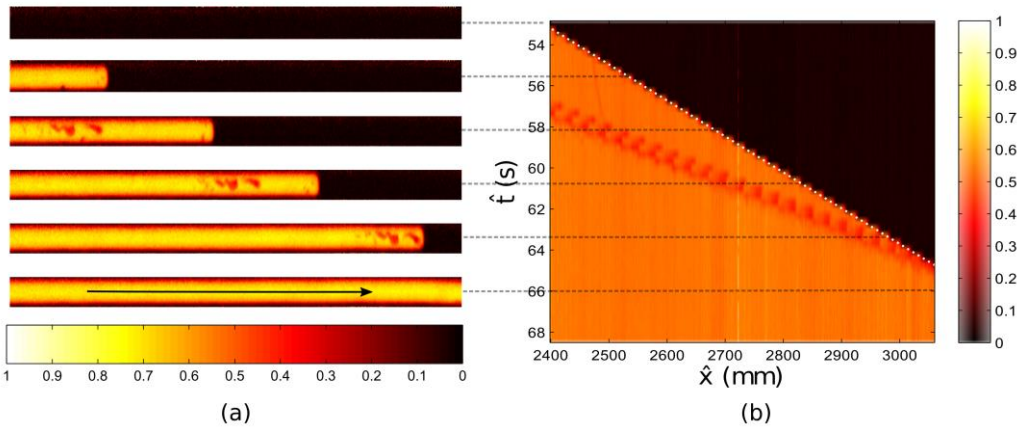

Figure 4-2: Displacement flow experiment carried for set A for $\hat{V}_0$=38.4 mm/s (Re=1.66, B=0.22 and M=400): a) Snapshots of the flow at $\hat{t}$ = 53.0, 55.7, 58.3, 61.0, 63.7, and 66.3 s after opening the gate valve. The flow is from left to right as indicated by the arrow. The field of view is 600 mm by 19 mm, taken 2400 mm after the gate valve. The bottom image is a colourbar of the concentration C. b) Spatiotemporal diagram of the same displacement showing the change in depth-averaged concentration $\bar{C}_y$ values with streamwise distance, $\hat{x}$, and time, $\hat{t}$.

In this case, the tank pressure is initially set to 70.3 kPa. After opening the gate valve at $\hat{t}$ = 0 s, the upstream pressure drops to a stable value of 48.3 kPa. Note that as flow develops over time, the pressure and flow rate approach a *mean* value indicated by the dashed lines in the figure. Once the experiment is over and the choke or gate valve is closed ($\hat{t} \approx$ 66 s) the flow rate and pressure naturally converge to their values prior to the experiment.

Figure 4-2.a presents the post processed images of the same experiment as in figure 4-1. The concentration contour for different time stamps shows a finger of the brighter displacing fluid moving through the dark displaced fluid from the left to the right. After the front passes, it is possible to identify dark regions with lower concentrations at the top and bottom of the pipe and intermediate bright regions in the middle, suggesting the presence of a uniform residual layer on the walls. Since the concentration appears to remain constant after the front passage, it seems that the front itself plays an important role in the formation of the residual layer. In figure 4-2.a it is also possible to identify detached Carbopol pieces moving inside fluid 1 that are represented by the squiggly line in figure 4-2.b.

If the mean concentration ($\bar{C}$) in a particular section of the flow is constant, it is possible to estimate the residual thickness $\hat{h} = (\widehat{D} - \hat{d}_C)/2$, where $\widehat{D}$ is the tube diameter and $\hat{d}_C = \sqrt{\bar{C}}\widehat{D}$ is the displacing fluid diameter obtained using a mass balance. As described in Taghavi et al. (2012) [29] and Alba et al. (2013) [49], the position of the displacing front in a spatiotemporal plot (figure 4-2.b) is defined by the boundary between the dark and light regions, with its slope being inversely proportional to the front velocity. It is possible, using a mass balance, to calculate another equivalent diameter of the front by $\hat{d}_f = \sqrt{\widehat{V}_0/\widehat{V}_f}\widehat{D}$, where $\widehat{V}_0$ and $\widehat{V}_f$ are the mean and the front velocities, respectively. The construction of $\hat{d}_c$ can be considered as localized in space: dependent on which $\bar{C}$ is used, whereas the construction of $\hat{d}_f$ may be considered to depend on the front velocity at a particular time.

If the displacement proceeds relatively steadily in time and space, we may justifiably compare $\hat{d}_f$ and $\hat{d}_c$. As an example, the spatiotemporal plot in figure 4-2.b provides the front velocity ($\widehat{V}_f$=56.7 mm/s) and the mean concentration ($\bar{C}$=0.54) after the front passage. For this displacement, we have $\hat{d}_f$ =0.82$\widehat{D}$, and $\hat{d}_c$. =0.73$\widehat{D}$. Note that the corresponding residual layer thickness to $\hat{d}_c$ is 0.27 radius of the pipe, which is close to those reported by Gabard and Hulin (2003) [14] for isodense displacement flows in a vertical pipe. In the case of buoyant displacement flows Alba and Frigard (2016) [15] showed that bulk measurements of the two diameters $\hat{d}_c$ and $\hat{d}_f$ were relatively close to each other over the range of experiments.

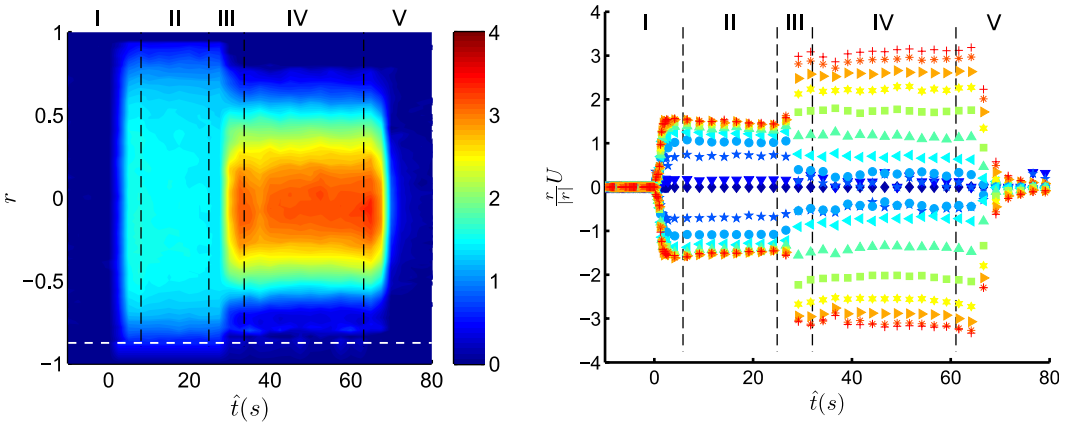

Figure 4-3: Data from Ultrasonic Doppler Velocimeter from experimental batch A for $\hat{V}_0$=38.4 mm/s (Re=1.66, B=0.22 and M=400): a) Contours of the dimensionless streamwise velocity profiles with scaled radial distance, $r = 2\hat{r}/\hat{D}$, and time $\hat{t}$. Dashed line represents the limit between the UDV data and model regression. b) Time evolution of the dimensionless streamwise velocity for different r: 0.0 (+), 0.1(*), 0.2(►), 0.3(✸), 0.4(□), 0.5(▲), 0.6(◄), 0.7(○), 0.8(★), 0.9 (▲) and 1.0 (◊).

The dimensionless velocity contour, $U = \hat{U}/\hat{V}_0$, obtained by the UDV probe, is presented in figure 4-3.a as a function of time, $\hat{t}$, and dimensionless radial position, $r = 2\hat{r}/\hat{D}$. It is possible to identify the symmetry with respect to the tube center line. Due to the nature of the UDV measurements there is always some refraction errors close to the lower wall of the pipe. To provide better understanding of the UDV data, the corresponding data points to the lower wall were suppressed, and a model prediction is instead added. Another way to interpret the UDV data is to study the streamwise velocity as a function of time at an averaged radial position, as shown in figure 4-3.b. The UDV probe is fixed at $\hat{x}$ =1560 mm and, as a static observer, it measures the velocity contour of the fluid at this particular location at different time stamps. Based on the data in figure 4-3, it is possible to identify 5 different stage in the local flow (described below) as the displacement front passes from upstream to downstream. These stages can each be important in processes related to the fluid displacement, specially in the context of the pipeline restart and shut-down:

I. Transient start-up: As the gate valve opens, displaced fluid 2 starts to move until the experiment steady state velocity ($\hat{V}_0$) is reached.

II. Fluid 2 steady state flow: Steady state flow of fluid 2 in a pipe of diameter $\hat{D}$, which shows a typical plug-type profile for viscoplastic fluids Alba and Frigaard (2016) [15] (see also figure 4-4).

III. Displacement front region: We observe a period of time when the measured velocity profile is influenced by the front region that contains both fluids 1 and 2.

IV. Displacing fluid 1 steady state flow: Steady state flow of fluid 1 in a pipe of effectively reduced diameter pipe ($\hat{d}_C = \hat{D} - \hat{h}$), due to the formation of the residual layer at the wall. For example in this stage, figure 4-3.a shows regions of zero velocity near the walls and figure 4-3.b shows an increase in the streamwise velocity, due to this diameter restriction.

V. Transient shut-down: As gate valve closes at the end of the experiment, the pressure drop goes to zero and the flow ceases.

Figure 4-4 shows the average streamwise velocity profile measured for regions II and IV of the same experiment shown in figure 4-3. Also marked on figure 4-4 are the analytical solutions for fully developed flow, based on the rheological parameters and the mean velocity. In the case of region IV, we have plotted analytical solutions for both reduced diameters, $\hat{d}_C$ and $\hat{d}_f$; in each case the displaced fluid wall layers are stationary. Note that regions I and II are very important for assessing the validity of the experiments. In region I the velocity increases to reach a plateau, and in region II the velocity should be constant. Any deviation from these behaviors could for instance be related to the *wall slippage* (Bertola et al., 2003 [50]) or flow rate variation.

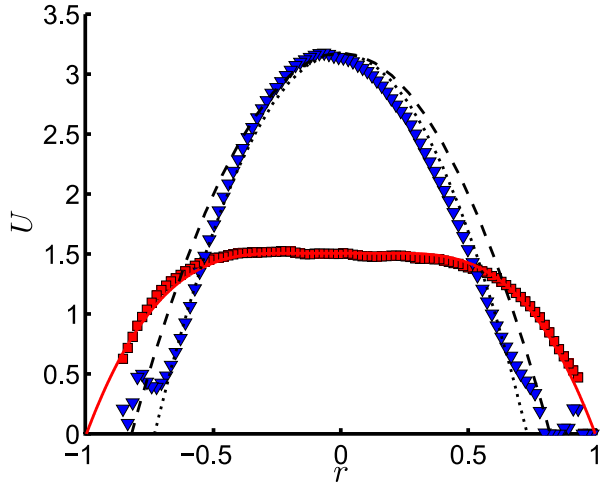

Figure 4-4: Average streamwise velocity profiles for regions II (□) and IV (▼) corresponding to the experiment shown in figure 4-3. The solid line shows the fitted profile obtained from the analytical solution of a Herschel-Bulkley fluid. The Newtonian Poiseuille profiles have also been indicated considering: $\hat{d}_f$ (dashed line), $\hat{d}_C$ (dotted line).

4.4
Residual layer thickness

In each experimental set, we observe variations in the residual layer thickness along the tube, as the mean imposed flow velocity is verified between experiments. Figure 4-5.a shows snapshots of the concentration field after the front passes and figure 4-5.b shows their respective depth-averaged profiles. As the imposed velocity decreases, the amplitude of the residual layer variation increases which is better quantified in figure 4-5.b. Note that the interface modulations shown in figure 4-5.a are similar to those reported by Swain et al. (2015) [48] for light-heavy displacement flow of a viscoplastic fluid by an immiscible Newtonian fluid in a horizontal 2D channel, simulated using lattice Boltzmann simulations.

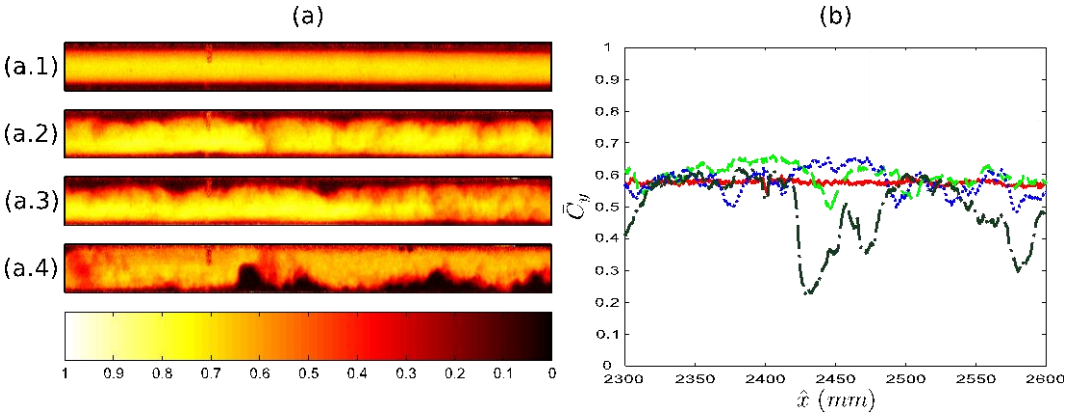

Figure 4-5: a) Snapshots of the concentration field for a 385 mm long section of the pipe located 2286 mm downstream of the gate valve after the passage of the front obtained for experimental set D given descending mean flow velocities: (a.1) $\hat{V}_0$=47.4 mm/s (Re=1.20, B=0.47 and M=532); (a.2) $\hat{V}_0$=20.7 mm/s (Re=0.30, B=0.71 and M=811); (a.3) $\hat{V}_0$=14.3 mm/s (Re=0.16, B=0.85 and M=982); (a.4) $\hat{V}_0$= 4.4 mm/s (Re=0.02, B=1.51 and M=1790). The bottom image is a colourbar of the concentration. b) Mean concentration for the same mean velocity from a: a.1 (solid line), a.2 (dotted line), a.3 (dashed line) and a.4 (dotted-dashed line).

The residual layer variation can also be identified from the spatiotemporal plot, as presented in figure 4-6 for different velocities belonging to experimental set D. The front velocity variation is very prominent in figure 4-6.d indicated by non-linear boundary between the two (dark and light) fluid regions. The vertical traces in the lighter region of figures 4-6.a-d correspond to the residual layers of viscoplastic fluid that remain static over long times after the passage of the front. This also confirms that there is no wall slip effect in our experiments. We note that there are considerable apparent differences in the spatial distribution and amplitude of the residual layers.

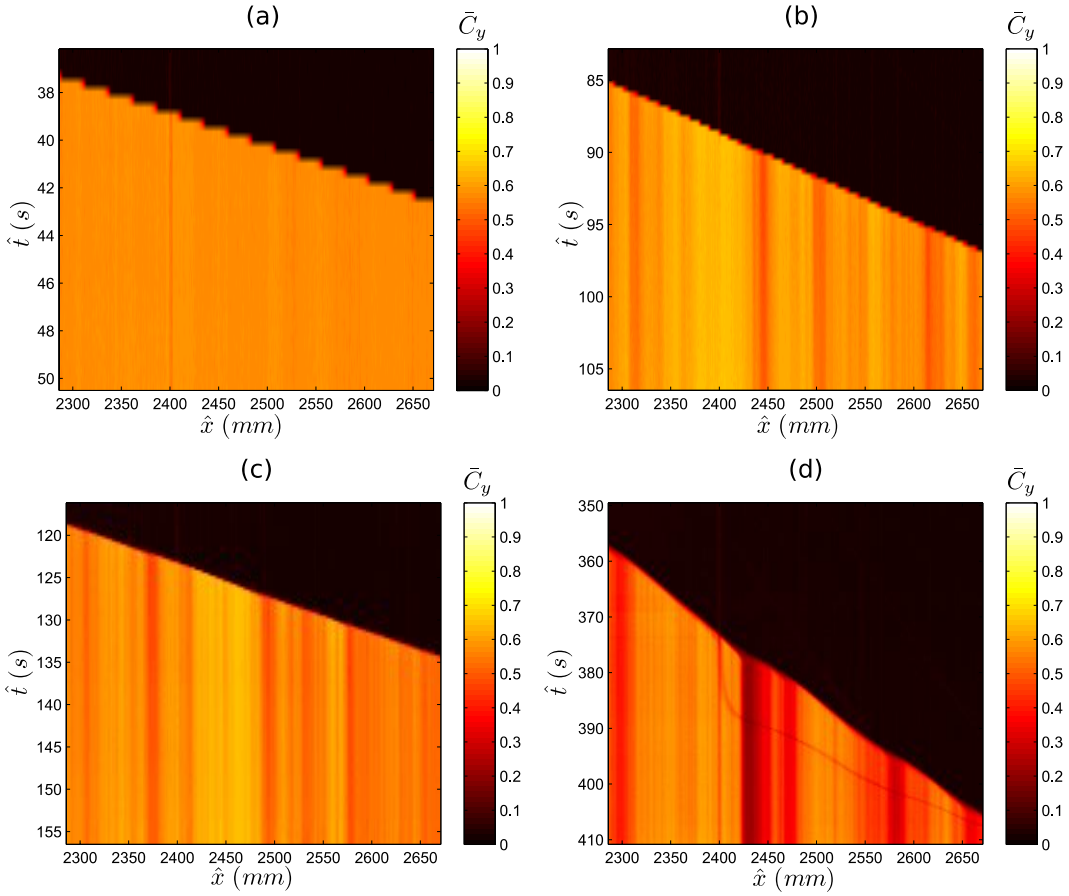

Figure 4-6: Spatiotemporal diagrams of the same experiments shown in figure 4-5.

The spatiotemporal diagram enables one to identify the position and speed of the front at every time stamp. Therefore, instead of showing the front velocity versus time, we can plot the front velocity variation against the position of the front, i.e. $\hat{V}_f(\hat{x})$ is the front velocity at the time when the front is at $\hat{x}$. Figures 4-7.a and b plot the variation of the dimensionless front velocity $V_f(x) = \hat{V}_f(\hat{x})/\hat{V}_0$ and the depth-averaged concentration $\overline{C}_y$ field along the tube section for two different experiments: low Reynolds number (Re=0.02, B=1.51, M=1791) and high Reynolds number (Re=1.85, B=0.3, M=378) respectively.

Figure 4-7.a shows a large amplitude variation of both front velocity and depth-averaged concentration whereas figure 4-7.b shows a comparatively lower amplitude variation of these variables. Note that, as suggested in these figures, the depth-averaged concentration is dynamically coupled to the front velocity, independently of Reynolds number, meaning that when the front velocity increases, the local depth-averaged concentration decreases and vice versa.

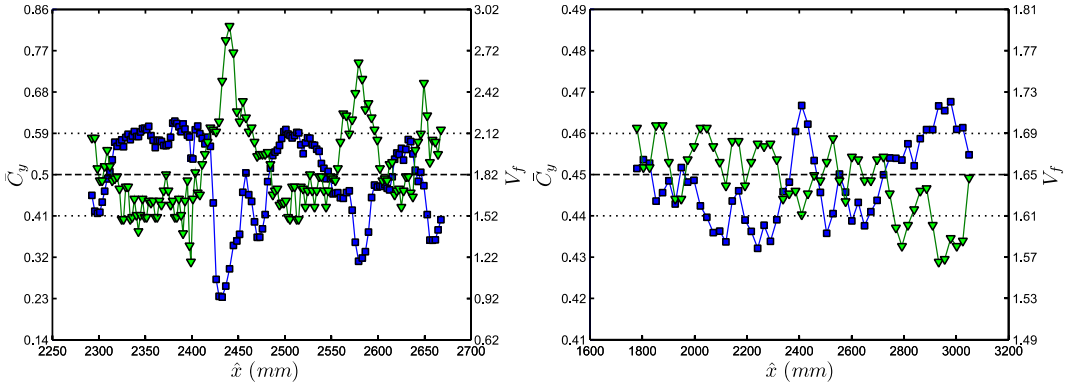

Figure 4-7: Variation of the mean depth-averaged concentration $\overline{C}_y$ (□) and front velocity V_f (▼) with the streamwise distance for a) Re=0.02, B=1.51 and M=1791 and b) Re=1.85, B=0.3 and M=378. Averages of V_f and $\overline{C}_y$ (dashed line) and the intervals of 95% confidence level (dotted lines) are also added to the figures.

From mass conservation we can define a parameter $\overline{Q}$ as follows to measure the bulk experimental data quality

$$\overline{Q} = \frac{\hat{V}_f \hat{d}_C^2}{\hat{V}_0 \hat{D}^2} = \overline{V}_f d_C^2/4 = \overline{V}_f \overline{C}, \qquad 4\text{-}8$$

where, $d_C/2 = \hat{d}_C/2\hat{R}$ is averaged dimensionless finger diameter of fluid 1, defined from $\overline{C}$ which is the mean of the depth-averaged concentration $\overline{C}_y$. Also above we have used the mean front velocity. For $\overline{Q} \approx 1$, mass conservation is closely respected. The slight errors associated with the data image processing, numerically calculating the derivatives required in computation of the front velocity and the snapshots sampling frequency, can all contribute to the quality value $\overline{Q}$ in each experiment. Having $\overline{Q} < 1$ (or $\overline{V}_f \overline{C} < 1$) can be due to the fact that the residual layers might not be perfectly *static* with part of it being washed away from the surface throughout the experiment, which consequently affects mass conservation (figure 10-5.b from appendix).

Figure 4-8.a shows the plot of quality $\overline{Q}$, versus Reynolds number *Re*, suggesting an average of 0.86 over the entire range of experiments. From (4-8), we can calculate an uncertainty of $\overline{Q}$ based on the standard deviation of the depth-averaged concentration $\overline{C}_y$, denoted $\delta\bar{C}$, and the standard deviation of the spatially varying front velocity $V_f(x)$, denoted δV_f. The uncertainty of $\overline{Q}$ is defined as:

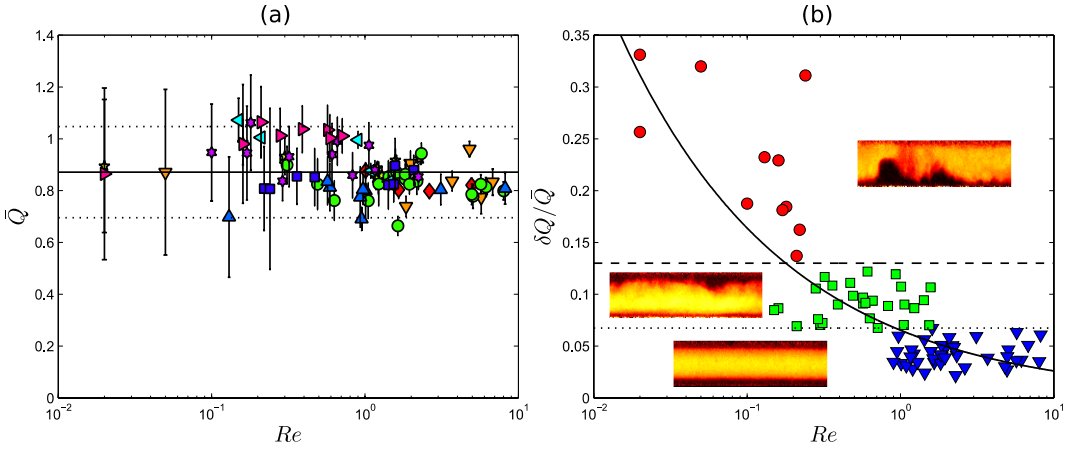

Figure 4-8: a) Mean quality $\overline{Q}$ and uncertainty, versus the Reynolds number *Re*, for the whole range of experiments; overall quality average (solid line) and intervals of 95 % of confidence level (dotted lines). Different markers represent experimental batch A(◊), B(▼), C(○), D(◄), E(★), F(▲), G(□), H(✸) and I(►). b) Change in the quality uncertainty with the Reynolds number (◊). The lines in b indicate: power law curve fitted to the data as $\delta\overline{Q}/\overline{Q}$ = 0.065 $Re^{-0.4}$ (solid line); transition between the smooth and wavy regimes at $\delta\overline{Q}/\overline{Q}$ = 0.067 (dotted line), transition between the wavy and corrugated regimes at $\delta\overline{Q}/\overline{Q}$ = 0.13 (dashed line).

$$\frac{\delta Q}{\overline{Q}} = \sqrt{\left(\frac{\delta\overline{C}}{\overline{C}}\right)^2 + \left(\frac{\delta V_f}{\overline{V}_f}\right)^2} \qquad 4\text{-}9$$

where $\overline{Q} = \overline{V}_f\overline{C}$ with $\overline{C}$ and $\overline{V}_f$ representing the mean value of the depth-averaged concentration and front velocity respectively.

Upon detailed analysis of the spatiotemporal diagrams of the experiments, we have been able to classify isodense viscoplastic displacement flows in three different categories, and match the observed behaviors to ranges of the uncertainty of $\overline{Q}$.

- *Smooth*: small amplitude residual layer variations characterized by a *linear* boundary between the two fluids in the the spatiotemporal diagram (e.g. figure 4-6.a). These experiments were found for $\delta Q/\overline{Q}$<0.067, as shown in figure 4-8.b;
- *Wavy*: medium amplitude residual layer variations characterized by *linear* boundary between the two fluids in the spatiotemporal diagram and clearly visible *vertical stripes* after the passage of the front (e.g. Figs. 4-6.b and c). These flows were found for 0.067< $\delta Q/\overline{Q}$<0.13, as shown in figure 4-8.b;

- *Corrugated*: large amplitude residual layer variation. In this category, apart from observing well-defined vertical stripes after the front has passed in the spatiotemporal diagram, there also exists a *non-linear* boundary between the two fluids, due to observable variations in the front velocity (e.g. figure 4-6.d). These flows were found to have $\delta Q/\overline{Q}$>0.13; see figure 4-8.b.

Figure 4-8 clearly shows that the quality uncertainty, $\delta Q/\overline{Q}$, which combines the variability in both local concentration and front velocity, visually corresponds to increased unevenness of the residual layers and this measure progressively increases from smooth to corrugated flows.

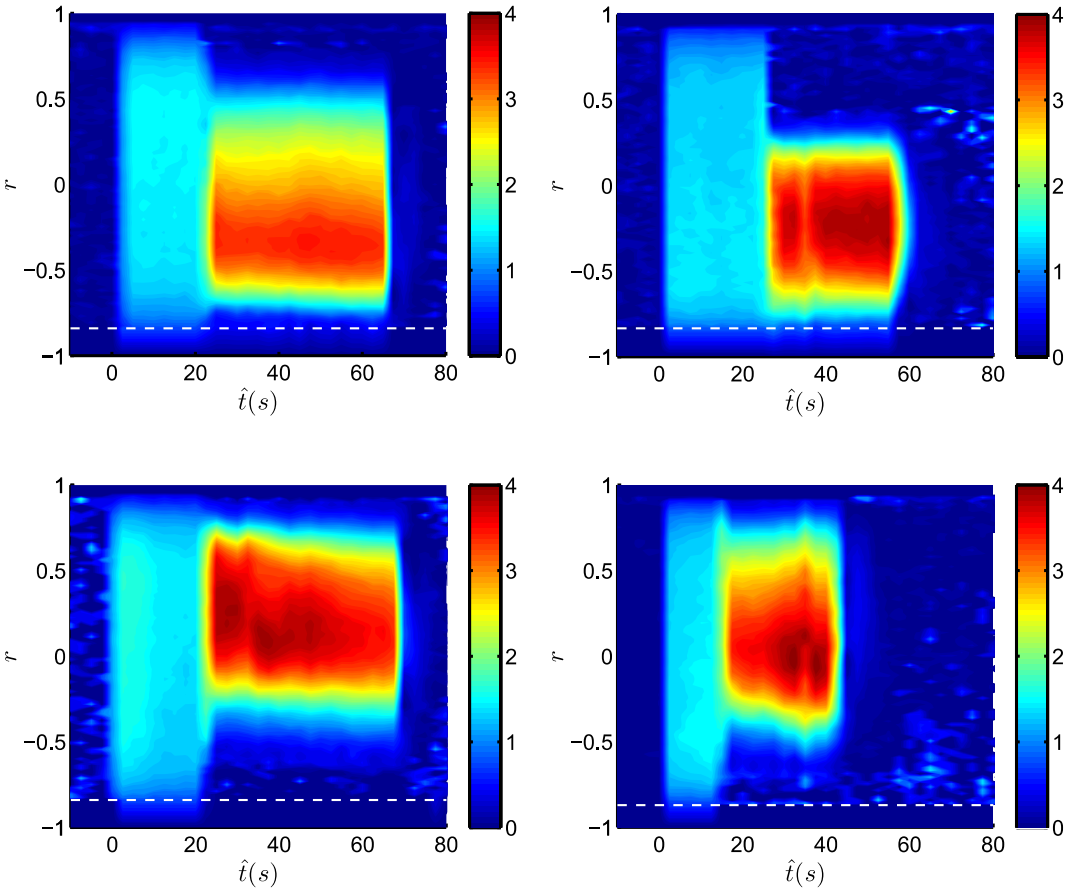

Figure 4-9: Contour of streamwise velocity obtained from UDV for experimental set G a) Re=1.01; B=0.4 and M=747, b) Re=0.93; B=0.4 and M=768 and for experimental set H c) Re=1.57; B=0.50 and M=693, d)Re=0.47; B=0.68 and M=1002. The UDV profiles for these experiments are given in figure 4-15.

The different flow regimes cannot be identified directly from the UDV data, as they correspond to a spatial variability while the velocity measurements are obtained at a specific location (UDV probe). Figure 4-3 and 4-4 earlier presented

typical examples of UDV data for the smooth regime, where the residual layer is uniform along the tube; see figure 4-3.a. In wavy and corrugated regimes, since the residual layer thickness fluctuates along the pipe, the UDV data can be affected as well. In fact, depending on the thickness of the viscoplastic residual layer around the pipe at the UDV probe location, the (displacing fluid) velocity can be displaced away from the pipe center. Figure 4-9 illustrates this for two different sets of experiments classified as *wavy*. Note that there is some noise in the contours shown in figure 4-9 which is associated with the UDV signals and is particularly higher when the flow is stopped. Note that we have also centralized UDV contours for wavy and corrugated regimes, i.e. similar to the smooth regime shown in figure 4-3.a.

In a few corrugated flow regime experiments, we were able to identify more then one displacing fluid finger, as shown in figure 4-10. This phenomenon could only be detected by the UDV system, and may be associated to instabilities of the front, perhaps similar to the *tip-splitting* mechanisms of Dimakopoulos and Tsamopoulos (2003) [43], which are not within the scope of this study.

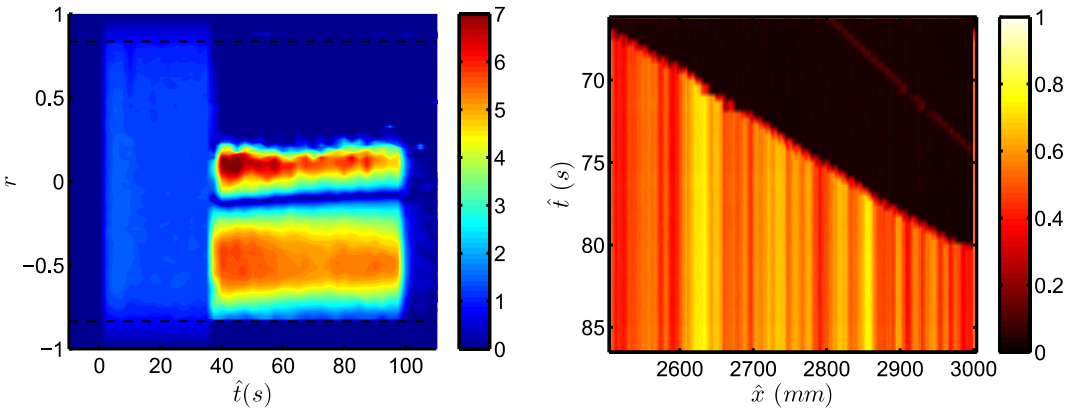

Figure 4-10: Example of isodense displacement with two fingers (Re=0.10; B=1.14 and M=1965): a) velocity contour; b) spatiotemporal diagram.

4.5
Flow regime results

We now consider how the main flow regimes defined in the previous section (*smooth*, *wavy* and *corrugated*), correspond to variations in the dimensionless groups of the problem. Figures 4-11. A and b show the flow regime classification plotted against dimensionless (Re-B) and (Re-M) respectively. With the aid of

figure 4-11 it is possible to identify two transitions: smooth-wavy and wavy-corrugated. The first transition occurs for Re≈1 and the second for Re≈0.20.

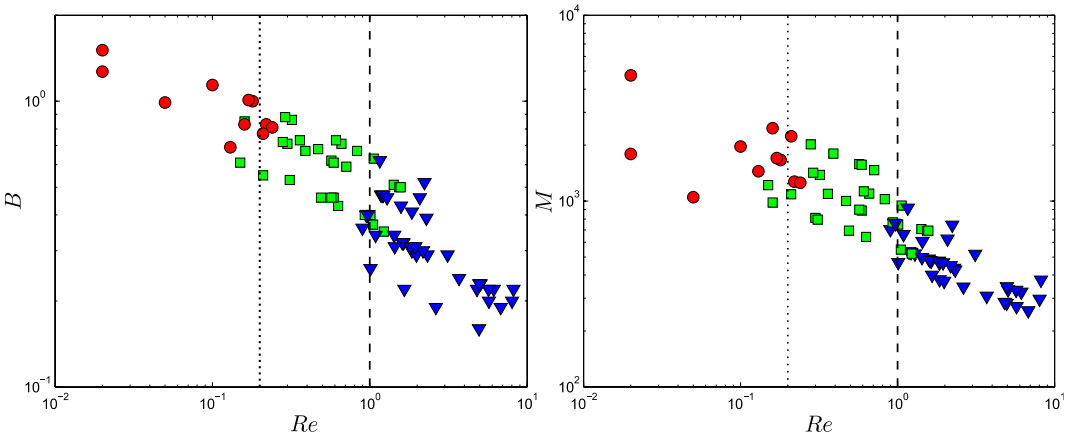

Figure 4-11: Flow regime maps: corrugated (○); wavy (□); smooth (▼) plotted in dimensionless planes of a) B and Re, b) M and Re.

Figure 4-11 suggests that the Reynolds number controls the level of the residual layer variation in viscoplastic displacement flow, emphasizing the importance of the inertial stress with respect to the characteristic viscous stresses of the displaced fluid. When inertial stresses become dominant, the residual layer is uniform (smooth regime) and fluid 1 flows smoothly in the center of the pipe. On the other hand, as inertial stress weakens, the residual layer amplitude variation increases, and the transition to the corrugated regime occurs. The effects observed are generally in agreement with the observations of Gabard and Hulin (2003) [14], but are also counter-intuitive as normally we associate instability (unevenness) with increasing inertia.

The Reynolds number also influences the front velocity and the effective diameter of fluid 1 as shown in figure 4-12. As the Reynolds number decreases, the front velocity $\overline{V}_f$ increases (figure 4-12.a) and the equivalent mean diameter of fluid 1 ($d_C/2 = \sqrt{\overline{C}}$) decreases (figure 4-12.b). The effects observed are in qualitative agreement with the findings of the numerical study of Wielage and Frigaard (2011) [18]. Figure 4-13.a shows how the front velocity affects the mean concentration $\overline{C}$ and figure 4-13.b, the relation between the d_C and d_f in the displacement experiments.

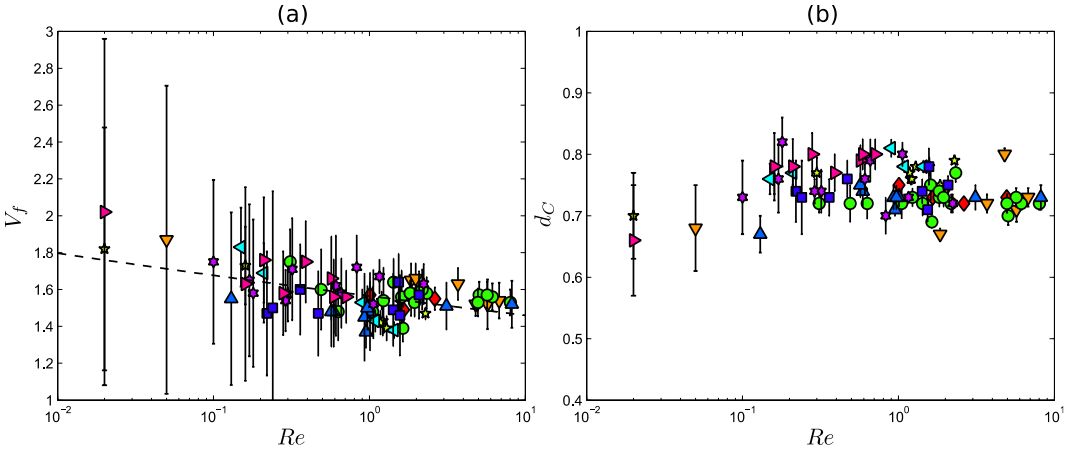

Figure 4-12: a) Dimensionless front velocity, $\overline{V}_f$, as a function of the Reynolds number and power law data regression $\overline{V}_f$ =1.6Re$^{-0.03}$ (dashed line). b) Fluid 1 mean diameter, $d_C/2 = \sqrt{\overline{C}}$. Different markers represent experimental batch A(◊), B(▼), C(○), D(◄), E(★), F(▲), G(□), H(✸) and I(►).

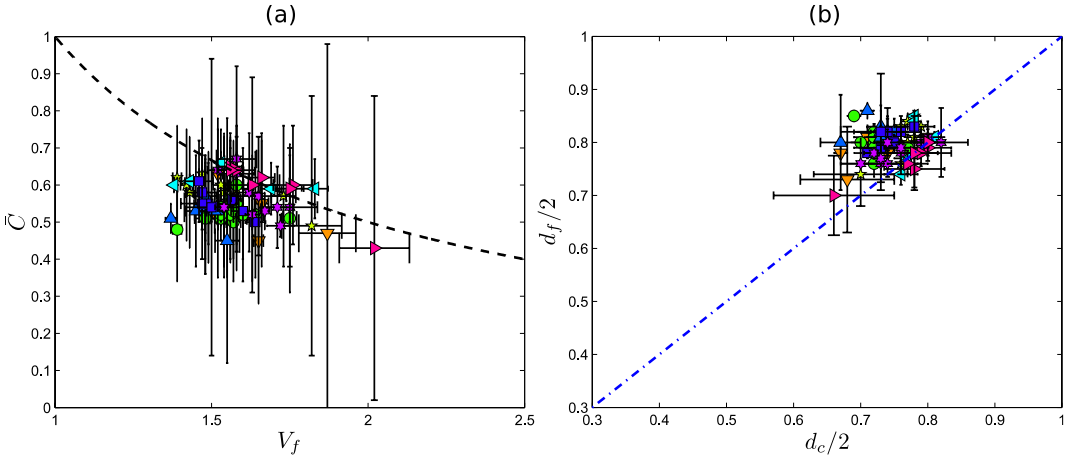

Figure 4-13: (a) Influence of $\overline{V}_f$, in the mean concentration $\overline{C}$. (b) Relation between d_c and d_f. Different markers represent experimental batch A(◊), B(▼), C(○), D(◄), E(★), F(▲), G(□), H(✸) and I(►).

We can use the front velocity ($V_f(x)$) and/or the mean concentration ($\overline{C}_y(x)$) variation to calculate the roughness of the residual layer, given by:

$$\epsilon_i = \frac{\delta d_i}{\overline{d}_i + \delta d_i}, i = f, C \qquad 4\text{-}10$$

where δd_i is the standard deviation of $d_i/2 = \hat{d}_i/2\hat{R}$ and $\overline{d}_i$ is the mean value of d_i. If the front velocity is considered, i=f, and if $\overline{C}_y(x)$ is considered, then i=C. Figure 4-14.a shows how the roughness calculated from front velocity (ϵ_f) relates to the one calculated from the mean concentration (ϵ_C). Since we have two data sets of roughness coming from different image processing algorithms and both are correlated, instead of using a specific set, an average roughness value has been

considered, defined as $\epsilon_{eq} = (\epsilon_C + \epsilon_f)/2$. It can be seen from figure 4-14.a that we are in the *large roughness* regime governed by completely different dynamics as laid out in the fundamental study of Huang et al. [51]. They showed that the flow in a duct with the hydraulic Reynolds number, Re_h, and relative roughness, ϵ, can be *laminar*, *transitional* and/or *turbulent*. The threshold Reynolds numbers were found to be

$$Re_L = -6340.3\epsilon + 2304.4, \qquad 4\text{-}11$$

from laminar to transitional flow and

$$Re_T = -3542\ln\epsilon - 3739.6, \qquad 4\text{-}12$$

from transitional to turbulent flow. In order to determine which of the laminar, transitional and turbulent regimes the Newtonian fluid is flowing at, besides the equivalent roughness calculated in Fig. 4-14.a, we need to compute the hydraulic Reynolds number for region IV as well. It is not difficult to show that

$$Re_h = \frac{\hat{\rho}\hat{V}_f\hat{d}_c}{\hat{\mu}}. \qquad 4\text{-}13$$

The results are presented in figure 4-14.b in the plane of Re_h and ϵ_{eq} over our full range of experiments. We can see that most of the experiments fall in the laminar regime with a few locating in the transitional regime. Note that similar findings were witnessed for non-isodense flows Alba and Frigaard (2016) [15].

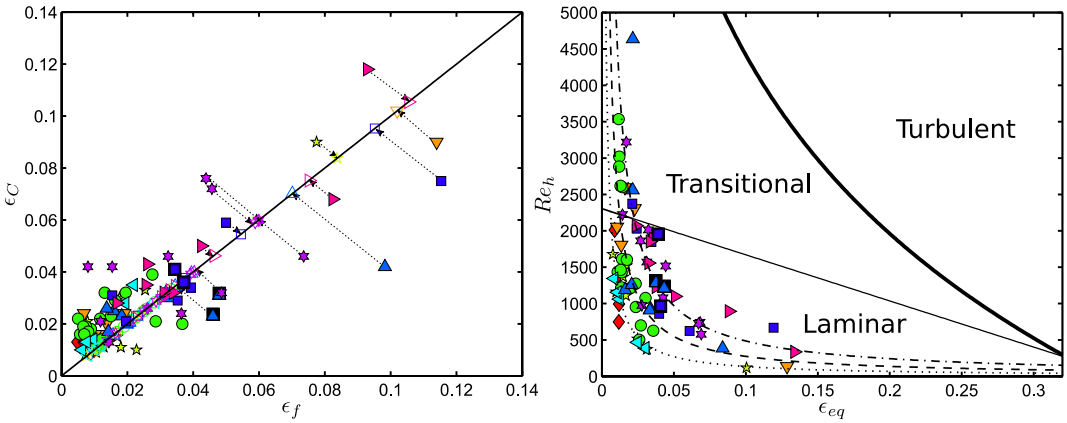

Figure 4-14: a) Correlation between the ϵ_C and ϵ_f (solid symbols), ϵ_{eq} (hollow symbols), $\epsilon_C = \epsilon_f$ (solid line). b) Flow dynamics classification of fluid 1 in region IV (Laminar, Transitional and Turbulent) in the plane of Re_h and ϵ_{eq}. $Re_L = -6340.3\epsilon + 2304.4$ (thin solid line), $Re_T = -3542\ln\epsilon - 3739.6$ (thick solid line), Re_h=13/ϵ_{eq} (- - -), Re_h= 26/ϵ_{eq} (.-.-.-), Re_h= 48/ϵ_{eq} (. . .). Different markers represent experimental batch A(◊), B(▼), C(○), D(◄), E(★), F(▲), G(□), H(✱) and I(►). The UDV profiles for the experiments marked by black squares are given in figure 4-15.

Also note that interestingly, the hydraulic Reynolds number seems to be inversely proportional to the equivalent roughness (figure 4-14.b), which is in line with our previous observation on the decrease of the interface modulations and variations with *Re* (figure 4-8.b). The example lines $Re_h = 13/\epsilon_{eq}$, $Re_h = 26/\epsilon_{eq}$ and $Re_h = 48/\epsilon_{eq}$ have been added to figure 4-14.b as eye guide. Also note that it seems as if surface roughness values in isodense displacement flows are overall lower than the ones in buoyant flows; see Fig. 9.b in Alba and Frigaard (2016) [15].

In order to check the validity of the results shown in figure 4-14.b on predicating the flow of the displacing layer to be in laminar regime, we have looked into the velocity profiles for a few flow examples marked by black squares. The mean velocity profile in region IV for these flows belonging to the experimental sets G and H are presented in figure 4-15. The velocity profiles overall suggest a parabolic shape which is typical of laminar flows. There is some asymmetry evident in case a (dotted line) which can be related to the skew in the UDV data (Taghavi et al., 2012 [11]). There is no clear *unsteadiness* and/or *flatne*ss appearing in the profiles similar to those of transitional and turbulent flows respectively. Some UDV examples of such flows are given in Alba and Frigaard (2016) [15] for buoyant flows for comparison.

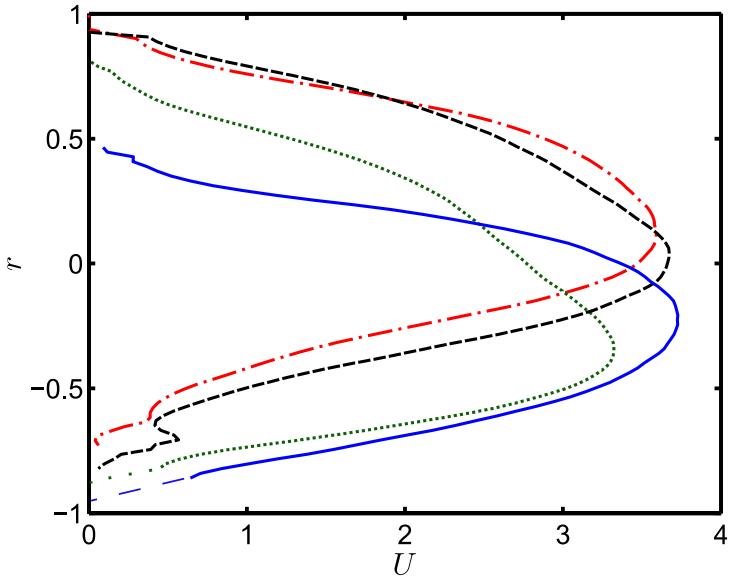

Figure 4-15: Average velocity profile at region IV for experimental set G a) Re=1.01; B=0.4 and M=747 (dotted line) b)Re=0.93; B=0.4 and M=763 (dashed-dotted line) and for experimental set H c)Re=1.57; B=0.50 and M=693 (solid line) d)Re=0.47; B=0.68 and M=1001 (dashed line).

The force balance for the developed steady state flow in region IV ($1/4\pi\hat{d}_c^2\Delta\hat{p} = \pi\hat{d}_C\hat{L}\hat{\tau}_i$) gives the shear stress at the interface between the two fluids Alba and Frigaard (2016) [15]:

$$\hat{\tau}_i = \frac{f\hat{\rho}\hat{V}_f^2}{8}, \qquad 4\text{-}14$$

where f is the Darcy friction factor. Since the stress varies linearly with the tube radius, we have the following expression for wall shear stress

$$\hat{\tau}_w = \hat{\tau}_i \frac{\hat{D}}{\hat{d}_f} = \hat{\tau}_i \sqrt{V_f}, \qquad 4\text{-}15$$

which is always larger than the interfacial stress, $\hat{\tau}_i$. The Darcy friction factor in laminar flow of a Newtonian fluid is given as $f = 1/64\ Re_h$ for small roughness values (ϵ_{eq}<0.05). However for large roughness (0.05<ϵ_{eq}<0.3) Huang et al. (2013) [51] proposed the following expression obtained experimentally

$$f = (10210\epsilon_{eq}^2 - 529.66\epsilon_{eq} + 64)/Re_h. \qquad 4\text{-}16$$

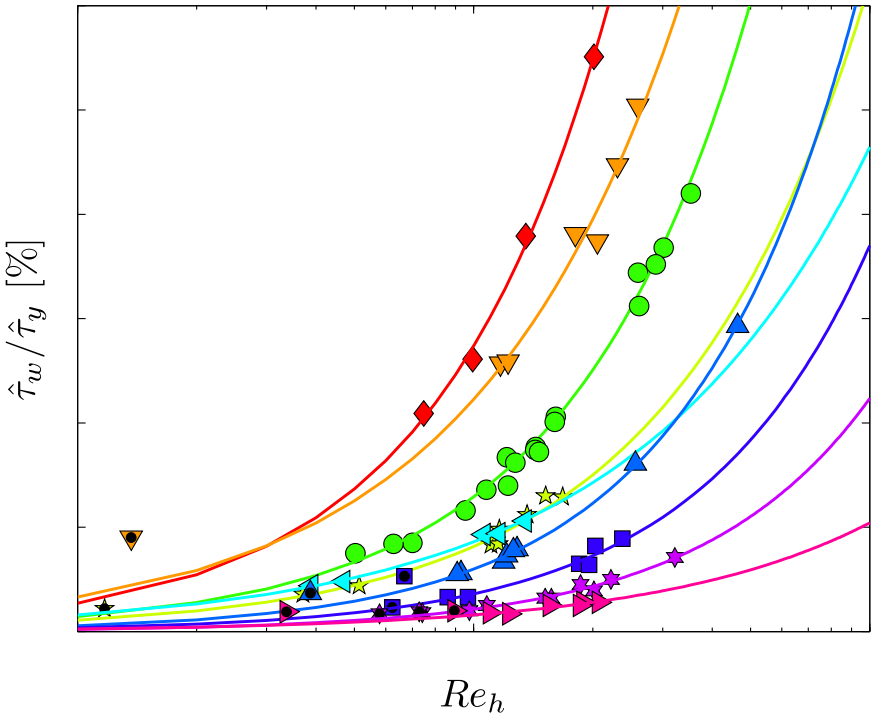

Figure 4-16: Dependency of the scaled wall shear stress in region IV with the hydraulic Reynolds number, Re_h, over the whole range of experiments. Corrugated flows are marked with superimposed black dots. The solid lines indicate power law regression with formulas $\hat{\tau}_w/\hat{\tau}_y = z_a Re_h^{n_A}$, $\hat{\tau}_w/\hat{\tau}_y = z_b Re_h^{n_B}$,... considering only ϵ_{eq}<0.05. Different markers represent experimental batch A(◊), B(▼), C(○), D(◄), E(★), F(▲), G(□), H(✸) and I(►).

The dependency of the percentage scaled wall shear stress, $\hat{\tau}_w/\hat{\tau}_y$, with the hydraulic Reynolds number, Re_h, has been plotted in figure 4-16. The figure shows that the wall stress in region IV is lower than 5% of the yield stress of the

viscoplastic fluid. Note that the interfacial stress would be even lower than this by $1/\sqrt{V_f}$, according to equation 4-15.

It is also possible to observe how that roughness approximation from Huang et al. (2013) [51] affects the wall stress, since the power law regression only considered Darcy friction factor from laminar flow of a Newtonian fluid.

This simple calculation shows that the Newtonian fluid flowing inside a reduced diameter geometry (region IV) does not produce a sufficiently large enough stress to yield the viscoplastic fluid at the interface or wall, which explains the reason of having a static residual layer after the front passage over long times. In other words, the residual layer formation is purely related to the front dynamics (region III).

4.6
Summary of fluid displacement experiments

In this chapter, we analyzed experimentally the isodense displacement of a viscoplastic fluid by a Newtonian one in a horizontal pipe. Velocity profiles and the fluids concentration field were acquired for several pair of fluids through Ultrasonic Doppler Velocimetry (UDV) and flow visualization respectively. The displaced fluids used were Carbopol solutions, while the Newtonian fluids were salt or glycerol-water solutions. The major flow pattern is characterized by a central displacement, with a residual layer of the displaced fluid left close to the tube wall.

Moreover, three distinct flow regimes could be identified within the central flows, namely *corrugated*, *wavy* and *smooth*, depending on the level of the residual layer variation along the pipe. The transition between these flow regimes is found to be a function of the Reynolds number defined as the ratio of the inertial stress to the characteristic stress of the viscoplastic fluid. In particular, *Re* = 0.2 and 1 for wavy-corrugated and smooth-wavy flow transitions respectively. The evaluation of the stress at the interface between the fluids showed that it remains below the yield stress, therefore the formation and modulation of the residual layer should be governed by the dynamics happening at the frontal region of the displacement.

5
Laponite - a thixotropic fluid with yield stress

This chapter presents the influence of different concentrations of NaCl and Laponite over the rheological properties of Laponite suspensions, specially yield stress and thixotropy. Before the rheological tests results, it is necessary to understand the Laponite suspension itself and a detailed bibliography review is presented. The extensive bibliography review was necessary to help to develop a reproducible Laponite protocol for sample preparation and to understand Laponite suspension rheological behavior.

5.1
Laponite Bibliography Review

Laponite (hydrous sodium lithium magnesium silicate) is a synthetic crystalline layered silicate colloid with crystal structure and composition closely resembling the natural smectite clay hectorite (Cummins, 2007 [32]). The Laponite particles are colloidal disks of 25 nm diameter and 1 nm thickness (Abou et al., 2001 [52]).

Because of the chemical structure of the clay, the faces of the disks are charged negatively when the particles are suspended in an aqueous solution. Depending on the pH of the solution, it appears that the sides of the disks can be charged positively (Bonn et al., 1999 [33]).

Laponite contains approximately 8 wt% water which is chemically absorbed into the crystal structure and can only be removed by baking at temperatures above 150 C°. In addition, Laponite is hygroscopic and will adsorb additional water from the atmosphere, typically up to 15% at 50% relative humidity (Cummins, 2007 [32]).

When Laponite is dispersed in water, the exchangeable sodium ions hydrate, causing the clay to swell initially and to separate completely (Cummins, 2007 [32]). This gives a clear colloidal dispersion of anionic Laponite platelets and hydrated sodium ions in solution (Escudier and Presti, 1996 [34]). In a salt-free aqueous

medium (Ravi Kumar et al., 2008 [53]), the aqueous dispersion results in the formation of nonergodic soft solids at very low concentration.

The synthetic colloid Laponite exhibits an array of different phases and behaviors due to both attractive and repulsive interactions, anisotropy and net charge, as well as an anisotropic charge distribution (Cummins, 2007 [32]).

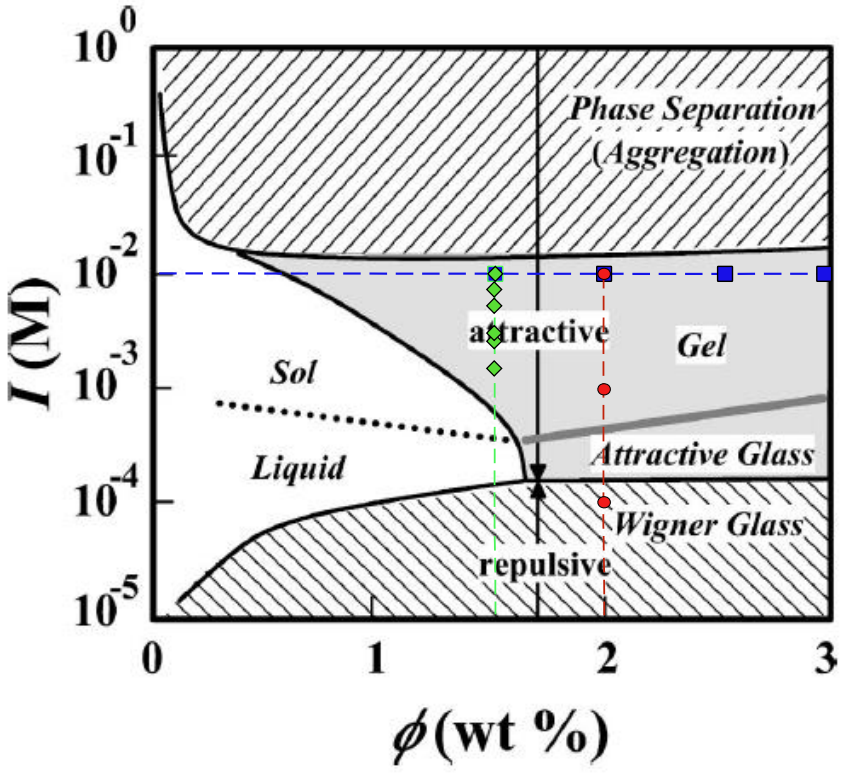

Figure 5-1: State diagram of Laponite suspension from Tanaka et al. (2004) [37]. Laponite suspensions: 2.0% (○); 1.5\% (◊) and I=10^{-2}mol/L (□).

As described by Tanaka et al. (2004) [37], the salt (NaCl) controls the interparticle interactions. Upon increasing of the ionic strength (I), electrostatic potential (Coulomb interactions between discs) is screened more strongly; eventually van der Waals attractions may prevail over electrostatic repulsion, leading to the colloids sticking together, i.e, gel formation. They also presented a detailed state diagram of Laponite suspension (pH=10) for the isotropic region (Figure 5-1) and showed that the competition between (anisotropic) long-range repulsions and van der Waals attractions induces the sequential transition between a repulsive glass, an attractive glass, and a gel in Laponite suspensions. The states observed in colloidal suspensions are:

- Aggregation (Flocculation)- At a very high ionic strength, a macroscopically homogeneous state becomes unstable and a system phase separates, possibly competing with gelation;
- Attractive gel - a multicomponent fluid that intrinsically has a hierarchic structure. Its elementary mechanical unit consists usually of chainlike aggregates of particles and is therefore much larger than the particle size. Attractive interactions play a dominant role; a percolated network forms (house of cards), which gives the system elasticity;
- Colloidal glasses: The elementary mechanical unit of glass is a particle itself. In general, glasses are much more rigid then gel for the same composition. The colloidal glasses can be classified in:
    1. Repulsive (Winger) glass is a colloidal glass with hard-core repulsive interactions. If crystallization is avoided, above a certain volume fraction of particles the system will jam, i.e., reorganization of the structure becomes exceedingly difficult. The result is that the system will fall out of equilibrium: a glassy state is formed. Long-range electrostatic repulsions dominate;
    2. Attractive glass (Intermediated state between gel and repulsive glass) is a colloidal glass where attractive interactions affect spatial distribution (i.e., the structure factor) but repulsive interactions still play the predominant role in the slow dynamics of the system. Depending on the depth of the attractive force and the particle concentration the system will jam.

A sol state would be characterized by the presence of clusters of Laponite particles with a finite lifetime and may consequently be inhomogeneous, which crucially differs from homogeneous liquid state.

The schematic figures representing repulsive (Wigner) colloidal glass, attractive glass and gel presented by Tanaka et al (2004) [37] are reproduced in figure 5-2.

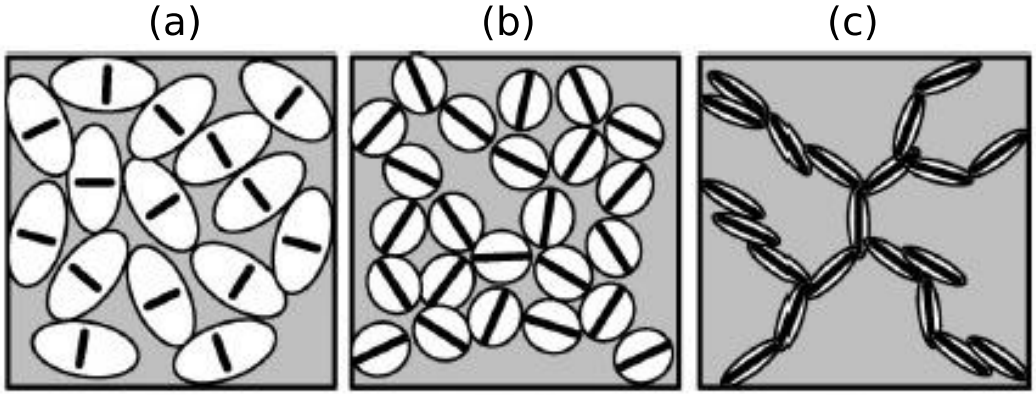

Figure 5-2: Schematic figures from Tanaka et al. (2004) [37] representing repulsive (Winger) colloidal glass (a), attractive glass (b), and gel (c). Each thick line represents a Laponite disk, while ellipsoid represents the range of electrostatic repulsions.

Therefore, it has been proposed that a salt-free ($I<10^{-4}$ mol/L) Laponite suspensions form the so called repulsive colloidal glasses, and are stabilized by electrostatic repulsion. In such systems, the ergodicity is lost due to blockage of particle movement by the dense surrounding cages formed by their nearest neighbors.

The addition of salt to a suspension of Laponite disks reduces electrostatic repulsion and can even lead to attraction Abou et al (2003) [54]. When the strength of short-ranged attraction becomes significantly greater than the thermal energy, the system can form a colloidal gel, in which particle motion will be completely jammed even at very low bulk volume fractions. The system behaves in a nonergodic fashion prior to complete blocking of the particle dynamics. Therefore, by varying the strength and range of attractive interactions, a reentrant transition of the liquid glass line and a glass-glass transition can be realized (Abou et al., 2003 [54]).

The rheological properties of Laponite dispersions are known to change over time. The aging period could be as long as a year. However, for Laband and Lorens (2005) [40], the major changes take place during the first 7 days after their preparation.

5.1.1
Colloidal Glass Aging

Many authors tried to understand the reason for Laponite suspensions aging process. Suspensions of Laponite become strongly viscoelastic over time, even at

low volume fraction. Bonn et al. (1999) [33] studied the structure of Laponite suspensions using static light scattering and showed that the large viscosity increase is not due to the formation of a fractal network and that the origin of this aging behavior is due to the glassy dynamics.

Glassy systems (Abou et al., 2003 [54]) exhibit two modes of relaxation: a fast mode that corresponds to the fast motion of particles in cages constituted by their neighbors and a slow mode of relaxation that results from structural rearrangement of these cages.

The Laponite suspensions age on time scales that depend on the particle concentration and ionic strength. For Abou et al. (2001) [52] the diffusion of particles can be described as a cage-diffusion process. The first relaxation time characterizes the short-time Brownian diffusion of a particle in the suspending liquid. For short times, the particle diffuses freely within a cage formed by the surrounding particles. Therefore, this diffusive motion does not depend on the aging time.

The second relaxation process, occurring for long times, can be interpreted as the escape from the cages. The corresponding characteristic time increases rapidly with the aging time, indicating that it becomes more and more difficult for a particle to escape. From this, it immediately follows that for short aging times the system is ergodic: the particles reside in the cages formed by surrounding particles and escape from them after a characteristic time that depends on the aging time. As the system ages, the escape from the cages becomes slower. The particles are subsequently constrained by the cages, resulting in an ergodicity breakage within the observation time scale.

Therefore, the collective diffusion process of particles can be interpreted as a cage-diffusion process. For short aging times, the system is ergodic and normal Brownian motion is observed. The particles reside in the cages formed by surrounding particles and escape from them after a characteristic time, which is aging time dependent. As the system ages, the escape from the cages become slower, resulting in a strong ergodicity breakage. Then, the slowing down of the diffusion is concomitant with the increase of viscosity of the sample. The viscosity should be given by the relaxation time of the slow mode of the glassy system (Bonn et al., 2002 [55]).

5.1.2
Colloidal Glass Rejuvenation

The detailed predictions of nonlinear rheological behavior and the microscopic dynamics for a typical soft glassy (colloidal glass) material described by Bonn et al. (2002) [55] are:

1. Without an external forcing, the systems evolve spontaneously: they are said to age, meaning that the relaxation time of the slow mode increases in time;
2. Under an external drive, the system can reach a steady state: the aging stops, and the relaxation time is constant;
3. Upon increasing the forcing, the relaxation time in steady state decreases;
4. Both in the presence of an external drive and during the aging, the viscosity is given by the (distribution of) relaxation time(s) of the slow mode of the glassy system;
5. The viscosity decreases strongly with the shear rate applied to the system.

In particular, as a result of these theoretical predictions, it is expected that if power is injected into aging systems, there is a possibility of stabilizing the age of the system on a power dependent level: the younger the larger the power input. The driving force that acts on the system results in the suppression of the aging process. Once driven is suppressed, the spontaneous aging process again takes place.

These theoretical predictions are confirmed by the experimental results described in Abou et al. (2003) [54] that made several experiments injecting power to aging Laponite suspensions. In order to compare the driven aging dynamics to the spontaneous one, they measured the complex viscosity modulus of the suspension under shear. Considering the complex viscosity modulus as a measure of the age of the system, Abou et al. (2003) [54] observed:

- The aging dynamics under flow is very slow compared to spontaneous aging dynamics: the complex viscosity modulus increase slower when the system is submitted to an external drive;
- If the drive was suppressed once the stationary state was attained, the spontaneous aging process again took place as was observed by

performing oscillatory shear experiments: the complex viscosity modulus changed very rapidly, by two orders of magnitude in about 1 h, in a way similar to that observed in the spontaneous aging process;

- The larger the shear rate applied, the smaller the value of the stationary viscosity it reaches. By reporting the values of the stationary viscosity as a function of the shear rate applied, shear-thinning behavior was observed;
- The larger the shear rate applied, the faster the stationary state is reaches. The time necessary to obtain steady state for constant respective shear rates of 50, 100 and 500 1/s, are 10, 5 and 1 h, respectively;
- Starting from different aging times, continuous shear strain with the same constant rate was applied to the system and the same non-equilibrium stationary state is attained, characterized by very similar viscosities;
- The steady-state viscosity thus appears to depend only on the shear rate applied;
- The complex viscosity modulus and the dynamic viscosity evolve in the same direction, both decreasing with time: the so-called rejuvenation of the suspension was observed;
- It is worth noting that, even by strongly shearing the suspension for hours, the initial liquid state was never reached again, and the final state is determined by the rate of the shear strain applied.
-

From Abou et al. (2003) [54] experimental results, it appears that the external drive leads to drastic slowing down of the spontaneous aging dynamics or, in some cases, in rejuvenation of the system. The occurrence of rejuvenation or driven aging depends on both the external drive power and the age of the system when applying the external drive. This is completely consistent with phenomenological models in which the final stationary state results from the competition between the spontaneous aging dynamics that strengthens the interactions between particles and leads to less and less accessible configurations in phase space as time evolves and the mechanically induced rejuvenation of the configurations the process that works against spontaneous aging and leads to its slowing down.

5.1.3
Thixotropy and yield stress

The competition between aging and rejuvenation ensures to Laponite suspension thixotropic characteristics. Barnes (1997) [56] did an extensive review over thixotropy and to provide a better understanding of how the competition between aging and rejuvenation is modeled, a few thixotropic models are detailed in the appendix 11 .

For Escudier and Presti (1996) [34] thixotropy is the term used to classify fluids for which there is an isothermal, time-dependent breakdown of some particulate structure under relatively high shear followed by structural build-up for lower shear. As Nguyen and Boger (1985) [57] point out, the applied shear acts to disrupt structural bonds interlinking fluid elements, which may be the primary particles and/or aggregates of such particles. At the same time, shear-induced collisions of the separated structural elements tend to reform part of the broken bonds so that a state of dynamic equilibrium is attained when these two processes balance. In the absence of sufficiently high shear, thixotropic fluids may become a gel and so exhibit a yield stress.

In practice, the yield stress for Coussot et al. (2002) [31] is mostly due to the microstructure of the fluid that resists large rearrangements: the system is jammed and stops or starts flowing abruptly. When submitted to flow, this microstructure is partly destroyed, which is generally observed in rheological tests as a viscosity that abruptly decreases in time. In addition, for most of these systems at rest the microstructure reforms or evolves spontaneously: the system is said to age. If the microstructure reestablishes at rest, one observes an increase of the apparent yield stress with time.

The mechanical behavior of these systems consequently results from the competition between aging and progressive rejuvenation (destruction of the microstructure) by shear. The incipient flow destructs the materials, entailing a viscosity decrease, which in turn accelerates the flow and so on: avalanche behavior results. The rheological measurements show that the viscosity jumps in a discontinuous way to infinity at a critical stress. In addition, due to the aging, this critical stress is not an intrinsic property, but depends on the (shear) history of the sample. All these observations show that yield stress is ill-defined.

Yield stress cannot be considered separately from thixotropy, both are strongly interconnected: they are the result of the jamming and unjamming of the microstructure of the materials.

5.2
Yield stress of Laponite suspensions

To understand the competition between aging and rejuvenation in the yield stress of Laponite suspensions, creep tests are performed. These tests are done in the rotational rheometer ARG-02, from TA instruments, with cross hatched plate-plate geometry with 50 mm diameter. Figure 5-3 presents a creep test example ($\hat{\tau}_y$=61 Pa) for Laponite suspension of 2.5% wt and I=10^{-2}mol/L, with aging time of 14 days.

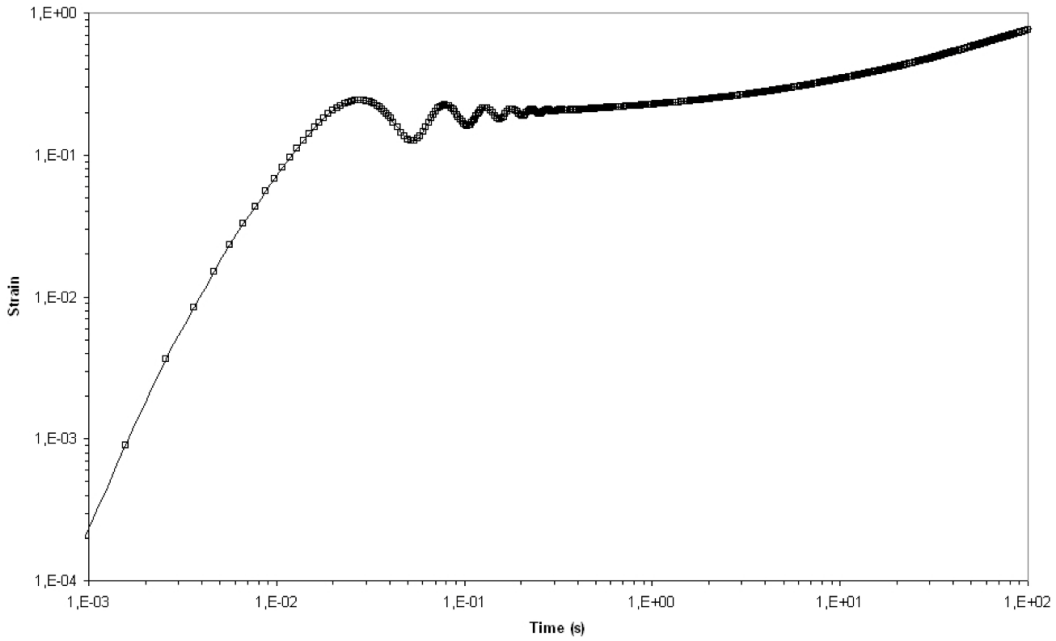

Figure 5-3: Creep test response of Laponite suspension of 2.5% wt and I=10^{-2} mol/L with aging time of 14 days for $\hat{\tau}_y$=61 Pa.

During a creep test, in the initial period ($\hat{t}$< 1 s), the system shows significant oscillations in strain that attenuate very quickly. Such behavior is known to occur as a result of the viscoelastic characteristic of the fluid coupled with the instrument inertia, as showed by Joshi et al. (2007) [58]. Since the instrument is the same for all experiments, if the same Laponite suspension batch (aging time, Laponite and NaCL concentrations) is considered, the initial response should be the same independently of the stress applied. This phenomenon only occurs if samples are

initially at rest. On the other hand, it may show the influence of aging in the viscoelastic characteristics of Laponite suspension.

Coussot et al. (2002) [31] performed bifurcation tests in yield stress fluids and observed that above the yield stress, the viscosity decreases to reach a steady-state value after a long time. For a stress smaller than the yield stress, the viscosity increases indefinitely. Therefore, the flow either stops completely or evolves towards a rapid flow, similar to an avalanche. Figure 5-4 presents an example of the bifurcation test for Laponite suspension of 2.5% wt, $I=10^{-2}$mol/L and aging time of 67 days. The bifurcation phenomena can be observed, since the steady-state viscosity jumps discontinuously from high to a low finite value.

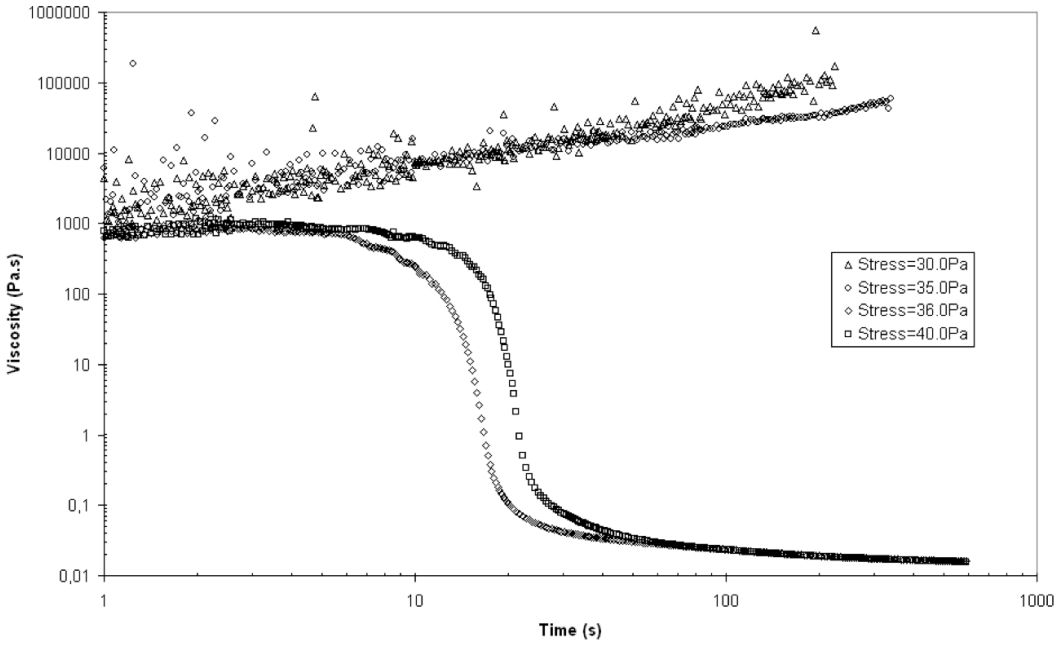

Figure 5-4: Bifurcation in the rheological behavior (viscosity) for Laponite suspension of 2.0%, $I=10^{-2}$ mol/L and aging time of 67 days. Different markers represent creep tests of 30 Pa (▲), 35 Pa (○), 36Pa (◊) and 40 Pa (□).

In our experiments the yield stress will be defined by the average between the upper (minimum stress that viscosity reaches a low steady state value) and lower (maximum stress that viscosity starts to increase) bounds obtained in the bifurcation test.

The same effect can be identified in the strain, for a stress smaller than the yield stress, the sample deforms as an elastic solid and the strain remains constant after the initial transient. On the other hand, when the stress is higher than the yield

stress the sample begins to deform continuously as a fluid, with a constant shear rate, as shown in figure 5-5.a.

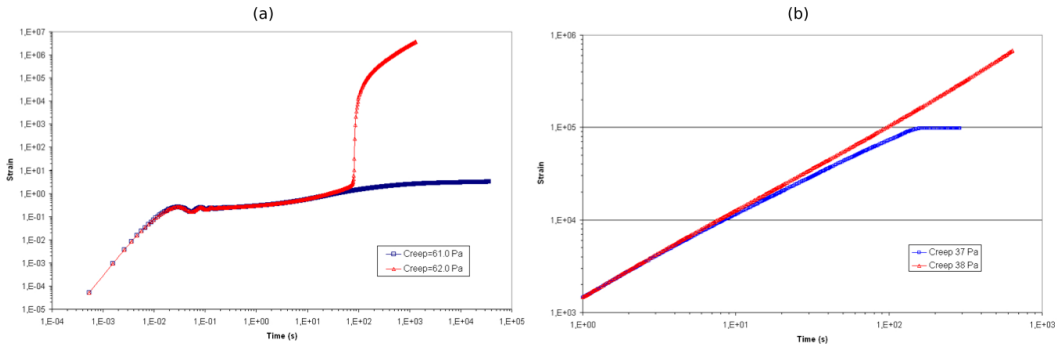

Figure 5-5: Creep test response of Laponite suspension of 2.5% wt, I=10^{-2} mol/L for yield stress determination: (a) aging time of 20 days: 61Pa (□) and 62Pa (○); (b) After pre-shearing: 37 Pa (□) and 38 Pa (○).

The sample initial condition affects the apparent yield stress. If we consider a rejuvenated sample (pre-shearing) before the bifurcation test, a different yield stress will be identified. Figure 5-5 presents the determination of yield stress for a laponite suspension of 2.5% (wt) and I=10^{-2} mol/L, with aging time of 20 days (a), and after pre-shearing (b). It can be observed that aging time influences the apparent yield stress of Laponite suspensions. Rejuvenated samples have lower apparent yield stress than aged Laponite samples. So different shear history implies different apparent yield stress. The yield stress with and without pre-shearing for different Laponite suspensions are presented in table Table 5-1. The pre-sheared samples are represented by aging time equal to 0.

Table 5-1: Laponite suspensions yield stress for different aging time, Laponite concentration and ionic strength.

Laponite Concentration	NaCl Concentration	Bifurcation Test			
		Aging time	$\hat{\tau}_y$	Aging Time	$\hat{\tau}_y$
(%wt)	(mol/L)	(days)	(Pa)	(days)	(Pa)
1.5	10^{-2}	0	11	12	22
2.0	10^{-4}	0	8.5	67	9.8
2.0	10^{-3}	0	10.5	77	13.5
2.0	10^{-2}	0	28.0	14	35.5
2.0	10^{-2}	0	27.3	67	43.5
2.5	10^{-2}	0	37.8	20	62.0
3.0	10^{-2}	0	52.5	77	101.5

The yield stress of rejuvenated Laponite suspension (pre-sheared) increases as the Laponite concentration increases, for the same ionic strength. The relation between yield stress and Laponite concentration seems to be linear. It is important

to address that Laponite suspensions are only yield stress fluids at gel and /or colloidal glasses states (see the state diagram of Laponite on figure 5-1). The Laponite suspension yield stress as a function of the Laponite concentration is presented in Figure 5-6.a.

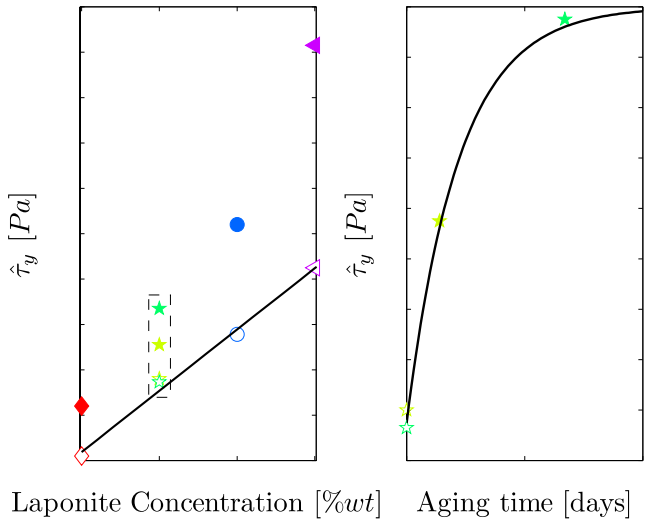

Figure 5-6: (a) Influence of Laponite concentration in yield stress for I=10^{-2} mol/L: 1.5% (◊); 2% (*); 2.5% (○); 3.0\% (◀). Hollow symbols represent pre-sheared samples and solid, aged samples. (b) Influence of aging time in yield stress for 2% (*) and I=10^{-2} mol/L.

As Laponite suspension ages, the apparent yield stress increases and tends to asymptote. Figure 5-6.b shows the results for the Laponite suspension of 2% and I=10^{-2} mol/L. The apparent yield stress of aged Laponite are always greater than the rejuvenated Laponite. The yield stress after pre-shearing is equivalent regardless of aging time.

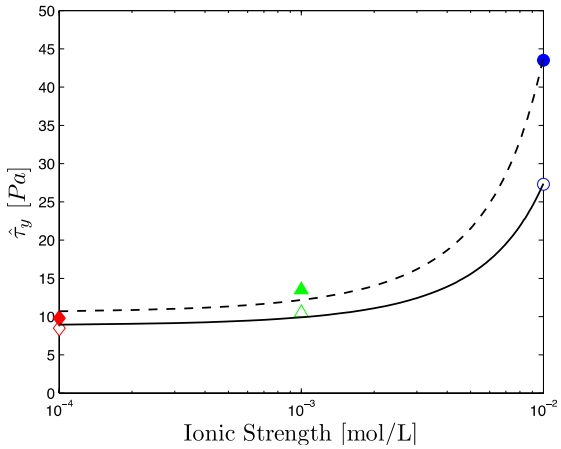

Figure 5-7: Influence of Ionic Strength in Yield Stress for Laponite concentration of 2% and aging time between 67 and 77 days.

As the ionic strength increases, the yield stress increases for both rejuvenated or aged Laponite suspension. The ionic strength seems to affect exponentially the

yield stress of Laponite suspensions. The influence of ionic strength in the yield stress for Laponite concentration of 2% is presented in figure 5-7.

We developed a simple test to identify the effect of resting time in the rheological properties of Laponite suspensions. It consists of a creep test just after a pre-shearing and resting time periods. The sample is pre-sheared until the steady state solution is achieved. The same stress that will be applied in the creep test is considered in the pre-shearing period. Then, the sample is kept at rest for a specific resting time before the creep test is performed.

Figure 5-8 shows the effect of resting time in a Laponite suspension with 1.5% wt and I=10^{-2}mol/L. In the example presented, the stress applied is equal to 22 Pa ($\hat{\dot{\gamma}}$=1500 Hz). It is clear from the initial period of the creep test that, as the suspension rests, the sample becomes more viscoelastic, as the ripple amplitude increases. The time to reach steady states ($\hat{\dot{\gamma}}$=1500 Hz and $\hat{\tau}$=22 Pa) is also influenced by the resting time. However, the steady state value does not depend on resting time.

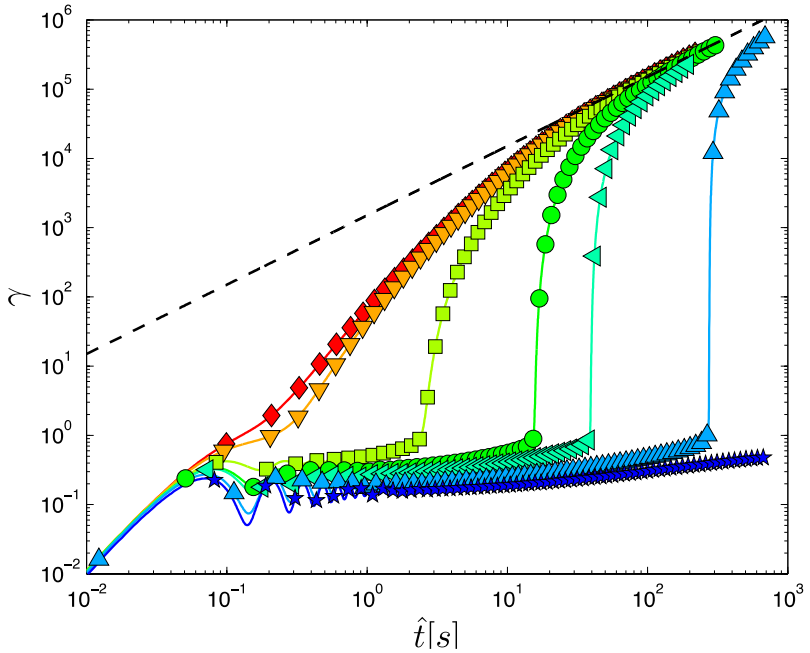

Figure 5-8: Influence of resting time in the creep test (22Pa) response of Laponite suspension 1.5% wt and I=10^{-2}mol/L: steady state solution (dashed line); resting time: 5 s (◊), 10s (▼), 100 s (□), 200 s (○), 300 s (◄) and 12 days(▲). Creep test after 12 days of aging for 20 Pa as reference (*).

Similar to rheological tests with waxy crude oil performed by Tarcha et al. (2015) [59], the transition between solid to liquid behavior of Laponite suspensions occurs for the same *critical strain* (≈0.06), regardless of resting time.

Coussot et al. (2012) [31] presented a typical steady-state flow curve for an ideal yield stress fluid and a real fluid. The rheological measurements show that in real fluids the viscosity jumps in a discontinuous way to infinity at a critical stress, contrary to the continuous divergence anticipated for ideal yield stress fluids. We evidenced that as the Laponite suspension ages, the apparent yield stress increases. As the sample rejuvenates (pre-shearing), the apparent yield stress decreases. A typical steady-state flow curve (viscosity vs shear stress), for Laponite suspension of 2.0% wt and I=10^{-4}mol/L, is presented in figure 5-9.

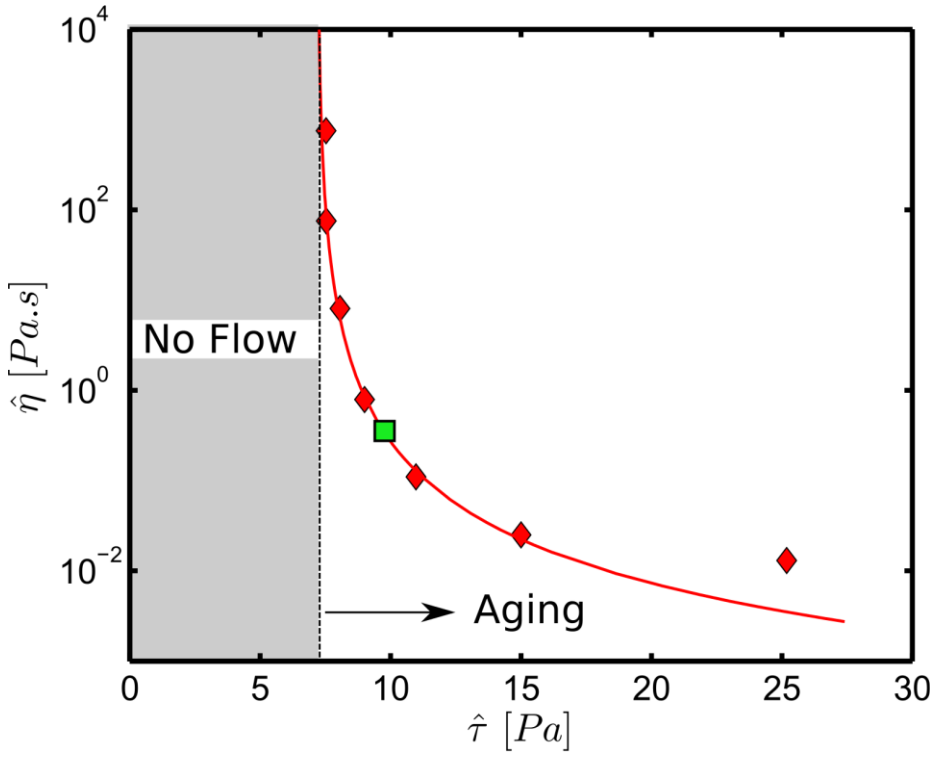

Figure 5-9: Schematic of a typical steady-state flow curve for Laponite suspension of 2.0% wt and I=10^{-4} mol/L: rheological experiment (◊) and Herschel-Bulkley model (continuous line); yield stress after 67 days of aging (□).

5.3
Thixotropy effects over Rheological Tests

The transient response of rheological tests shows the thixotropy effect in the Laponite suspensions. Figure 5-10.a shows the transient responses of a shear rate step change from 100 to 10 Hz, obtained in a stress controlled rheometer (ARES-G2) with cross-hatched plate-plate (50mm), for the same Laponite concentration of 2% wt, but for two different NaCl concentrations, one associated to the gel state (10^{-3}mol/L) and other to the Winger glass state (10^{-3} mol/L).

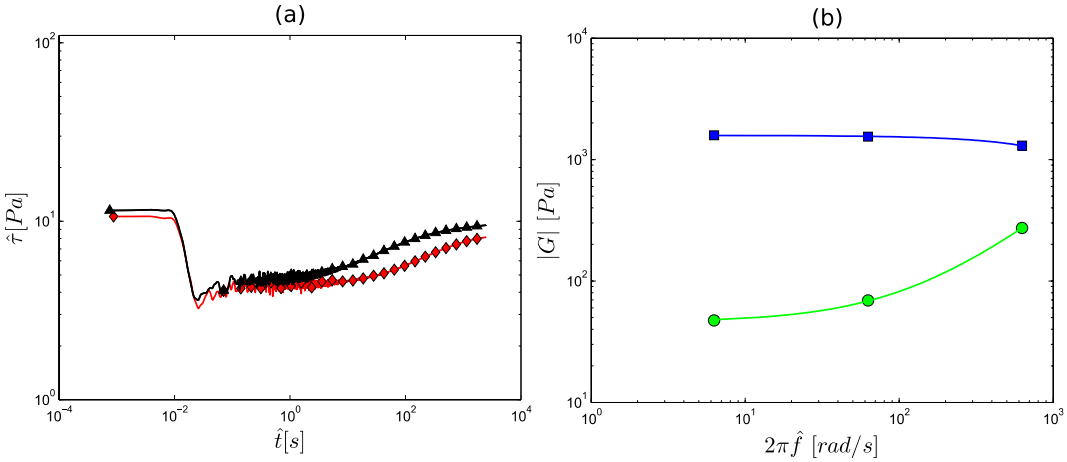

Figure 5-10: (a) Response to shear rate step change from 100 to 10 1/s for two Laponite suspensions of 2%: one with I=10^{-3} mol/L (▲) and the other with I=10^{-4} mol/L (◊). (b) Frequency sweep response of Laponite suspension of 2.5% wt and I=10^{-2} mol/L at an oscillation strain of 1%: Elastic Modulus (□) and Viscous Modulus (○).

The results confirm the shear thinning behavior of Laponite suspensions. In both experiments, it was necessary to wait more than 5000 s to reach the steady state after a shear rate change. The ionic strength seems to impact the viscosity and transient response of Laponite suspension.

The thixotropy effect on Laponite suspension is also detected in the oscillatory tests. Besides the frequency sweep, the Lissajous plots are used to illustrate this effect. The frequency sweep is an oscillatory test with fixed amplitude that measures the output response (amplitude and phase) of changes in frequency of a cosine input. The storage and viscous modulus can be calculated based on the output variables. Figure 5-10.b presents the frequency sweep response of a Laponite suspension of 2.5% wt and I=10^{-2} mol/L after pre-shearing at an oscillation strain of 1% and figure 5-11, the associated Lissajous-Bowditch plots.

Figure 5-11.a show the first oscillatory test ($\hat{f}$=100 Hz) after pre-shearing. After 1000 s the amplitude is still increasing and the phase seems to be stable. As the frequency decreases from 100 to 10 Hz (figure 5-11.b), the amplitude stress continues to increase (figure 5-13.a) even after the phase stabilization around 5000s (figure 5-13.b). This characterisctic is reproduced in the last frequency change from 10 to 1Hz (figure 5-11.c). It seems that, for the low frequency experiments, the external force is not sufficient to overcome the aging effect, and the system continues evolving and steady state solution is not achieved during the rheological experiment. In all the frequency sweep experiments the phase angle increases and approaches $\pi/2$, as frequency decreases, an evidence that the fluid is under construction.

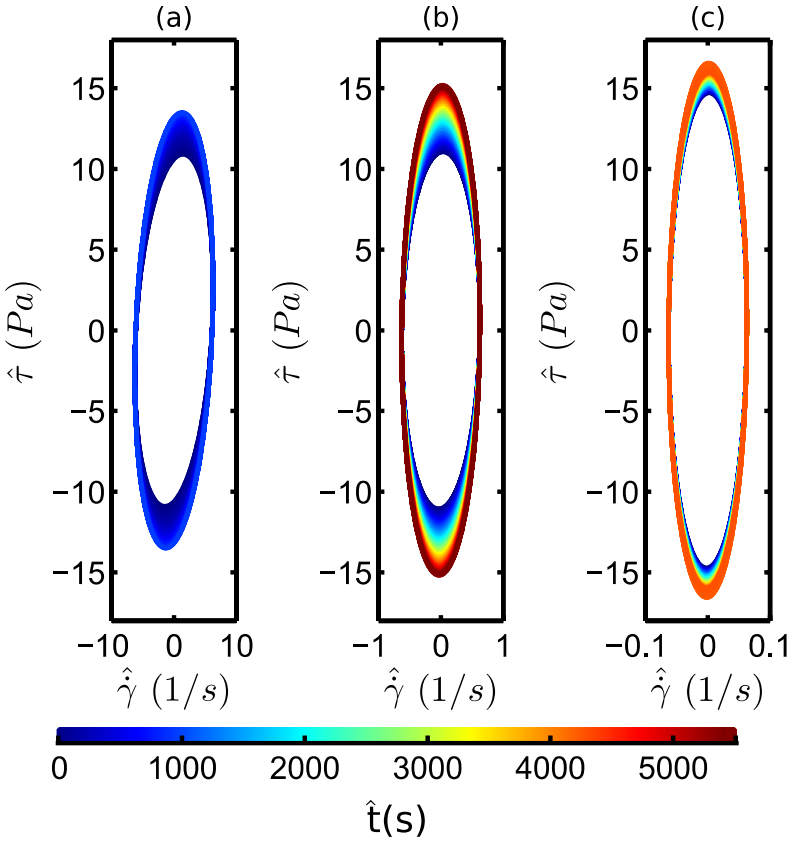

Figure 5-11: Lissajous plot of frequency sweep from figure 5-10.b: (a)100 Hz; (b) 10Hz and (c) 1Hz.

Figure 5-12 shows the opposite, the Laponite suspension 2.0% wt and I=10^{-3} mol/L rejuvenation as the strain goes to 10% for frequency of 1 Hz. After the pre-shearing, phase goes from $\approx \pi/2$ to $\approx 3\pi/10$ and the amplitude stress increases. In this case, the external force is sufficient to overcome aging, but steady state is not achieved in the oscillatory experiment period (4500s).

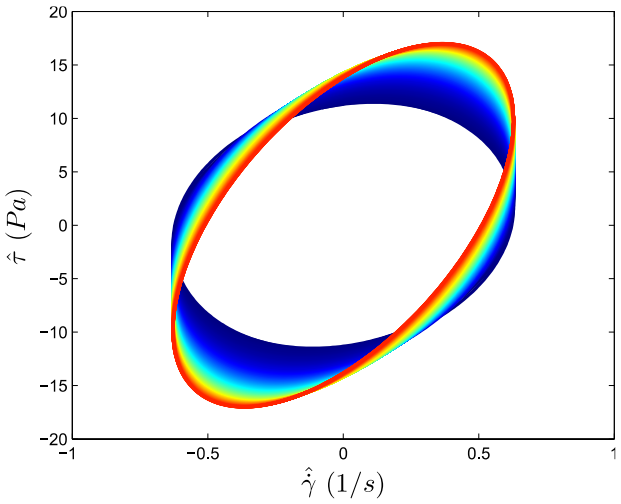

Figure 5-12: Oscillatory test of Laponite suspension 2.0% wt and I=10^{-3} mol/L for strain=10% and frequency of 1 Hz. Time scale is equal to the one presented on figure 5-11.

In the oscillatory experiment it is possible to observe the aging effect over the Laponite suspension rheological parameters when amplitude increases (figure 5-13.a) and phase angle $\pi/2$ (figure 5-13.b). On the other hand, when the amplitude increases and the phase decreases, the fluids rejuvenate.

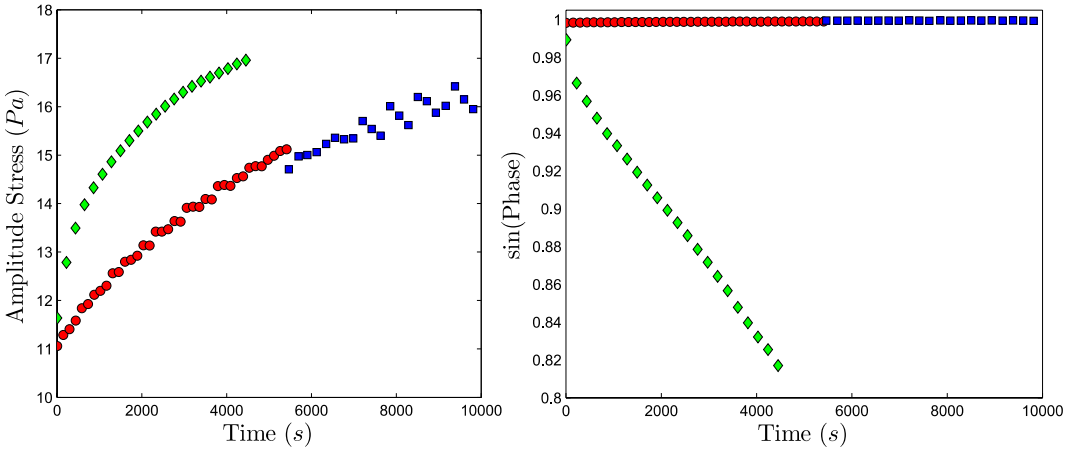

Figure 5-13: Response of oscillatory tests for strain of Laponite suspensions: 2.5% wt, I=10^{-2} mol/L for strain=1% at $\hat{f}$=10Hz (○) and strain=1% and $\hat{f}$=1 Hz (□) and 2.0% wt, I=10^{-3}mol/L for strain=10% at $\hat{f}$=1Hz: (a) amplitude; (b) phase.

In the end, the transient response of step change or an oscillatory tests are influenced by the shear rate/stress level and laponite suspension characteristics: laponite concentration; ionic strength and aging time.

5.4
Thixotropy model regression

This section is dedicated to thixotropic model regression for parameter tuning based on rheological experiments. Barnes (1997) [56] presented a great diversity of constitutive models (Coussot et al., 2002 [31]; Labanda and Lorens, 2005 [40], Tiu and Boger, 1974 [60]) in his thixotropy review paper. A few thixotropic models are presented in the appendix 11 . In this work, we chose the model from de Souza Mendes (2011) [61] to describe the thixotropic behavior of Laponite suspensions. It is characterized by Oldroyd-B type equation:

$$\tau + \Theta_1 \dot{\tau} = \eta_v(\dot{\gamma} + \Theta_2 \ddot{\gamma}) \qquad 5\text{-}1$$

with viscosity, relaxation and retardation times, represented by η_v, Θ_1 and Θ_2, respectively, are given as functions of a structure parameter λ, which gives the level of the material structure:

$$\lambda = ln\frac{\eta_v}{\eta_\infty} \qquad 5\text{-}2$$

where η_∞ is the viscosity as shear rate goes to infinity. In particular, the equilibrium structure parameter λ_{eq} is given by

$$\lambda_{eq} = ln\frac{\eta_v(\lambda_{eq})}{\eta_\infty} \qquad 5\text{-}3$$

where $\eta_v(\lambda_{eq})$ is the steady-state viscosity when the microstructure is in equilibrium, i.e., when buildup and breakdown rates are equal. When the fluid is fully structured, we have:

$$\lambda_0 = ln\frac{\eta_0}{\eta_\infty} \qquad 5\text{-}4$$

and for yield stress fluids, for which $\eta_0 \to \infty$, hence $\lambda_0 \to \infty$.

We considered the structured parameter evolution equation model proposed by de Souza Mendes and Thompson (2013) [62] for yield stress fluids:

$$\frac{d\lambda}{dt} = \frac{1}{t_{eq}}\left[\left(\frac{1}{\lambda}\right)^a - \left(\frac{1}{\lambda_{eq}}\right)^a\left(\frac{\lambda}{\lambda_{eq}}\right)^b\right] \qquad 5\text{-}5$$

where t_{eq} is the equilibrium time, and *a* and *b* are other rheological parameters that control the build-up and break-down terms.

We will focus our analysis in the evolution equation parameters identification, which consists of:

1. Apply a step change (stress or shear rate);
2. Calculate the structure parameter based on the viscosity for every time stamp;
3. Numerically calculate the structured parameter derivative over time;
4. Identify the model parameters by regression.

To test the methodology we applied a creep test (step change) from 80 to 60 Pa in a Laponite suspension of 3.0% wt and I=10^{-2} mol/L, and calculated the structured parameter and its derivative, as presented in figure 5-14. We considered η_∞=0.015 Pa.s. The equilibrium structured parameter for 60 Pa and 80 Pa is equal to 8.71 and 8.79, respectively. After the step change, the structure parameter decreases almost instantaneously for 8.43, so we considered λ_0=8.43. Fixing *a* =1 and *b*=1, the equilibrium time was evaluated as t_{eq}=0.061s. The tuned evolution equation is presented in figure 5-14, showing that a good agreement is obtained between the model and the experimental data.

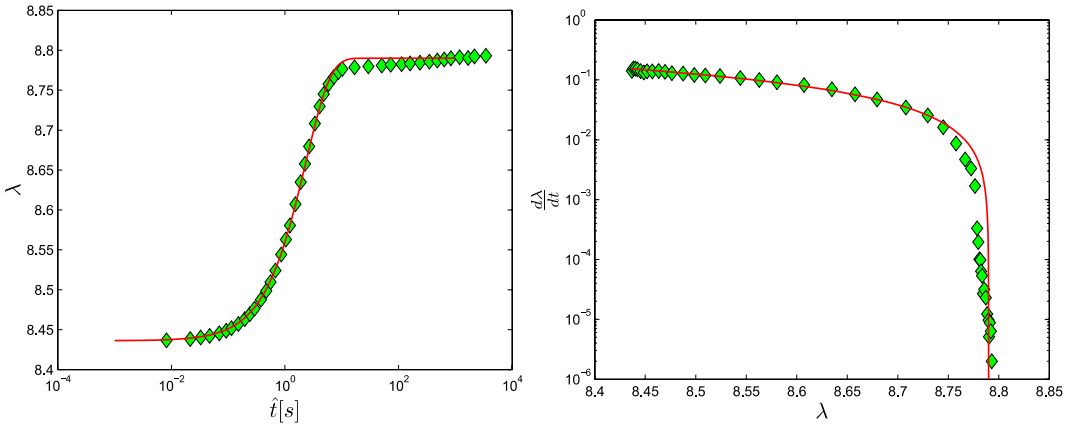

Figure 5-14: (a) Structure Parameter evolution. (b) Evolution equation. Rheological experiments (◊). Tuned model from de Souza Mendes (2011) [61] (continuous line).

The model regression for parameter tunning is very important to allow the comparison between experimental with numerical results. Although the Laponite supensions are not considered in the numerical model described in this thesis, the data acquired may be applied in future numerical model validation.

5.5
Summary of Laponite thixotropic and yield stress characteristics

From the Laponite literature review it was possible to understand the colloidal glass aging and rejuvenation phenomena acting over the Laponite particles interaction. The NaCL (ionic strength) and the Laponite concentrations effect over the rheological properties of Laponite suspensions, specially yield stress and thixotropy, was presented. From the rheological tests we detected that aging time influences the apparent yield stress of Laponite suspensions, for instance, low yield stress values are related to rejuvenated samples and high values to aged Laponite samples.

Independently of aging time, for the same ionic strength, the yield stress of Laponite suspension increases with the Laponite concentration increment. On the other hand, for the same Laponite concentration, the apparent yield stress decreases as the ionic strength decreases.

Besides, the importance of a standard Laponite protocol for sample preparation was emphasized to guarantee a reproducible rheological similarity for different samples.

6
Start-up experiments

The fluid start-up represents the transient response of a single fluid from rest when a differential pressure is applied in a specific geometry, e.g. a tube or parallel plates, until steady state flow is achieved.

Start-up experiments of yield stress and/or thixotropic fluids for different inlet velocities are performed in a 4 m long horizontal pipe for different Carbopol solutions and Laponite suspensions. The effects of yield stress and thixotropy in the transient response are analyzed.

6.1
Bibliography Review - Start-up

Escudier and Presti (1996) [34] performed fully developed pipe flow experiments with aqueous Laponite solutions in 13.35 mm horizontal glass tube of 0.1004 m inner diameter. The velocity fluctuation levels (axial, tangential and radial) were measured by a laser Doppler anemometer and laminar and turbulence regimes were considered. They showed that for low Reynolds numbers (<1500) the velocity profiles are symmetrical with a well defined *plastic* plug, and are well represented by the theoretical profile for fully developed laminar flow of Herschel-Bulkley fluid derived by Soto and Shah (1976) [63].

Dapra and Scarpi (2005) [7] developed an analytical solution based on Laplace transform of axisymmetric motion for a Bingham fluid initially at rest subjected to a constant pressure gradient applied suddenly (step function). They obtained expressions in terms of known transcendental functions which allow the calculation of the instantaneous velocity, plug radius and flow rate as a function of time. An expression for the shear stress in the Newtonian region was also obtained. To illustrate the analytical start-up solution, two start-up examples were presented considering different Bingham fluids and one is reproduced in figure 6-1, 6-2 and 6.3.

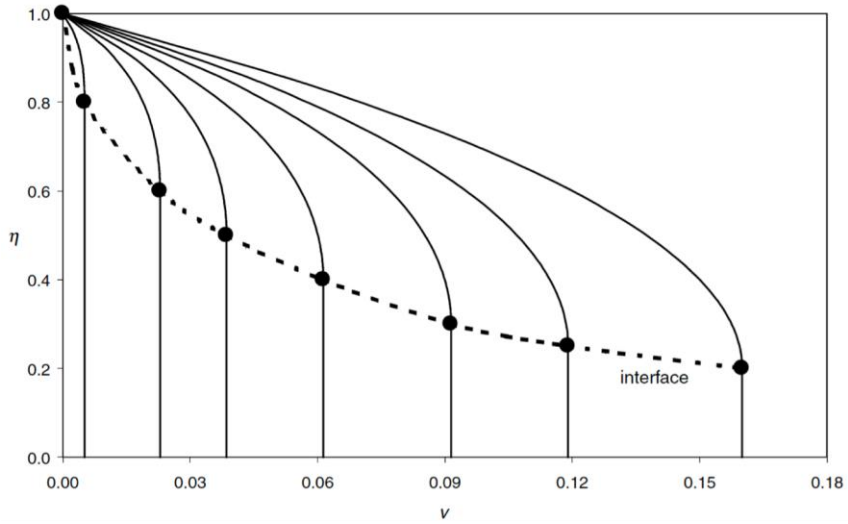

Figure 6-1: Velocity profile for yield stress $\theta^{Dapra} = \hat{\tau}/\hat{R}\Delta\hat{P} = 0.1$ and asymptotic plug radius $\eta_{\infty}^{Dapra} = r_{plug} = 0.2$ during start-up reproduced from Dapra and Scarpi (2005) [7].

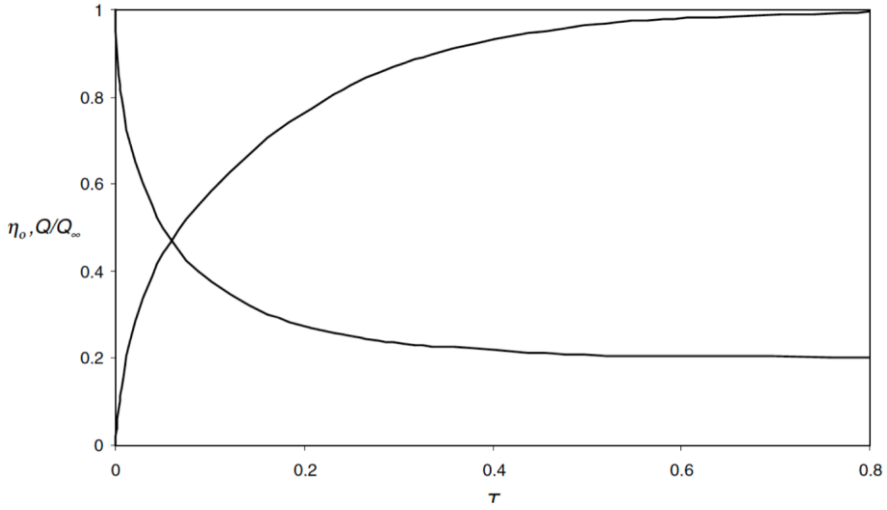

Figure 6-2: Flowrate and plug radius evolution for yield stress $\theta^{Dapra} = \hat{\tau}/\hat{R}\Delta\hat{P} = 0.1$ and asymptotic plug radius $\eta_{\infty}^{Dapra} = r_{plug} = 0.2$ during start-up reproduced from Dapra and Scarpi (2005) [7].

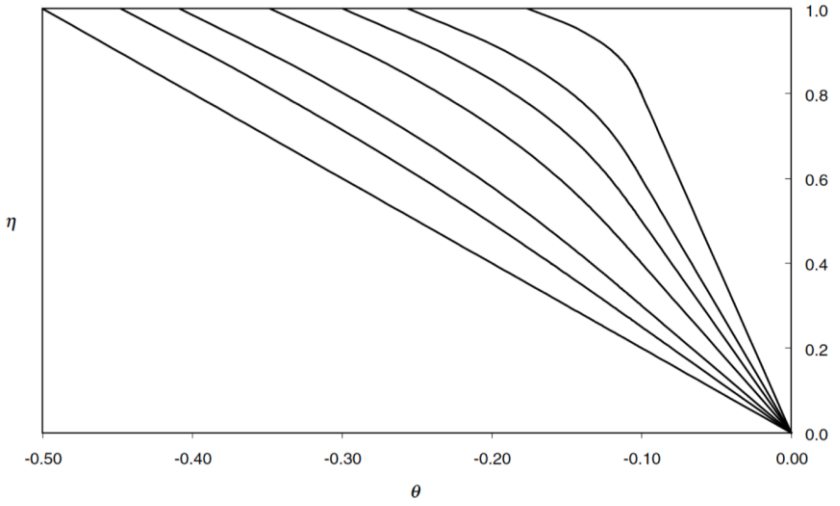

Figure 6-3: Stress evolution for yield stress $\theta^{Dapra} = \hat{\tau}/\hat{R}\Delta\hat{P} = 0.1$ and asymptotic plug radius $\eta_{\infty}^{Dapra} = r_{plug} = 0.2$ during start-up reproduced from Dapra and Scarpi (2005) [7].

Different waxy crude oil start-up numerical models were developed based on viscoplasticity, compressibility and thixotropy. Numerical simulations of transient non-isothermal flows of viscoplastic fluid in a pipe were examined by Vinay et al. (2005) [3]. Although the axisymmetric transient model was considered, only the steady state response was analyzed. The viscoplasticity was modeled by a Bingham model with temperature dependent rheological parameters. Adding compressibility and considering isothermal flow, Vinay et al. (2006) [4] present the transient response of pressure along the pipe, and inlet and outlet flow rate for weak compressibility. An example of the axial velocity profile evolution for compressible viscoplastic flow is also presented.

Continuously improving the one-dimensional axisymmetric transient model, Vinay et al. (2007) [5] presents the start-up transients of isothermal waxy crude oil flows and shows that the re-start transients are effectively controlled by three dimensionless parameters: Reynolds, compressibility and Bingham numbers.

Thixotropy was added and 1.5 D numerical was applied in Wachs et al. (2009) [6], which investigated the isothermal start-up problem of a weakly compressible flow in a pipeline filled with a viscoplastic and thixotropic fluid. The complex fluid rheology was characterized by the Houska model (Houska, 1981 [64]).

6.2
Start-up Fluids

The Carbopol solutions and Laponite suspensions applied in the start-up experiments are presented below.

6.2.1
Carbopol Solutions

Figure 6-4 presents the flow curves and the respective Herschel-Bulkley tuned model of the Carbopol solutions used in the start-up experiments. The Herschel-Bulkley parameters are defined in Table 6-1. The model tuning methodology is defined in section 3.2.2 .

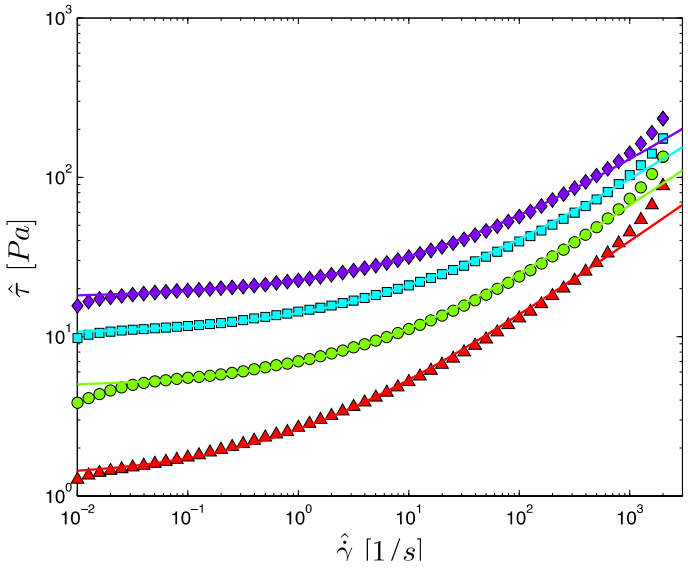

Figure 6-4: Flow curve of Carbopol solution and respective Herschel-Bulkley tuned model: 0.07%(▲); 0.08% (○); 0.10% (□) and 0.11% (◊).

Table 6-1: Set of experiment of Carbopol solution start-up.

Carbopol	Herschel-Bulkley Model		
Concentration	$\hat{\tau}_y$	n	$\hat{K}$
(%wt)	(Pa)	( )	(Pa.s^n)
0.07	1.3	0.49	1.32
0.08	4.8	0.49	2.10
0.10	10.3	0.46	3.77
0.11	17.5	0.45	5.20

6.2.2
Laponite Suspensions

Table 6-2 presents the tuned Herschel-Bulkley parameters of Laponite suspensions 1.5% wt with different NaCl concentrations. These results show that for ionic strength lower than 3.00 x 10^{-3} mol/L the Laponite suspension yield stress is very low (≈0 Pa); the power law index is approximately 1; and as the ionic strength increases, the fluid consistency index increases. From figure 5-1 it is possible to identify that the transition between solution (sol) and gel for Laponite for 1.5% wt occurs in the NaCl concentration around 1.00 10^{-3} mol/L. Therefore, all the Laponite suspensions in the start-up experiments are in the gel state. Although the Laponite suspensions seem to be Newtonian, it is a thixotropic fluid.

Table 6-2: Set of experiments of 1.5%wt of Laponite solution start-up.

Laponite Concentration (wt)	NaCl Concentration (10^{-3} mol/L)	Herschel-Bulkley Model			
		Aging time (min)	$\hat{\tau}_y$ (Pa)	n ( )	$\widehat{K}$ (Pa.s^n)
1.5	1.5	30	≈0	≈1	0.007
1.5	1.75	30	≈0	≈1	0.015
1.5	2.00	30	≈0	≈1	0.016
1.5	2.50	30	≈0	≈1	0.019
1.5	3.00	30	1.5	0.71	0.115
1.5	5.00	30	8.5	0.76	0.052
1.5	7.50	30	19	0.65	0.076

The Herschel-Bulkley parameters are defined based on the creep tests of Laponite suspensions in the same day of the experiment, after the loop conditioning. The same resting time is reproduced in the rheometer. Unfortunately only a few data points were obtained. Although the yield stress value is reliable, other parameters are ill defined. The yield stress increases as the ionic strength increase above I> 3.00 x 10^{-3} mol/L.

6.3
Studied parameters range - Start-up

The parameter ranges covered in our start-up experiments are given in Table 6-3. The characteristic shear rate range for all experiments is 1.6 - 64 1/s, so the fitted Herschel Bulkley model represents the rheological Carbopol and Laponite behavior quite well during the fluid start-up experiments. Every experiment can be represented by a set of dimensionless parameters (Re, B) or dimensionally by a corresponding Carbopol solution or Laponite suspension, and the mean velocity ($\hat{V}_0$).

Table 6-3: Parameter ranges used in the start-up experimental study.

Parameter	Range
β (°)	90
$\hat{V}_0$ (mm/s)	4 - 135
$\hat{\dot{\gamma}}_c$	1.6 - 64
$\hat{\tau}_y$ (Pa)	≈0 - 19
Re	6 10^{-4} - 367
B	≈0-20

6.4
Start-Up Experiment Procedure

The start-up procedure consists of filling the tube with yield stress and/or thixotropic fluid and let it rest. The transference of the fluid from the PVC buckets to the acrylic tanks are performed by centrifugal pumps of constant 1725 rpm and 0.5 HP from Moyno Inc. The pumps pre-shear the fluid and help to homogenize the Carbopol solutions and Laponite suspensions. For thixotropic solutions, mainly Laponite suspensions, the fluid is set to rest in the loop for a specific resting time. All the Laponite suspensions applied in the start-up experiments are prepared at least 7 days prior to the experiment itself, as oriented by Labanda and Lorens (2005) [40].

It is important to point out that initially the flow loop pipe and the pressurized tank were segregated by a solenoid valve that was replaced later on by a simple ball valve. The reason for this replacement will be clarified in section 6.7.1 . The tank is filled with the same fluid and pressurized by an air compressor. The tanks's pressure is controlled by a pneumatic valve.

At the end of the loop, a magnetic flowmeter and a choke valve are installed. In addition, as in the displacement experiments, the fluid discharge mass during each experiment is measured. Upstream the gate valve, a pressure gage recorded the pressure evolution over time. The steady state velocity is defined by the pressure tank and choke position.

The experiment inputs are the pneumatic valve and choke positions. A local manometer helps to define the initial pressure tank in the absence of flow. After the aging time, the ball valve that segregates the two systems is opened and a differential pressure is applied to the fluid.

Supplementary velocity field measurement from Ultrasonic Doppler Velocimeter (UDV) probe is also considered. As a result, after the signal processing, the experiments output are:

1. $\hat{V}_0(\hat{t})$ - Mean velocity (mm/s) from the magnetic flowmeter;
2. $\hat{P}(\hat{t})$ - Pressure (kPa) before the gate valve;
3. $\hat{w}$ - Fluid discharge mass (kg);
4. $\hat{\rho}$ - Fluid density (kg/m^3);
5. $\hat{t}_{exp}$ - Experiment duration (s);

6. Velocity profiles at UDV probe position ($\hat{x}$=1560mm).

The fluid discharge mass (w) during the experiment is equivalent to

$$\widehat{w}(\hat{t}) = \frac{\pi}{4}\hat{\rho}\widehat{D}^2 \int_0^{\hat{t}} \hat{V}_0(\epsilon)d\epsilon. \quad 6\text{-}1$$

Here, $\hat{V}_0(\hat{t})$ represents the mean velocity evolution modelled by

$$\hat{V}_0(\hat{t}) = \hat{V}_0[H(\hat{t}) - g(\hat{t})] \quad 6\text{-}2$$

where $\hat{V}_0$ represents the mean velocity at steady state, $H(\hat{t})$ the Heaviside function and $g(\hat{t})$ the mean velocity transient function, considering $g(\hat{t}) = 0$ for $\hat{t}$<0 and $\lim_{\hat{t}\to\infty} g(\hat{t}) = 0$. From equation 6-2, we have

$$\widehat{w}(\hat{t}) = \frac{\pi}{4}\hat{\rho}\widehat{D}^2\hat{V}_0 \int_0^{\hat{t}} [H(\epsilon) - g(\epsilon)]\, d\epsilon \quad 6\text{-}3$$

$$\widehat{w}(\hat{t}) = \frac{\pi}{4}\hat{\rho}\widehat{D}^2\hat{V}_0 \left[\hat{t} - \int_0^{\hat{t}} g(\epsilon)d\epsilon\right]. \quad 6\text{-}4$$

When the steady state solution is achieved ($\hat{t} = \hat{t}_{SS}$), $g(\hat{t}) = 0$ for $\hat{t} > \hat{t}_{SS}$. So equation 6-4 can be rewritten as

$$\widehat{w}(\hat{t}) \quad = \frac{\pi}{4}\hat{\rho}\widehat{D}^2\hat{V}_0 \left[\hat{t} - \int_0^{\hat{t}_{SS}} g(\epsilon)d\epsilon\right]. \quad 6\text{-}5$$

Assuming that $g(t)$ is a bounded function $0 \le |g(\hat{t})| \le 1$, for $\forall\hat{t}$ we have

$$\frac{\pi}{4}\hat{\rho}\widehat{D}^2\hat{V}_0(\hat{t} - \hat{t}_{SS}) \le \widehat{w}(\hat{t}) \le \frac{\pi}{4}\hat{\rho}\widehat{D}^2\hat{V}_0\hat{t}. \quad 6\text{-}6$$

For $\hat{t}_{SS} \approx 0$ (short time transient response), $\widehat{w}$ is approximately equal to

$$\widehat{w}(\hat{t}) \quad \approx \frac{\pi}{4}\hat{\rho}\widehat{D}^2\hat{V}_0\hat{t} \quad 6\text{-}7$$

and the mean velocity at steady state is

$$\hat{V}_0 \quad \approx \frac{4}{\pi}\frac{1}{\hat{\rho}\widehat{D}^2}\frac{\widehat{w}(\hat{t})}{\hat{t}}. \quad 6\text{-}8$$

On the other hand, for long transient response ($\hat{t}_{SS}$), $\hat{V}_0$ is calculated by the average of the mean velocity at steady state from the flowmeter response

$$\hat{V}_0 = \frac{1}{\hat{t}_f - \hat{t}_{SS}} \int_{\hat{t}_{SS}}^{\hat{t}_f} \hat{V}_0(\epsilon)d\epsilon \quad 6\text{-}9$$

where $\hat{t}_f$ is the time prior to the ball valve closing.

6.5
Start-up Typical Experimental Results

In this section we will present in details the analysis of an experiment with 0.08% Carbopol solution for $\hat{V}_0$=31.8mm/s (Re=26.3 and B=0.19), considered as a typical yield stress start-up experiment.

After setting the tank pressure the ball valve is opened. The signals of the upstream pressure and flow rate over time are presented in figure 6-5. In this case the upstream pressure was initially at 0.0 kPa. After opening the ball valve at $\hat{t}$=0s, the upstream pressure increases to a stable value of 49.31 kPa. Note that as flow develops with time the pressure and flow rate approach a *mean* value indicated by dashed lines in the figure. Once the experiment is over and the ball valve is closed ($\hat{t}_f$ ≈168 s) the flow rate and pressure naturally converge to their values prior to the experiment.

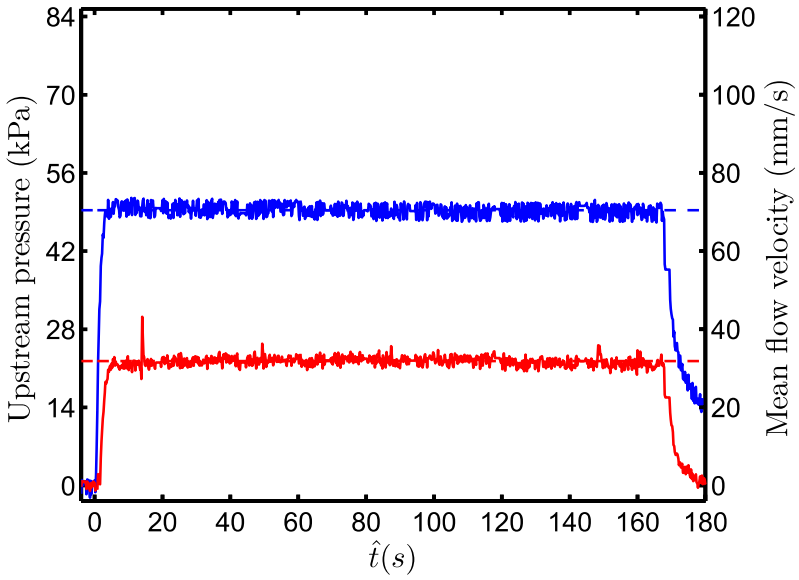

Figure 6-5: Variation of the signals of the upstream pressure (top curve) close to the gate valve ($\hat{x}$=0) and the mean flow velocity (bottom curve) over time for a typical start-up experiment carried using the Carbopol solution of 0.08% for $\hat{V}_0$=31.8 mm/s (Re=26.3 and B=0.19). The dashed lines show the corresponding mean values to the developed flow. The experiment is started at $\hat{t}$=0 s and finished at $\hat{t}_f$ ≈168 s.

There are many ways to present the UDV results and three types of graphs will be used along the start-up analysis:

- Velocity contour - It shows a broad view of the velocity profile evolution over time. The typical velocity contour of a start-up experiment of yield stress fluid with almost no thixotropy is presented

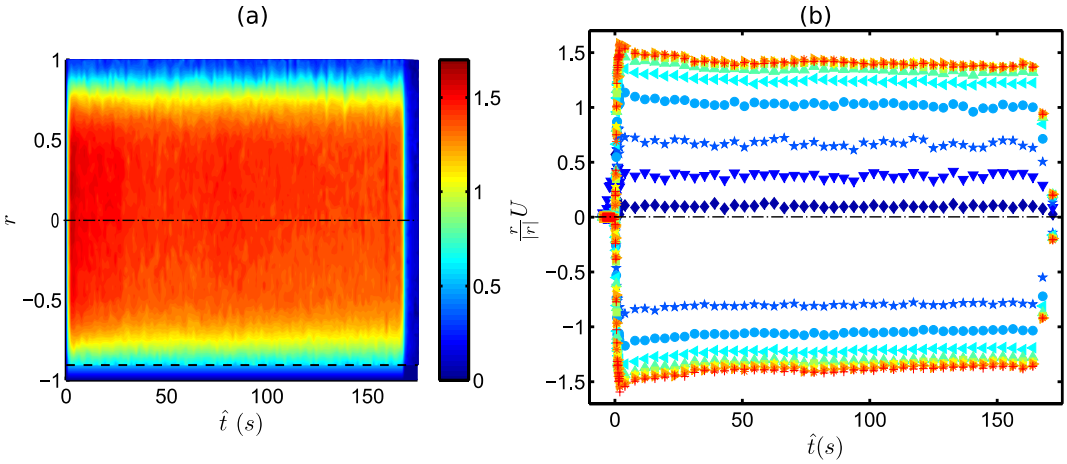

Figure 6-6: Data from Ultrasonic Doppler Velocimeter from Carbopol solution of 0.08% for $\hat{V}_0$=31.8 mm/s (Re=26.3 and B=0.19): (a) Contours of the dimensionless streamwise velocity profiles with scaled radial distance, $r = 2\hat{r}/\hat{D}$, and time $\hat{t}$. Dashed line represents the limit between the UDV data and model regression. (b) Time evolution of the dimensionless streamwise velocity for different r: 0.0 (+), 0.1(*), 0.2(►), 0.3(●), 0.4(□), 0.5(▲), 0.6(◄), 0.7(○), 0.8(★), 0.9 (▲) and 1.0 (◊). The symmetry line is represented by dashed-dotted lines.

in figure 6-6.a. For $\hat{t}$<0, the velocity is zero (dark blue) for every *r* and a short transient response is observed at $\hat{t} \approx 0$, approximately, by an abrupt color change. The steady state solution is characterized by the plug area in the center of the tube represented by the red color, and by the smooth transition of colors to the sides, which represent the velocity decay to the tube walls due to the shear thinning characteristics of the non-Newtonian fluid;

- Velocity at position r - It shows the velocity evolution for different positions r. This type of graph for the typical start-up experiment is provided in figure 6-6.b. As $r \to 0$ (close to the center) the velocity tends to the plug velocity. On the other hand, as the position gets closer to the tube wall, the velocity tends to zero. In this example the time to reach the steady state solution is close to 1 s ($\hat{t}_{SS} \approx 1s$);
- Velocity profiles - It shows the velocity profiles for different times at a fixed axial position ($\hat{x}$=1560mm). The steady state response of the typical start-up experiment is presented in figure 6-7. The steady state solution of a Herschel-Bulkley fluid in a pipe represents quite well the velocity profile of Carbopol solutions.

The same characteristics described by Escudier and Presti (1996) [34] for fully developed pipe flow experiments of Laponite suspensions for low Reynolds

numbers (<1500) are observed in our start-up experiment at steady state: velocity profiles symmetry; well defined *plastic* plug; and the average profile in the steady state period is well represented by the theoretical profile for fully developed laminar flow of Herschel-Bulkley fluid for the same $\hat{V}_0$. The start-up experiment represents the regions I and II of the displacement experiment (figure 4-3).

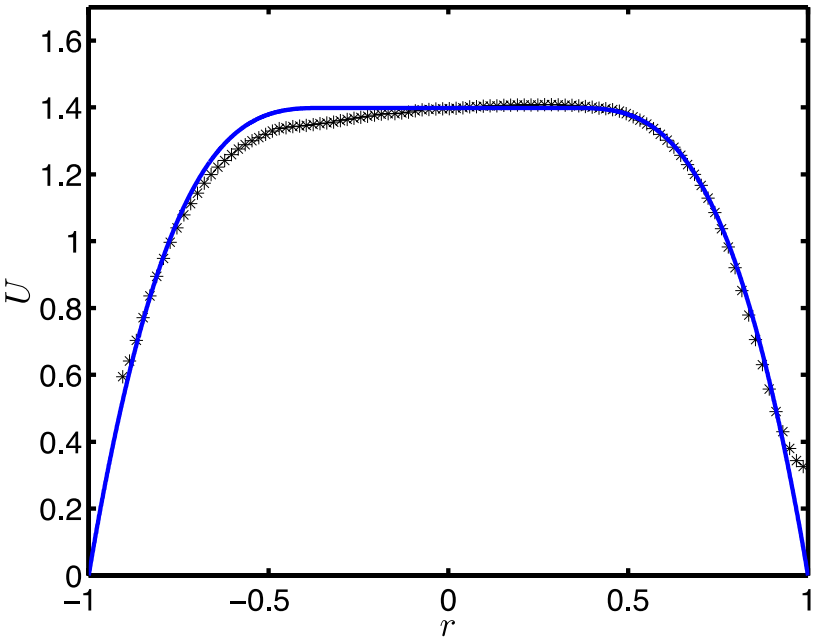

Figure 6-7: Steady sate velocity profile for Carbopol solution of 0.08% for $\hat{V}_0$=31.8 mm/s: steady state solution of a Herschel-Bulkley fluid in a pipe (continuous line) and average profile in the steady state region for 10<$\hat{t}$<160s (*).

6.6
Yield stress fluid experiments

The start-up experiments are performed for the Carbopol solutions described in Table 6-1, for different mean velocities. Figure 6-8 shows how the average velocity during steady state ($\hat{V}_0$) is related to the total fluid discharge mass. Since $\hat{t}_{SS} \approx$ 1s for all Carbopol start-up experiments, equation 6-8 applies. Besides, the short transient after the ball valve opening for any differential pressure applied is an evidence of a fluid with low thixotropy. In this thesis, Carbopol solutions are considered yield stress without thixotropy (neglected thixotropy).

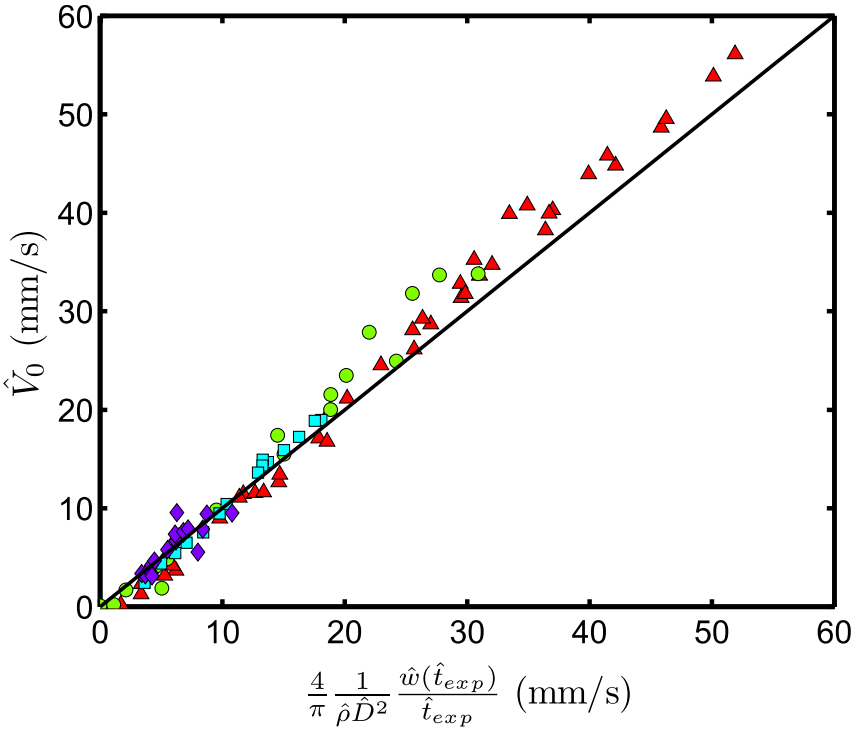

Figure 6-8: Relation between $\hat{V}_0$ and $\frac{4}{\pi}\frac{1}{\hat{\rho}\hat{D}^2}\frac{\hat{w}(\hat{t}_{exp})}{\hat{t}_{exp}}$ for Carbopol start-up experiments. Different markers represent Carbopol solutions:0.07%(▲); 0.08%(○); 0.10%(□) and 0.11%(◊). $\hat{V}_0 = \frac{4}{\pi}\frac{1}{\hat{\rho}\hat{D}^2}\frac{\hat{w}(\hat{t}_{exp})}{\hat{t}_{exp}}$ (continuous line).

Figure 6-9 shows how the pressure gage response is related to $\hat{V}_0$. For high average mean velocity, the response diverges from the developed steady state solution of Herschel-Bulkley fluid flow in a pipe (Soto and Shah, 1976 [63]) for 6.5 m total pipe length. The total length consists of 3.2 m pipe from the gate valve to the end of the loop, and 3.3 m of plastic hose with the same pipe diameter that is part of the drainage system. The discrepancy in the results is related mainly to the localized pressure loss through the flow meter. Although the flow meter is not intrusive, its diameter is 1/4".

The pressure gage located before the gate valve helps to identify any disturbance in the compressor system, such as pressure fluctuation, but it doesn't measure the pressure drop in the loop pipe section. Ideally a differential pressure gage is indicated. Since the pressure signal cannot be use as a measure of the flow dynamics, the average mean velocity at steady state will be applied. Although the differential pressure is imposed, the average mean velocity at steady state will be considered as a measure of the fluid dynamics.

The results presented in figures 6-6 and 6-7 are representative for all the Carbopol solution start-up experiments.

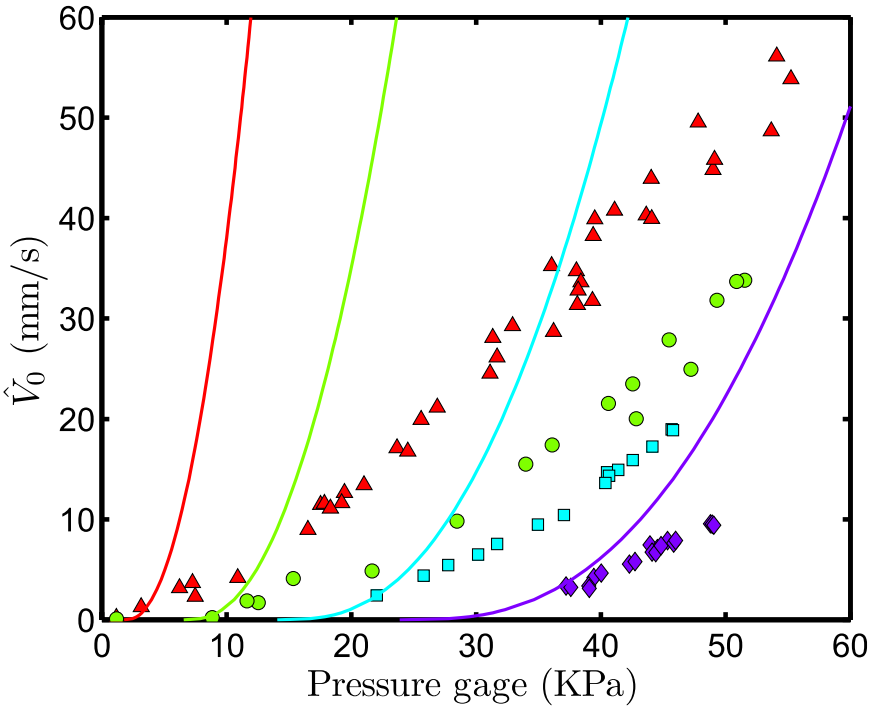

Figure 6-9: Experimental data of mean velocity as a function of pressure for Carbopol solutions: 0.07% (▲); 0.08% (○); 0.10% (□) and 0.11% (◊). Steady state solution of Herschel-Bulkley fluid in a pipe for 6.5 m of tube length (continuous line).

6.7
Thixotropic fluid experiments

Prior to the start-up experiments of Laponite suspensions, the effect of the solenoid valve replacement by a ball valve in a thixotropic fluid is presented.

6.7.1
Influence of shear history - An experimental example

Thixotropic fluids are influenced by resting time and shear history, thus it is necessary to be very careful in the experimental loop design. The loop used in the experiments was initially developed to analyze fluid displacement in inclined pipes and the solenoid valves were inserted to avoid fluids mixing. Besides, it facilitates the opening and closing of valves when the pipe is inclined.

The solenoid valves disturb the flow due to its design and should not be applied when thixotropic fluids are considered. During earlier loop tests using Carbopol solutions, no impact was detected. However, when Laponite suspensions were used, we evidenced the impact of the solenoid valve in flow dynamics.

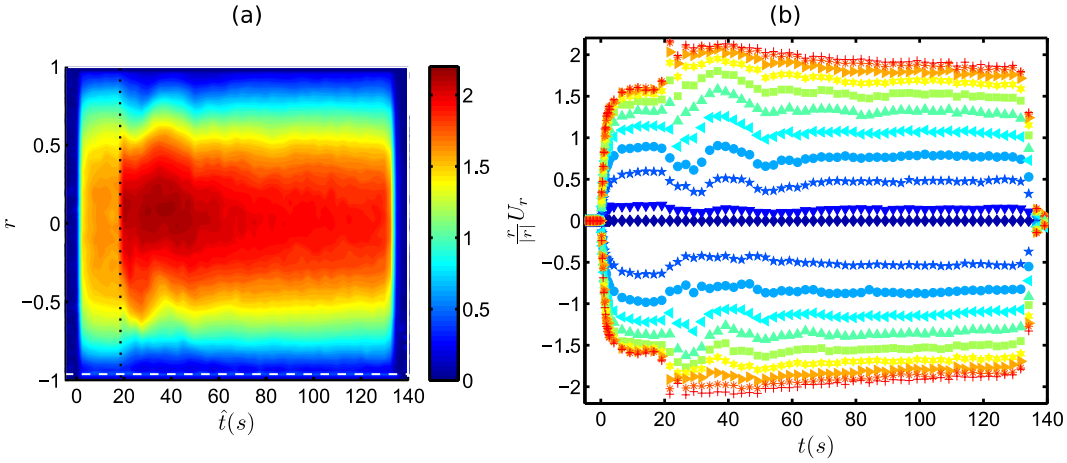

Figure 6-10: Data from Ultrasonic Doppler Velocimeter from Laponite suspension of 1.5% and I=3 10^{-3} mol/L for $\hat{V}_0$=94.3 mm/s (Re=22.3 and B=0.89) before the solenoid valve replacement: (a) Contours of the dimensionless streamwise velocity profiles with scaled radial distance, $r = 2\hat{r}/\hat{D}$, and time $\hat{t}$. Dashed line represents the limit between the UDV data and model regression. (b) Time evolution of the dimensionless streamwise velocity for different r: 0.0 (+), 0.1(*), 0.2(►), 0.3(●), 0.4(□), 0.5(▲), 0.6(◄), 0.7(○), 0.8(★), 0.9 (▼) and 1.0 (◊). Dotted line divides the Laponite suspension over two different shear history.

During the loop commissioning, the fluid is pre-sheared by the pump, but the solenoid valve located in the beginning of the loop provides an extra pre-shearing to the fluid. After the resting time, normally around 30min, the solenoid valve was opened. Figure 6-10 shows the UDV data for Laponite suspension of 1.5% and I=3x10^{-3} mol/L, for $\hat{V}_0$=94.3 mm/s (Re=22.3 and B=0.89). It is possible to identify two different behaviors: one for 0<$\hat{t}$<20s and the other for $\hat{t}$>20s. The first period represents the fluid that rested for 30 min after being pre-sheared during comissioning by both the pump and the solenoid valve. The second period represents the fluid that was pre-sheared during the loop comissioning by the pump, rested for 30 min and suffered an extra shearing during the experiment by the solenoid valve. It can be observed that the solenoid valves rejuvenates the thixotropic fluid.

The solenoid valve was replaced by a ball valve with the same pipe area, and the start-up tests were repeated. Figure 6-11 shows the results obtained with this new configuration for the Laponite suspension of 1.5% and I=3x10^{-3} mol/L, for $\hat{V}_0$=123.8 mm/s. In this case, the same test procedure was considered.

The impact of resting time in the apparent yield stress is also identified in the start-up experiments. The apparent yield stress for the Laponite suspension of 1.5% and I=3x10^{-3} mol/L with different shear history in the start-up experiments is presented in table 6.4, and its effect over the velocity pofile in figure 6-12.

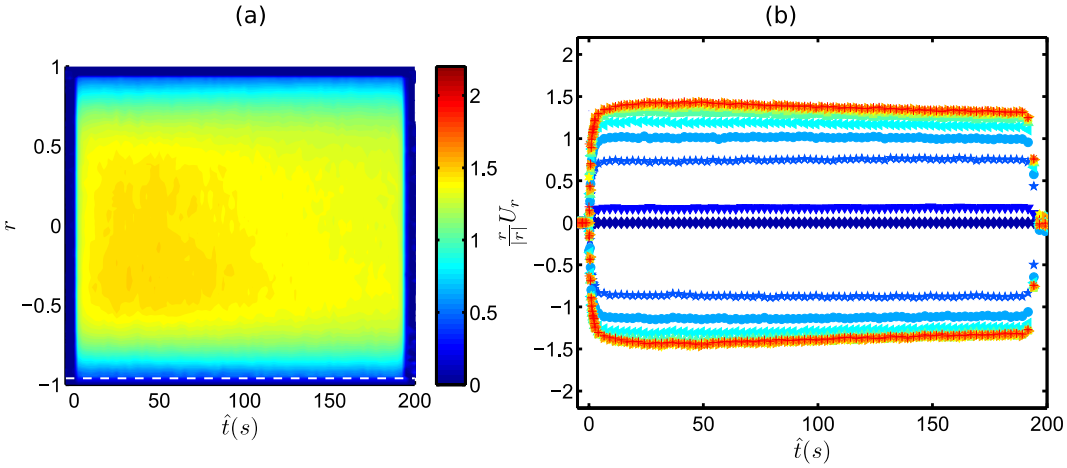

Figure 6-11: Data from Ultrasonic Doppler Velocimeter from Laponite suspension of 1.5% and I=3x10^{-3} mol/L for $\hat{V}_0$=123.8 mm/s (Re=34.6 and B=0.74) after the solenoid valve replacement: (a) Contours of the dimensionless streamwise velocity profiles with scaled radial distance, $r = 2\hat{r}/\hat{D}$, and time $\hat{t}$. Dashed line represents the limit between the UDV data and model regression. (b) Time evolution of the dimensionless streamwise velocity for different r: 0.0 (+), 0.1(*), 0.2(►), 0.3(●), 0.4(□), 0.5(▲), 0.6(◄), 0.7(○), 0.8(★), 0.9 (▼) and 1.0 (◊).

Table 6-4: Influence of shear history in the apparent yield stress for Laponite suspension of 1.5% and I=3 10^{-3} mol/L from start experiments.

Pre-shearing		Resting time	Apparent yield stress
Comissioning	During Experiment	(min)	(Pa)
Pump	Solenoid valve	0	0
Pump + Solenoid valve	-	30	0.35
Pump	-	30	1.5

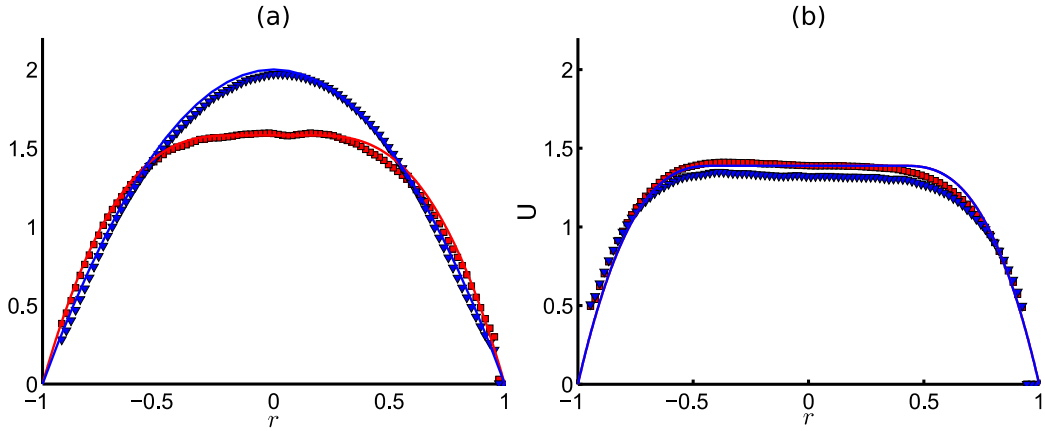

Figure 6-12: Impact of the solenoid replacement in the steady state velocity profile for Laponite suspension of 1.5% and I=3x10^{-3} mol/L: (a) Before the solenoid replacement for $\hat{V}_0$=94.3 mm/s. Average velocity profile for 5<$\hat{t}$<20s (□) and 20<$\hat{t}$<130s (▲). Steady state solution of a Herschel-Bulkley fluid in a pipe for n=0.583, $\hat{K}$=0.0095Pa.s^n and $\hat{\tau}_y$=0.35 Pa (red continuous line). Steady state solution of a shear-thinning fluid in a pipe for n=0.583, and $\hat{K}$=0.0095Pa.s^n (blue continuous line); (b) After the solenoid replacement $\hat{V}_0$=123.8 mm/s. Average velocity profile for 10<$\hat{t}$<50s (□) and 125<$\hat{t}$<175s (▲). Steady state solution of a Herschel-Bulkley fluid in a pipe for $\hat{\tau}_y$=1.5 Pa, n=0.583 and $\hat{K}$=0.0095 Pa.s^n (continuous line).

6.8
Start-up of Thixotropic fluid

To understand the influence of thixotropy in the start-up flow in a pipe, experiments with different Laponite suspensions are performed. For low ionic strength (I<3x10^{-3} mol/L), the yield stress of Laponite suspension of 1.5% can be neglected ($\hat{\tau}_y \approx 0$ Pa). Figures 6-13 and 6-14 show the transient response for start-up experiments with NaCl concentration equal to I=1.5x10^{-3} mol/L for $\hat{V}_0$=57.9mm/s (Re=157.3 and B≈0).

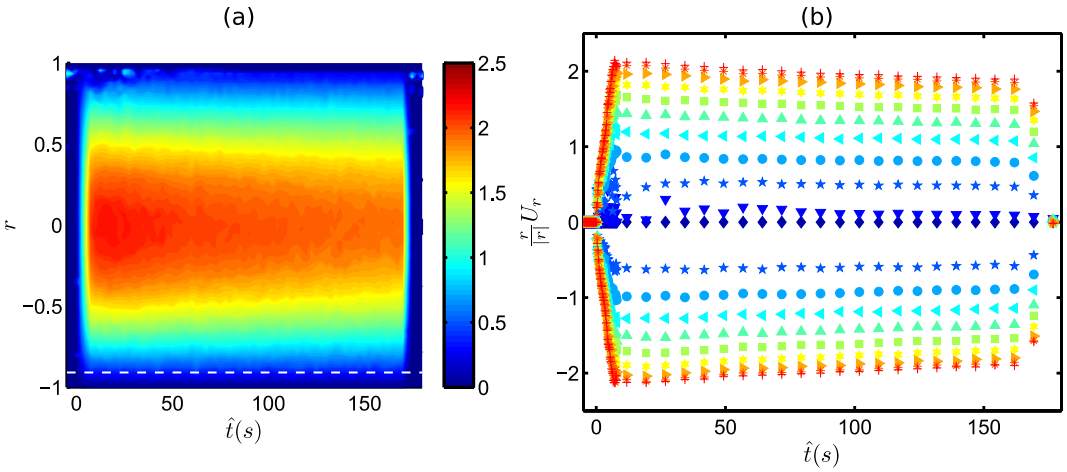

Figure 6-13: Data from Ultrasonic Doppler Velocimeter from Laponite suspension of 1.5% and I=1.5x10-3 mol/L for $\hat{V}_0$=57.9 mm/s (Re=157.3 and B≈0): (a) Contours of the dimensionless streamwise velocity profiles with scaled radial distance, $r = 2\hat{r}/\hat{D}$, and time $\hat{t}$. Dashed line represents the limit between the UDV data and model regression. (b) Time evolution of the dimensionless streamwise velocity for different r: 0.0 (+), 0.1(*), 0.2(►), 0.3(●), 0.4(□), 0.5(▲), 0.6(◄), 0.7(○), 0.8(★), 0.9 (▲) and 1.0 (◊).

Figure 6-13.b show that the plug velocity goes from zero to its maximum value in 8 s. It is important to point out that the velocity is normalized by the average mean velocity of the experiment at steady state. Since the differential pressure decreases due to the tank drainage, the plug velocity slightly decreases. The velocity profiles during 8 s after the beginning of the experiment are shown in figure 6-14.a. The velocity profile evolves from a plug like profile to a perfect parabola, similar evolution of a Newtonian fluid start-up. The average profile at steady state condition is similar to the steady state solution of a Newtonian fluid flowing in a pipe. No water hammer effect was detected during Laponite suspension start-up experiments. Since Laponite suspensions are incompressible fluids, thixotropy seems to alter the fluid start-up dynamics, delaying its response.

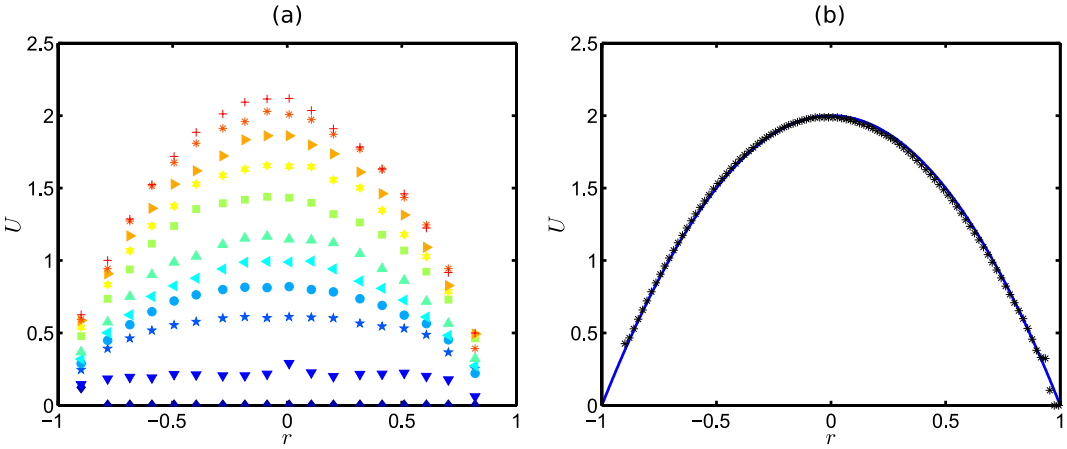

Figure 6-14: Velocity profile for Laponite suspension of 1.5% and I=1.5x10^{-3} mol/L for $\hat{V}_0$=57.9 mm/s: (a) Transient response for $\hat{t}$ equal to 0.6(◊), 1.2(▼), 1.8(★), 3.0(○), 3.6(◄), 4.2(▲), 4.8(□), 5.4(●), 6.0(►), 6.6(*) and 7.2(+);b) Average velocity profile for 8<$\hat{t}$<170s (*). Steady state solution of Newtonian fluid in a pipe for $\hat{K}$=0.007 Pa.s, $\hat{\tau}_y$ ≈0 and n≈ 1 (continuous line).

If we compare these results with the Carbopol, the time to achieve steady states ($\hat{t}_{SS}$) increases from 1 to 8 s. As transient response slows down, the velocity profile evolution becomes less noisy. The same flow conditions are observed for the Laponite suspension of 1.5% and I=2.5x10^{-3} mol/L, as shown in figures 6-15 and 6-16.

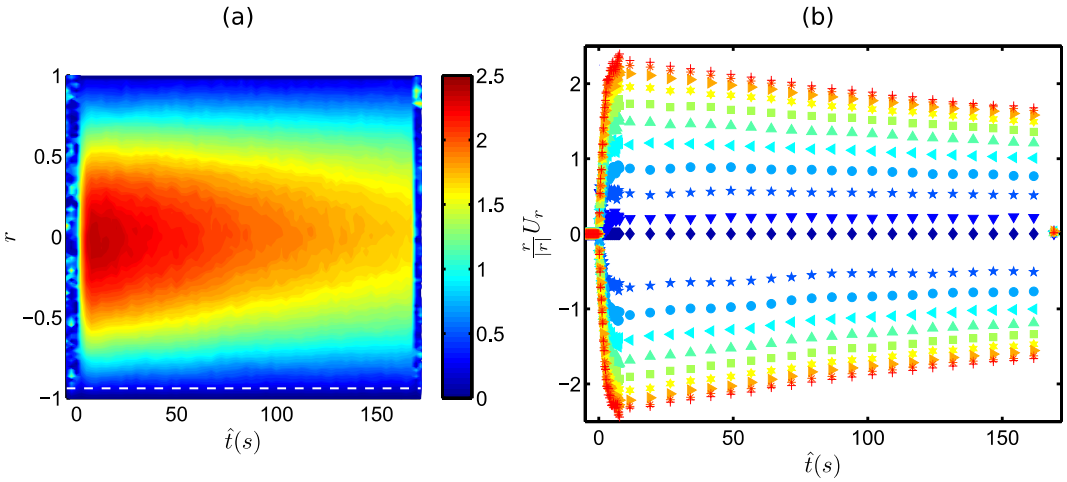

Figure 6-15: Data from Ultrasonic Doppler Velocimeter from Laponite suspension of 2.5% and I=2.5x10^{-3} mol/L for $\hat{V}_0$=60.0 mm/s (Re=6.0 and B≈0): (a) Contours of the dimensionless streamwise velocity profiles with scaled radial distance, $r = 2\hat{r}/\hat{D}$, and time $\hat{t}$.Dashed line represents the limit between the UDV data and model regression. (b) Time evolution of the dimensionless streamwise velocity for different r: 0.0 (+), 0.1(*), 0.2(►), 0.3(●), 0.4(□), 0.5(▲), 0.6(◄), 0.7(○), 0.8(★), 0.9 (▼) and 1.0 (◊).

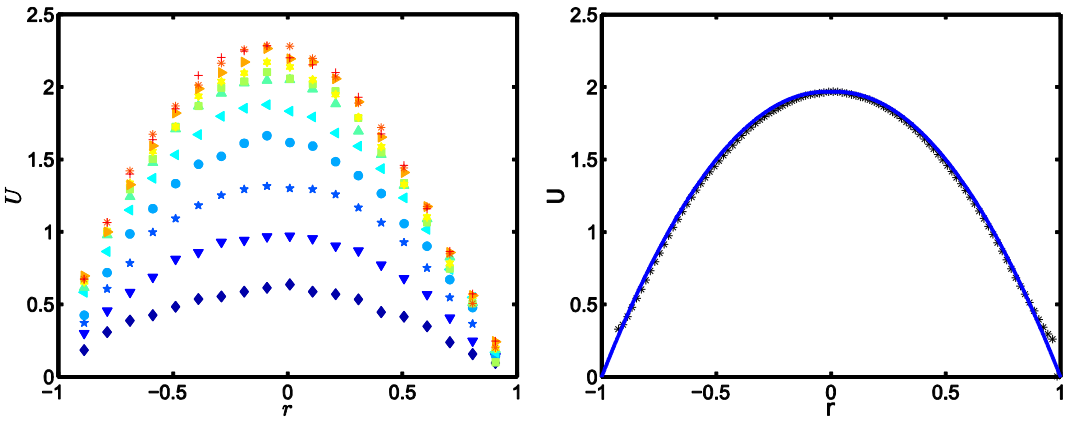

Figure 6-16: Velocity profile for Laponite suspension of 1.5% and I=2.5x10^{-3} mol/L for $\hat{V}_0$=60.0 mm/s: (a) Transient response for $\hat{t}$ equal to 0.6(◊), 1.2(▼), 1.8(★), 3.0(○), 3.6(◄), 4.2(▲), 4.8(□), 5.4(●), 6.0(►), 6.6(*) and 7.2(+); b) Average velocity profile for 8<$\hat{t}$<170s (*). Steady state solution of Newtonian fluid in a pipe for $\hat{K}$=0.019 Pa.s, $\hat{\tau}_y \approx 0$ and n≈1(continuous line).

As the ionic strength increases, yield stress of Laponite suspensions increases. Figure 6-17 shows the dimensionless streamwise velocity contours for start-up experiments, performed with Laponite suspension 1.5% and I=5.010^{-3} mol/L , for mean velocity equal to 36.0 (a), 56.1 (b) and 115.4 (c) mm/s. For low differential pressure ($\hat{V}_0$=36 mm/s) even after the beginning of the experiment the velocity is null (≈ 0), and as time goes by it evolves slowly to steady state condition ($\hat{t}_{SS}$=240s). As the pressure drop increases, the time to achieve steady state decreases to 120 s and 80 s for $\hat{V}_0$=56.1 mm/s and $\hat{V}_0$=115.4 mm/s, respectively.

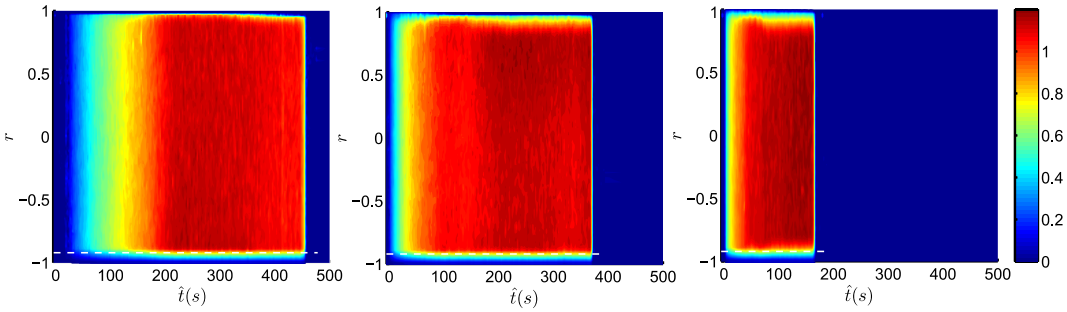

Figure 6-17: Contours of the dimensionless streamwise velocity profiles of Laponite suspension of 1.5% and I=5.0x10^{-3} mol/L: (a) $\hat{V}_0$=36.0 mm/s; (b) $\hat{V}_0$=56.1 mm/s and (c) $\hat{V}_0$=115.4 mm/s. Dashed line represents the limit between the UDV data and model regression.

Figure 6-18 presents the plug velocity (V_{plug} evolution for the start-up experiments of Laponite suspension of 1.5% wt and I=5.0x10^{-3} mol/L for different mean velocities.

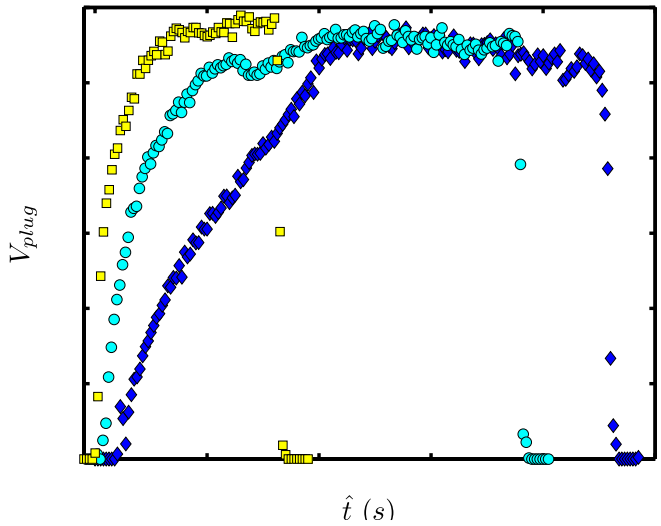

Figure 6-18: Dimensionless plug velocity of Laponite suspension of 1.5% and I=5.0x10^{-3} mol/L: (a) $\hat{V}_0$=36.0 mm/s (◊); (b) $\hat{V}_0$=56.1 mm/s (○) and (c) $\hat{V}_0$=115.4 mm/s (□).

Figures 6-19, 6-20 and 6-21 the velocity profiles during the transient response and the steady state solution for mean velocities $\hat{V}_0$=36.0; 56.1; 115.4 mm/s, respectively.

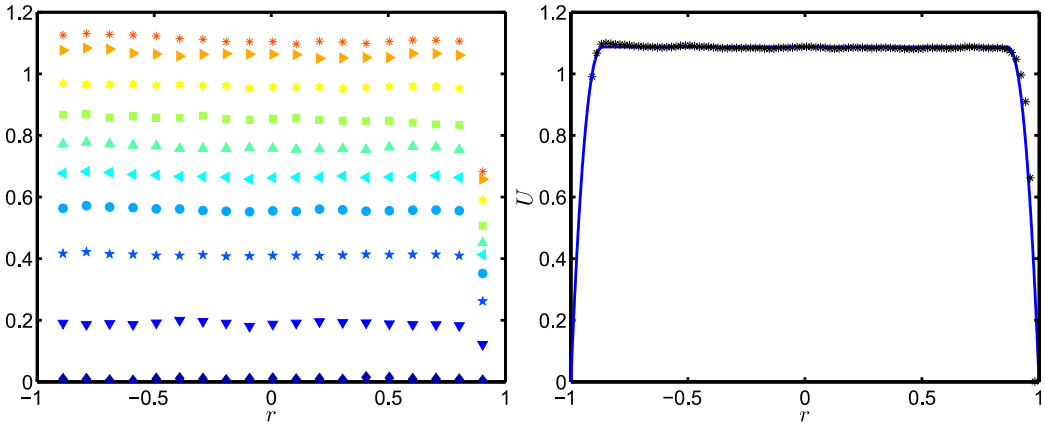

Figure 6-19: Velocity profile for Laponite suspension of 1.5% and I=5.0x10^{-3} mol/L for $\hat{V}_0$=38.7 mm/s: (a) Transient response for $\hat{t}$ equal to 0 s(◊), 24 s(▼), 48 s(★), 72 s(○), 96 s(◄), 120 s(▲), 144 s(□), 168 s(●), 192 s(►), 216 s(*) and 240 s(+); b) Average velocity profile for 240<$\hat{t}$<440s (*). Steady state solution of a Herschel-Bulkley fluid in a pipe for $\hat{\tau}_y$=8.5 Pa, n=0.760 and $\hat{K}$=0.052 Pa.s^n(continuous line).

At steady state, the average mean velocity profile is represented well by Herschel-Bulkley fluid flowing in a pipe. As time goes by, from rest, the plug diameter decreases from tube diameter to its final steady state diameter, similar results are obtained by the analytical solution from Dapra ans Scarpi (2005) [7] for a Bingham fluid startup in a pipe as reproduced in figure 6-1.

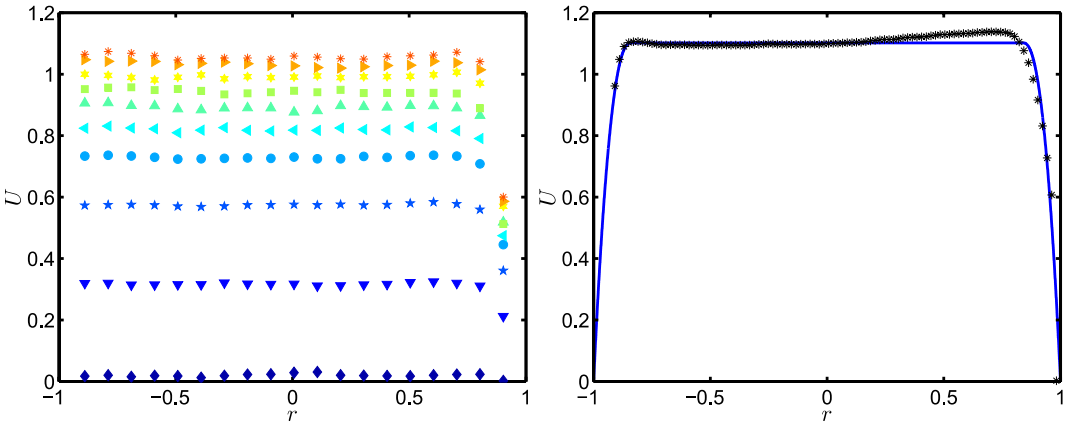

Figure 6-20: Velocity profile for Laponite suspension of 1.5% and I=5.0x10^{-3} mol/L for $\hat{V}_0$=56.1 mm/s: (a) Transient response for $\hat{t}$ equal to 0 (◊), 12 s(▼), 24 s(★), 36 s(○), 48 s(◄), 60 s(▲), 72 s(□), 84 s(●), 96 s(►), 108 s(*) and 120 s(+); b) Average velocity profile for 120<$\hat{t}$<370s (*). Steady state solution of a Herschel-Bulkley fluid in a pipe for $\hat{\tau}_y$=8.5 Pa, n=0.760 and $\hat{K}$=0.052 Pa.s^n (continuous line).

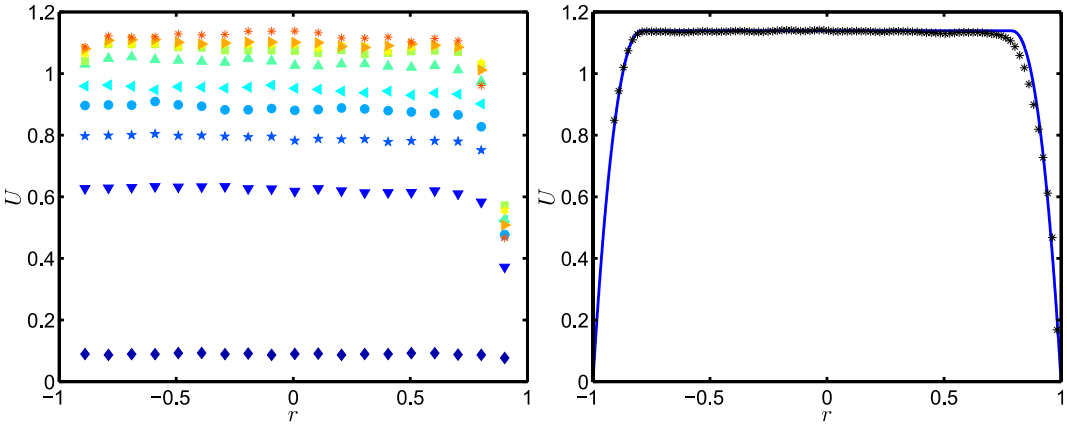

Figure 6-21: Velocity profile for Laponite suspension of 1.5% and I=5.0x10^{-3} mol/L for $\hat{V}_0$=115.4 mm/s: (a) Transient response for $\hat{t}$ equal to 0 s(◊), 8 s(▼), 16 s(★), 24 s(○), 32 s(◄), 40 s(▲), 48 s s(□), 56 s(●), 64 s(►), 72 s(*) and 80 s(+); b) Average velocity profile for 80<$\hat{t}$<150s (*). Steady state solution of a Herschel-Bulkley fluid in a pipe for $\hat{\tau}_y$=8.5 Pa, n=0.760 and $\hat{K}$=0.052 Pa.s^n (continuous line).

A similar behavior is detected in Laponite suspension of 1.5% and I=7.5x10^{-3} mol/L, as shown in figure 6-22. Figure 6-23 presents the evolution of the velocity profile and the steady state solution for $\hat{V}_0$= 25.6 mm/s.

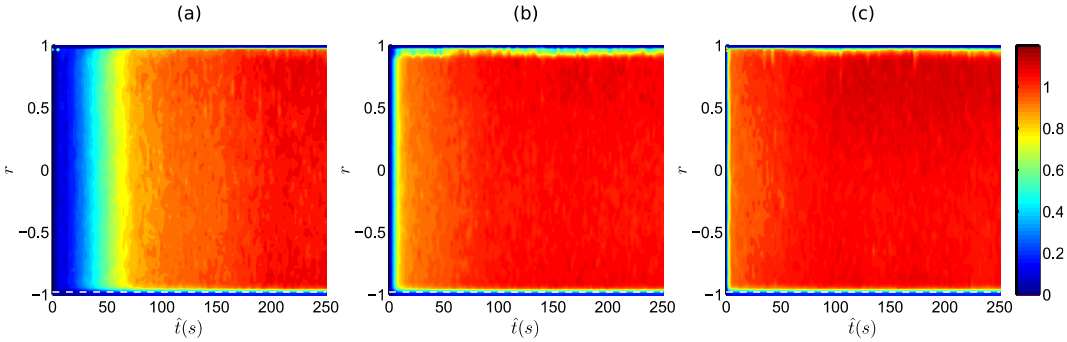

Figure 6-22: Contours of the dimensionless streamwise velocity profiles of Laponite suspension of 1.5% and I=7.5x10^{-3} mol/L: (a) $\hat{V}_0$=25.6 mm/s; (b) $\hat{V}_0$=51.7 mm/s and (c) $\hat{V}_0$=92.8 mm/s. Dashed line represents the limit between the UDV data and model regression.

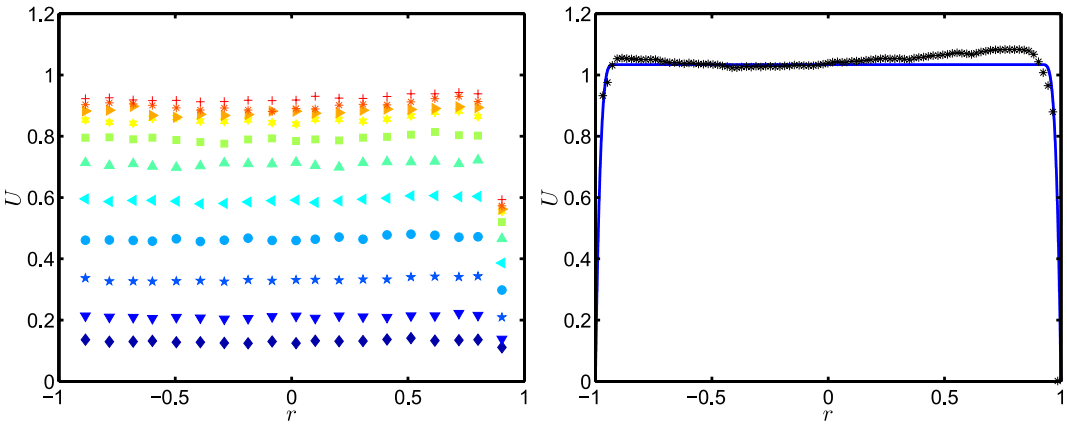

Figure 6-23: Velocity profile for Laponite suspension of 1.5% and I=7.5x10^{-3} mol/L for $\hat{V}_0$=25.6 mm/s: (a) Transient response for $\hat{t}$ equal to 5 s(◊), 15 s(▼), 25 s(★), 35 s(○), 45 s(◄), 55 s(▲), 65 s(□), 75 s(●), 85 s(►), 95 s(*) and 105 s(+); b) Average velocity profile for 150<$\hat{t}$<250s (*). Steady state solution of a Herschel-Bulkley fluid in a pipe for $\hat{\tau}_y$=19.0 Pa, n=0.650 and $\hat{K}$=0.076 Pa.s^n (continuous line).

In the case of high average mean velocity ($\hat{V}_0$= 92.8 mm/s), in the beginning of the experiment ($\hat{t}$ <1 s), the velocity increases and decreases very fast, as shown in figure 6-24. The sudden change in the velocity may be associated to wall slippage. After the sudden velocity change, the velocity profile evolves similar to the other high ionic strength Laponite suspension experiments.

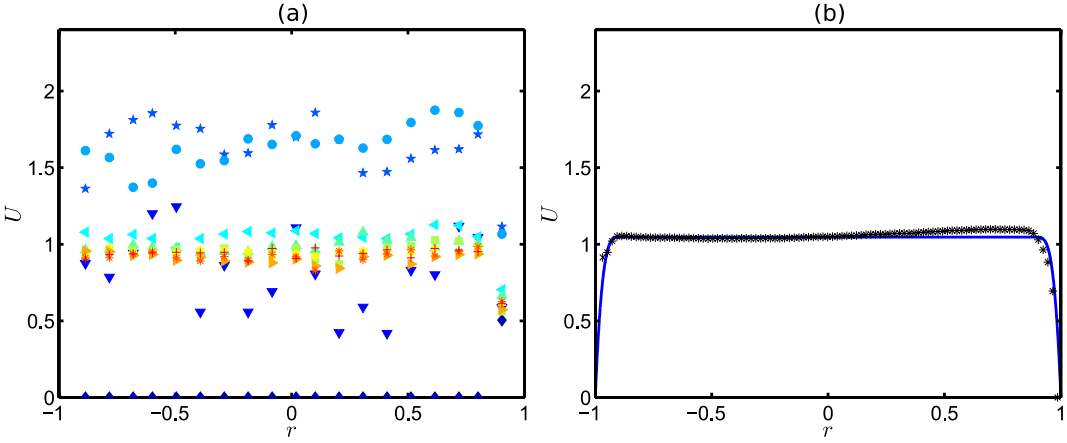

Figure 6-24: Velocity profile for Laponite suspension of 1.5% and I=7.5x10^{-3} mol/L for $\hat{V}_0$=92.8 mm/s: (a) Transient response for $\hat{t}$ equal to 0.00 s(◊), 0.25 s(▼), 0.50 s(★), 0.75 s(○), 1.00 s(◄), 1.25 s(▲), 1.50 s(□), 1.75 s(●), 2.00 s(►), 2.25 s(*) and 2.50 s(+); b) Average velocity profile for 150<$\hat{t}$<250s (*). Steady state solution of a Herschel-Bulkley fluid in a pipe for $\hat{\tau}_y$=19.0 Pa, n=0.650 and $\hat{K}$=0.076 Pa.s^n(continuous line).

Figure 6-25 shows the plug velocity evolution for the start-up experiments of Laponite suspension of 1.5% and I=7.5x10^{-3} mol/L for different mean velocities. It can be observed that the time to reach steady state condition increases as the differential pressure decreases.

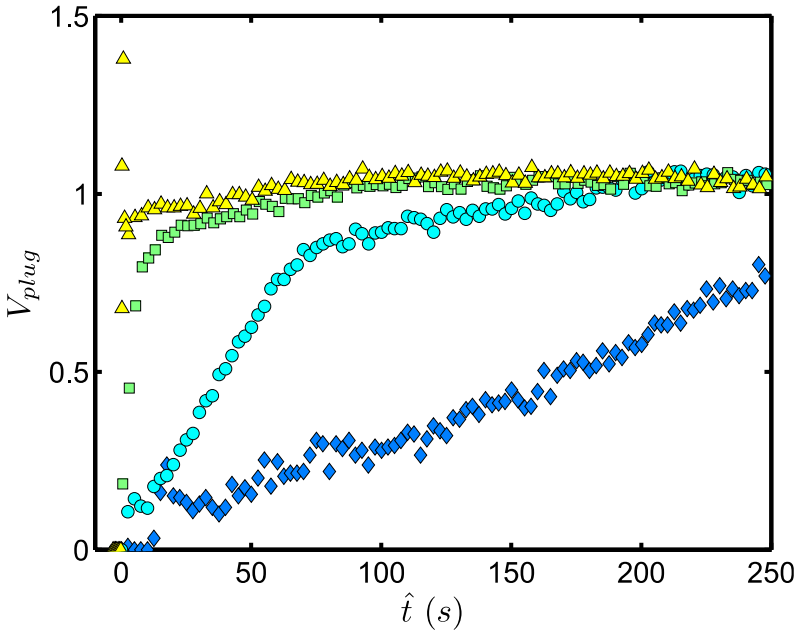

Figure 6-25: Dimensionless plug velocity of Laponite suspension of 7.5% and I=1.5x10^{-3} mol/L: $\hat{V}_0$=8.9 mm/s (◊); $\hat{V}_0$=25.6 mm/s (○); $\hat{V}_0$=51.7 mm/s (□) and $\hat{V}_0$=92.8 mm/s (▲).

Figure 6-26 shows the effect of ionic strength in the start-up experiment on the dimensionless form. Instead of time ($\hat{t}$), its dimensionless form is applied ($t = \hat{t}\hat{\dot{\gamma}}_c$), for Laponite suspension of 1.5%. Figure 6-26.a shows the results for I=5.0x10^{-3} mol/L and figure 6-26.b, for I=7.5x10^{-3} mol/L. As the ionic strength increases, the steady state plug velocity decreases, due to the increase of the yield stress, also detected in the rheological experiment.

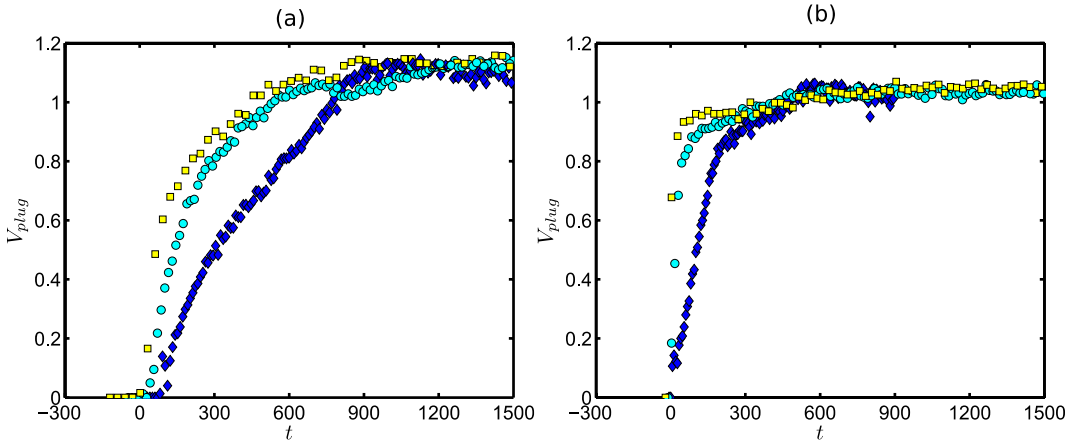

Figure 6-26: Dimensionless plug velocity of Laponite suspension of 1.5%: (a) I=5.0x10^{-3} mol/L with $\hat{V}_0$=36.0 mm/s (◊); $\hat{V}_0$=56.1 mm/s (○) and $\hat{V}_0$=115.4 mm/s (□); (b) I=7.5x10^{-3} mol/L with $\hat{V}_0$=25.6 mm/s (◊); $\hat{V}_0$=51.7 mm/s and (○); $\hat{V}_0$=92.8 mm/s (□).

In the Laponite experiments with low ionic concentration (I<3.0x10^{-3} mol/L) it is not possible to identify the differential pressure influence in the plug velocity transient in the mean velocities experimental range.

As described in chapter 5, the ionic strength plays an important role in the Laponite disks interaction. It seems that in gel state, near the transition to solution (sol), as the ionic strength increase the dimensionless time to reach steady state increases. On the other hand, near the flocculation transition, the opposite occurs, as the salt concentration increases, the dimensionless time to reach steady state solution also decreases. It seems that, initially, as the salt concentration increases, the equilibrium time increases but after a specific ionic strength, the opposite occurs, the equilibrium time decreases as the salt concentration goes to the transition between gel and flocculation states.

6.9
Thixotropic model application

The impact of Houska (1981) [64] and de Souza Mendes (2011) [61] models parameters in numerical simulations from Wachs et al. (2009) [6] implemented in the StarWaCs software is evaluated by Lima (2015) [65]. She also compared the numerical results with the experimental data of Laponite suspensions start-up presented in this thesis.

Alencar (2016) [66] coupled the thixotropic model from de Souza Mendes (2011) [61] in Fluent suite and obtained the relation between restart time and inlet pressure for different thixotropic conditions. The numerical results are compared to the experimental data set from Laponite suspension $I=5.0x10^{-3}$ mol/L and he showed that the numerical simulations qualitatively represent the thixotropic behavior detected in the start-up experiments. Therefore, the Laponite start-up experiments results allow thixotropic numerical model validation.

6.10
Summary of start-up experiments

In this chapter the start-up experiments, transient response of a single fluid from rest when a differential pressure is applied, of yield stress and/or thixotropic fluids for different inlet velocities were performed in a 4 m long horizontal pipe for different Carbopol solutions and Laponite suspensions.

In all the start-up experiments, for low Reynolds numbers (<1500) at fully developed pipe flow, velocity profiles symmetry and well defined *plastic* plug were observed. Besides, the average profile in the steady state period were well represented by the theoretical profile for fully developed laminar flow of Herschel-Bulkley fluid for the same $\hat{V}_0$.

The analysis of the influence of a solenoid valve in the start-up experiments with Laponite confirmed that the fluid shear history (rejuvenation versus resting time) affects in the apparent fluid yield stress as described in the previous chapter by rheological tests.

The comparison between start-up results of Laponite solutions, including different NaCl concentration and inlet flow velocities, showed that thixotropy delays the steady state flow development and high differential pressure implies fast transient responses for Laponite solutions with high ionic strength ($I>3.0x10^{-3}$ mol/L). On the other hand, it was not possible to identify the differential pressure influence in the plug velocity transient in the mean velocities experimental range for suspensions with low ionic concentration ($I<3.0x10^{-3}$ mol/L). The state diagram of Laponite seems to play an important role in the dimensionless time to reach steady state.

7
Fluid Displacement - Numerical Simulation

To understand the *isodense* displacement of yield stress fluid by a Newtonian fluid with low viscosity, numerical simulations are performed in Fluent, a finite volume commercial software by ANSYS. After the numerical formulation, the Fluent configuration is detailed. The numerical code is validated with displacement fluid results from bibliography considering the displaced fluid as Newtonian and shear-thinning. The yield stress displacement is then analyzed and the impact of flow rate and rheological parameters on the displacement flow is presented.

7.1
Numerical Model

The numerical model should represent a Newtonian fluid (fluid 1) displacing a generalized Newtonian fluid (fluid 2) along a tube of diameter $\widehat{D}$ for fluids of same density, $\hat{\rho}$. Cylindrical coordinates $(\hat{x}, \hat{r})$ are chosen such that $\hat{x}$ points follow the displacement direction. The tube is initially filled with fluid 2 (a generalized Newtonian fluid) which is displaced by fluid 1 (Newtonian fluid), injected at $\hat{x}$ =0 with mean velocity $\widehat{V}_0$. The length of the tube is $\hat{L}>>\widehat{D}$. We adopt the convention of denoting dimensional quantities and variables with the hat symbol and dimensionless quantities without.

We consider laminar flows and assume that the fluids are miscible and incompressible. In the large Peclet number limit (ineffective transport via molecular diffusion), the equations of motions are:

$$\frac{\hat{\rho}\widehat{V}_0^{\,2}}{\hat{\tau}_c}\left[\frac{\partial}{\partial t}\mathbf{v} + (\mathbf{v}\cdot\nabla)\mathrm{v}\right] = -\nabla p + \nabla\cdot\boldsymbol{\tau} \qquad 7\text{-}1$$

$$\nabla\cdot\mathbf{v} = 0 \qquad 7\text{-}2$$

$$\frac{\partial}{\partial t}C + \mathbf{v}\cdot\nabla C = 0 \qquad 7\text{-}3$$

Here, $\mathbf{v}$ denotes the velocity, p the pressure, $\boldsymbol{\tau}$ the deviatoric stress, C is the concentration of fluid 2 and $\hat{\tau}_c$ is the characteristic stress of the fluid displacement. These equations have been made dimensionless with the following scaling:

$$\mathbf{x} = \frac{\hat{\mathbf{x}}}{\hat{R}}, t = \frac{\hat{V}_0}{\hat{R}}\hat{t}, \mathbf{v} = \frac{\hat{\mathbf{v}}}{\hat{V}_0}, p = \frac{1}{\hat{\tau}_c}\hat{p}, \boldsymbol{\tau} = \frac{1}{\hat{\tau}_c}\hat{\boldsymbol{\tau}} \qquad 7\text{-}4$$

where $\hat{R}$ is the tube radius.

The multiphase flow is modeled using the volume of fluid method (VOF). The VOF method solves a set of mass conservation equations and obtains the volume fraction of each phase through the domain, which sum up unity inside each control volume. As described by Wielage-Burchard and Frigaard (2011) [18] the fluid concentration acts as a passive tracer, advected with the flow. Therefore, if C=0, the cell is empty of fluid 2 (full of fluid 1); if C=1, the cell is full of fluid 2 (empty of fluid 1); and if 0<C<1, the cell contains the interface between fluids. It is important to point out that the velocity is equal for all phases. Although no intermediate concentration is expected in the tube in principle, numerical intermediate concentrations do arise and the deviatoric stress $\boldsymbol{\tau}$ is defined at intermediate concentrations by interpolating from the deviatoric stress of the pure fluid components.

In pure fluid 1, the constitutive law is:

$$\boldsymbol{\tau}_1 = \frac{8\hat{\mu}_1\hat{V}_0}{\hat{D}}\frac{1}{\hat{\tau}_c}\dot{\boldsymbol{\gamma}} \qquad 7\text{-}5$$

where $\dot{\boldsymbol{\gamma}}$ is the strain tensor:

$$\dot{\boldsymbol{\gamma}} = \nabla \mathrm{v} + (\nabla \mathrm{v})^T. \qquad 7\text{-}6$$

The deviatoric stress of the fluid 2 depends on the type of fluid considered:

1. Newtonian Fluid

$$\boldsymbol{\tau}_2 = \frac{8\hat{\mu}_2\hat{V}_0}{\hat{D}}\frac{1}{\hat{\tau}_c}\dot{\boldsymbol{\gamma}}. \qquad 7\text{-}7$$

2. Carreau Fluid

$$\boldsymbol{\tau}_2 = \overline{k}\left(\frac{\hat{V}_0}{\hat{R}}\right)^n \frac{1}{\hat{\tau}_c}\dot{\boldsymbol{\gamma}} \qquad 7\text{-}8$$

where $\dot{\gamma}$ and $\overline{k}$ are defined by

$$\dot{\gamma} = \left[\frac{1}{2}\sum_{i,j=1}^{2}\left[\dot{\gamma}_{ij}\right]^2\right]^{\frac{1}{2}} \qquad 7\text{-}9$$

$$\overline{k} = \hat{\eta}_\infty\left(\frac{\hat{V}_0}{\hat{R}}\right)^{1-n} + (\hat{\eta}_0 - \hat{\eta}_\infty)\left[\left(\frac{\hat{V}_0}{\hat{R}}\right)^{-2} + \hat{K}_c\dot{\gamma}^2\right]^{\frac{(n-1)}{2}}. \qquad 7\text{-}10$$

3. Herschel Bulkley Fluid

$$\boldsymbol{\tau}_2 = \left[\hat{k}\left(\frac{\hat{V}_0}{\hat{R}}\right)^n \frac{1}{\hat{\tau}_c}\dot{\gamma}^{n-1} + \frac{\frac{\hat{\tau}_y}{\hat{\tau}_c}}{\dot{\gamma}}\right]\dot{\boldsymbol{\gamma}} \Leftrightarrow \tau_2 > \frac{\hat{\tau}_y}{\hat{\tau}_c}, \qquad 7\text{-}11$$

$$\dot{\gamma} = 0 \Leftrightarrow \tau_2 \leq \frac{\hat{\tau}_y}{\hat{\tau}_c} \qquad 7\text{-}12$$

where γ and τ_2 are defined by

$$\dot{\gamma} = \left[\frac{1}{2}\sum_{i,j=1}^{2}\left[\dot{\gamma}_{ij}\right]^2\right]^{\frac{1}{2}} \tau_2 = \left[\frac{1}{2}\sum_{i,j=1}^{2}\left[\tau_{2,ij}\right]^2\right]^{\frac{1}{2}}. \qquad 7\text{-}13$$

Taking into account the dimensionless parameters defined in section 4.2 and considering, for instance, fluid 2 as a Newtonian fluid, we have:

$$\hat{\dot{\gamma}}_c = \frac{8\hat{V}_0}{\hat{D}}, \hat{\tau}_c = \frac{8\hat{\mu}_2\hat{V}_0}{\hat{D}}, Re = \frac{\hat{\rho}\hat{V}_0\hat{D}}{\hat{\mu}_2}, M = \frac{\hat{\mu}_2}{\hat{\mu}_1}, B = 0, \frac{\hat{\rho}\hat{V}_0{}^2}{\hat{\tau}_c} = \frac{Re}{8}. \qquad 7\text{-}14$$

7.2
Fluent Code Characteristics

The Fluent code with finite volume method is applied to model the displacement of two fluids in a tube geometry. The two fluids are modeled using Volume of Fluid (VOF) method that determines the shape and location of the free surface based on the concept of a fractional volume of fluid (Ansys Inc., 2013 [67]). A unit value of the volume fraction, or concentration, corresponds to a full element occupied by the fluid 2 (displaced fluid), and a zero value indicates an empty element containing no fluid 2. In this case the element is totally occupied by fluid 1 (displacing fluid). A concentration (C) value between zero and one indicates that the corresponding element is a partial (or surface) element. In general, the evolution of the free surface is computed either through a VOF advection algorithm or through equation (7-3). Besides, the initial interface between fluid 1 and 2 was considered flat. It is important to point out that we performed transient simulations using a cluster of 16 processors in parallel.

7.2.1
Fluent Configuration

The numerical simulations are performed in Fluent Academic version 14.5 with double precision. The pressure Navier-Stokes method is applied to solve the transport equations (pressure-based solver) for a transient axisymmetric 2D geometry. The PISO scheme with skewness-neighbor is applied for pressure and velocity coupling. Two Eulerian phases are considered in the Volume of Fluid multiphase model with an implicit scheme and volume fraction cutoff of 10^{-6}. Laminar viscous flow model is applied. The solution methods for spatial discretization are:

- Least square cell based for gradient;
- PRESTO! for pressure;
- Power-law for momentum;
- Second order Upwind for volume fraction.

For the transient formulation a second order implicit method is considered. The under relaxation factors are shown in table 7-1 and the absolute convergence absolute criteria for each residual in table 7-2.

Table 7-1: Relaxation factors of Fluent solution for variables controls.

Variable	Under-Relaxation factors
Pressure	0.3
Density	1
Body Forces	1
Momentum	0.7
Volume fraction	0.5

Table 7-2: Fluent configuration for convergency absolute criteria.

Equation	Maximum Residual
Continuity	10^{-6}
Axial velocity	10^{-6}
Radial Velocity	10^{-6}
Volume of fluid	10^{-6}

7.2.2
Boundary Conditions

Figure 7-1 presents the the schematic of the solution domain considered in the numerical model.

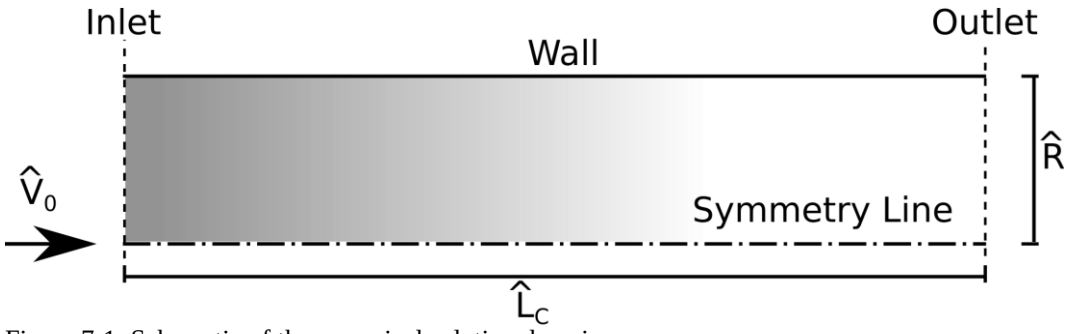

Figure 7-1: Schematic of the numerical solution domain.

The following boundary conditions are considered:

- Inlet - velocity profile input of fluid 1 is considered parabolic (Poiseuille flow);
- Outlet - constant pressure ($\hat{P}_{outlet} = P_{atm}$);
- Symmetry - $\frac{\partial V_x}{\partial r} = 0$ and V_r=0;
- Wall - impermeability and no slip conditions;

7.2.3
Initial Condition

Initially the flow domain is completely filled with fluid 2 at rest.

7.2.4
Mesh

A uniform rectangular mesh is used ($\hat{R} \times \hat{L}_C$) where $\hat{L}_C$=300mm represents the computational tube length. Typically we use 100 elements across the tube radius and 3000 along the tube length. We have the aspect ratio of $\hat{L}_C/\hat{R} \approx 31.5$ with the element size in the axial and radial directions of $\hat{s}_x \approx \hat{s}_r \approx$0.1 mm. This give a tube radius approximately equal to the experimented apparatus. The refined mesh is considered to improve the spatial resolution in the radial direction in order to

identify residual layer fluctuation along the tube visualized in the yield stress fluid displacement experiments presented in chapter 4 .

7.2.5
Time Step definition

The time step definition takes under consideration four parameters:

1. element size in the axial direction ($\hat{s}_x$);
2. mean velocity ($\hat{V}_0$) at inlet;
3. tube Diameter ($\widehat{D}$);
4. minimum inner diameter of the displacing fluid ($\hat{d}_{min}$).

The minimum time ($\hat{t}_{min}$) required to cross one mesh element in the axial direction is

$$\hat{t}_{min} = \frac{\hat{s}_x}{\hat{V}_{max}} \qquad 7\text{-}15$$

where $\hat{V}_{max}$ represents the maximum axial velocity along the tube. If the displacing fluid is Newtonian and a residual layer is observed after the front passage, we have

$$\hat{V}_{max} = 2\hat{V}_0 \left(\frac{\widehat{D}}{\hat{d}_{min}}\right)^2. \qquad 7\text{-}16$$

Here, $\hat{d}_{min}$ is related to the maximum remaining fluid fraction (m_{max}) in the tube. The ratio between the tube diameter ($\widehat{D}$) and displacing diameter ($\hat{d}$) can be written as a function of the remaining fluid fraction (m) using equation 2-3:

$$\left(\frac{\widehat{D}}{\hat{d}}\right)^2 = \frac{1}{1-m}. \qquad 7\text{-}17$$

Therefore, from equations (7-15), (7-16) and (7-17), we have

$$\hat{t}_{min} = \frac{\hat{s}_x}{2\hat{V}_0 \left(\frac{\widehat{D}}{\hat{d}_{min}}\right)^2} = \frac{\hat{s}_x}{2\hat{V}_0 \frac{1}{1-m_{max}}} = \frac{(1-m_{max})}{2}\frac{\hat{s}_x}{\hat{V}_0}. \qquad 7\text{-}18$$

Considering the maximum remaining fluid fraction of a Newtonian displacement (m_{max}=0.61) for low viscosity ratio $M \approx 0$ from figure 2-8, we have $\hat{t}_{min}$ as a function of the mean velocity ($\hat{V}_0$) and the element size in the axial direction ($\hat{s}_x$):

$$\hat{t}_{min} = 0.195\frac{\hat{s}_x}{\hat{V}_0}. \qquad 7\text{-}19$$

Table 7-3 shows the minimum and the time steps considered for the numerical simulations for different mean velocities.

Table 7-3: Minimum and the time steps considered for the numerical simulations for different mean velocities.

$\hat{V}_0$ [mm/s]	Minimum Time step [s]	Time step [s]
100	0.000195	0.00015
10	0.00195	0.0015
1	0.0195	0.015
0.1	0.195	0.15

7.2.6
Fluid model

The viscosity models from Fluent database (Ansys Inc., 2013 [67]) are considered for the numerical simulation for both fluids. The software Fluent employs a regularization model to deal with the infinity viscosity of the Herschel-Bulkley model given by:

$$\hat{\eta} = \frac{\hat{\tau}_y}{\hat{\dot{\gamma}}} + \hat{K}\left(\frac{\hat{\dot{\gamma}}}{\hat{\dot{\gamma}}_c^F}\right)^{n-1}, \hat{\dot{\gamma}} > \hat{\dot{\gamma}}_c^F \qquad 7\text{-}20$$

$$\hat{\eta} = \hat{K}\left[(2-n) + (n-1)\frac{\hat{\dot{\gamma}}}{\hat{\dot{\gamma}}_c^F}\right] + \frac{\hat{\tau}_y\left(2 - \frac{\hat{\dot{\gamma}}}{\hat{\dot{\gamma}}_c^F}\right)}{\hat{\dot{\gamma}}_c^F}, \hat{\dot{\gamma}} < \hat{\dot{\gamma}}_c^F. \qquad 7\text{-}21$$

where $\hat{\dot{\gamma}}_c^F$ is a critical shear rate. Below $\hat{\dot{\gamma}}_c^F$, the viscosity tends to the upper (high) viscosity limit. It is worth to mentioning that decreasing $\hat{\dot{\gamma}}_c^F$, the regularized model tends to the Herschel-Bulkley equation.

This critical shear rate has the same effect of limit viscosity for low shear rate ($\hat{\eta}_0$) of the modified Papanastasiou equation for a Herschel-Bulkley fluid proposed by de Souza Mendes and Dutra (2004) [44]

$$\hat{\eta} = \left(\frac{\hat{\tau}_y}{\hat{\dot{\gamma}}} + \hat{K}\hat{\dot{\gamma}}^{n-1}\right)\left(1 - e^{-\frac{\hat{\eta}_0\hat{\dot{\gamma}}}{\hat{\tau}_y}}\right). \qquad 7\text{-}22$$

Originally this regularization method was developed by Papanastasiou (1987) [68] for an ideal Bingham fluid. Alencar (2016) [66] analyzed the Fluent regularization model and the one proposed by [44] and compared the effect of $\hat{\dot{\gamma}}_c^F$

and $\hat{\eta}_0$ variation in both models, respectively. These two variables control the regularization in each respective model. The effect of high values of $\hat{\eta}_0$ in de Souza Mendes and Dutra (2004) [44] model is equivalent to the effect of low values of $\hat{\dot{\gamma}}_c^F$ in the Fluent regularization model. We consider $\hat{\dot{\gamma}}_c^F$=10^{-4} 1/s for all yield stress fluid displacement simulations to subside any numerical discontinuities.

In the numerical code validation, rheological parameters from the literature were applied. In the numerical simulation of yield stress fluid displacement, the displaced fluid is modelled by a Herschel-Bulkley model whose parameters are presented in Table 7-4. It emulates the Carbopol solutions applied in the displacement and start-up experiments presented in chapters 4 and 6. Letter *a* is related to the fluid with lowest yield stress and letter *i* to the highest yield stress fluid used in the experimental set up.

The lower case letter are related to numerical simulations and upper case letter to yield stress displacement experiments. This notation is used to emphasize the difference between experiments and numerical simulations. It is important to point out that fluid 2 from the set with a specific upper letter from table 4-1 is not equivalent to the fluid with the lower letter from Table 7-4.

Table 7-4: Herschel-Bulkley rheological parameters of yield stress fluids considered in the numerical simulations.

Fluid	Density	Herschel-Bulkley Model		
		$\hat{\tau}_y$	n	$\widehat{K}$
#	kg/m^3	(Pa)	( )	(Pa.s^n)
a	998.4	1.5	0.49	1.3
b	998.4	1.9	0.54	1.3
c	997.5	4.6	0.45	2.4
d	997.5	5.1	0.43	2.8
e	998.2	6.2	0.45	3.2
f	997.6	10.0	0.42	4.3
g	998.6	17.0	0.41	5.9
h	997.5	20.0	0.41	8.0
i	998.1	25.0	0.36	11.2

The displacing fluid is modelled by a Newtonian fluid with the same density of displaced fluid with viscosity close to the water at 20°C ($\hat{\mu} = \hat{\mu}_1$= 0.001 Pa.s).

7.3
Parameters range studied

The parameter range covered in our yield stress displacement simulations is given in Table 7-5. Every experiment can be represented by a corresponding yield stress fluid (Table 7-4), and the mean velocity ($\hat{V}_0$) or, alternatively, by a set of dimensionless parameters (*Re,B,M*).

Table 7-5: Parameter ranges used in the displacement numerical simulations.

Parameter	Range
β (°)	90
$\hat{V}_0$ (mm/s)	0.1 - 100
$\hat{\dot{\gamma}}_c$ (1/s)	0.05 - 61
$\hat{\tau}_y$ (Pa)	1.5 - 25.0
Re	2.75 10^{-6} - 7.50
B	0.16 - 9.32
M	216 - 97245
Re_N	1.9 - 1900
B_N	35.7 - 595312
At	0
Fr	∞

7.4
Numerical code validation

To compare the numerical results with experimental data, two variables are commonly used in fluid displacements: the percentage of mass of the fluid that remains in the tube after the front passage (m) and residual layer thickness normalized by the tube radius ($h = 1 - \hat{r}/\hat{R}$). These two variables are related:

$$m = 1 - \frac{\hat{r}^2}{\hat{R}^2} = 1 - (1-h)^2 \qquad 7\text{-}23$$

$$h = 1 - \sqrt{1-m} \qquad 7\text{-}24$$

Three methodologies are commonly applied for the remaining mass calculation:

1. Taylor method – Taylor (1961) [23] performed immiscible experiments displacing golden syrup by air. To calculate *m*, he measured the mass of the discharged fluid ($\hat{w}$) and the length of the

tip of the air front ($\hat{L}_{Ta}$). Based on the specific gravity ($\hat{\rho}$) and the tube diameter ($\widehat{D}$), m_1 is calculated by:

$$m_1 = 1 - \frac{\widehat{w}}{\hat{\rho}\hat{L}_{Ta}\frac{\pi\widehat{D}^2}{4}}. \qquad 7\text{-}25$$

The mass of the discharged fluid $\widehat{w}$ is equivalent to:

$$\widehat{w}(\hat{t}) = \hat{\rho}\frac{\pi\widehat{D}^2}{4}\hat{L}_0(\hat{t}) \qquad 7\text{-}26$$

where $\hat{L}_0(\hat{t}) = \int_0^{\hat{t}} \hat{V}_0(\epsilon)d\epsilon$. Therefore, the residual layer m_1 is given by

$$m_1(\hat{t}) = 1 - \frac{\hat{L}_0(\hat{t})}{\hat{L}_{Ta}(\hat{t})}. \qquad 7\text{-}27$$

Here, $\hat{L}_{Ta}(\hat{t}) = \int_0^{\hat{t}} \hat{V}_f(\epsilon)d\epsilon$ and $\hat{V}_f(\hat{t})$ represents the front velocity measured in the bubble tip (meniscus). Therefore, equation (7-27) can be rewritten as

$$m_1(\hat{t}) = 1 - \frac{\int_0^{\hat{t}} \hat{V}_0(\epsilon)d\epsilon}{\int_0^{\hat{t}} \hat{V}_f(\epsilon)d\epsilon}. \qquad 7\text{-}28$$

2. Front Velocity method - Many authors (Gabard ,2001 [69]; Gabard and Hulin, 2003 [14], Petitjeans and Maxworthy, 1996 [26]; Chen and Meiburg, 1996 [27]) calculated *m* based on the relation between the front velocity ($\hat{V}_f$) and the mean velocity ($\hat{V}_0$) at a fully developed flow:

$$m_2 = 1 - \frac{\hat{V}_0}{\hat{V}_f} \qquad 7\text{-}29$$

which is equivalent to equation (7-28) at long-times provided the flow becomes steady.

3. Residual layer method - This methodology is the simplest one and consists of measuring the inner diameter ($\hat{d}$) of the displacing fluid, away from the influence of the displacing front; and the tube inflow and outflow:

$$m_3 = 1 - \left(\frac{\hat{d}}{\widehat{D}}\right)^2 = 1 - \left(\frac{\hat{r}}{\widehat{R}}\right)^2 \qquad 7\text{-}30$$

This methodology is applied if a static residual layer is detected after the front passage.

Due to the VOF advection, the interface between fluids is defined by the elements whose concentration lies between 0 and 1. In this region, the element properties are interpolated considering the element concentration from the properties of the pure fluid components. To show the numerical diffusion effects in the interface, the front velocity at symmetry line (r=0) is presented in figure 7-2 as a function of the concentration. $\hat{V}_f$ is taken as the velocity of the position where C=0.5 on the symmetry line (r=0), when fully developed flow is achieved. Also, the interface is defined as the loci of points where C=0.5.

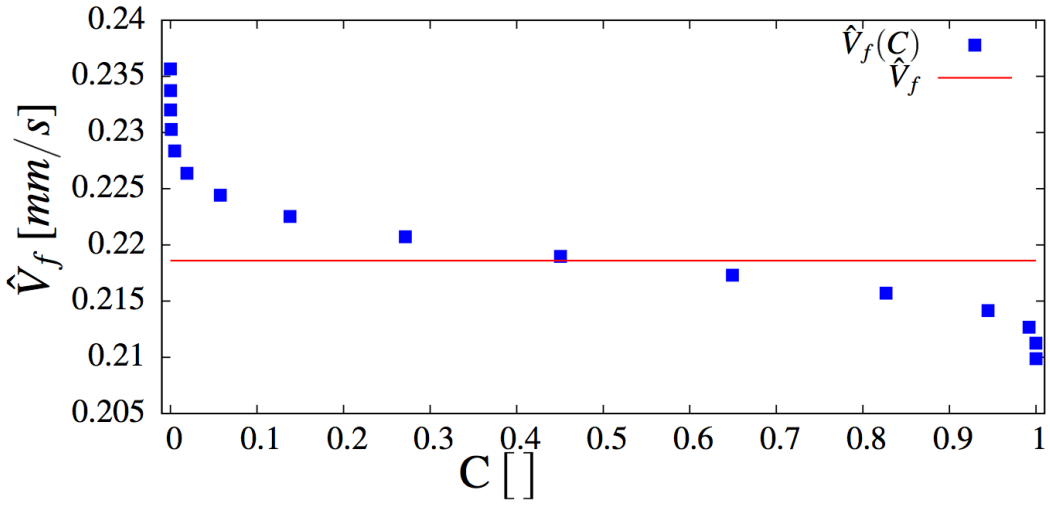

Figure 7-2: Example of the concentration influence in the front velocity at symmetry line (r=0): $\hat{V}_f$ (C) (□) and $\hat{V}_f$ (C=0.5) (continuous line).

Figure 7-3 shows the front velocity of 3 g/L Xanthan solution from Gabard and Hulin (2003) [14] for $\hat{V}_0$= 0.1 mm/s along the front position $\hat{x}_f$ in the interface edges (C=0^+ and C=1^-). $\hat{x}_f$ represents the position of the interface (finger) tip along the axial position $\hat{x}$. As the the front advances, the front velocity on the position where C=0^+ and C=1^- asymptotically converge to $\hat{V}_f$. It also shows the maximum velocity in the reduced pipe $\hat{V}_{max} = 2(\hat{D}/\hat{d})^2\hat{V}_0$. For the displacement under analysis, we observe that $\hat{V}_f < \hat{V}_{max}$.

The remaining mass fractions based on the three methodology presented for 3 g/L Xanthan solution from Gabard and Hulin (2003) [14] displaced by an isodende Newtonian fluid ($\hat{\mu}$=0.001 Pa.s) for $\hat{V}_0$=0.1mm/s are presented in figure 7-4. As expected, the remaining mass fraction m_1 is a function of the front tip

position ($\hat{x}_f$) and asymptotically converge to m_2. On the other hand, m_3 is not equivalent to m_2 for the shear thinning fluid under consideration. The finger shape itself seems to affect m_2 values and the ratio between m_2 and m_3.

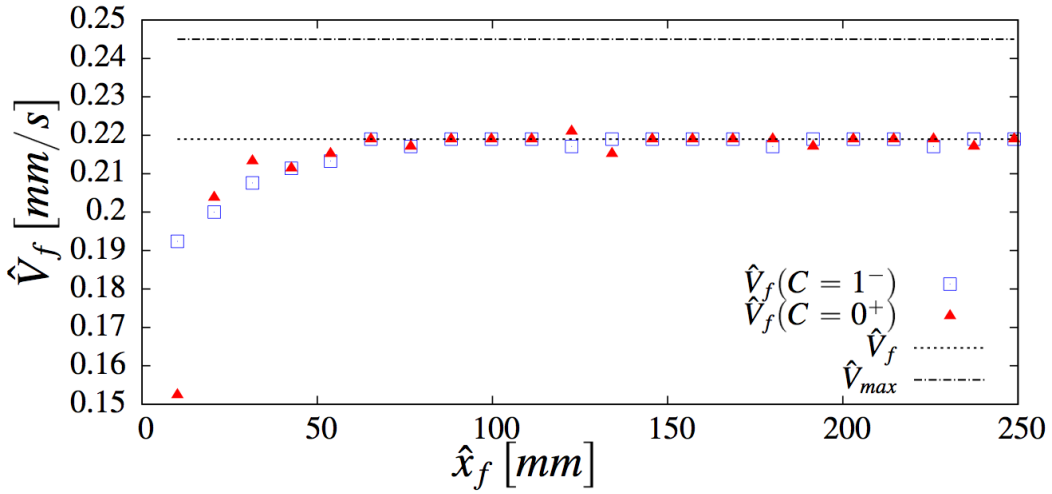

Figure 7-3: Front velocity in the interface edges along the front position $\hat{x}_f$ for 3 g/L Xanthan solution from Gabard and Hulin (2003) [14] at $\hat{V}_0$ = 0.1mm/s: $\hat{V}_f$ (C=0$^+$) (▲); $\hat{V}_f$ (C=1$^-$) (□); $\hat{V}_f$ (dashed line); and $\hat{V}_{max} = 2\left(\frac{\hat{D}}{\hat{a}}\right)^2 \hat{V}_0$ (dotted-dashed line) .

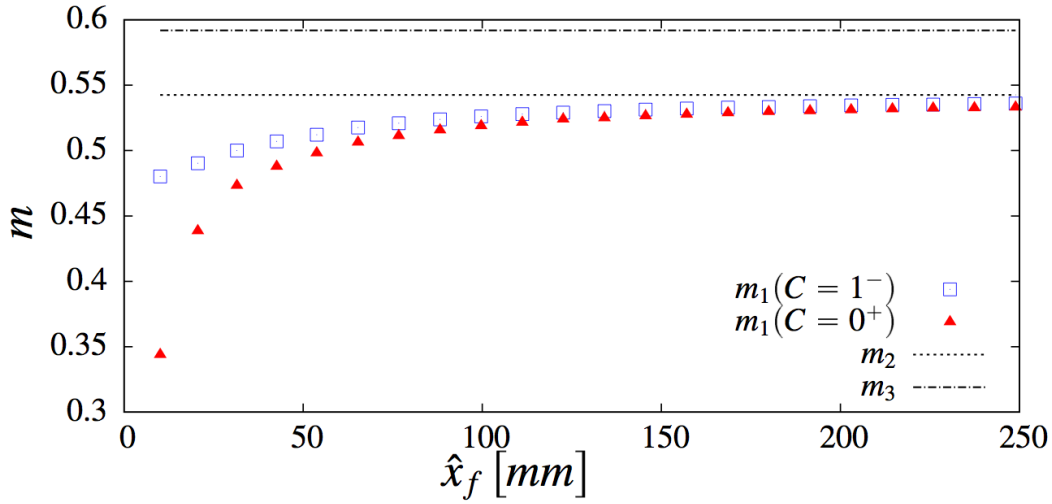

Figure 7-4: Residual layer along the front position $\hat{x}_f$ for Xanthan solution of 3 g/L from Gabard and Hulin (2003) [14] for $\hat{V}_0$ = 0.1mm/s: m_1(C=0$^+$) (▲); m_1(C=1$^-$) (□); and m_2 (dashed line); and m_3 (dotted-dashed line).

7.4.1

Newtonian Fluid displacement

For Newtonian displacements, as mentioned in section 2.1 the residual layer is a function of the viscosity ratio. Table 7-6 presents the numerical simulation of Newtonian-Newtonian fluid displacement developed for code validation. For

M=0.002, the residual layer is independent of the mean velocity in the range 0 to 100 mm/s. As M increases the residual layer decreases. Since there is no static residual layer in Newtonian-Newtonian displacement and the Taylor's methods is influenced by the position of the front, the front velocity method is applied ($m = m_2$).

Table 7-6: Numerical simulation for Newtonian-Newtonian fluid displacement.

M	$\hat{V}_0$ [mm/s]	m
0.0002	100	0.599
0.0002	10	0.597
0.0002	1	0.600
0.1	1	0.561
0.25	1	0.523
0.45	1	0.499
1	1	0.494

The residual layers are plotted as a function of the viscosity ratio M in figure 7-5. They agree with the numerical simulations of Chen and Meiburg (1996) [27], experimental results of Petitjeans and Maxworthy (1996) [26], and Gabard and Hulin (2003) [14], also plotted in the figure.

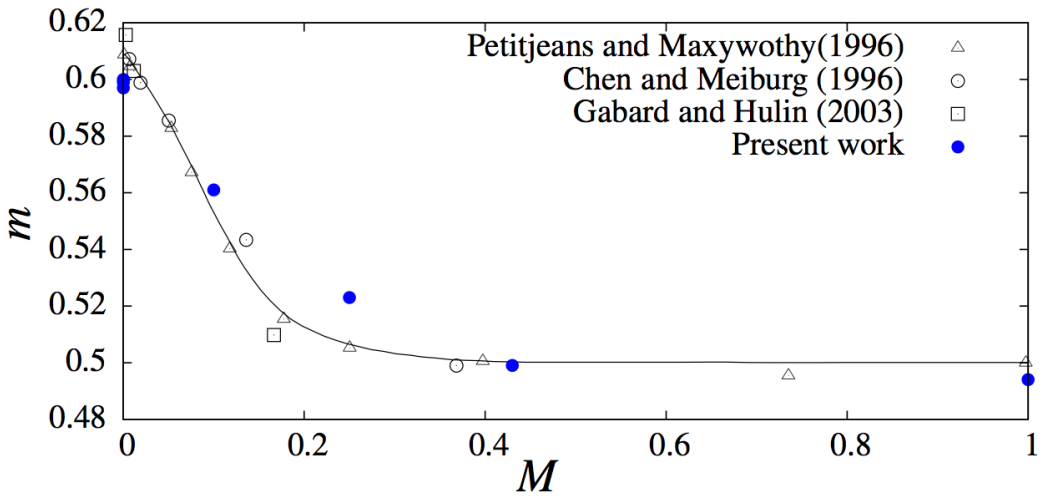

Figure 7-5: Influence of viscosity ratio M in the residual layer of a Newtonian-Newtonian isodense fluid displacement.

For viscosity ratio close to 0 ($M \approx 0$), the residual layer approaches the asymptotical value of 0.6 with an error lower than 1.7%. On the other hand, when the viscosity is greater then 0.4, the residual layer m tends to 0.5. For 0.1<M<0.4

the numerical simulation provides the same trend, but over estimates the residual layer with error less than 4%.

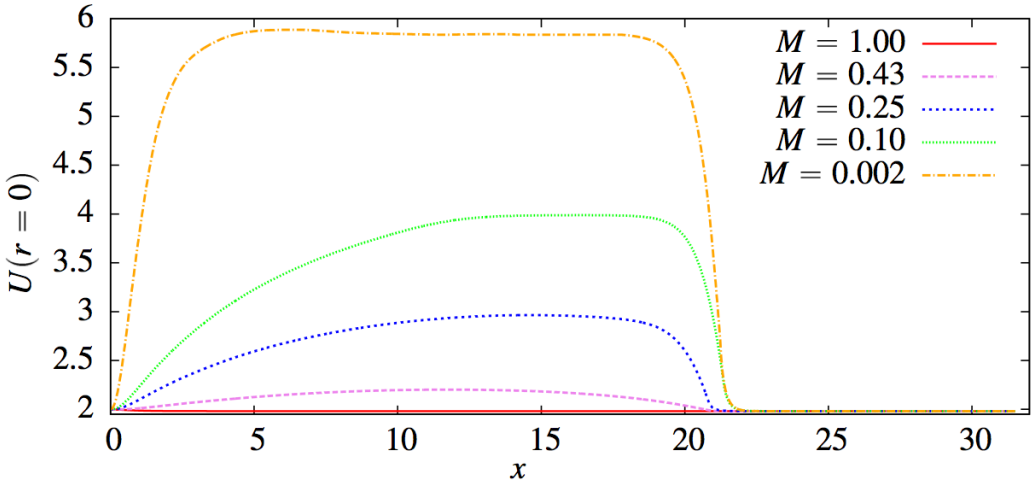

Figure 7-6: Axial velocity at symmetry line for different viscosity ratio of a Newtonian-Newtonian isodense fluid displacement for $x_f \approx 20$ and $\hat{V}_0$ = 1mm/s.

Figure 7-6 shows the profile of the axial velocity at symmetry line for different viscosity ratios, when the front is close to x_f=20 for $\hat{V}_0$ = 1mm/s. From U(r=0, x), it is possible to identify four regions along the tube length:

i. Entrance length: flow development;

ii. Fluid 1 steady state solution - fluid 1 flowing in a reduced diameter pipe due to the formation of the residual layer. This region is more evident for small *M*;

iii. Displacing front region - a region where the velocity profile is influenced by the front region containing both fluids 1 and 2;

iv. Fluid 2 steady state solution- steady state solution of fluid 2 flowing in a pipe of diameter $\hat{D}$ which is a typical parabolic profile of Newtonian fluid in Poiseuille flow;

v. Outlet region.

In the tube entrance, we have U(x=0, r=0)=2. It reflects the inlet boundary condition. As we move along the tube, the velocity U in the symmetry line increases and stabilizes when the flow is fully developed. This is associated to the influence of the tube entrance ($\hat{L}_{inlet}$) where the flow is under development. It is important to point out that $\hat{L}_{inlet}$ is a function of the viscosity ratio *M*. For the same mean

velocity, $\hat{L}_{inlet}$ decreases as *M* decreases. In figure 7-6 it is not possible to identify the influence of the tube outlet (region *v*). The front influence (region *iii*) is identified by the rapidly decay in the velocity at symmetry line, and region *iv* can be observed when a constant low velocity is achieved after this abrupt change.

Figure 2-6 from Petitjeans and Maxworthy (1996) [26] shows the fully developed flow of Newtonian-Newtonian fluid displacement without the influence of the tube inlet and outlet where regions *ii*, *iii* and *iv* can be identified.

The velocity profiles in regions *i* and *ii* at different axial position *x* for *M*=0.1, $\hat{V}_0$=0.1mm/s and $x_f \approx 29$ ($\hat{t}$ =124.5s) are presented in figure 7-7. The entrance influence is represented by the increase of U(*r=0*) from *x*=0 to 9.4. The inlet profile is identified at *x=0* and the velocity profile representative of region *ii* at *x*=22. It is clear that the residual layer is not static. Therefore, after the front passage, the residual layer at $x<x_f$ decreases, as the displacing front moves in the outlet direction.

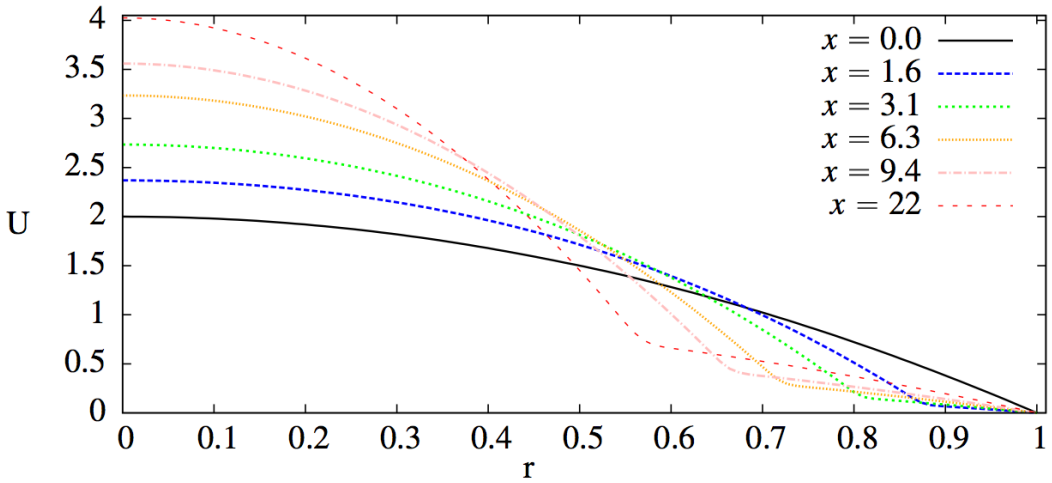

Figure 7-7: Velocity profile in regions *i* and *ii* for the Newtonian- Newtonian isodense fluid displacement at different axial positions: *M*=0.1, $\hat{V}_0$=0.1mm/s and $x_f \approx 29$ ($\hat{t}$=124.5s).

Figure 7-8 shows the impact of the displacing front on the velocity profile in region *iii*. The front influence is detected by the abruptly decay of U(*r*=0) from *x*=28.3 to 31.5. The velocity profile characteristic of regions *ii* and *iv* are represented by the profile for *x*=22 and *x*=31.5, respectively.

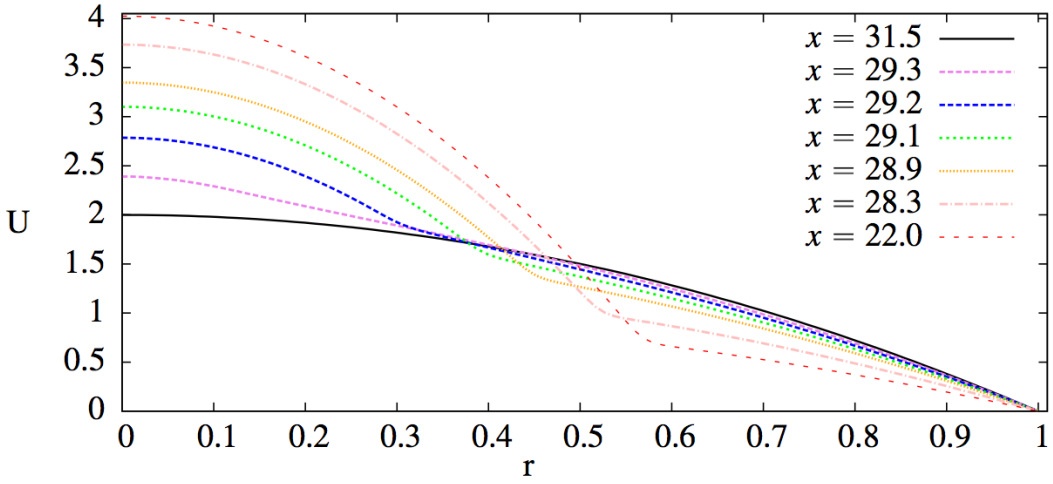

Figure 7-8: Velocity profile in regions *ii*, *iii* and *iv* for the Newtonian-Newtonian isodense fluid displacement at different axial positions: M=0.1, $\hat{V}_0$=0.1mm/s and $x_f \approx 29$ ($\hat{t}$=124.5s).

7.4.2
Shear Thinning Fluid Displacement

Table 7-7 presents the numerical simulation of shear thinning fluid displacement by an isodense Newtonian fluid with $\hat{\mu}$=0.001 Pa.s developed for code validation. The rheological properties of Xanthan solution of 3g/L from Gabard and Hulin (2003) [14] are considered (table 2-2). For shear thinning displacements the residual layer is a function of the mean velocity in the range 0.1 to 10 mm/s. As mean velocity increases, the residual layer decreases.

Table 7-7: Numerical simulation for Xanthan solution of 3g/L from Gabard and Hulin (2003) [14] displacement.

$\hat{V}_0$ [mm/s]	m
0.1	0.594
1	0.577
4	0.538
10	0.532

For shear thinning fluids, high velocities (high shear rates) are related to low viscosities. In fact, as in the Newtonian-Newtonian isodense fluid displacements, the viscosity ratio defines the residual layer of shear thinning fluid displacement. Figure 7-9 shows how the residual layer is affected by the mean velocity. The numerical results follow the same trend of the experimental data from Gabard (2001) [69], as the mean velocity increases, the residual layer decreases. Away from

the asymptotic value, the numerical results is consistently higher than the experiments. The results are plotted in dimensional quantities to respect the original data.

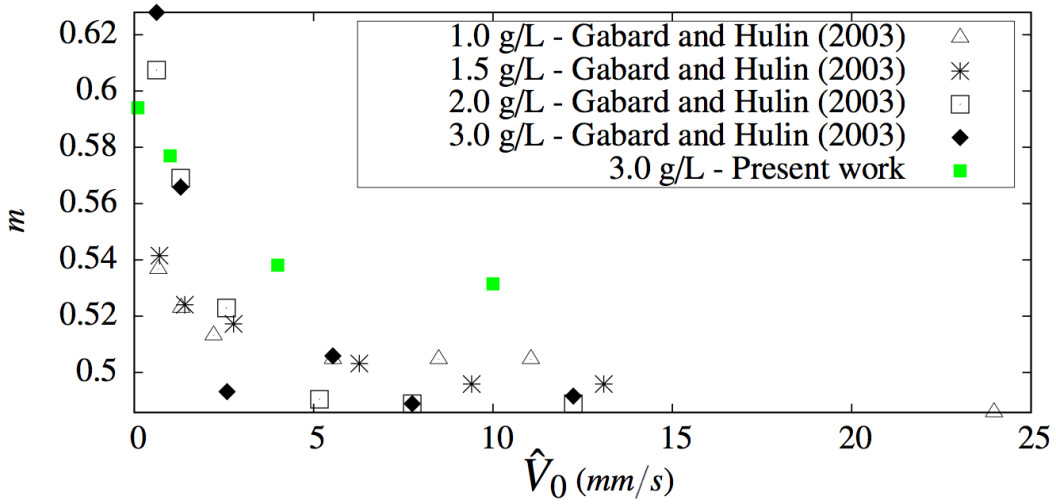

Figure 7-9: Influence of mean velocity $\hat{V}_0$ in the residual layer of Xanthan 3g/L solution from Gabard and Hulin (2001) [69] (shear thinning fluid) isodense displacement by a Newtonian fluid ($\hat{\mu}$=0.001Pa.s).

For higher viscosity ratio, lower mean velocity, the residual layer approaches the Newtonian-Newtonian isodense displacement asymptotically value for $M \approx 0$. On the other hand, when the viscosity ratio decreases, the mean velocity increases, the residual layer decreases, and approaches 0.5 limit for $M \approx 1$. Although the numerical simulation provides the same trend, the residual layer is over estimated with an error lower than 6.4%.

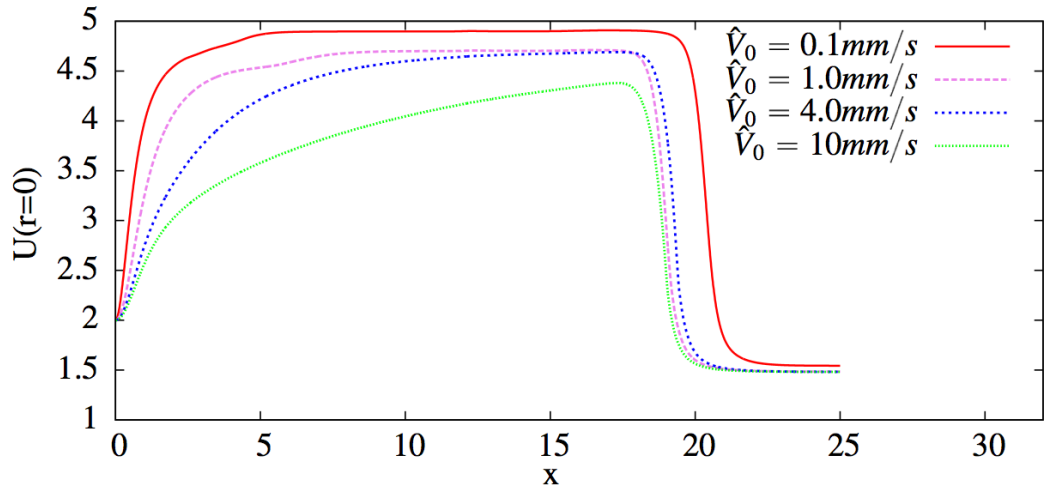

Figure 7-10: Axial velocity at symmetry line for different mean velocities of Xanthan 3g/L solution from Gabard and Hulin (2003) [14] isodense displaced by a Newtonian fluid ($\hat{\mu}$=0.001 Pa.s) for $x_f \approx 20$.

Figure 7-10 presents U(r=0, x) along the tube length of an isodense Newtonian fluid ($\hat{\mu}$=0.001 Pa.s) displacing Xanthan 3g/L solution from Gabard and Hulin (2003) [14] for different mean velocities when the front is close to $x_f \approx 20$ ($\hat{t}$=27.6s). The same regions mapped in the Newtonian-Newtonian isodense fluid displacement are also identified in the shear thinning displacement by a Newtonian fluid with $\hat{\mu}$=0.001 Pa.s.

For $\hat{V}_0$>4mm/s, it is possible to identify that x_f is not far away from the inlet to avoid the effect of the tube entrance ($\hat{x}_f < \hat{L}_{inlet}$). Figure 7-10 suggests that the numerical solution are far from steady for high $\hat{V}_0$. If $\hat{x}_f$ or $\hat{L}_{inlet}$ is sufficiently long to guarantee the full development of the flow, the numerical results would get closer to the experiments from Gabard and Hulin (2003) [14]. $\hat{V}_f$ would increase and the residual layer would decrease. No evidence of instabilities is detected in the numerical simulation for high velocities, as visualized in the Gabard and Hulin (2003) [14] experiments.

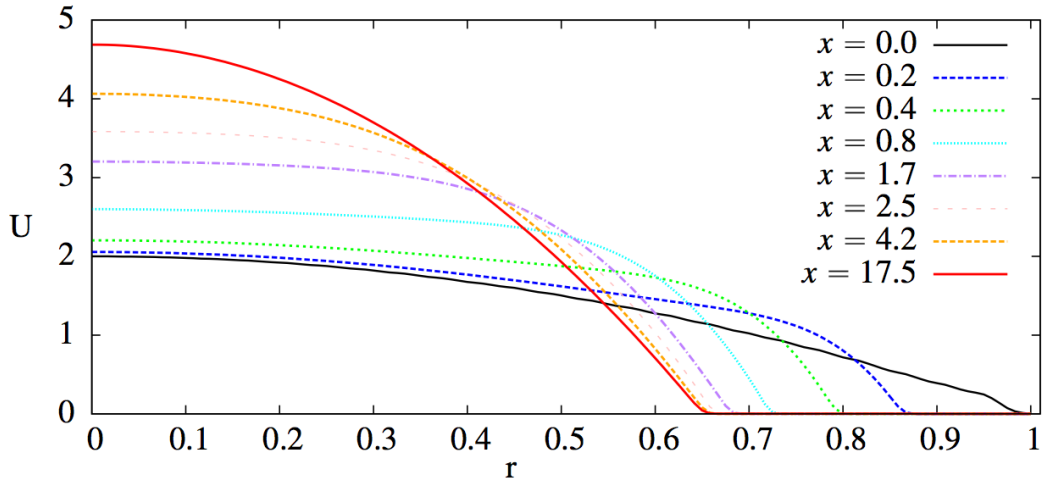

Figure 7-11: Velocity profile in regions *i* and *ii* of Xanthan 3g/L solution from Gabard and Hulin (2003) [14] solution isodense displaced by a Newtonian fluid ($\hat{\mu}$=0.001 Pa.s) at different axial positions: $\hat{V}_0$=4 mm/s and $x_f \approx 20$ ($\hat{t}$=27.65 s).

Figure 7-11 shows the velocity profiles in regions *i* and *ii* at different axial position *x* for $\hat{V}_0$=4mm/s and $x_f \approx 20$ ($\hat{t}$=27.65 s). The effect of the entrance is represented by the increase of U(r=0) from *x*=0 to 17.5. The inlet velocity profile is identified at *x*=0, and the region *ii* profile at *x*=17.5. The residual layer is approximately static and increases from *x*=0 to 17.5. It shows the development

region where the Poiseuille flow at tube full bore ($\widehat{D}$) gradually evolves to Poiseuille flow in reduced pipe diameter ($\hat{d}$).

Figure 7-12 shows the impact of the displacing front on the velocity profile in region *iii*. The front influence is detected by the abrupt decay of U(r=0) in the region from *x*=17.5 to 19.6. The velocity profile of region *iv* is represented by the profile for *x*=25.0. It shows the gradual velocity profile transition from a Poiseuille flow in a reduced pipe diameter ($\hat{d}$) into the steady state solution of a shear thinning fluid flowing at full pipe bore $\widehat{D}$. In this transition both fluids are flowing.

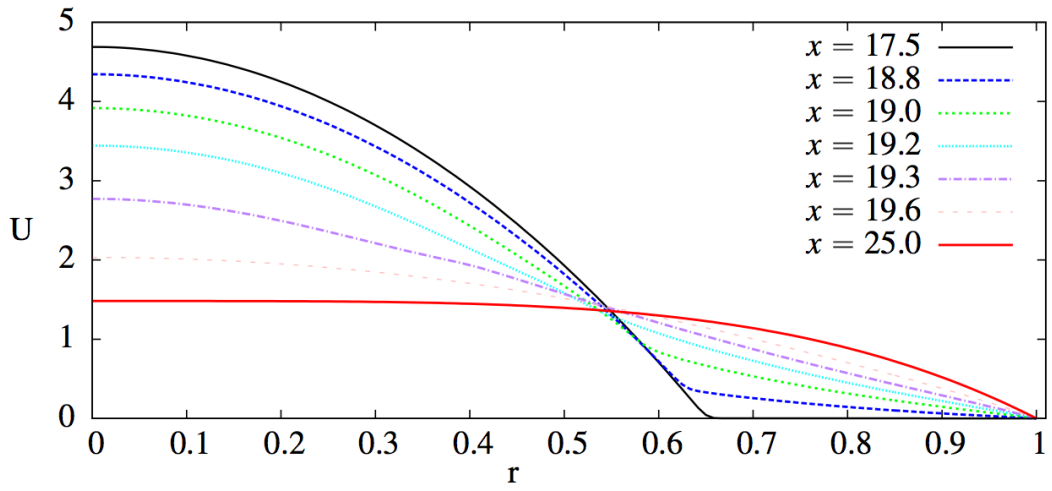

Figure 7-12: Velocity profile in regions *iii* and *iv* at different axial position of Xanthan 3g/L solution from Gabard and Hulin (2003) [14] isodense displaced by a Newtonian fluid ($\hat{\mu}$=0.001 Pa.s) at different axial positions: $\hat{V}_0$=4 mm/s and $x_f \approx 20$ ($\hat{t}$=27.65 s).

7.4.3
Fluent Herschel-Bulkley model

The velocity profile of region *iv* for an isodense Newtonian fluid ($\hat{\mu}$=0.001 Pa.s) displacing fluid *g* (Table 7-4), for $\hat{V}_0$=100 mm/s, is compared to the analytical solution for a fully developed laminar flow of fluid *g* (Table 7-4) in a pipe, for the same mean velocity and pipe diameter ($\widehat{D}$). The profiles are presented in figure 7-13. The maximum error for the numerical solution is 1% compared to the analytical solution.

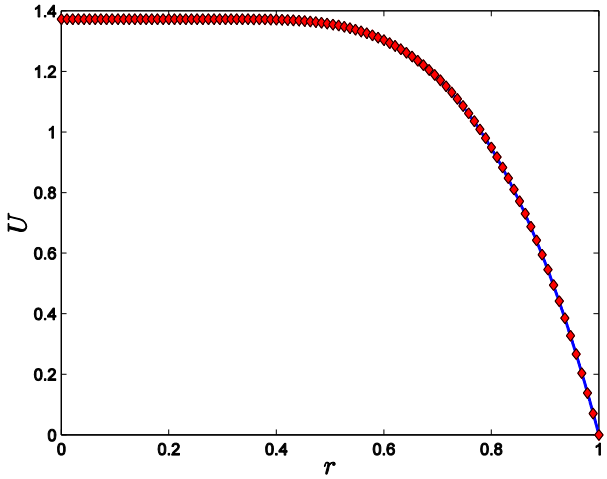

Figure 7-13: Velocity profile of region *iv* of an isodense Newtonian fluid ($\hat{\mu}$=0.001 Pa.s) displacing fluid *g* (Table 7-4) for $\hat{V}_0$=100 mm/s (◊); Analytical solution of a fully developed laminar flow of fluid *g* in a pipe of diameter $\hat{D}$ derived by Soto and Shah (1976) [63] for $\hat{V}_0$=100 mm/s (continuous line).

7.5
Fluid displacement of Yield Stress Fluid

The displacement of a yield stress fluid by a low viscosity Newtonian fluid ($\hat{\mu}$ = 0.001Pa.s) is characterized by a clear interface between the two fluids. Besides, a residual layer is formed after the front passage. At the tube inlet, the Newtonian fluid is injected with mean velocity equal to $\hat{V}_0$. Regardless of the residual layer formed, due to mass conservation, the same mean velocity is achieved at outlet.

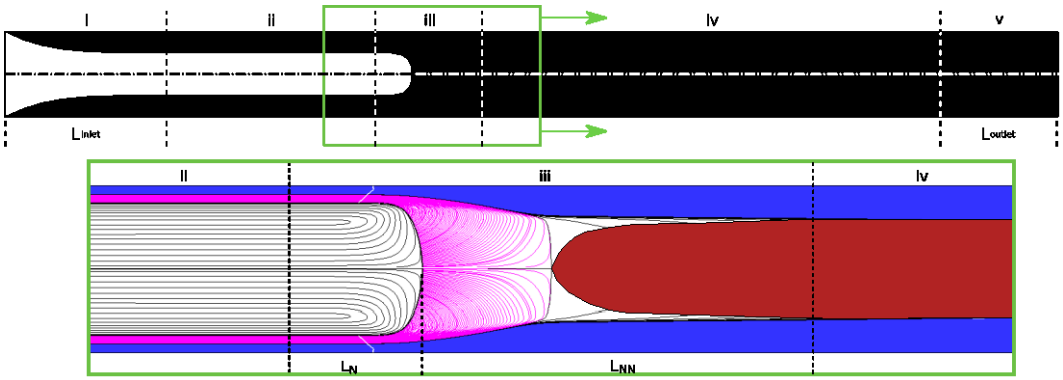

Figure 7-14: Schematic of yield stress fluid displacement by a less viscous Newtonian fluid in the *isodense* limit.

Figure 7-14 shows a schematic of the yield stress fluid displacement, mapped in five regions, as described below:

i. Inlet influence - flow development entrance region;
ii. Fluid 1 steady state solution - fluid 1 flowing in a reduced diameter pipe ($\hat{d} = \hat{D} - 2\hat{h}$), due to the formation of the residual layer;
iii. Displacing front region - region where the velocity profile is influenced by the front region containing both fluids 1 and 2;
iv. Fluid 2 steady state solution- fluid 2 flowing in a pipe of diameter $\hat{D}$, which is a typical plug-type profile for viscoplastic fluids;
v. Outlet region - flow under the influence of the outlet boundary.

Fully development of yield stress fluid flow is achieved far away from the entrance ($L_C >> L_{inlet}$) and for long tubes to avoid the outlet influence. Besides L_{inlet} and L_{outlet}, two other characteristic lengths related to the front influence must be considered: one related to the Newtonian fluid (L_N) and the other to the non-Newtonian fluid (L_{NN}). They are measured in the center (symmetric) line considering the finger tip as a reference point (x_f). L_N and L_{NN} define the limits between the regions *ii* and *iii* and *iii* and *iv*, respectively. As the front of fluid 1 moves along the pipe, the length of region *ii* increases and the length of region *iv* decreases. The region *iii* length is constant when the flow is fully developed.

All the characteristic lengths of the fluid displacement (L_{inlet}, L_{outlet}, L_N and L_{NN}) are influenced by the rheological properties of the two fluids involved, tube geometry and inlet mean velocity. The numerical simulations that consider steady state velocity profiles at entrance and outlet as boundary conditions should take into account the characteristics lengths L_N and L_{NN}.

For a better understanding of the fluid dynamics of the isodense displacement of a yield stress fluid by a Newtonian fluid ($\hat{\mu}$ =0.001 Pa.s), an example of the velocity, shear rate, stress and viscosity contours is presented for fluid *i* (Table 7-4) and $\hat{V}_0$ =1mm/s. We focus our analysis in region *iii* when the flow is fully developed. The following scaling is considered:

$$\tau = \frac{\hat{\tau}}{\hat{\tau}_c}, \dot{\gamma} = \frac{\hat{\dot{\gamma}}}{\hat{\dot{\gamma}}_c}, \eta = \frac{\hat{\eta}}{\hat{\eta}_c}. \qquad 7\text{-}31$$

Here, $\hat{\eta}_c = \hat{\tau}_c/\hat{\dot{\gamma}}_c$ is the characteristic viscosity. Prior to the contours results, a streamline analysis is presented.

7.5.1
Streamlines analysis

The analysis of both fluids streamlines is a good way to understand what is happening when the displacement flow is fully developed in region *iii*. Figure 7-5 shows the streamlines in region *iii* of the isodense displacement of fluid *i* (Table 7-4) by a Newtonian fluid with $\hat{\mu}$ =0.0001 Pa.s for $\hat{V}_0$=1mm/s.

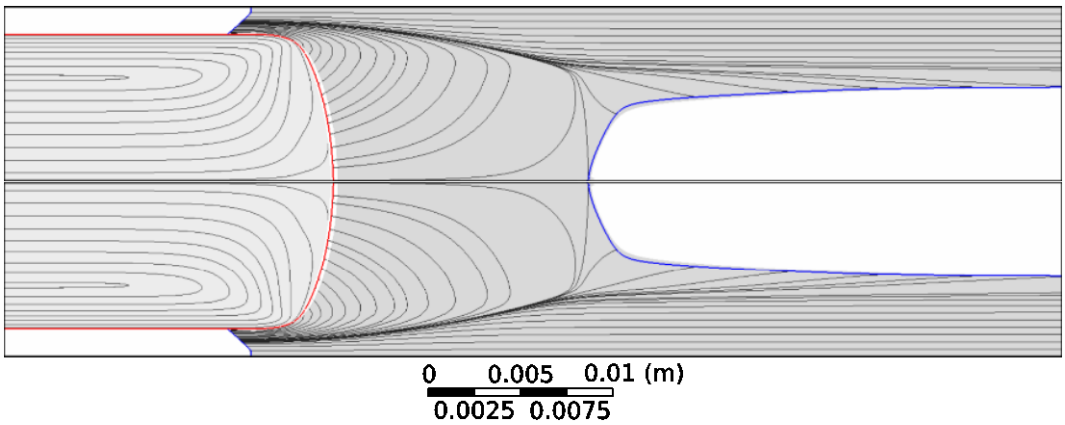

Figure 7-15: Streamlines in region *iii* of an isodense displacement of fluid *i* (Table 7-4) by a Newtonian fluid ($\hat{\mu}$=0.0001 Pa.s) for $\hat{V}_0$=0=1mm/s: Newtonian fluid area (light gray); non-Newtonian fluid area: unyielded zone (white area) and yielded zone (dark gray); interface (red line); yielded/ unyielded limit (blue line); streamlines (black line). The bar scale is presented in the bottom.

The streamline analysis considered:

1. No diffusion between the two fluids;
2. The presence of an interface that segregates the two fluids;
3. A mixed approach for streamline calculation: one for the Newtonian fluid area (front velocity as reference) and other for the non-Newtonian fluid area (plug velocity as reference);
4. Fully developed flow, no influence of tube entrance and outlet.

In region *ii*, the streamlines are horizontal. In region *iii*, as the Newtonian fluid approaches the front, it recirculates from the center to the tube walls constrained by the two fluids interface, i.e. relative to the front velocity. Fluid close to the pipe center line is moving faster than the front upstream and is pushed to the wall in region *iii*.

For the non-Newtonian fluid, a different reference velocity is considered. Instead of the front velocity, the plug velocity (V_{plug}) is applied. In this approach the plug is at rest, the wall is moving at - V_{plug} toward the inlet direction and the

interface is moving to the outlet direction at V-V_{plug} . We divided region *iii* into six zones:

- Zone 1 - Non-Newtonian fluid recirculation;
- Zone 2 - Plug deconstruction;
- Zone 3 - Wall influence area;
- Zone 4 - Residual layer;
- Zone 5 - Plug flow;
- Zone 6 - Newtonian fluid recirculation.

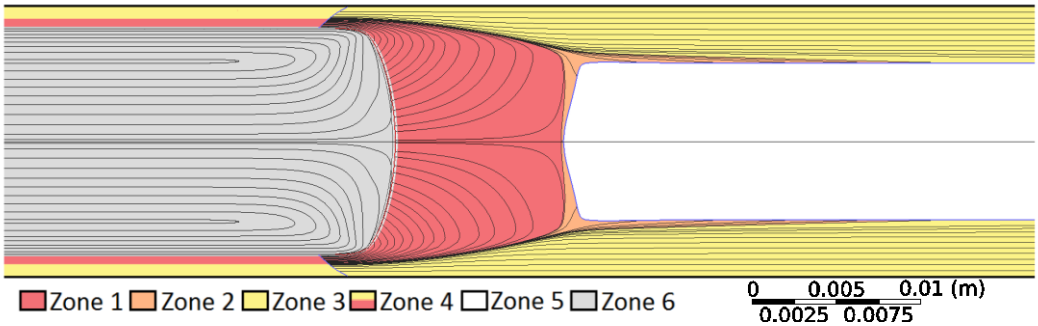

Figure 7-16: Schematic of yield stress fluid *i* (Table 7-4) displaced by an isodense Newtonian fluid ($\hat{\mu}$=0.0001 Pa.s) in region *iii* based on the streamline analysis: non-Newtonian fluid recirculation (Zone 1); plug deconstruction (Zone 2); wall influence area (Zone 3); residual layer (Zone 4); Plug flow (Zone 5); Newtonian fluid recirculation (Zone 6); streamlines (black lines). The zone mapping and scale bars are presented in the bottom.

The zone mapping in region *iii* is shown in figure 7-16. Zones 1, 2 and 3 contribute to the residual layer formation. The residual layer contribution of each zone is marked by the zone color and number, i.e, red for Zone 1 (H_1), orange for Zone 2 (H_2), and yellow for Zone 3 (H_3).

Zone 2 shows the plug being destroyed and moving toward the wall. Zone 3 represents the fluid that moves near the wall and is affected by the front influence as it gets closer to it. All three zones (1, 2 and 3) represent yielded fluid areas. On the other hand, zones 4 and 5 are related to unyielded fluid areas.

One important point to be addressed is how to define a plug numerically. The definition of a yield stress fluid says that below the yield stress the rate of deformation is zero or negligible (solid like behavior). Beyond the yield stress the viscous behavior takes place and the fluid begins to deform continuously. Below the yield stress, the material is modelled as a fluid with very high viscosity and a regularization method is applied to allow a smooth transition near the yield stress from the high viscosity plateau to the shear-thinning behavior. The same critical

shear rate applied to the regularization model ($\hat{\dot{\gamma}}_c^F$) described in section 7.2.6 is used to define the plug limits. Therefore, zones 4 and 5 represent the fluid that flows under this critical value.

7.5.2
Velocity Contour

Figure 7-17 shows the dimensionless velocity contours for the displacement of fluid *i* (Table 7-4) by the isodense Newtonian fluid ($\hat{\mu}$ =0.001 Pa.s), for $\hat{V}_0$=1mm/s. In the Newtonian fluid area, the maximum velocity $V_{max}^N = \frac{2}{(1-h)^2}$ is achieved at the center line, in the transition between regions *ii* and *iii*. Since the front moves at lower velocity V_f, as the fluid approaches the front, its direction is disturbed by the interface proximity.

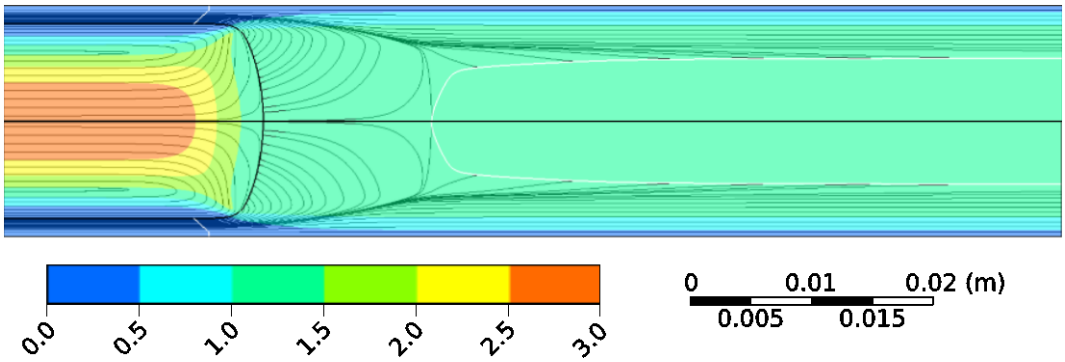

Figure 7-17: Dimensionless velocity contour of fluid *i* (Table 7-4) displaced by an isodense Newtonian fluid ($\hat{\mu}$=0.001 Pa.s) for $\hat{V}_0$=1mm/s: unyielded/yielded limit (white line); streamlines (black lines). The color and scale bars are presented in the bottom.

The front velocity defines the maximum velocity in the non-Newtonian fluid area ($V_{max}^{NN} = V_f$). As the non-Newtonian fluid moves along the center line, its velocity decreases and the influence of the plug is detected by the change on the velocity direction. The fluid tends to the walls contributing to the residual layer formation.

7.5.3
Shear Rate Contour

Figure 7-18 shows the dimensionless shear rate contour for the displacement of fluid *i* (Table 7-4) by the Newtonian fluid ($\hat{\mu}$=0.001 Pa.s) for $\hat{V}_0$=1mm/s. In

region *ii*, the shear rate is null ($\hat{\dot{\gamma}} < \hat{\dot{\gamma}}_c^F$) in the residual layer, while it varies linearly in the Newtonian fluid area. In region *iv*, the opposite occurs; the shear rate is null at the center (plug zone) and increases in the wall direction, reaching its maximum value close to the wall.

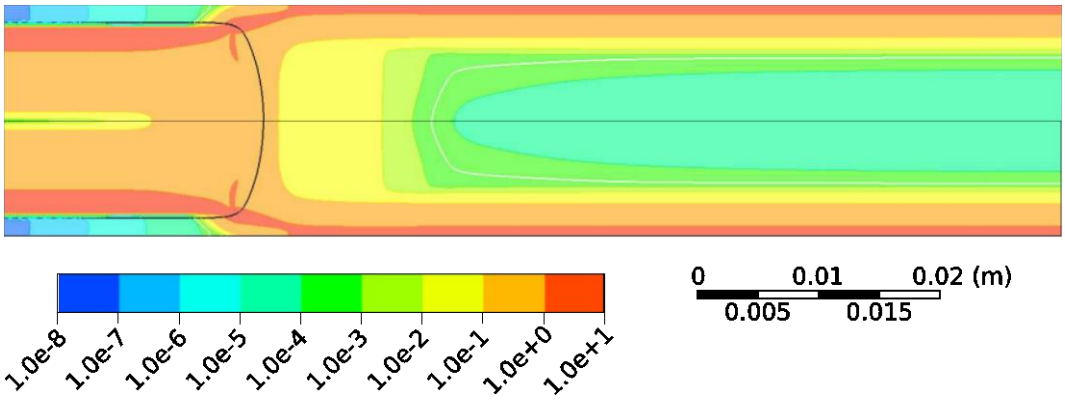

Figure 7-18: Dimensionless shear rate contour for the displacement of fluid *i* (Table 7-4) by the isodense Newtonian fluid ($\hat{\mu}$=0.001 Pa.s) for $\hat{V}_0$=1mm/s: unyielded zone limit (white line); interface (black line). The color and scale bars are presented in the bottom.

The front interface seems to affect the shear rate distribution in region *iii*. In the non-Newtonian fluid area, higher shear rates are expected near the interface and the tube walls, away from the yielded/unyielded limit in the outlet direction. Away from the front and walls, the shear rate decreases, allowing the plug and residual layer formations.

7.5.4
Viscosity Contour

Figure 7-19 shows the dimensionless viscosity contours for the displacement of fluid *i* (Table 7-4) by the isodense Newtonian fluid ($\hat{\mu}$=0.001 Pa.s), for $\hat{V}_0$=1mm/s. The viscosity contours show very clearly the residual layer and plug transition by the abruptly color change near the unyielded/yielded limit. The low viscosity of the non-Newtonian fluid area is located at the interface and near the tube walls, away from the yielded/unyielded limit in the outlet direction.

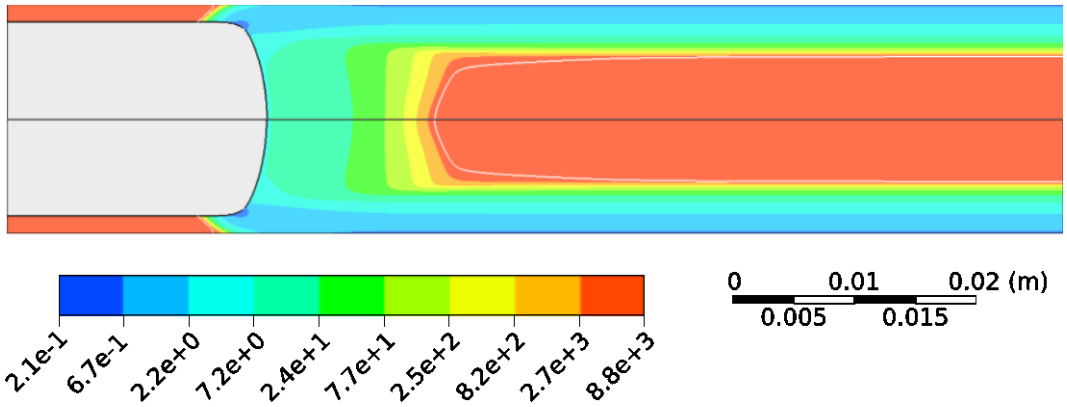

Figure 7-19: Dimensionless viscosity contour for the displacement of fluid *i* (Table 7-4) by the isodense Newtonian fluid ($\hat{\mu}$=0.001 Pa.s), for $\hat{V}_0$=1mm/s: unyielded zone limit (white line); interface (black line); Newtonian fluid (gray area). The color and scale bars are presented in the bottom.

7.5.5
Stress Contour

Figure 7-20 presents the dimensionless stress contours in the non-Newtonian area of region *iii* for the displacement of fluid *i* (Table 7-4) for $\hat{V}_0$=1mm/s by a Newtonian fluid ($\hat{\mu}$=0.001 Pa.s).

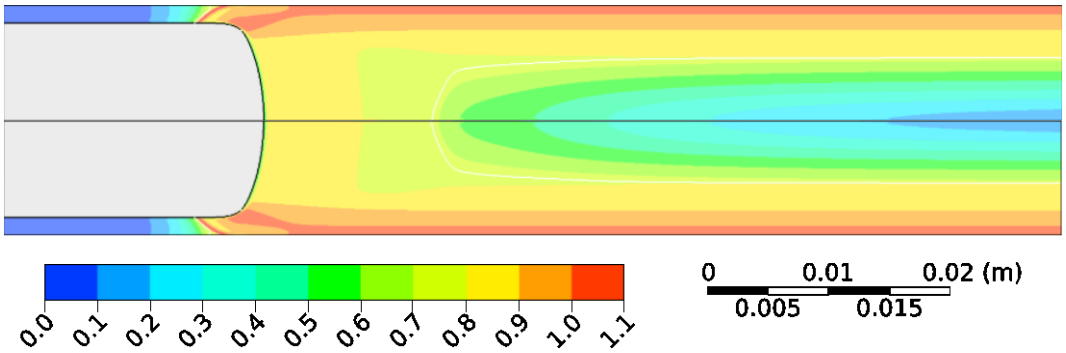

Figure 7-20: Dimensionless stress contour for the displacement of fluid *i* (Table 7-4) by the isodense Newtonian fluid ($\hat{\mu}$=0.001 Pa.s) for $\hat{V}_0$=1mm/s: unyielded limit (white line); interface (black line); Newtonian fluid (gray area); The color bar and scale are presented in the bottom.

In regions *ii* and *iv* the stress varies linearly in both fluids, as expected for circular pipes. The higher stress regions mimic the position of the higher shear rates and the low viscosities regions on the interface and near the tube walls away from the yielded/unyielded limit in the outlet direction. A numerical perturbation is observed in the stress contours at the transition region between yielded and unyielded zones, as will be explained in the next section.

7.6
Influence of the mean velocity in the yield stress displacement

Next sections will graphically present a set of numerical results of an isodense Newtonian fluid ($\hat{\mu}$=0.001 Pa.s) displacing fluid *b* (Table 7-4), for different flow rates. These simulations considered $\hat{V}_0$ equal to 0.1, 1, 10, 30, 50, 80, 100 mm/s. The displacement dynamics and evolution are shown and analyzed. Fluid *b* (Table 7-4) is chosen due to the large number of experimental data points with similar rheological properties of both displaced and displacing fluids.

7.6.1
Streamlines

Figure 7-21 presents the streamlines for different flow rates. Based on the streamline analysis it is possible to visualize that the residual layer is formed mainly by two different mechanisms: non-Newtonian fluid recirculation and non-Newtonian flow near the wall. Both mechanisms help to deconstruct the plug and contribute to the residual layer formation.

The non-Newtonian fluid recirculation represents the fluid over the influence of the front (high velocity) that changes its direction due to the plug ($V_{plug}<V_f$) and moves toward the wall. After the front passage, the fluid stops moving. In the other mechanism, the fluid that is moving toward the outlet close to the wall stops moving after the front passage. In both cases, the front and the wall play important but different roles in each fluid dynamics. In the end, the residual layer is formed, mainly by two different shear histories: the outer part of residual layer (close to the tube center) comes from upstream plug and the inner part from the fluid that was flowing near the wall. From the streamline analysis, we can conclude:

1. In the Newtonian fluid area, as the mean velocity decreases, the fluid recirculation moves toward the front;
2. In the non-Newtonian area, as the mean velocity decreases, the plug approaches the front;
3. As the mean velocity decreases, the shape of the front (bubble nose) becomes flat.

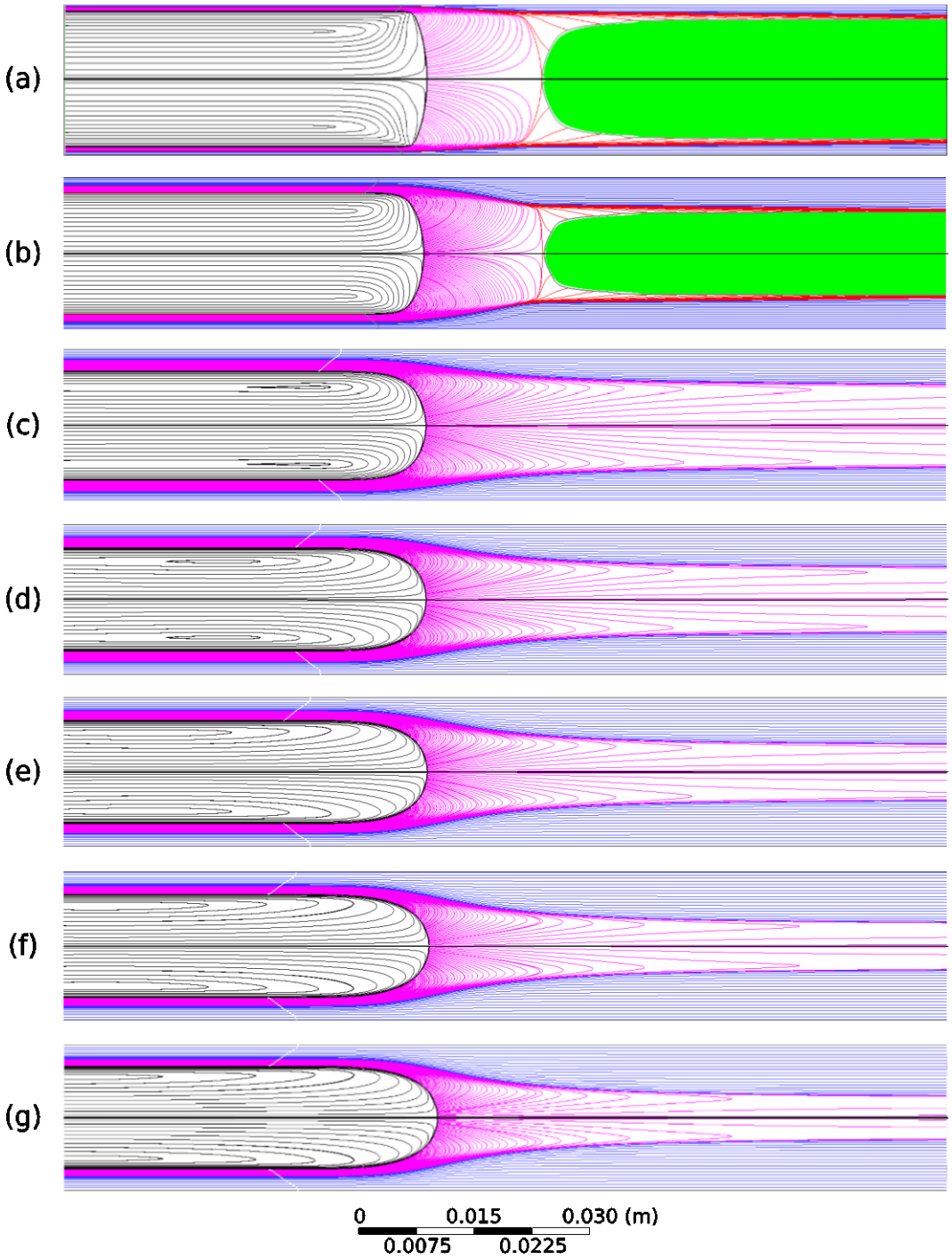

Figure 7-21: Streamlines of the isodense Newtonian fluid ($\hat{\mu}$=0.001 Pa.s) displacing fluid *b* (Table 7-4) for different flow rates: a) Re=3.7e-5; B=7.90 and M=5725 ($\hat{V}_0$=0.1 mm/s); b) Re=2.9e-3; B=2.28 and M=1985 ($\hat{V}_0$=1 mm/s); c) Re=1.7e-1; B=0.66 and M=688 ($\hat{V}_0$=10 mm/s); d) Re=1.0; B=0.36 and M=415 ($\hat{V}_0$=30 mm/s); e) Re=2.3; B=0.28 and M=328 ($\hat{V}_0$=50 mm/s); f) Re=4.7; B=0.21 and M=264 ($\hat{V}_0$=80 mm/s); g) Re=6.7; B=0.19 and M=237 ($\hat{V}_0$=100 mm/s). Newtonian fluid recirculation streamlines (black line); non-Newtonian fluid recirculation streamlines (magenta line); wall influence streamlines (blue line); plug deconstruction streamlines (red line) and plug (green area). The scale bar is presented in the bottom.

We can assume that the plug acts like a static wall moving toward the front with increasing radius as mean inlet velocity decreases. In this case two limits can be considered:

- Limit 1: The plug is far away from the front with degenerated radius (r_{plug}=0). It represents the displacement with no influence of the plug, for instance, a Newtonian-Newtonian isodense fluid displacement, where the bubble nose has smooth and round interface;
- Limit 2: The wall is near the front with the same radius of the tube (r_{plug}=1) where mean, front and plug velocities are equal (V_f=V_{plug}=1) and the bubble nose is completely flat.

From limit 1 to 2, the bubble nose (interface) changes from a round (smooth) to square corner like shape. Figure 7-22 shows the interface (bubble) evolution from low to high inlet velocities. It is important to point out that as V_f approaches V_{plug} (Limit 2), m_2 tends to m_3.

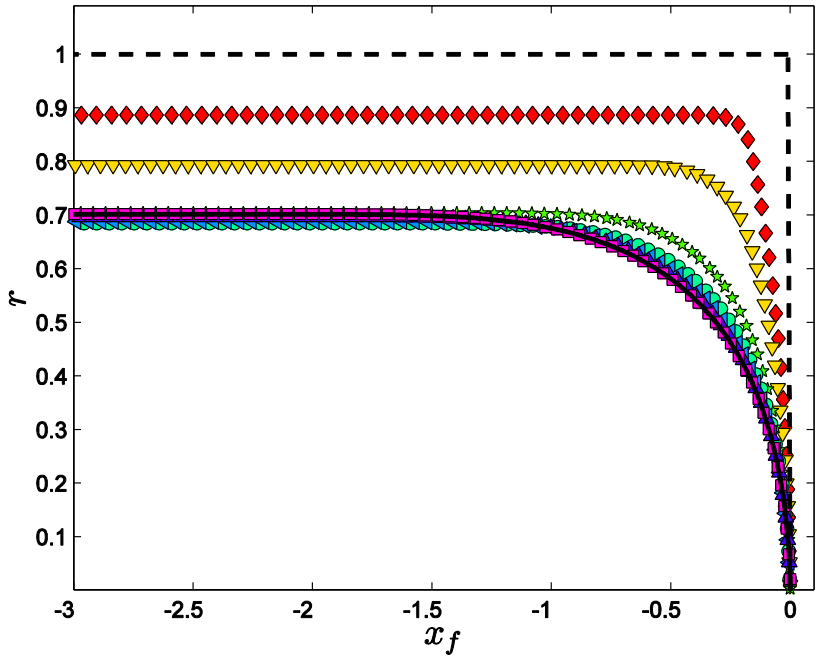

Figure 7-22: Interface profile for the displacement of fluid *b* (Table 7-4) by an isodense Newtonian fluid ($\hat{\mu}$=0.001Pa.s): $\hat{V}_0$=0.1 mm/s (◊); $\hat{V}_0$=1 mm/s (▼); $\hat{V}_0$=10 mm/s (*); $\hat{V}_0$=30 mm/s (○); $\hat{V}_0$=50 mm/s (◄); $\hat{V}_0$=80 mm/s (▲); $\hat{V}_0$=100 mm/s (□). Illustration of Limit 1 (continuous line) and Limit 2 (dashed line).

7.6.2
Velocity contour for different flow rates

In this section we present how the dimensionless velocity contour is influenced by the flow rate in a yield stress fluid displacement. The dimensionless velocity contour for fluid *b* (Table 7-4) displacement is presented in figure 7-23.

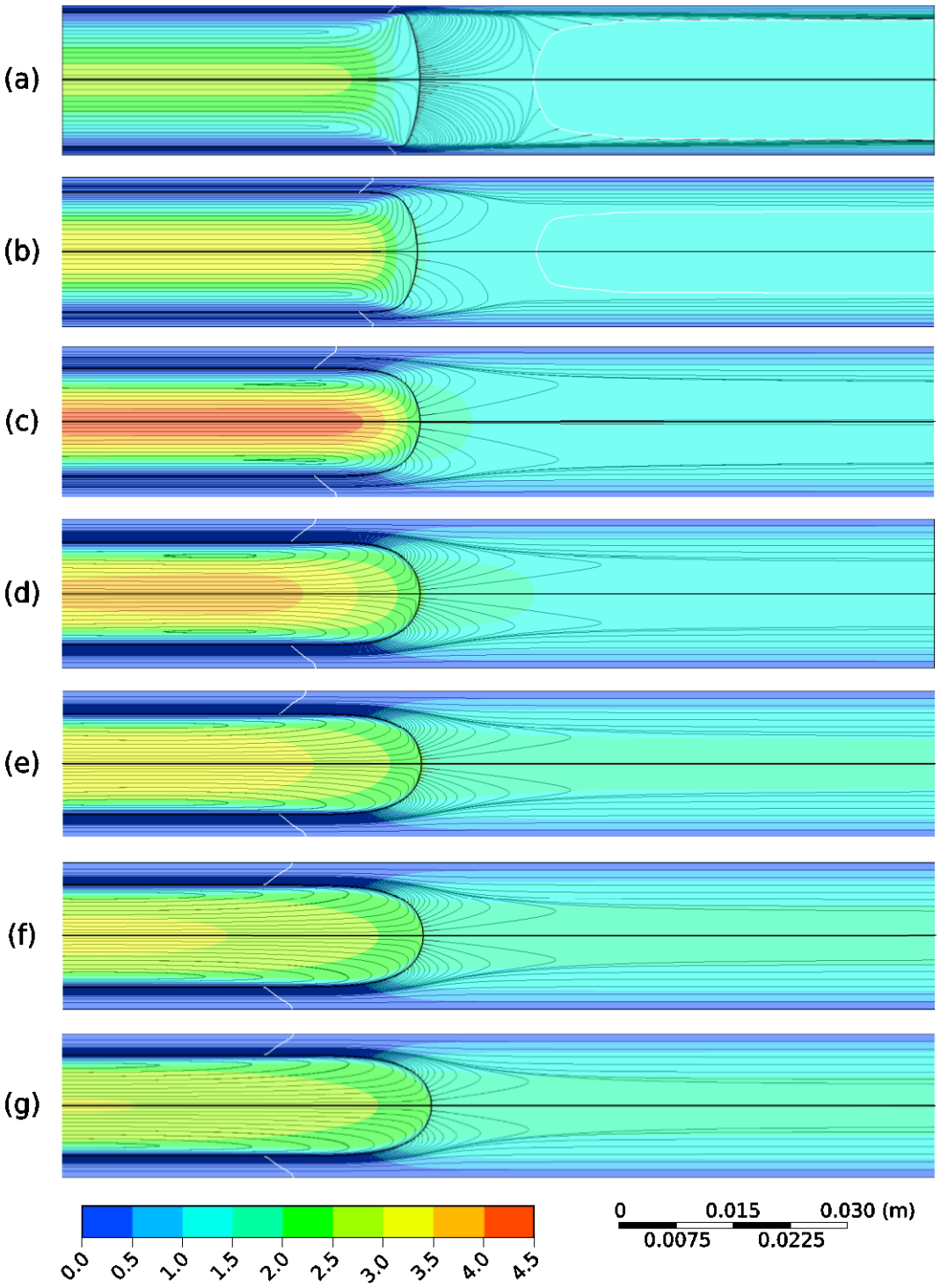

Figure 7-23: Dimensionless velocity contour of an isodense Newtonian fluid with $\hat{\mu}$=0.001 Pa.s displacing fluid *b* (Table 7-4) for different flow rates: a) Re=3.7e-5; B=7.90 and M=5725 ($\hat{V}_0$=0.1 mm/s); b) Re=2.9e-3; B=2.28 and M=1985 ($\hat{V}_0$=1 mm/s); c) Re=1.7e-1; B=0.66 and M=688 ($\hat{V}_0$=10 mm/s); d) Re=1.0; B=0.36 and M=415 ($\hat{V}_0$=30 mm/s); e) Re=2.3; B=0.28 and M=328 ($\hat{V}_0$=50 mm/s); f) Re=4.7; B=0.21 and M=264 ($\hat{V}_0$=80 mm/s); g) Re=6.7; B=0.19 and M=237 ($\hat{V}_0$=100 mm/s); streamlines (black line); unyielded zone limit (white line); The color and scale bars are presented in the bottom.

Since the front velocity is lower than the maximum velocity in the Newtonian area, as the displaced fluid approaches the front it deviates to the walls. As the inlet velocity decreases, the maximum velocity area approaches the front. Besides, for

very low velocities ($\hat{V}_0$=0.1 and 1 mm/s), it is possible to identify a change in the velocity contours near the bubble edge (interface).

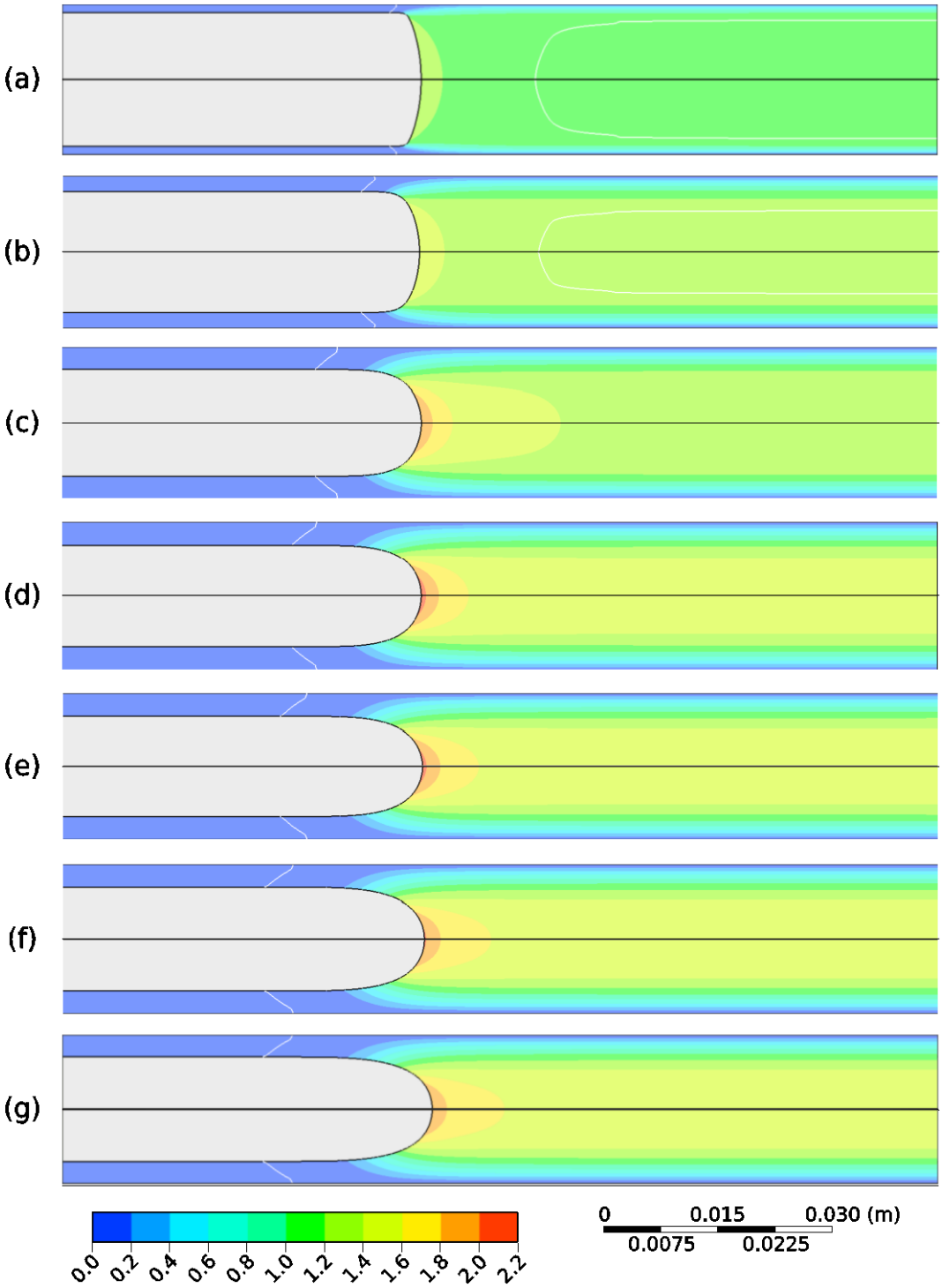

Figure 7-24: Dimensionless velocity contour in the non-Newtonian area of an isodense Newtonian fluid ($\hat{\mu}$=0.001Pa.s) displacing fluid *b* (Table 7-4) for different flow rates: a) Re=3.7e-5; B=7.90 and M=5725 ($\hat{V}_0$=0.1 mm/s); b) Re=2.9e-3; B=2.28 and M=1985 ($\hat{V}_0$=1 mm/s); c) Re=1.7e-1; B=0.66 and M=688 ($\hat{V}_0$=10 mm/s); d) Re=1.0; B=0.36 and M=415 ($\hat{V}_0$=30 mm/s); e) Re=2.3; B=0.28 and M=328 ($\hat{V}_0$=50 mm/s); f) Re=4.7; B=0.21 and M=264 ($\hat{V}_0$=80 mm/s); g) Re=6.7; B=0.19 and M=237 ($\hat{V}_0$=100 mm/s); unyielded zone limit (white line); Newtonian fluid (gray area); interface (black line). The color and scale bars are presented in the bottom.

The maximum velocity in the non-Newtonian area is located at the bubble tip as shownin figure 7-24, when the fluid moves along the symmetry line in the outlet direction, the velocity decreases until the plug velocity is achieved.

The velocity magnitude along the interface (bubble) is shown in figure 7-25. The interface length (x_i) is referenced by the tip of the bubble.

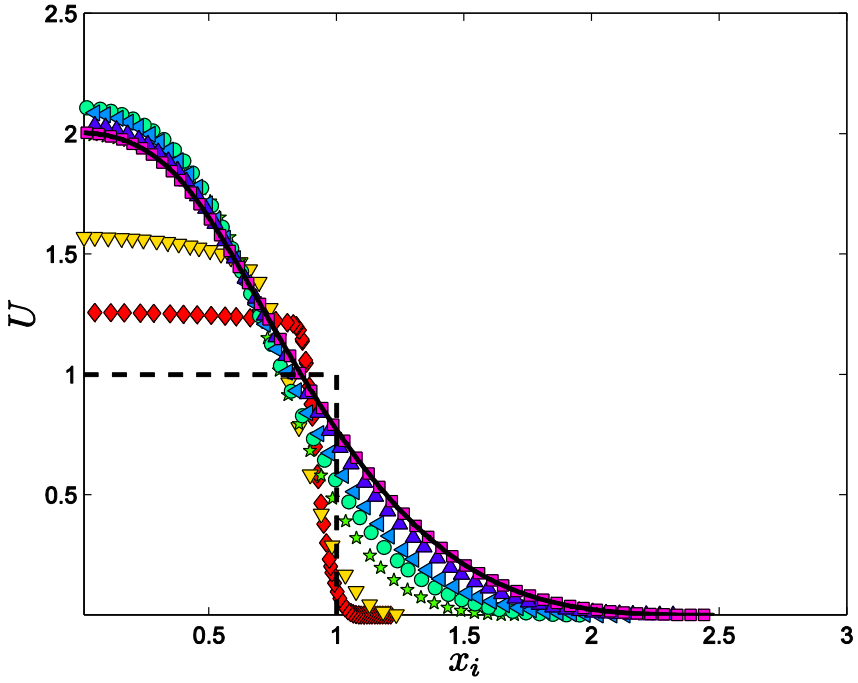

Figure 7-25: Axial velocity along the interface x_i for the displacement of fluid *b* (Table 7-4) by the isodense Newtonian fluid ($\hat{\mu}$=0.001Pa.s): $\hat{V}_0$=0.1 mm/s (◊); $\hat{V}_0$=1 mm/s (▼); $\hat{V}_0$=10 mm/s (*); $\hat{V}_0$=30 mm/s (○); $\hat{V}_0$=50 mm/s (◄); $\hat{V}_0$=80 mm/s (▲); $\hat{V}_0$=100 mm/s (□). Illustration of Limit 1 (continuous line) and Limit 2 (dashed line).

It can be observed that the velocity decays along the interface x_i. As the inlet velocity decreases, the unyielded zone limit approaches x_i=1 and U(x_i=0) tends to 1.

7.6.3
Shear Rate Contours

The dimensionless shear rate contours for fluid *b* (Table 7-4) displacement for different flow rates are presented in the figure 7-26. For high flow rates ($\hat{V}_0$>50mm/s) the maximum shear rate occurs in the Newtonian area near the interface. The shear rate contours are very similar for $\hat{V}_0$=80mm/s and $\hat{V}_0$=100mm/s, but as the velocity decreases, the shear rate contours start to change in both areas.

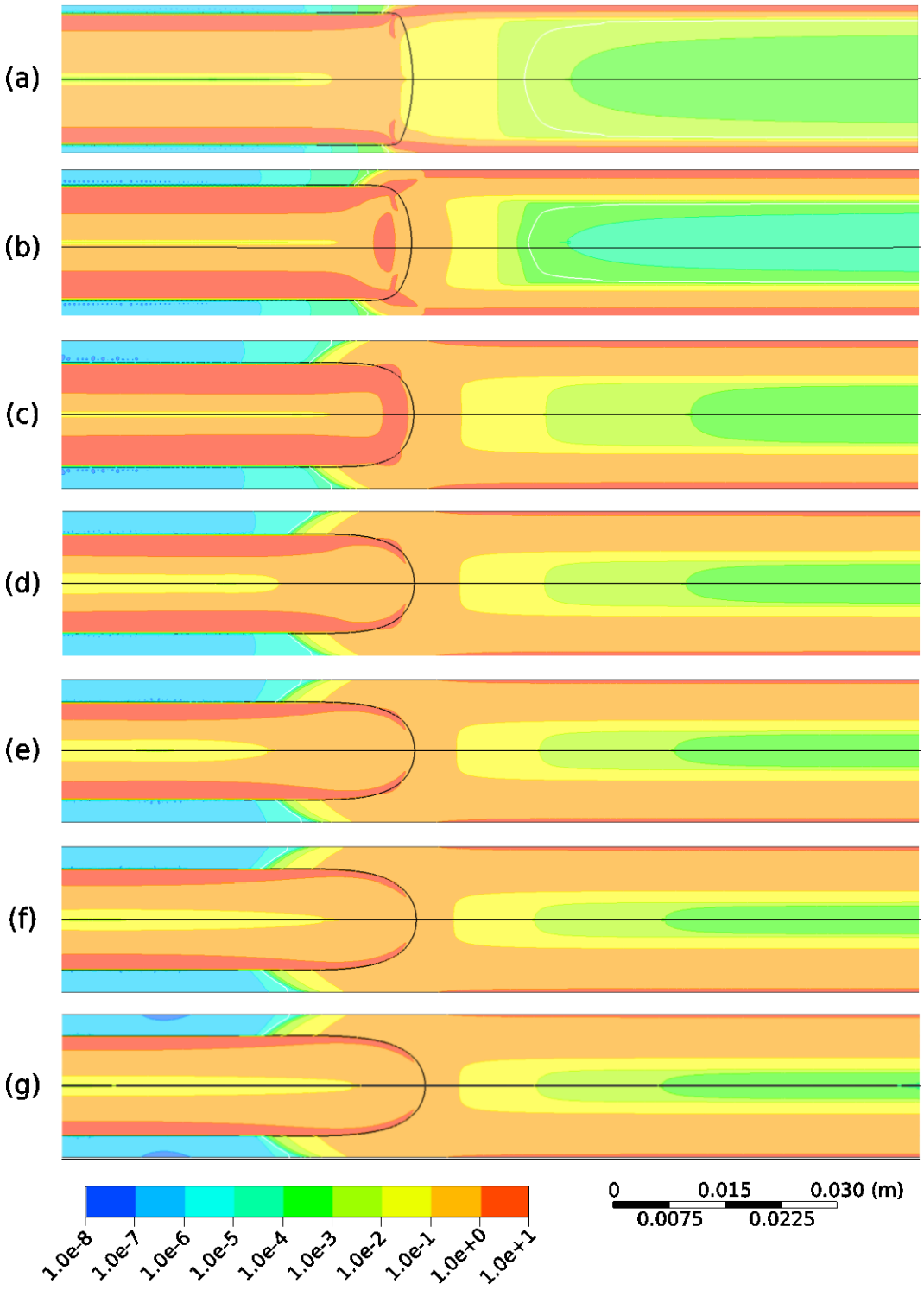

Figure 7-26: Dimensionless shear rate contours for the displacement of fluid *b* (Table 7-4) by an isodense Newtonian fluid ($\hat{\mu}$=0.001Pa.s) for different flow rates: a) Re=3.7e-5; B=7.90 and M=5725 ($\hat{V}_0$=0.1 mm/s); b) Re=2.9e-3; B=2.28 and M=1985 ($\hat{V}_0$=1 mm/s); c) Re=1.7e-1; B=0.66 and M=688 ($\hat{V}_0$=10 mm/s); d) Re=1.0; B=0.36 and M=415 ($\hat{V}_0$=30 mm/s); e) Re=2.3; B=0.28 and M=328 ($\hat{V}_0$=50 mm/s); f) Re=4.7; B=0.21 and M=264 ($\hat{V}_0$=80 mm/s); g) Re=6.7; B=0.19 and M=237 ($\hat{V}_0$=100 mm/s); unyielded zone limit (white line); interface (black line).The color and scale bars are presented in the bottom.

In the Newtonian area the high shear rate area approaches the tip of the bubble. In the non-Newtonian area, on the bubble edges, the shear rates achieves

the same order of magnitude of the wall shear. When the mean inlet velocity reaches its minimum value, the maximum shear rate gets concentrated at the bubble corner where the velocity at interface changes abruptly. The dimensionless shear rate along the interface is shown in figure 7-27, it can be observed that:

1. The shear rate at the interface is lower than the shear rate at wall along all the interface for higher flow rates (inlet mean velocity higher than 80mm/s);
2. Near the tip (x_i < 0.5) the shear rate is lower than the shear rate at the wall;
3. The shear rate increases from the bubble tip until its maximum is achieved and starts to decrease, for all inlet velocities;
4. The highest shear rate peak is related to the minimum inlet velocity;
5. The same shear rate is obtained for all inlet velocities at x_i=1.

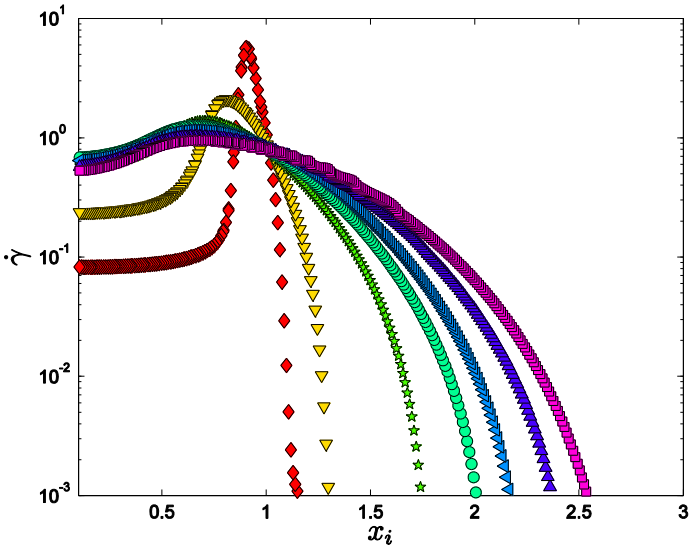

Figure 7-27: Dimensionless shear rate distribution along the interface x_i for the displacement of fluid *b* (Table 7-4) by an isodense Newtonian fluid ($\hat{\mu}$=0.001Pa.s): $\hat{V}_0$=0.1 mm/s (◊); $\hat{V}_0$=1 mm/s (▼); $\hat{V}_0$=10 mm/s (*); $\hat{V}_0$=30 mm/s (○); $\hat{V}_0$=50 mm/s (◄); $\hat{V}_0$=80 mm/s (▲); $\hat{V}_0$=100 mm/s (□).

7.6.4
Viscosity Contours

The dimensionless viscosity contours in the non-Newtonian area for fluid *b* (Table 7-4) displacement is presented in figure 7-28. The residual layer formation and the plug deconstruction are characterized by the intense color variation. It is clear that as the velocity decreases, the plug approaches the bubble nose.

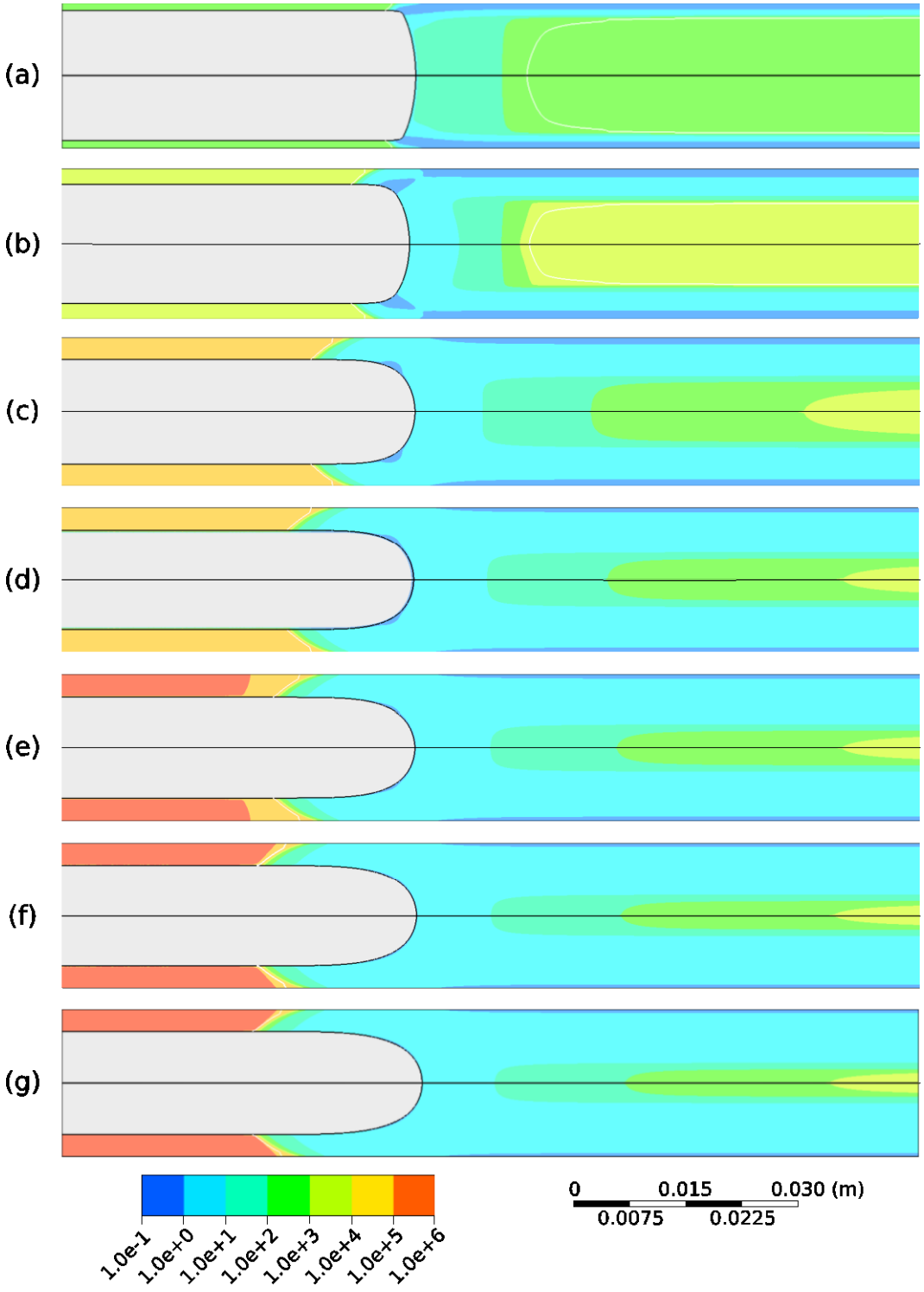

Figure 7-28: Dimensionless viscosity contours for the displacement of fluid *b* (Table 7-4) by an isodense Newtonian fluid ($\hat{\mu}$=0.001Pa.s) for different flow rates: a) Re=3.7e-5; B=7.90 and M=5725 ($\hat{V}_0$=0.1 mm/s); b) Re=2.9e-3; B=2.28 and M=1985 ($\hat{V}_0$=1 mm/s); c) Re=1.7e-1; B=0.66 and M=688 ($\hat{V}_0$=10 mm/s); d) Re=1.0; B=0.36 and M=415 ($\hat{V}_0$=30 mm/s); e) Re=2.3; B=0.28 and M=328 ($\hat{V}_0$=50 mm/s); f) Re=4.7; B=0.21 and M=264 ($\hat{V}_0$=80 mm/s); g) Re=6.7; B=0.19 and M=237 ($\hat{V}_0$=100 mm/s);unyielded zone limit (white line); interface (black line); Newtonian fluid (gray area). The color and scale bars are presented in the bottom.

Figure 7-29 shows that the viscosity distribution along the interface behaves very similar to the shear rate distribution, but instead of reaching its maximum, the minimum viscosity is achieved. It is also possible to observe the non-Newtonian fluid regularization for low flow rates, where a constant maximum viscosity is considered.

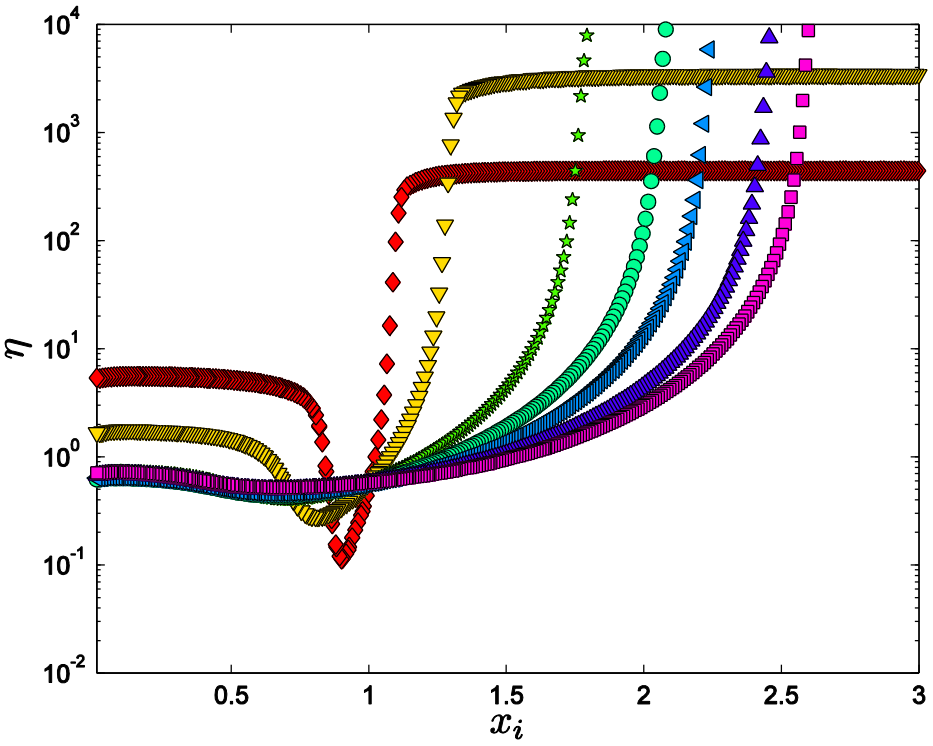

Figure 7-29: Dimensionless viscosity distribution along the interface x_i for the displacement of fluid *b* (Table 7-4) by an isodense Newtonian fluid ($\hat{\mu}$=0.001Pa.s) for different flow rates: $\hat{V}_0$=0.1 mm/s (◊); $\hat{V}_0$=1 mm/s (▼); $\hat{V}_0$=10 mm/s (*); $\hat{V}_0$=30 mm/s (○); $\hat{V}_0$=50 mm/s (◄); $\hat{V}_0$=80 mm/s (▲); $\hat{V}_0$=100 mm/s (□).

7.6.5
Stress Contours

The dimensionless stress contours in the non-Newtonian area for fluid *b* (Table 7-4) displacement is presented in figure 7-30. The dimensionless stress behavior in the Newtonian area is similar to its respective dimensionless shear rate multiplied by Newtonian fluid viscosity.

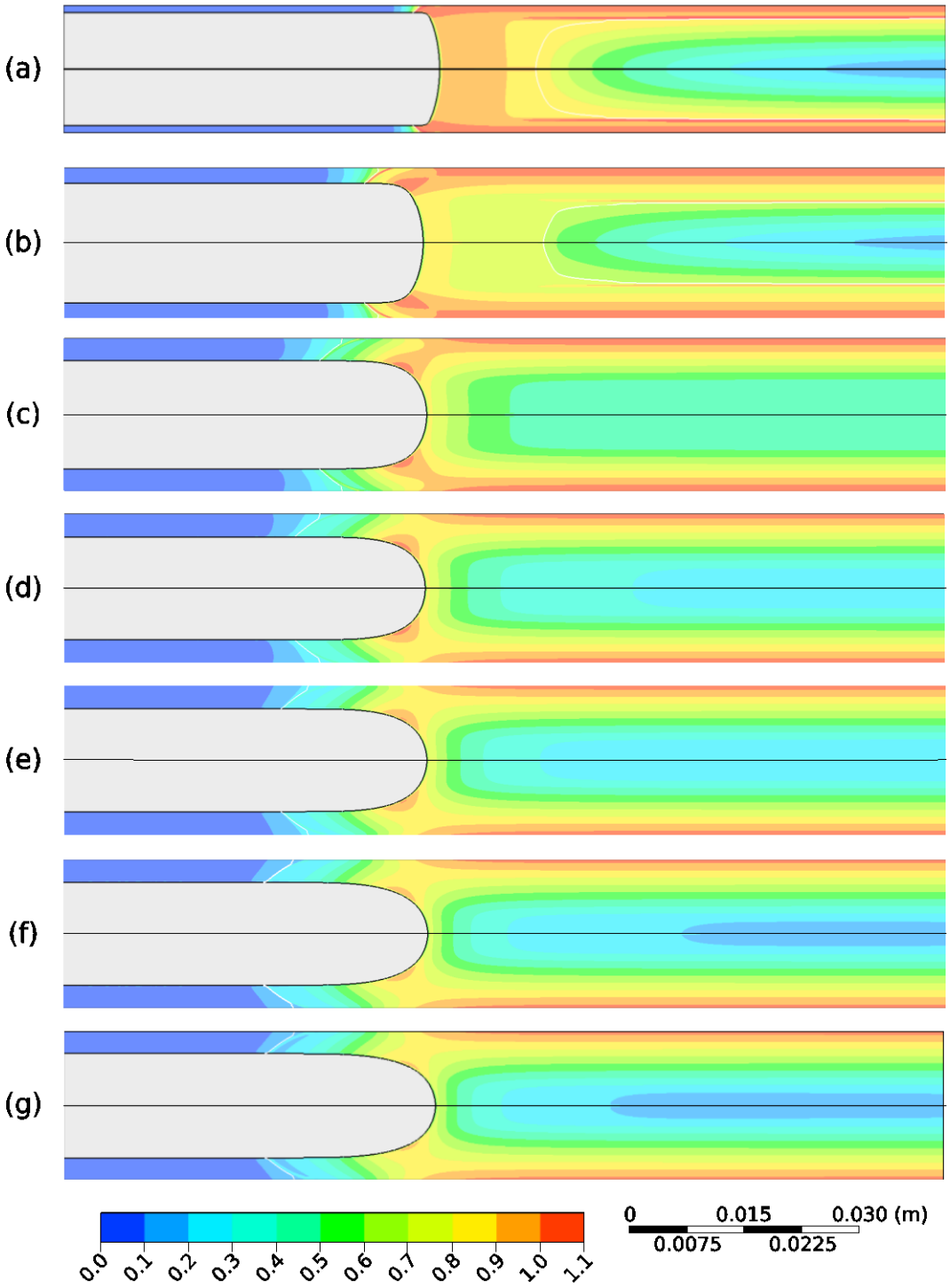

Figure 7-30: Dimensionless stress contours for the displacement of fluid *b* (Table 7-4) by an isodense Newtonian fluid ($\hat{\mu}$=0.001Pa.s) for different flow rates: a) Re=3.7e-5; B=7.90 and M=5725 ($\hat{V}_0$=0.1 mm/s); b) Re=2.9e-3; B=2.28 and M=1985 ($\hat{V}_0$=1 mm/s); c) Re=1.7e-1; B=0.66 and M=688 ($\hat{V}_0$=10 mm/s); d) Re=1.0; B=0.36 and M=415 ($\hat{V}_0$=30 mm/s); e) Re=2.3; B=0.28 and M=328 ($\hat{V}_0$=50 mm/s); f) Re=4.7; B=0.21 and M=264 ($\hat{V}_0$=80 mm/s); g) Re=6.7; B=0.19 and M=237 ($\hat{V}_0$=100 mm/s); unyielded zone limit (white line); interface (black line); Newtonian fluid (gray area). The color and scale bars are presented in the bottom.

From figure 7-30, for higher flow rates ($\hat{V}_0$>50mm/s), the stress contours seem quite the same, except by a small perturbation observed in the transition between

yielded to unyielded areas. As the inlet velocity increases, similar behavior of shear rate contour is observed. For very low velocities ($\hat{V}_0$<1mm/s), the perturbation is more prominent. The dimensionless stress along the interface is shown in figure 7-31 for different inlet velocities.

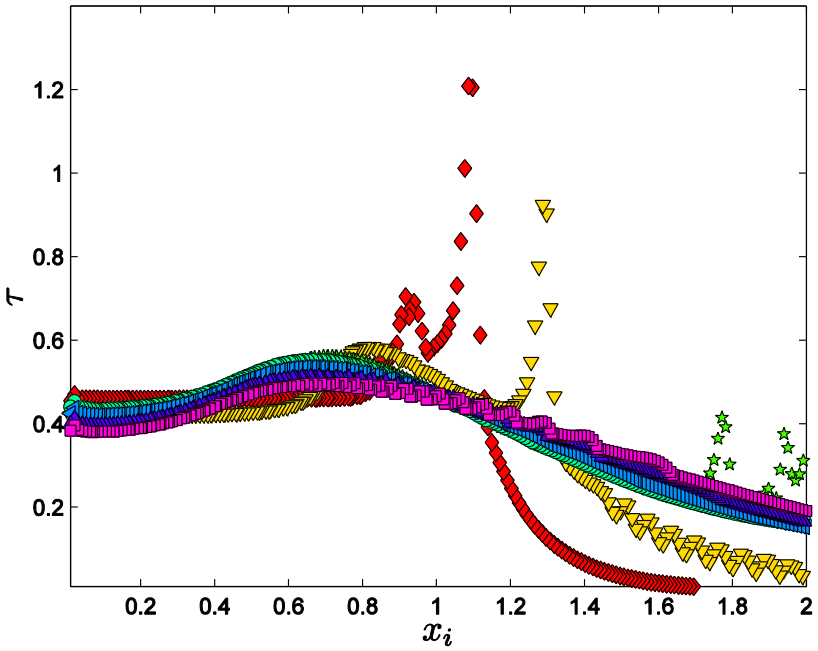

Figure 7-31: Dimensionless stress distribution along the interface x_i for the displacement of fluid *b* (Table 7-4) by an isodense Newtonian fluid ($\hat{\mu}$=0.001Pa.s) for different flow rates: $\hat{V}_0$=0.1 mm/s (◊); $\hat{V}_0$=1 mm/s (▼); $\hat{V}_0$=10 mm/s (*); $\hat{V}_0$=30 mm/s (○); $\hat{V}_0$=50 mm/s (◄); $\hat{V}_0$=80 mm/s (▲); $\hat{V}_0$=100 mm/s (□).

The numerical perturbation detected in the dimensionless stress contour and distribution along the interface is related to the regularization applied in the yield stress rheological model. It is not possible to eliminate these perturbation with the regularization model applied, even if a lower $\hat{\gamma}_c^F$ is considered. It will only move the perturbation along the interface in the inlet direction. The adjustment of the regularization parameter as the velocity decrease will subside the perturbation but not eliminate its effect.

7.6.6
Experimental versus numerical results

The numerical simulations of the displacement of fluid fluid *b* (Table 7-4) by an isodense Newtonian fluid ($\hat{\mu}$=0.001Pa.s) were not be able to get the residual layer

fluctuation detected in the experiments, even for set *B* (table 4-1) whose fluid 2 is rheological equivalent to fluid *b*. However, it is possible to identify changes in the contours and in the interface distribution of flow variables, as the Reynolds number decreases that can help to explain these fluctuations.

For high Reynolds number (Re>2.3), *smooth* type regime, in the non Newtonian fluid area, the maximum stress is located near the tube walls away from the yielded/unyielded limit in the outlet direction (figures 7-30.f and g). In the Newtonian fluid area, it is located along the interface. Since the fluid is Newtonian the shear rate contour (figures 7-26.f and g) shows the same effect.

As the Reynolds number approaches the unity value, *wavy* type regime, it is possible to observe the appearance of a stress concentration in the interface in the non-Newtonian fluid area also reflected in the shear rate (figures 7-26.d and e) and viscosity (figures 7-28.d and e) contours.

For *corrugated* type regime, as the Reynolds decreases even more (Re< 0.2), the stress along the interface becomes greater and it is possible to observe peaks of shear rate (figure 7-27 and figures 7-26.a, b and c) and minimum viscosity data points (figure 7-29 and figures 7-28.a, b and c).

The increment of the stress and shear rate along the interface, as Reynolds decreases, may be associated to the waviness detected in the yield stress fluid displacement experiments, but we were not able to reproduce the residual layer fluctuation in our numerical model.

7.7
Influence of Carbopol concentration in the Residual Layer

Numerical simulations of an isodense Newtonian fluid ($\hat{\mu}$=0.001Pa.s) displacing yield stress fluids from Table 7-4 are developed considering inlet velocities $\hat{V}_0$ from 0.1 to 100 mm/s. Due to the numerical diffusion of the volume of fluid method (VOF) applied in Fluent's simulations, all variables across the interface are related to the element's concentration *C*. All variables at the interface are presented by its mean value for C=0.5 and the error bar, by an interval of 98% of confidence (0.01<C<0.99).

In the Newtonian-Newtonian isodense fluid displacement the residual layer is independent of Reynolds number, and relies on the fluids viscosity ratio. On the

other hand, in shear thinning fluid displacement, the residual layer monotonically decreases as Reynolds number increases due to the viscosity ratio variation, where low Reynolds numbers are related to high viscosity ratios and high Reynolds numbers to low viscosity ratios. The residual layer decay rate depends on the rheological parameters of the shear thinning fluid.

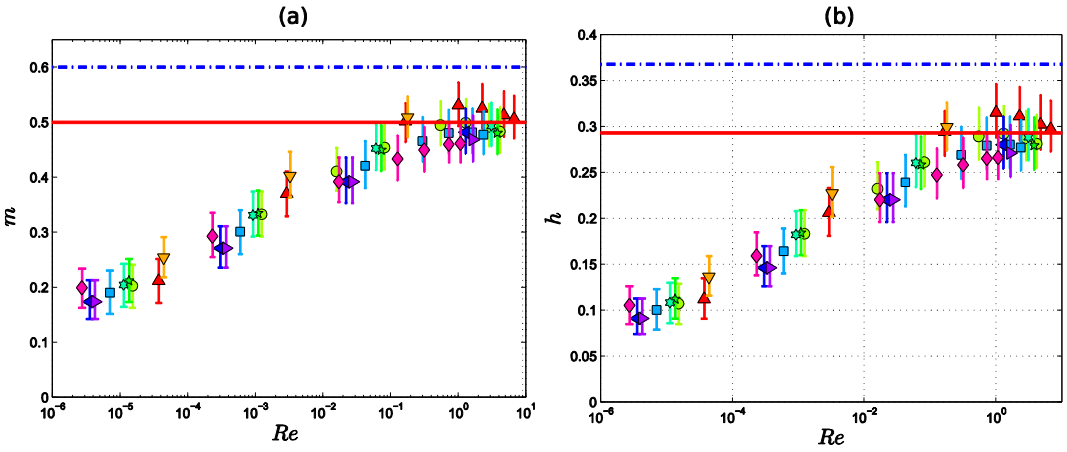

Figure 7-32: Influence of Reynolds number in the residual mass fraction (a) and in the residual layer thickness (b) for an isodense displacement of fluid: *a* (▲); *b* (▼) ; *c* (○); *d* (*); *e* (●); *f* (□); *g* (◀); *h* (▶); *i* (◊). Newtonian limits: M=1 (continuous line) and M≈0 (dashed-dotted line).

Figure 7-32 shows the influence of Reynolds number in the the residual layer thickness (h) and residual mass fraction (m) for an isodense displacement of yield stress fluids from Table 7-4 by a Newtonian fluid ($\hat{\mu}$=0.001 Pa.s). The displacement of yield stress fluids behaves differently from shear thinning fluids. Instead of decreasing, the residual layer increases as Reynolds number increases. For high Reynolds number all yield stress fluids tend to the Newtonian-Newtonian isodense fluid displacement limit for M=1. For fluid *a* (Table 7-4), the residual layer overshoots this limit and gets closer to the other Newtonian-Newtonian isodense fluid displacement limit (M≈0).

The same effect is detected in the front velocity presented in figure 7-33.a. Figure 7-33.b shows that the average concentration across the pipe ($\overline{C} = (d/2)^2$) is a function of the front velocity. In the Newtonian limits, we have $\overline{C}$=0.4 and V_f=2.5 for M=0 and $\overline{C}$=0.5 and V_f=2 for M=1. If $V_f \approx 1$ we expect $\overline{C} \approx 1$ that is equivalent to Limit 2 (d/2=1) as shown in figure 7-34.a and no residual layer is expected.

We compared the inner diameter of the displacing fluid (d) to the equivalent diameter from front velocity ($d_f/2 = \sqrt{1/V_f}$) in figure 7-34.b. As expected $d < d_f$. However for yield stress fluid this difference can be neglected and $d \approx d_f$.

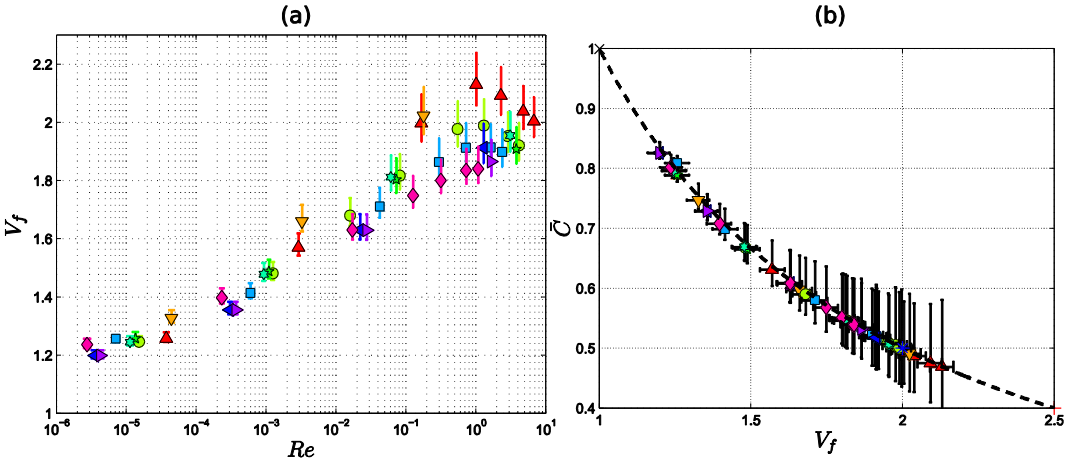

Figure 7-33: (a) Influence of Reynolds number in the front velocity for an isodense yield stress fluid displacement; (b) Relation between front velocity and concentration across the pipe. Different markers represent yield stress fluids: *a* (▲); *b* (▼); *c* (○); *d* (*); *e* (●); *f* (□); *g* (◀); *h* (▶); *i* (◊). $\hat{C}=1/V_f$ (dashed line); Newtonian limits: M=1(*) and M≈0 (+); Limit 2 (X).

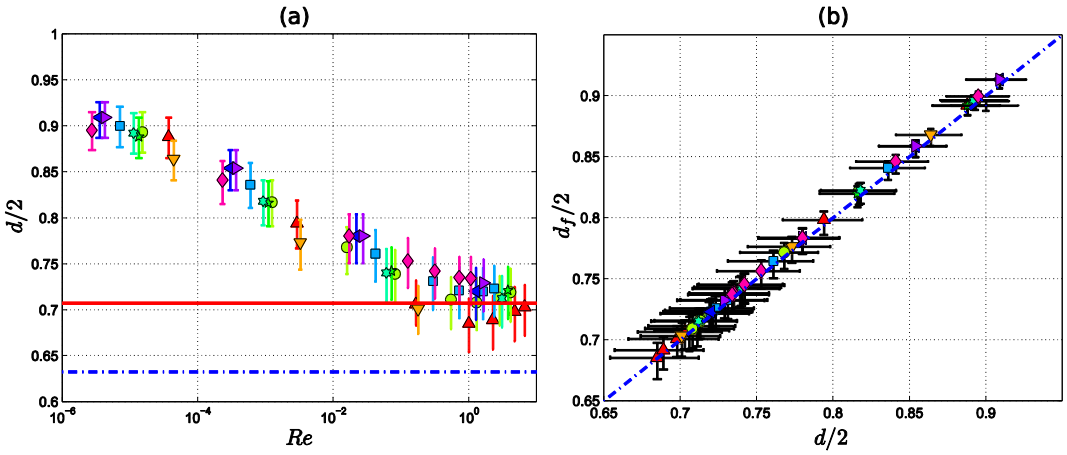

Figure 7-34: (a) Influence of Reynolds number in the displacing diameter d for an isodense yield stress fluid displacement; (b) Relation between inner diameter d and the front equivalent diameter d_f. Different markers represent yield stress fluids: *a* (▲); *b* (▼); *c* (○); *d* (*); *e* (●); *f* (□); *g* (◀); *h* (▶); *i* (◊).

7.7.1

Numerical and experimental results comparison

If we consider the inner displacing diameter to compare the numerical and experimental results, for Reynolds number in the range of 0.1 and 1, the inner diameter fluctuates between 0.7 and 0.8 in both cases. In the experiments results

(figure 4-12.b) it is not possible to observe any trend in respect to Reynolds number. In contrary, in the numerical simulations (figure 7-34.a), the influence of the rheological properties of the displaced fluid is evident. For low Reynolds numbers (Re<0.1), the numerical results diverges from the experimental ones. As Reynolds number decreases, the numerical model shows an increase of the displacing diameter. On the other hand, in the experiments, the inner diameter (d_c) decreases.

This behavior is also observed in the front velocity, but since the front velocity is inversely proportional to the displacing diameter, the opposite occurs. As Reynolds number decreases (Re<0.1), the numerical model shows that the front velocity decay (figure 7-33.a) and in the experiments, the front velocity increases (figure 4-12.a). For high Reynolds number (Re>0.1), the front velocity seems to be constant in the experiments, but it is a function of the rheological properties of the displaced fluid in the numerical results. Although the front velocity values are in the same order of magnitude, the numerical results seems to overestimate the experimental results.

7.7.2
Yield stress parametric study

We also performed a parametric study to understand the importance of yield stress in the fluid displacement simulations. We considered the same power law and consistency indexes of fluid *b* (Table 7-4), but with different yield stress with values, from 0 to 25 Pa.

The results are presented in figure 7-35 and shows the transition of shear thinning fluid behavior to a yield stress fluid behavior. The numerical results obtained with and without yield stress are very similar to Gabard and Hulin (2003) [14] experiments for Carbopol and Xanthan. When the yield stress is applied, it is possible to observe that the residual layer is always lower than the numerical results without yield stress. As the yield stress increases, the residual layer decreases for Reynolds number from 10^{-5} to 10.

As the yield stress increases, the shear thinning characteristic of the fluid is subsided. The yield stress is responsible for the residual layer behavior for low Reynolds number. It is possible to identify a smooth change in the residual layer behavior around Re=1, where the residual layer starts to mimic the same trend of

the fluid without yield stress. For Re>1, the shear thinning characteristics appears, although a small influence of the yield stress is observed due to residual layer reduction, when shear thinning displacement is considered as reference. If a Bingham fluid was considered, the residual layer would tend to the one defined by the viscosity ratio between the plastic and inlet Newtonian fluid viscosities.

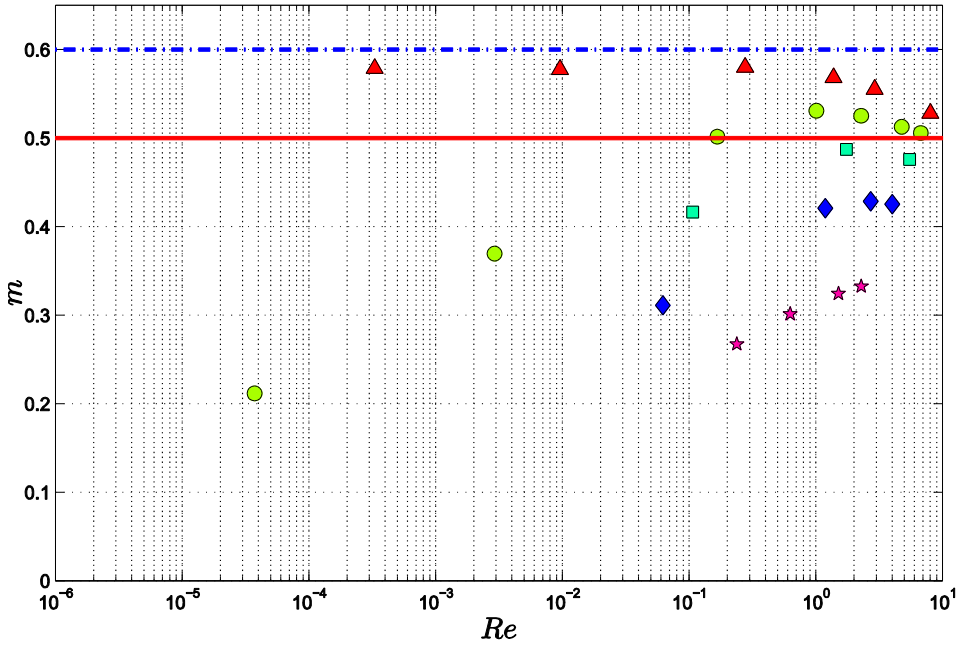

Figure 7-35: Influence of yield stress in the mass fraction of fluid *b* displacement: $\hat{\tau}_y$=0 Pa (▲); $\hat{\tau}_y$=1.9 Pa(○);$\hat{\tau}_y$=4.6 Pa (□); $\hat{\tau}_y$=10 Pa(◊);$\hat{\tau}_y$=25 Pa(*). Newtonian limit for M=1 (continuous line) and for M≈0 (dashed-dotted line).

7.8
Numerical simulation summary

In this chapter we presented the results of the numerical simulation of an isodense Newtonian fluid with low viscosity (fluid 1) displacing yield stress fluids. The same mean velocity range and rheology of the displaced and displacing fluids of the experiments from chapter 4 were considered.

The finite volume commercial software FLUENT by ANSYS was configured to solve the transport equations for a transient 2D tube geometry. The code validation procedure consisted of comparing the numerical results for different types of displaced fluids (fluid 2), i.e. Newtonian or shear thinning, with experimental and numerical data from literature. Only isodense displacement is considered. Besides, the displacing fluid in all simulations was a Newtonian fluid

with viscosity equal to $\hat{\mu}$=0.001 Pa.s. In all the displacement numerical results where an uniform residual layer was detected, five regions were mapped: inlet influence; fluid 1 steady state solution; displacing front region; fluid 2 steady state solution and outlet region.

In the case of yield stress fluids from the streamline analysis we detected that the residual layer is forged by two different mechanisms, mainly two different shear histories influenced by the front and the walls. In the end, the outer part of residual layer (close to the tube center) comes from upstream plug and the inner part from the fluid that was flowing near the wall.

In the analyses of the influence of the mean velocity in the displacing of the yield stress fluid *b* (Table 7-4), we have:

- The inlet mean velocity influences the interface format, where round edges are expected for high Reynolds numbers (Re>1) and as the Reynolds number decreases, the finger nose changes from a smooth to a square corner like shape;
- Along the interface from the bubble tip the velocity decays for any mean inlet velocity. As the mean velocity decreases, the unyielded zone limit approaches the tube radius and the front velocity tends to the mean velocity;
- It is possible to observe a peak in the shear rate (or minimum viscosity value) along the interface for low inlet velocities (1 and 0.1 mm/s) located at the bubble corner where the velocity along the interface changes abruptly;
- A numerical perturbation in the dimensionless stress contour and distribution along the interface related to the regularization rheological model of the yield stress fluid (fluid 2) was detected.

The numerical results of an isodense Newtonian fluid ($\hat{\mu}$=0.001Pa.s) displacing fluid *b* (Table 7-4) could not represent the residual layer fluctuation detected in the experiments, even for set *B* (table 4-1) whose fluid 2 is rheological equivalent to fluid *b*. However, it is possible to identify changes in the contours and in the interface distribution of flow variables as the Reynolds number decreases:

- For high Reynolds number (Re>2.3), *smooth* type regime, in the non Newtonian fluid area, the maximum stress is located near the tube

walls away from the yielded/unyielded limit in the outlet direction. In the Newtonian fluid area, it is located along the interface;

- As the Reynolds number approaches the unity value, *wavy* type regime, it is possible to observe the appearance of a stress concentration in the interface in the non-Newtonian fluid area also reflected in the shear rate and viscosity contours;
- For *corrugated* type regime, as the Reynolds decreases even more (Re< 0.2), the stress along the interface becomes greater and it is possible to observe peaks of maximum shear rate and minimum viscosity;

The increment of the stress and shear rate along the interface, as Reynolds decreases, may be associated to the waviness detected in the yield stress fluid displacement experiments but we are not able to reproduce the residual layer fluctuation in our numerical model.

The influence of the displaced fluid (fluid 2) rheology in the residual layer was study numerically and compared with the experimental results. If we consider the inner displacing diameter to compare the numerical and experimental results, for Reynolds number in the range of 0.1 and 1, the inner diameter fluctuates between 0.7 and 0.8 in both cases. In the experiments results it is not possible to observe any trend in respect to Reynolds number, in contrary, in the numerical experiments, the influence of the rheological properties of the displaced fluid is evident. For low Reynolds numbers (Re<0.1), the numerical model diverges from the experimental results, as Reynolds number decreases, the numerical model shows an increasing of the displacing diameter. On the other hand, in the experiments, the inner diameter (d_C) decreases. This behavior is also observed in the front velocity, but since the the front velocity is inversely proportional to the displacing diameter, the opposite occurs.

Finally, a parametric study to understand the importance of yield stress in the fluid displacement simulations was performed. When the yield stress is applied, it is possible to observe that the residual layer is always lower than the numerical experiment without yield stress. As the yield stress increases, the residual layer decreases for Reynolds number from 10^{-5} to 10.

8
Conclusion

In this chapter we summarize the main scientific conclusions and the novel contributions of this thesis. We then discuss briefly some of the main industrial implications of our results. Finally, we make recommendations for future work.

8.1
Viscoplastic fluid displacement

In this thesis, we analyzed experimentally and numerically the isodense displacement of a viscoplastic fluid by a less viscous Newtonian fluid in a horizontal pipe. Carbopol solution and salt or glycerol-water solution were considered as displaced and displacing fluids, respectively. In the numerical simulations, the impact of flow rate and rheological parameters of viscoplastic fluid in the displacement flow were presented. Streamline analysis, contours and distribution along the interface of the flow characteristics showed the importance of the front in the residual layer formation. We also identified that the residual layer is forged by fluids with two different shear histories that relies on the front and wall influences.

In the experimental analysis, velocity profiles and the fluids concentration field were acquired for several pair of fluids through Ultrasonic Doppler Velocimetry (UDV) and flow visualization respectively. The major flow pattern is characterized by a central displacement, with a residual layer of the displaced fluid left close to the tube wall. Moreover, three distinct flow regimes could be identified within the central flows, namely *corrugated*, *wavy* and *smooth*, depending on the level of the residual layer variation along the pipe. The transition between these flow regimes is found to be a function of the Reynolds number defined as the ratio of the inertial stress to the characteristic stress of the viscoplastic fluid. In particular, Re=0.2 and 1 for wavy-corrugated and smooth-wavy flow transitions respectively. The evaluation of the stress at the interface between the fluids showed that it remains below the yield stress, therefore the formation and modulation of the

residual layer should be governed by the dynamics happening at the frontal region of the displacement.

The isodense displacement of a viscoplastic fluid by a less viscous Newtonian fluid in a horizontal pipe were mapped in regions for both numerical and experimental data. In the numerical simulation, the regions were localized in space whereas in the experiments in time. At fully developed flow, regions *ii*, *iii* and *iv* may be associated to II, III and IV, respectively. The numerical results couldn't reflect the waviness in roughness from wavy and corrugated regimes detected in the experiments. The absence of instabilities in the numerical simulation may be associated to non-ideal characteristics of the real displaced fluids modelled as homogenous yield stress fluid without thixotropy and to the numerical model assumptions (isothermal, axisymmetry and isodensity). For smooth regime, the numerical model emulates the experimental results.

8.2
Laponite rheology

The influence of NaCl and Laponite concentrations in the rheological parameters of Laponite suspensions, mainly yield stress and thixotropy, was also detailed. The rheological tests showed the competition between aging and rejuvenation and how it affects the apparent yield stress. We showed that low yield stress values are related to rejuvenated samples and high values to aged Laponite samples.

Independently of aging time, for the same ionic strength, the yield stress of Laponite suspension increases with the Laponite concentration increment. On the other hand, for the same Laponite concentration, the apparent yield stress decreases as the ionic strength decreases.

Besides, the importance of a standard Laponite protocol for sample preparation was emphasized to guarantee a reproducible rheological similarity for different samples.

8.3
Influence of Thixotropy in the viscoplastic fluid start-up

We performed start-up experiments, transient response of a single fluid from rest when a differential pressure is applied, of yield stress and thixotropic fluids. The transient response of Laponite suspensions start-up and the thixotropy influence were described.

In all the start-up experiments, for low Reynolds numbers (<1500) at fully developed pipe flow, velocity profiles symmetry and well defined *plastic* plug were observed. Besides, the average profile in the steady state period were well represented by the theoretical profile for fully developed laminar flow of Herschel-Bulkley fluid for the same $\hat{V}_0$.

The analysis of the influence of a solenoid valve in the start-up experiments with Laponite confirmed that the fluid shear history (rejuvenation versus resting time) affects in the apparent fluid yield stress.

The comparison between start-up results of Laponite solutions, including different NaCl concentration and inlet flow velocities, showed that thixotropy delays the steady state flow development and high differential pressure implies fast transient responses for Laponite solutions with high ionic strength ($I>3.0x10^{-3}$ mol/L). On the other hand, it was not possible to identify the differential pressure influence in the plug velocity transient in the mean velocities experimental range for suspensions with low ionic concentration ($I<3.0x10^{-3}$ mol/L). The state diagram of Laponite seems to play an important role in the dimensionless time to reach steady state.

8.4
Industrial Value

One of the major motivations for our work is to better understand the displacement flows present in a pipeline restart. There exist gaps in industrial understanding of displacement flows in horizontal pipes. The key findings of the thesis in this regards are as follows.

- We identified that in the laminar regime the stationary layer is influenced by Reynolds number and as Reynolds number gets lower than one the level of residual layer variation increases;
- From the experiments results, the depth-averaged concentration is dynamically coupled to the front velocity, independently of Reynolds number;
- In region II, the interface stress between the fluids remains below the yield stress;
- The formation and modulation of the residual layer should be governed by the dynamics in region III (front influence);
- Three distinct flow regimes could be identified and their transitions is found to be a function of the ratio of the inertial stress to the characteristic stress of the viscoplastic fluid;
- The experimental results can help the design of facilities for yield stress fluid displacement and the residual layer prediction.

8.5
Future Work

The thixotropy model coupling with the displacement model is suggested as future work. Besides, the Laponite suspensions rheological characterization may be improved for thixotropy model regression. In the experimental loop, the insertion of differential pressure in the tube section and the development of a new system to control the pressure in the tank base would improve the quality of the experimental data.

To reproduce the streamline analysis developed in the numerical simulations and experimentally show the two different shear rate history in the residual layer formation, a different displacement experiments can be designed considering two colors for the same yield stress fluid. During the loop commissioning, part of the loop should be filled with a yield stress fluid with color *a* and the other part with the same yield stress fluid with color *b*.

9
Bibliography

1 VENKATESAN, R. et al. The strenght of paraffin gels formed under static and flow conditions. Chem. Eng. Sc., v. 60, p. 3587-3598, 2005.

2 FRIGAARD, I. A.; VINAY, G.; WACHS, A. Compressible displacement of waxy crude oils in long pipeline startup flows. Journal of non-Newtonian Fluid Mechanics, v. 147, p. 45-64, 2007.

3 VINAY, G.; WACHS, A.; AGASSANY, J. F. Numerical simulation of non-isothermal viscoplastic waxy crude oil flows. Journal of non-Newtonian Fluid Mechanics, v. 128, p. 144-162, 2005.

4 VINAY, G.; WACHS, A.; AGASSANT, J. F. Numerical simulation of weakly compressible Bingham flows: the restart of pipeline flows of waxy crude oils. Journal of non-Newtonian Fluid Mechanics, v. 136, p. 93-105, 2006.

5 VINAY, G.; WACHS, A.; A., F. I. Start-up transients and efficient computation of isothermal waxy crude oil flows. Journal of non-Newtonian Fluid Mechanics, v. 143, p. 141-156, 2007.

6 WACHS, A.; VINAY, G.; FRIGAARD, I. A 1.5D numerical model for the start up of weakly compressible flow of a viscoplastic and thixotropic fluid in pipelines. Journal of Non-Newtonian Fluid Mechanics, v. 159, p. 81-94, 2009.

7 DAPRA, I.; G., S. Start-up flow a Bingham fluid in a pipe. Meccanica, v. 40, p. 49-63, 2005.

8 FUNG, G. et al. To pig or not to pig: the Marlin experience with sruck pig. Offshore Technology Conference, 2006.

9 THOMASON, W. H. Start-up and shut-in issues for subsea production of high paraffinic crudes. Offshore Technology Conference, 2000.

10 PINHO, S. P. G.; R., M. J.; ZUR NEDDEN, A. G. P. Definition of shut down operational procedures for ultra-deep water extended well tests. Multiphase Production Technology, p. 165, 2011.

11 TAGHAVI, S. M. et al. Incomplete fluid-fluid displacement of yield stress fluids in near-horizontal pipes: Experiments and theory. Journal of non-Newtonian Fluid Mechanics, v. 167-168, n. 59-74, 2012.

12 ALBA, K. et al. Incomplete fluid-fluid displacement of yield stress fluids. Part 2: Highly inclined pipes. Journal of non-Newtonian Fluid Mechanics, v. 201, p. 80-93, 2013.

13 ALLOUCHE, M.; FRIGAARD, I. A.; SONA, G. Static wall layers in the displacement of two visco-plastic fluids in a plane channel. Journal of Fluid Mechanics, v. 424, p. 243-277, 2000. ISSN 1469-7645.

14 GABARD, C.; HULIN, J. P. Miscible displacements of non-Newtonian fluids in a vertical tube. Eur. Phys. J. E, v. 11, p. 231-241, 2003.

15 ALBA, K.; FRIGAARD, I. A. Dynamics of the removal of viscoplastic fluids from inclined pipes. Journal of non-Newtonian Fluid Mechanics, v. 229, p. 43-58, 2016.

16 COLE, P. A. et al. Comparison of cleaning of toothpaste from surfaces and pilot scale pipework. Food Bioprod. Process, v. 88, p. 392-400, 2010.

17 PALABIYIK, I. et al. Flow regimes in the emptying of pipes filled with a Herschel-Bulkley fluid. Chem. Eng. Res. Des., v. 92, p. 2201-2212, 2014.

18 WIELAGE-BURCHARD, K.; FRIGAARD, I. A. Static wall layers in plane channel displacement flows. Journal of non-Newtonian Fluid Mechanics, v. 166, p. 245-261, 2011.

19 ALBA, K.; TAGHAVI, S. M.; FRIGAARD, I. A. A weighted residual method for two-layer non-Newtonian channel flows:steady-state results and their stability. Journal of FLuid Mechanics, v. 731, p. 509-544, 2013.

20 MOYERS-GONZALEZ, M. et al. A semi-analytical closure approximation for pipe flows of two Herschel-Bulkley fluids with a stratified interface. Journal of non-Newtonian Fluid Mechanics, v. 193, p. 49-67, 2013.

21 SAFFMAN, P. G.; TAYLOR, G. I. The penetration of a fluid into a porous medium or Hele-shaw cell containing a more viscous liquid. Proceedings of the Royal Society of London: Mathematical, Physical and Engineering Sciences, London, v. 245, p. 312-329, 1958.

22 SAFFMAN, P. G. Viscous fingering in Hele-Shaw cells. Journal of Fluid Mechanics, v. 173, p. 73-94, 1986.

23 TAYLOR, G. I. Deposition of a viscous fluid on the wall of a tube. Journal of Fluid Mechanics, v. 10, p. 161-165, 1961.

24 FAIRBROTHER, F.; STUBBS, A. E. Studies in electroendosmosis. Part VI. The bubble-tube methods of measurement. Journal of Chemical Society, v. 1, p. 527-529, 1935.

25 COX, B. G. On driving a viscous fluid out of a tube. Journal of Fluid Mechanics, v. 14, p. 81-96, set. 1962.

26 PETITJEANS, P.; MAXWORTHY, T. Miscible displacements in capillary tubes. Part 1. Experiments. Journal of Fluid Mechanics, v. 326, p. 37-56, 1996.

27 CHEN, C. H.; MEIBURG, E. Miscible displacement in capillary tubes Part 2. Numerical simulations. Journal Fluid Mechanics, v. 326, p. 57-66, 1996.

28 DE SOUZA MENDES, P. R. et al. Gas displacement of viscoplastic liquids in capillary tubes. Journal of Non-Newtonian Fluid Mechanics, v. 145, p. 30-40, 2007.

29 TAGHAVI, S. M. et al. Miscible displacement flows in near-horizontal ducts at low Atwood number. Journal of Fluid Mechanics, v. 696, p. 175-214, 2012.

30 ALBA, K. Displacement flow of complex fluids in an inclined duct. Vancouver: University of British Columbia, 2013.

31 COUSSOT, P. et al. Avalanche behavior in yield stress fluids. Phys. Rev. Lett., v. 88, p. 1-4, 2002.

32 CUMMINS, H. Z. Liquid, glass, gel: the phases of colloidal Laponite. Non-Crystalline Solids, v. 353, p. 3891-3905, 2007.

33 BONN, D. et al. Laponite: What is the difference between a gel and a glass? American Chemical Society, v. 15, p. 7534-7536, 1999.

34 ESCUDIER, M. P.; PRESTI, F. Pipe flow of a thixotropic liquid. Journal of non-Newtonain Fluid Mechanics, v. 62, p. 291-306, 1996.

35 MOURCHID, A. et al. Phase diagram of colloidal dispersions of anisotropic charged particles: equilibrium propperties, structure, and rheology of Laponite suspensions. Langmuir, p. 1942-1950, 1995.

36 MOURCHID, A.; LECOLIER, E.; VAN DAMME, H.. L. P. On viscoelastic, birefringent, and swelling properties of Laponite clay suspensions: revised phase diagram. Langmuir, v. 14, p. 4718-4723, 1998.

37 TANAKA, H.; MEUNIER, J.; BONN, D. Nonergodic states of charged colloidal suspensions: repulsive and attractive glasses and gels. Physical Review, v. 49, 2004.

38 RUZICKA, B.; ZULIAN, L.; RUOCCO, G. More on the phase diagram of Laponite. Langmuir, v. 22, p. 1106-1111, 2006.

39 MONGONDRY, P.; TASSIN, J. F.; NICOLAI, T. Revised state diagram of Laponite dispersions. Journal of Colloid and Interface Science, v. 283, p. 397-405, 2005.

40 LABANDA, J.; LORENS, J. Influence of sodium polyacrylate on the rheology of aqueous Laponite dispersions. Journal of Colloid and Interface Science, v. 289, p. 86-93, 2005.

41 POSLINSKI, A. J.; OEHLER, P. R.; STOKES, V. K. Isothermal gas-assisted displacement of viscoplastic liquids in tubes. Polym. Eng. Sci., v. 35, p. 877-892, 1995.

42 DIMAKOPOULOS, Y.; TSAMOPOULOS, J. Transient displacement of a viscoplastic material by air in straight and suddenly constricted tubes. Journal of non-Newtonian Fluid Mechanics, v. 112, p. 43-75, 2003.

43 DIMAKOPOULOS, Y.; TSAMOPOULOS, J. On the gas-penetration in straight tubes completelely filled with a viscoelastic fluid. Journal of non-Newtonain Fluid Mechanics, v. 117, p. 117-139, 2004.

44 DE SOUZA MENDES, P. R.; DUTRA, E. S. S. Viscosity Function for Yield-Stress Liquids. Journal of Applied Rheology, v. 14, n. 6, p. 296-302, 2004.

45 DE SOUSA, D. A. et al. Numerical investigation on gas-displacment of a shear-thinning liquid and a visco-plastic material in capillary tubes. Journal of non-Newtonian Fluid Mechanics, v. 144, p. 149-159, 2007.

46 THOMPSON, R. L.; SOARES, E. J.; BACCHI, R. D. A. Further remarks on numerical investigation on gas displacement of a shear-thinning and visco-plastic material in capillary tubes. Journal of non-Newtonian Fluid Mechanics, v. 165, p. 448-452, 2010.

47 FREITAS, J. F.; SOARES, E. J.; THOMPSON, R. L. Viscoplastic-viscoplastic displacement in a plane channel with interfacial tension effects. Chem. Eng. Sci., v. 91, p. 54-64, 2013.

48 SWAIN, P. A. P. et al. Numerical simulation of pressure-driven displacement of a viscoplastic material by a Newtonain fluid using lattice Boltzmann method. Eur. J. Mech. B-Fluid, v. 49, p. 197-207, 2015.

49 ALBA, K.; TAGHAVI, S. M.; FRIGAARD, I. A. Miscible density-unstable displacement flows in inclined tube. Phys. FLuids, v. 25, p. 1-21, 2013.

50 BERTOLA, V. et al. Wall slip and yileding in pasty materials. Journal of Rheology, v. 47, p. 1211-1226, 2003.

51 HUANG, K. et al. Experimental investigation in friction factor in pipes with large roughness. Exp. Therm. Fluid. Sci., v. 50, p. 147-153, 2013.

52 ABOU, B.; BONN, D.; MEUNIER, J. Aging dynamics in a colloidal glass of Laponite. Physics, 2001.

53 RAVI KUMAR, N. V. N.; MURALIDHAR, K.; JOSHI, Y. M. On the refractive index of ageing dispersions of Laponite. Applied Clay Science, v. 42, p. 326-330, 2008.

54 ABOU, B.; BONN, D.; MEUNIER, J. Nonlinear rheology of Laponite suspensions under external drive. Journal of Rheology, v. 47, p. 979-988, 2003.

55 BONN, D. et al. Laponite: aging and shear rejuvenation of a colloidal glass. Physical Review Letters, v. 89, 2002.

56 BARNES, H. A. Thixotropy - a review. Journal of Non-Newtonian Fluid Mechanics, v. 70, p. 1-33, Janeiro 1997.

57 NGUYEN, Q. D.; BOGER, D. V. Thxitropic behaviour of concentrated bauxite residue suspensions. Rheol. Acta, v. 24, 1985.

58 JOSHI, Y. M. et al. Rheological behaviour of aqueous suspensions of Laponite: new insights into the ageing phenomena. The Royal Society, v. 464, 2007.

59 TARCHA, B. A. et al. Critical quantities in the yielding process of waxy crude oils. Rheologica Acta, v. 54, p. 479-499, 2015.

60 TIU, C.; BOGER, D. V. Complete rheological characterization on time-dependent food products. Journal Texture Stud., v. 5, 1974.

61 DE SOUZA MENDES, P. R. Thixotropic elasto-viscoplastic model for structured fluids. Soft Matter, n. 7, p. 2471–2483, 2011. ISSN DOI: 10.1039/c0sm01021a.

62 DE SOUZA MENDES, P. R.; THOMPSON, R. L. A Unified Approach to Model Elasto-viscoplastic Thixotropic Yield-stress Materials and Apparent Yield-stress Fluids. Rheol Acta, Berlin, 23 Abril 2013. 22.

63 SOTO, R. J.; SHAH, V. L. Entrance flow of yield-power law fluid. Appl. Sci. Res., v. 32, p. 73, 1976.

64 HOUSKA, M. Engineering aspects of the rheology of thixotropic liquids. PhD Thesis. ed. [S.l.]: Czech Technical University of Prague, 1981.

65 LIMA, D. D. S. Startup flow of gelled crudes after a shutdown comparison between simulations and experimental data. Pontifícia Universidade Católica do Rio de Janeiro, Departamento de Engenharia Mecânica. Rio de Janeiro: [s.n.]. 2015. p. 132.

66 ALENCAR, L. S. Numerical simulation of the restart problem for thixotropic fluids. Puc-Rio, Rio de Janeiro, 2016.

67 ANSYS INC. Ansys Help 15.0. [S.l.]: [s.n.], 2013.

68 PAPANASTASIOU, T. C. Flows of Materials with Yield. Journal of Rheology, v. 31, p. 385-404, 1987. ISSN 10.1122/1.549926.

69 GABARD, C. Etude de la stabilité de films liquides sur le parois d'une conduite verticale lors de l'ecoulement de fluides miscibles non-Newtoniens. Phd Thesis, Orsay, 2001.

70 CROSS, M. M. Rheology of non-Newtonian fluids: a new flow equation for pseudoplastic systems, v. 20, 1965.

10
Appendix A - Experimental procedures

10.1
Flowmeter calibration

The fluids discharge mass ($\widehat{w}$) during each experiment and the fluids densities are considered in the flowmeter calibration procedure. The flow rate is recorded using a magnetic flow meter (Omega, low-flow type) that can be applied to fluids with varying viscosities and densities whose conductivity is higher than 20 μS. The flow rate output signal is connected to National Instrument board PCI/PXI-6221 (68-Pin).

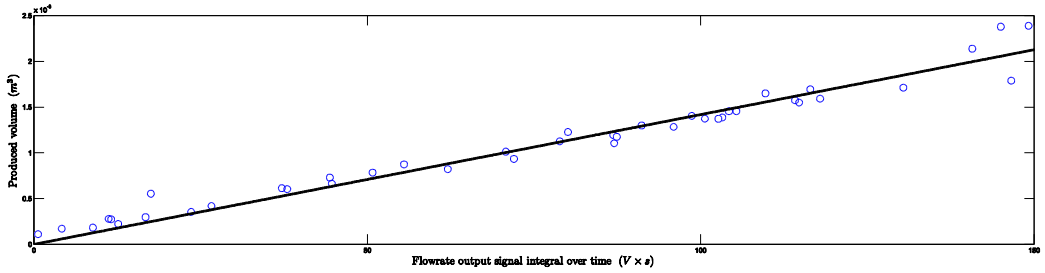

Figure 10-1:Volume versus output flow rate integral for carpool 0.07%.

The flow rate calibration consists of computing a linear regression between the integral of the flow rate output signal (Volts.s) and the discharge fluids volume ($\widehat{Vol} = \widehat{w}/\hat{d}$). The data points of 0.07% Carbopol batch and its respectively linear regression can be seen in the figure 10-1.

Table 10-1: Linear coefficient for different Carbopol concentration.

Carbopol Concentration [%]	Linear Coefficient [10-6 m3/V.s]
0.07	14.4
0.08	14.8
0.09	16.4
0.10	17.2
0.11	20.5

Each fluid batch has a specific linear coefficient that correlates the output voltage to the flow rate. The accuracy of the flowmeter calibration can be inferred by the standard deviation of the linear coefficient. Table 10-1 present the linear coefficient for different carbopol concentration.

10.2
Visualization measurement

Video recordings of the displacement are realized simultaneously to provide quantitative image analysis and extract information regarding the large-scale features of the flow such as the velocity of the displacing front. The same image acquisition and processing system has been applied by Taghavi et al. (2012) [29] and Alba (2013) [30]. The imaging system consist of 2 high-speed digital cameras with 4096 gray-scale levels (basler Scout scA1600 and scA1400) with images recorded at a frequency of 3 Hz. Stripes of Light Emitting Diode (LED) have been used along with light diffusers in order to provide homogeneous lighting. To reduce light refraction errors and further enhance the quality of the images, two *fish* tanks have been also placed around the main pipe.

The cameras are positioned to ensure that the front pipe view is captured and two points of reference are considered to match the size of the captured image and the real object.

10.2.1
Light absorption calibration procedure

To guarantee an exponential dependency between the light intensity and the ink concentration, a light absorption calibration procedure defined in Alba (2013) [30] is necessary to determine the ink concentration of fluid 2. The calibration procedure consists of calculating the light intensity in the tube for different ink concentrations. Considering the same lighting scenario, the mean light intensity is calculated in the net pipe area (area that will be considered for image processing) for each *fish* tank for different ink concentration. As can be seen in the semilog plot in figure 10-2, for low ink concentration, there is as an exponential decay of the pipe average light intensity when the ink concentration increases.

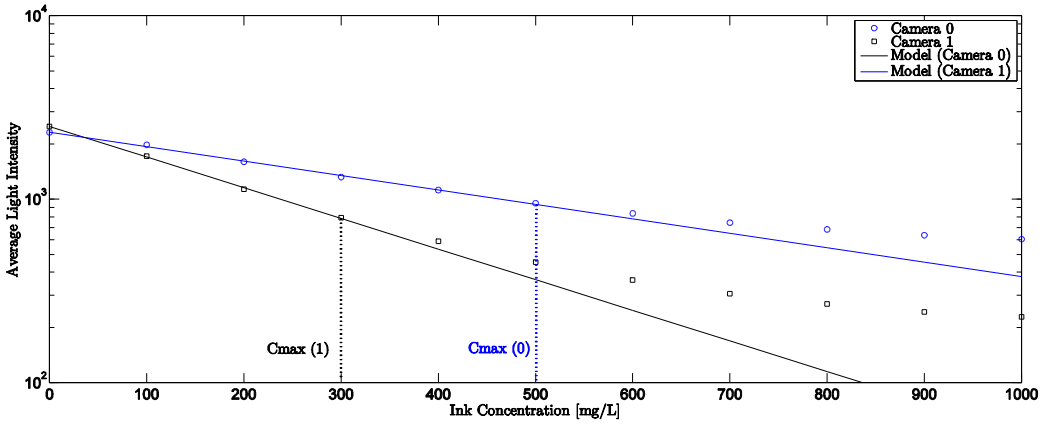

Figure 10-2: Average Light Intensity versus ink concentration for each set of camera and fish tank.

The maximum ink concentration (C_{max}) defines the application limit of the exponential model. In our experiments two maximum ink concentrations are obtained one for each set of camera and *fish* tank. The lower concentration is considered since the black fluid flows inside both fish tanks. In our case the maximum concentration ink that could be added was found to be 300 mg/L as shown in figure 10-2.

10.2.2
Image Post Processing

Once the images are recorded, if an exponential dependency of the light intensity on ink concentration is considered, it is possible to convert the light intensity in a normalized concentration varying from 0 to 1:

$$\hat{I} = \hat{\beta}_L exp^{\hat{\alpha}_L C}, \qquad 10\text{-}1$$

where $\hat{I}$ and C are light intensity and fluid concentration respectively and $\hat{\beta}_L$ and $\hat{\alpha}_L$ physical constant.

For the light intensity conversion it is necessary to take two reference photos: pure fluid 2 photo (displaced fluid) and pure fluid 1 photo (displacing fluid). For C=0 (pure displaced fluid), the constant $\hat{\beta}_L$ will be equal to the light intensity for the pure fluid 1 reference photo ($\hat{I}^0$).

For C=1 (pure displacing fluid), the constant $\hat{\alpha}_L$ can be calculated from

$$\hat{\alpha}_L = \log\frac{\hat{I}^1}{\hat{\beta}_L} = \log\frac{\hat{I}^1}{\hat{I}^0} \qquad 10\text{-}2$$

where $\hat{I}^1$ is the light intensity for the pure fluid 1 reference photo. Instead of calculating the average of the physical constants along the tube, the constants are calculated for every pixel to minimize tube defects such as color spots and marks. As a result, the pixel light intensity is converted to a normalized concentration value varying from 0 (pure displaced fluid or fluid 1) to 1 (pure displacing fluid or fluid 2).

Consider the image of a tube section $S=(1{:}n_x, 1{:}n_y)$, its pure fluid 1 reference image $S^0=(1{:}n_x, 1{:}n_y)$, and its pure fluid 2 reference image $S^1=(1{:}n_x, 1{:}n_y)$ where n_y represents the number of pixel in the vertical axis, n_x the number o pixels in the horizontal axis, and $n_p=n_x\, x\, n_y$ the number of pixels in the section, the normalized concentration of each pixel (x,y) in the section can be described as

$$C^S(x,y) = \frac{1}{\hat{\alpha}_L(x,y)} \log \frac{\hat{I}^S(x,y)}{\hat{\beta}_L(x,y)} \qquad 10\text{-}3$$

for $x=\{1,2...,n_x\}$ and $y=\{1,2,...,n_y\}$ where $\hat{\beta}_L(x,y) = I^{S_0}(x,y)$ and $\hat{\alpha}_L(x,y) = \log \frac{I^{S_1}(x,y)}{I^{S_0}(x,y)}$.

The images are recorded at a frequency of $\hat{f}$=3 Hz. If $\hat{t}_{exp}$ is the time of the experiment in seconds, the total number of images (N) taken during the experiments is going to be $N = \hat{t}_{exp} \times \hat{f}$ and its discrete time sequence ($\hat{t}$) can be described as $\hat{t} = \frac{k}{\hat{f}}$ for k=1,..,N.

For every experiment the normalized concentration in a section S can be described as

$$C^S(\hat{t},x,y) = \frac{1}{\hat{\alpha}_L(x,y)} \log \frac{I^S(\hat{t},x,y)}{\hat{\beta}_L(x,y)} \qquad 10\text{-}4$$

for $x=\{1,2...,n_x\}$, $y=\{1,2,...,n_y\}$, and $\hat{t} = \frac{1}{\hat{f}}, \frac{2}{\hat{f}}, \ldots, \frac{N}{\hat{f}}$.

Once the light calibration is performed, images obtained at regular time intervals during the experiment are post processed to give calibrated snapshots of the concentration. One way to represent the interface evolution is shown in figure 10-3 where the concentration in a section S for different time stamps is presented. It is possible to identify the fluid 1 moving from the left to the right and the residual layer formation of fluid 2 after the fluid 1 passage.

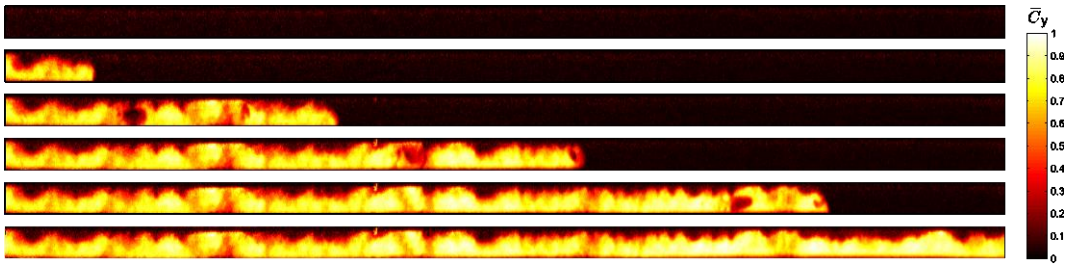

Figure 10-3: Example of the interface evolution where every rectangle represents a different time stamp. The time advance from top to bottom.

In addition, an image processing algorithm that compares the difference between two reference images is applied to identify the tube wall. Firstly, a rectangular area near the pipe is selected. Secondly, the algorithm compares the two references photos (fluid 1 and fluid 2) and identify the pixel area where the light intensity changed (area inside the pipe). An example of the pipe identification of a section S is presented in figure 10-4.

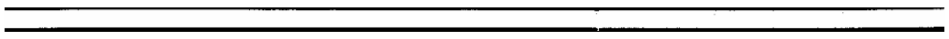

Figure 10-4: Example of pipe identification algorithm.

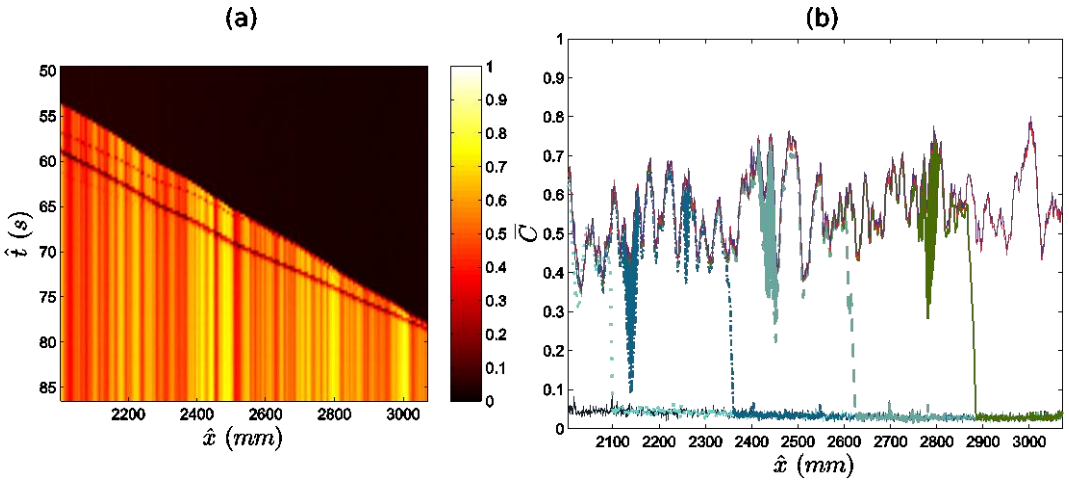

Figure 10-5: (a) Example of a spatioltemporal diagram; (b) $\overline{C}_y^S$ along the tube for $\hat{t}$=55.0s (dotted line); $\hat{t}$=60.5s (dotted-dashed line); $\hat{t}$=66.0s (dashed line); $\hat{t}$=71.5s (continuos line). Shaded areas represents the washed fluid.

The spatiotemporal diagram is another way to represent the concentration evolution in a pipe section and is based on the averaged concentration profiles along the pipe given by:

$$\overline{C}_y^S(\hat{t},x) = \frac{\sum_{i=1}^{n_y} C^S(\hat{t},x,y)\hat{A}_y}{\frac{\Pi\widehat{D}^2}{4}} \qquad 10\text{-}5$$

where $\hat{A}_y$= circular area related to the pixel at y for x={1,2...,n_x}, y={1,2,...,n_y} , and $\hat{t} = \frac{1}{\hat{f}}, \frac{2}{\hat{f}}, \ldots, \frac{N}{\hat{f}}$. Examples of a spatiotemporal diagram and $\overline{C}_y^S$ along the tube for specific time stamps are presented on figures 10-5.a and 10-5.b, respectively.

From figure 10-5.b is possible to identify change in concentration along the tube marked with shaded areas. These areas represent residual layer that has been washed after the front passage.

As described by Taghavi et al. (2012) [29], the position of the displacing front in a spatiotemporal plot is defined by the boundary between the dark and light regions with its slope being inversely proportional to the front velocity. The mean concentration of section S in a discrete time $\hat{t}$ can be calculated as

$$\overline{C}^S(\hat{t}) = \frac{\sum_{x=1}^{n_x} \overline{C}^S(\hat{t}, x)}{n_x} \qquad 10\text{-}6$$

where n_x represents the number of discrete elements of the section length.

The front velocity estimative is based on the mean concentration evolution. When the front is far away, the mean concentration is zero (black fluid). As the front passes, the mean concentration increases. The change in the mean concentration from zero defines when the front reaches a specific position ($\hat{x}$) along the tube section (*S*).

Due to the stochastic characteristic of the light intensity, it is necessary to introduce a threshold to detect the mean concentration variation from zero. If the threshold is close to zero any small disturbance will influence the front detection. On the other hand, if the threshold is very high, the concentration change may not represent the front passage. For every experiment a tradeoff should be considered to find the minimum threshold that can provide an accurate front detection.

The front detection algorithm identify where in the pipe the front is in a specific time stamp. So, it is possible to identify the position of the front in the tube along time. Thus, the front velocity and its error can be calculated from the derivative of the front position versus time. The front evolution, is presented on figure 10-6.a and front vrlocity in figure 10-6.b.

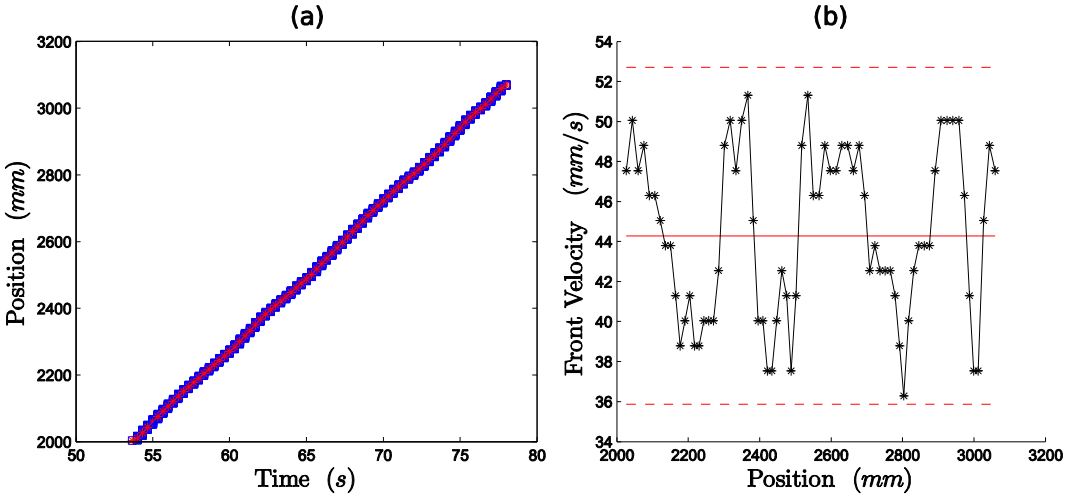

Figure 10-6: Example of front evolution over time: (a) Front position for every time stamp; (b) Front velocity: data points (*), mean front velocity (red continuous line) and interval of confidence of 95% (dashed line).

10.3
Velocity Measurement – UDV

Supplementary velocity field measurement is achieved using an Ultrasonic Doppler Velocimeter (UDV) probe that is placed in between the two *fish* tanks. The UDV used is DOP2000 (model 2125, Signal Processing SA) with 8 MHz, 5 mm (TR0805LS) transducers at a duration of 0.5μs. This velocimetry technique does not require any transparent medium and a non-intrusive approach is considered. The probe is mounted outside the pipe. In this case the slightly diverging ultrasonic beam enters the fluids by first going through a 3.175 mm-thick plexiglass pipe wall. The axial resolution is around 0.375mm and the lateral resolution is equal to the transducer diameter (5mm) but varies slightly with depth due to divergence.

The UDV technique is based on sending the sound pulse and receiving its echo and allows measurement of the flow velocity projection on the ultrasound beam, on real time. This projection therefore gives only the stream wise component of velocity. Thus it is important to know exactly the relative angle between the probe and the pipe axis. The instrument sends a series of 4-cycles of short bursts and records the echoes back scattered from the particles suspended in fluids. For tracking particles, we have used polyamid seeding particles with a mean particle diameter of 50 micrometer and a volumetric concentration equal to 0.2 g/L in both fluids to obtain robust UDV echo. Through the time elapsed between the pulse and the received echo, the distance of the particles from the transducers is computed;

meanwhile the associated increased/decreased Doppler frequency shift gives the value of the velocity at each distance. Reflection effects at pipes wall, mainly the lower wall, affect the velocity measurement locally and makes it hard to measure a zero velocity at the walls.

The acquisition time of the velocity profiles is not considered constant for all experiments. For experiments with high mean velocities, lower acquisition time is considered. In this case, the signal noise ratio increases when the acquisition time is reduced. No real time signal filter is applied during the recording process.

The probe is mounted at an angle in the range 60 - 80 degrees relative to the axis of the pipe considering the compromise between a good signal-to-noise ratio and small ultrasonic signal reflections. Although we tried to keep the probe steadily during the experiments, after the UDV processed analysis, we realized that in some experiments its position was slightly altered. The change in the probe position was diagnosed by a small deviation of the plug plateau. Instead of a flat, a slightly deviation was detected in a few experiments.

To provide a better understanding of the UDV results, instead of using the raw UDV data, the UDV profiles are multiplied by a velocity correction factor.This correction considers the ratio between plug velocity from UDV and from the steady state solution of Herschel-Bulkley fluid flowing in a pipe for the experiment mean velocity. The correction factor overcomes other UDV limitation, the sound velocity definition for more than one fluid, including a yield stress one, since the sound velocity influences the velocity modulus and the axial range. The UDV is a supplementary experimental data and can only be used as a qualitative measure.

The UDV coordinate system is transformed to guarantee the center of the tube as the system origin. The ordinate axis will be represented by the UDV beam oriented from the center to the UDV probe. So if the position $\hat{r}$ is located between the tube center and the probe, $\hat{r} > 0$, otherwise, $\hat{r} < 0$.

10.3.1
UDV Post Processing

Velocity contour figures shows dimensionless velocity modulus ($U = \widehat{U}/\widehat{V}_0$) for different position ($r = 2\hat{r}/\widehat{D}$) as a function of time ($\hat{t}$). In start-up experiment, the maximum velocity is the plug velocity at steady state (figure 10-7.a) and in the

displacement experiment, the maximum velocity of the fluid 1 flowing inside the residual layer of fluid 2 (figure 10-7.b). The reference time $\hat{t}$=0s represents the moment that a differential pressure is applied to the loop.

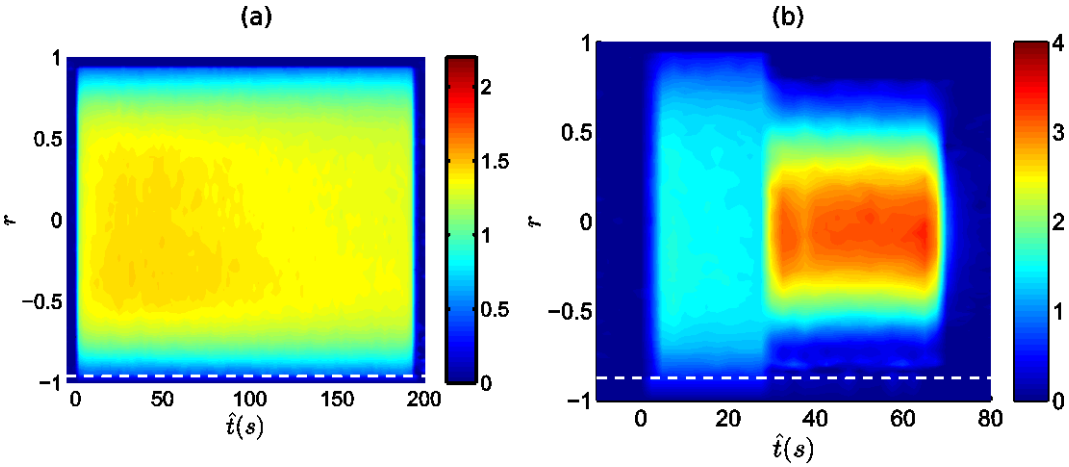

Figure 10-7: Velocity contour example of carbopol: (a) start-up experiment; (b) displacement experiment.

Due to the nature of the UDV measurements there is always some refraction errors, mainly close to the lower wall of the pipe. To provide better understanding of the UDV data, the corresponding data points to the lower wall were suppressed and a model prediction is added. This area is marked by dashed line.

The UDV system is set to acquire data points in a high frequency and an average filter routine was developed to treat the data and smooth the noise. Figure 10-8 shows the filter application considering different average frequency for a specific start-up experiment. Most of the contour velocity figures in this thesis will present an average for every 10 samples.

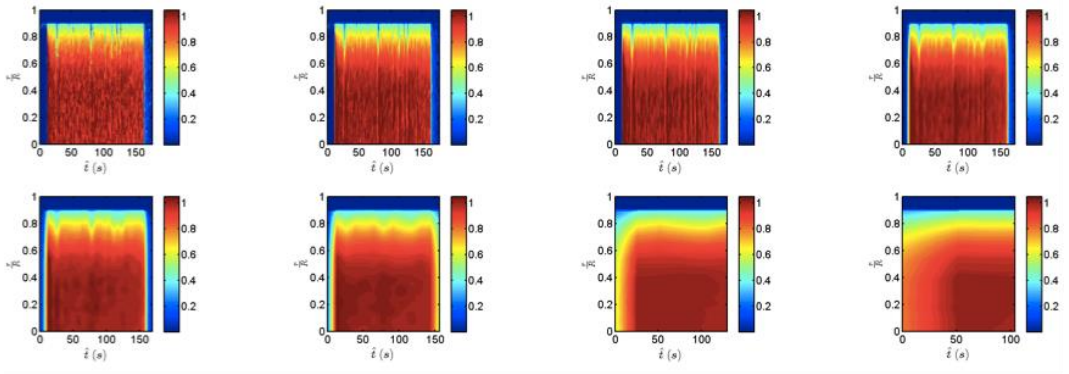

Figure 10-8: Impact of filtering in the velocity contour of an start-up experiment.

Another way to interpret the UDV data is to study the streamwise velocity as a function of time at an averaged radial position, as shown in figure 10-9 where every symbol represents a specific position *r*.

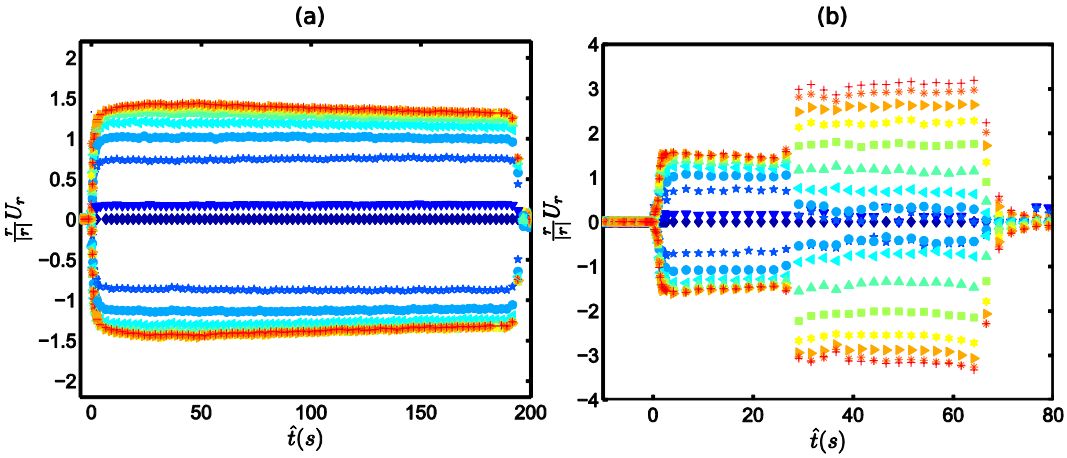

Figure 10-9: Example of streamwise velocity as a function of time at an averaged radial position for carbopol: (a) start-up experiment; (b) displacement experiment. Different symbols represent a position r: 0.0 (+), 0.1(*), 0.2(►), 0.3(●), 0.4(□),0.5(▲), 0.6(◄), 0.7(○), 0.8(★), 0.9 (▼) and 1.0 (◊).

A matlab routine was developed to show velocity profiles in a given time frame where the velocity is averaged in each time interval. This type of graph shows the velocity profile evolution during transient and/or steady state solutions as illustratedin figure 10-10.a and 10-10.b, respectively.

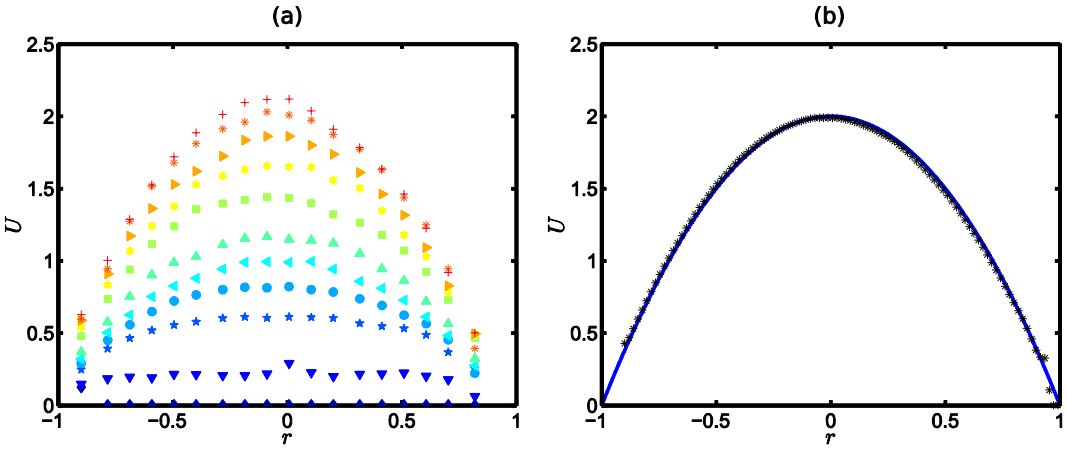

Figure 10-10: Velocity profile for Laponite suspension of 1.5% and I=3x10^{-3} mol/L for $\hat{V}_0$=57.9 mm/s: (a) Transient response for $\hat{t}$ equal to 0.6(◊), 1.2(▼), 1.8(★), 3.0(○), 3.6(◄), 4.2(▲), 4.8(□), 5.4(●), 6.0(►), 6.6(*) and 7.2(+);b) Average velocity profile for 8<$\hat{t}$<170s (*). Steady state solution of Newtonian fluid in a pipe for $\hat{K}$=0.007 Pa.s.(continuous line).

11
Appendix B - Thixotropy Models

In the thixotropy literature there are a great diversity of models, Barnes (1997) [56] did an extensive review over thixotropy and grouped the current viscous theories for thixotropy into three major groups: indirect microstructural, direct structure and simple viscosity.

For Barnes (1997) [56] the indirect microstructural theories use a very general description of microstructure described by a numerical value of a scalar parameter, typically λ, and then use $d\lambda/dt$ as the working parameter. Using this simplistic cypher, completely built structure is represented by $\lambda = 1$ and completely broken-down structure as $\lambda = 0$. In the simplest case of a typical, inelastic, non-Newtonian liquid with upper and lower Newtonian viscosity plateaus, $\lambda = 1$ corresponds to η_0 and λ_0 corresponds to η_∞, with points between taking intermediate values. Then the structural parameter is usually modelled via an evolution equation, $d\lambda/dt$, which is given by the sum of the buildup and breakdown terms. The next step in this kind of approach is to relate the structure λ to viscosity $\eta(\lambda)$.

The direct structure theories attempt some direct description of the temporal change of microstructure as for instance, the number of bonds, or an attempt at describing real floc architecture using fractal analysis.

The simple viscosity theories use the viscosity time data itself where viscosity is a direct measure of structure.

Barnes (1997) [56] says that almost any viscoelastic theory can have thixotropy introduced if the particular parameters that give the viscous and elastic responses are made to change in the way we have described for purely viscous behavior.

The next sections present a few models found in literature as examples of viscous theories for thixotropy.

11.1
Degree of Jamming

A simple model proposed by Coussot et al. (2002) describes the competition between aging and rejuvenation. The concept of the degree of jamming (λ), indirect microstructure theory, is applied , a single parameter that represents, for instance, the degree of flocculation for clays, is a measure of the free energy landscape for glasses, or gives the fraction of particles in potential wells for colloidal suspensions. For an aging system at rest, λ increases at a constant rate $1/t_\tau$ where t_τ is the characteristic time of evolution of the structure (build up term). The rate of decrease of λ under shear is assumed proportional to both the shear rate and the degree of jamming, (breakdown term) leading to an evolution equation for λ.

$$\frac{d\lambda}{dt} = \frac{1}{t_\tau} - \alpha\lambda\dot{\gamma} \qquad 11\text{-}1$$

To relate flow and structure, as a general viscosity function is considered

$$\eta = \eta_0[1 + \lambda^n] \qquad 11\text{-}2$$

when the structure is entirely destroyed, η tends towards an asymptotic value η_0. For high shear rates, the fluid behaves as a Newtonian fluid.

In steady state it follows that

$$\lambda_{ss} = \frac{1}{\alpha t_\tau \dot{\gamma}}, \qquad 11\text{-}3$$

so that the steady state shear stress writes

$$\sigma_{ss} = \eta_{ss}\dot{\gamma} = \eta_0\dot{\gamma}[1 + (\alpha t_\tau \dot{\gamma})^{-n}] \qquad 11\text{-}4$$

for:

- n < 1 the fluid has no yield stress and it is a simple shear-thinning fluid ($\sigma \to 0$ when $\dot{\gamma} \to 0$);
- n =1 represents ideal yield stress fluids (σ tends to a finite value $\frac{\eta_0}{\alpha\tau}$ when $\dot{\gamma} \to 0$);
- n >1 represents yield stress fluids when $\sigma \to \infty$.

The model thus shows that the competition between aging and shear rejuvenation directly leads to a viscosity that does not diverge when the flow velocity goes to zero but jumps discontinuously to infinity at a critical stress, in accordance with the rheological measurements. Consequently, when a constant

shear rate rather than a constant stress is applied to the material, stable homogeneous flows can occur only when $\dot{\gamma}$ is greater than $\dot{\gamma}_c$. For smaller shear rates the flows are unstable; in practice, the material will either fracture or produce shear banding instabilities (shear localization).

The viscosity is a function of η_0 and *n*, constants parameters and λ that evolves with time. The problems is that λ is an unobserved state that cannot be measured, only estimated $\lambda(t, \eta, \dot{\gamma})$.

11.2
Kinetic Models

Kinetic models proposed by Labanda and Lorens (2005) [40] to describe thixotropy can predict the evolution of viscosity over time at constant shear rate, after sudden changes of the shear rates (simple viscosity theory). One of the first models to describe thixotropy was postulated by Cross (1965) [70]. This model is based on a first-order kinetic equation with a reversible reaction of breakdown and build-up of aggregates.

$$\frac{d\eta}{dt} = k_1(\eta - \eta_e) \qquad 11\text{-}5$$

Later, a second-order kinetic equation was postulated by Tiu and Boger (1975) [60]. This second-order kinetic equation is mathematically expressed as follows,

$$\frac{d\eta}{dt} = k(\eta - \eta_e)^2 \qquad 11\text{-}6$$

where η is the viscosity, *t* is the time, *k* is the kinetic constant, and η_e is the equilibrium viscosity at the applied shear rate. The breakdown process is represented by a definite value of *k*, k_{down}, and the build-up process by k_{up}, which is usually negative. The buildup has been found to be faster than the break-down. The evolution of viscosity over time can be obtained by integrating Equation 11-6,

$$\frac{(\eta - \eta_e)}{(\eta_i - \eta_e)} = \frac{1}{1 + k(\eta_i - \eta_e)t} \qquad 11\text{-}7$$

where η is the instantaneous viscosity, η_i is the viscosity just after the sudden change of the shear rate, when t = 0, and η_e is the equilibrium viscosity for the shear

rate of this period. The value of the normalized viscosity, $(\eta - \eta_e)/(\eta_i - \eta_e)$, ranges from 1 (for t = 0) to 0 (for t tending to infinite).

Labanda e Lorens (2005) [40] showed that the kinetic constants, k_{down} and k_{up}, depend on applied shear rate and the shear rate power law dependence of both kinetic constants. Thus, the second-order kinetic equation can be rewritten as

$$\frac{(\eta - \eta_e)}{(\eta_i - \eta_e)} = \frac{1}{1 + \alpha\dot{\gamma}^{\beta}(\eta_i - \eta_e)t} \qquad 11\text{-}8$$

where α and β are kinetic parameters collected by α_{down} and β_{down} for the breakdown process, and α_{up} and β_{up} for the build up process.